

ZnSe-based laser diodes with quaternary CdZnSSe quantum wells as active region:

- Chances and limitations -

Matthias Klude



A dissertation submitted in partial satisfaction of the requirements for the degree of Doktor der Naturwissenschaften.

Contents

In	trodu	iction		V
1	Bacl	kgroun	d and prerequisites	1
	1.1	•	cs of semiconductor lasers	1
		1.1.1	Electromagnetic wave inside a crystal	
		1.1.2	Fabry-Pérot cavity filled with a gain medium: condition for lasing	4
	1.2	Desig	n of a semiconductor laser diode	7
	1.3		-VI material system ZnSe	
		1.3.1	Physical properties	
		1.3.2	Epitaxy	
		1.3.3	Defects	
		1.3.4	Alloys	15
		1.3.5	Doping	19
	1.4	State	of the art and solved problems	
		1.4.1	History of ZnSe-based laser diodes	
		1.4.2	GaAs/ZnSe heterointerface: growth start	
		1.4.3	p-type doping	
		1.4.4	p-side contact	
		.	tel te deutenne en dieten deud dientere	29
2	2.1		atal techniques and standard devices	
	2.1		cular beam epitaxy	
		2.1.1	Principle of operation	
		2.1.2	The Bremen MBE system	
		2.1.3	Calibration of the growth parameters	
	2.2	2.1.4	Standardization of the growth process	
	2.2 2.3	Devic	e processing	38
	2.3			
		2.3.1 2.3.2	Layer sequence	
		2.3.2	Growth	
		2.3.4	Structural and optical characterization	
			Electrical and electro-optical characterization	
		2.3.3	Reproducibility	56
3	Deg	radatio	on in ZnSe-based laser diodes	63
	3.1	Initial	observations	63
	3.2		defects	65
		3 2 1	Experimental observations	65

Contents

		3.2.2 Microscopic nature and generation of new defects 67
	3.3	Dynamics of recombination enhanced defect reaction
		3.3.1 Defect generation mechanisms and long-term behavior
		3.3.2 Experimental verification
		3.3.3 Analytical solution
	3.4	Driving forces of the degradation mechanism
		3.4.1 p-type doping
		3.4.2 Strained quantum well and Cd diffusion
		3.4.3 Current injection and accumulation of heat
	3.5	Improving the quantum well stability
		3.5.1 Alternative growth modes
		3.5.2 Low-temperature growth
		3.5.3 Strain reduction in the active region
		3.5.4 Sony's approach
	3.6	High-power operation
	3.7	Summary
	0.,	
4	Adv	anced processing technologies 9'
	4.1	Overview
	4.2	Top-down mounting
		4.2.1 Idea and background
		4.2.2 Pelletizing of laser bars
		4.2.3 Design of the heat sink
		4.2.4 Solder
		4.2.5 Results and outlook
	4.3	High-reflectivity facet coating
		4.3.1 Dielectric mirrors
		4.3.2 Influence on the threshold current density
	4.4	Summary
5		loring the limits and possibilities of Cd-rich quantum wells
	5.1	Motivation
	5.2	Growth optimization
	5.3	Quantum wells
	5.4	First laser diodes emitting at 560 nm
	5.5	Operational characteristics in comparison: 500 nm vs. 560 nm emission 112
	5.6	Degradation
	5.7	Summary
6	An a	alternative approach: CdSe quantum dots 12
U	6.1	Quantum dot laser
	6.2	Self-organized growth of CdSe quantum dots
	6.3	CdSe quantum dot stacks as active region
	0.5	6.3.1 Design of the active area and structural characterization
		6.3.2 Electroluminescence
	6.4	Lasing operation
	6.5	U 1
	0.3	Degradation

	าท	te	n.	tc
~	_,,,	··		L

	6.6	Outloo	ok	 138
Su	ımma	ry and	conclusion	141
A	Exte	rnally	processed devices	145
	A.1	Ridge	waveguide by ion implantation	 145
		A.1.1	Lateral index guiding	 145
			Implantation-induced disordering	
			Technological realization	
			Results	
	A.2		ex-situ p-side contacts	
			Idea	
			Results and discussion	
	A.3		buted feedback laser	
			Longitudinal mode control	
			DFB laser fabrication	
			Characterization	
	A.4		summary and outlook	
В	Inde	ex of las	ser structures	16 1
C	Pub	lication	าร	163
	Bibl	iograpl	hy	17 1

Introduction

The beginning of the 21st century is marked by a tremendous change in communication technology. With the development of *data communication technologies*, a new area has begun – connecting the mass communication systems radio, television, and telecommunication with computer technology. Thus, information becomes available – for everyone, always, and everywhere. The medium that provides this new flexibility is the internet; the backbone of the internet is data communication. Given the vast amount of information that is transfered, the transmission has to be as fast as possible. Consequently, optical data transmission provides the foundation of this new form of communication, so that the new century is sometimes referred to as the *century of the photon* [1].

But the transmission of data is only one aspect – it is of equal importance to store the data. Again, light provides the solution. *Optical data storage* systems allow to store information with a high density and fast access. Both applications have in common that they pose special requirements to the *light source*. Its light has to be as monochromatic as possible and of defined color, of high intensity, and easy to focus – even over long distances. In addition, the source should be small, efficient, robust, and cheap. A light source that satisfies all these conditions is the *semiconductor laser diode*: lasers provide *light amplification by stimulated emission of radiation*, which results in monochromatic, coherent light of high intensity; semiconductor technology allows mass-production of small devices with high reliability. Thus, the semiconductor laser diode is the ultimative light source of the communication age.

The use of semiconductor lasers is not limited to communication systems. Other applications include systems for environmental detection, health science, biotechnology, medicine, and even production [1]. The most attractive and fascinating application, however, is reserved for the special set of laser diodes – devices that produce the three primary colors red, green, and blue: *display technology*. Using lasers, new, sharp, and brilliant displays with a color spectrum, never seen before, can be fabricated – in a size smaller than a box of cigars.

The first electrically pumped semiconductor laser diodes were realized in 1962. In the last 40 years, these devices transformed from pure academic curiosities to commercial products that can be found in almost every household nowadays. Commercially available laser diodes cover an emission spectrum from the red to the infrared. Recently, blue-violet emitting laser diodes based on galliumnitride (GaN) were commercialized. The emission wavelength of these devices is specially optimized for optical data storage systems, where data density is mainly determined by the emission wavelength – the shorter the emission wavelength, the higher the density. Thus, the emission of these devices is not true-blue (around 480 nm), as required for display application. Such lasers are expected for the near future – at present, the longest emission wavelength obtained

from a GaN-based laser diode is 465 nm [2]. That leaves a green-emitting semiconductor laser diode as remaining task.

Until today, there exists only one semiconductor material system that enables the realization of electrically pumped lasers in the green part of the visible spectrum: the II-VI material system based on zincselenide (ZnSe). Initially, the research activities on these devices were motivated by the demand to develop a short-wavelength semiconductor laser source for optical data storage systems. In the recent years, the research intensity cooled down considerably due to the overwhelming success of the GaN-based emitters. Nowadays the motivation to continue the research on ZnSe-based laser diode devices is directly connected to their unique possibility *to emit green laser light*. Naturally, the display technology dominates this motivation – yet, there is a broad spectrum of applications beyond this. Especially the fact, that the human eye has its highest sensitivity in the green spectral region, gives rise to numerous applications, mainly connected to optical feedback devices, such as laser pointers or guiding-lasers for medical surgery systems.

The research on ZnSe-based laser devices was stimulated by the development of a reliable *p*-type doping technique in 1990 [3, 4]. In the following years, these devices have been brought from short-lived pulsed-operation at low-temperatures (77 K) to continuous wave (cw)-operation at room-temperature, with a record-lifetime of 389 h at present [5]. This limited lifetime is the primary reason that ZnSe-based lasers have not been commercialized, yet, and are still in the research-stage. Obviously, the most interesting and pressing problem here is to develop an understanding for the underlying degradation mechanism that causes the insufficient stability, which is closely connected to the active region of the laser diode – the Cd-containing quantum well. Consequently, a significant part of this thesis is concerned with the *limitations of quaternary CdZnSSe quantum wells* in terms of degradation. However, the investigations will not be restricted to the characterization of the process – novel approaches to slow it down or to minimize its effect will also be presented – revealing the *unique possibilities* of this special material.

The work of this thesis was performed in the *Halbleiterepitaxie* group of the *Institut für Festkörperphysik* of the *Universität Bremen*, which took part in the research on ZnSebased devices as soon as the epitaxy system was installed in the beginning of 1996. In the course of several Ph.D. and Diploma thesises, some of the most basics problems involved in the growth and fabrication of ZnSe-based laser diodes were investigated, such that at the beginning of the experimental work of this thesis, the principle devices design and fabrication process could be considered as established. Accordingly, the foundation of the experimental work of this thesis, which is presented in *Chapter 1*, does not only contain a brief introduction into the physics of semiconductor laser diodes, but also describes the present state of the art of ZnSe-based laser diodes, including a summary of the results of the preceeding thesises mentioned afore.

A laser diode is one of the most complex semiconductor devices that can be fabricated. In order to achieve electrically pumped laser oscillation, a stacking of several thin, individual layers of different electronic and optical properties is necessary. Such a stacking is commonly fabricated using epitaxial¹ methods, e.g. *molecular beam epitaxy* (*MBE*), which allow a precise control of the composition as well as of the layer thickness on an atomic scale. Due to the complexity of the structure, a variety of different exper-

¹*epitaxy*, the term is formed from the greek words *epí* (above) and *táxis* (stacking)

imental techniques is necessary in order to characterize it completely. These methods – that are in part performed by other members of the group – will be introduced in *Chapter* 2, during the course of a standard characterization of an exemplary laser structure. This standard procedure was developed to compare results from different laser structures. Thus, it is possible to utilize the laser structure as a *tool* for the investigation of specific aspects and problems.

In *Chapter 3* the new tool laser diode will be used to characterize the degradation process of the Cd-containing active region formed by the quantum well in detail. The main focus of the characterization is to identify the driving forces of this process, especially from a device-relevant point of view. Being not only concerned with the *limitations* of CdZnSSe quantum wells, also new approaches to improve the stability will be investigated – thus exploring some *chances* of these active regions.

Approaches to improve the device characteristics are not limited to the epitaxial growth process alone. The *ex-situ* device fabrication process is of equal importance. In *Chapter 4*, some more advanced processing technologies will be developed and tested. For this processing, the leitmotiv is to optimize the heat management of the device, so that the driving-force-effect of the heat is minimized. This work was performed in co-operation with external partners.

The last part of the thesis is focused on the unique possibilities of CdZnSSe quantum wells and the chances connected to them. Motivated by the demand of a new light source for plastic optical fibers – a transmission medium for short- and medium-ranged communication networks – devices with an emission wavelength in the 560 nm region are developed in *Chapter 5*. In order to achieve such long emission wavelengths from conventional ZnSe-based quantum well laser diodes, a high Cd content is necessary, which will result in a highly lattice-mismatched quantum well, when grown on the standard galliumarsenide (GaAs) substrate. It will not only be investigated which growth conditions are required for high Cd contents, but also how the high lattice mismatch affects the device performance.

An extreme composition limit of CdZnSSe is the binary compound CdSe. In *Chapter* 6 the chances of such binary CdSe layers as active region of a laser diode will be investigated. Again, a special motivation is responsible for this research work. Due to the large lattice mismatch of CdSe and ZnSe, the self-assembled growth of CdSe *quantum dots* is possible. This phenomenom was extensively studied in a parallel Ph.D. thesis [6]. During the experimental work of that thesis, a technique that allows the fabrication of a CdSe quantum dot stack without the massive generation of defects was developed. Thus, it is possible to study – for the first time – the effects of three-dimensional confinement on the characteristics of ZnSe-based laser diodes.

The results of this work will be summarized in *Chapter 7*. Also an outlook will be given, which does not only concern the potential of ZnSe-based devices, but also gives some hints, which kind of experimental work should be performed next, in order to understand the degradation mechanism in these devices better on the one hand, and improve the stability on the other hand.

Some of the laser structures, grown in the framework of this thesis, were also made available to external research groups. In these co-operations, more advanced device concepts and novel processing technologies were applied to the ZnSe-laser diodes. The results obtained from these works illustrate nicely the potential of these devices, therefore, they are reported in *Appendix A*.

Chapter 1

Background and prerequisites

1.1 Physics of semiconductor lasers

The interaction of electromagnetic radiation and matter is one of the most fascinating and most complex fields of modern physics. Only a small part of this field is concerned with the amplification of light in semiconductors, yet it covers a wide range of experimental techniques and theoretical methods. It is outside the scope of this thesis to give a complete overview and introduction into the physics of semiconductor laser diodes. Only the most basic concepts – as they are necessary to understand the presented work – are introduced. For a thorough theoretical description of lasing in semiconductors, it is advised to refer to the work of Chow *et al.* in Ref. [7]. A general description of the basics of semiconductor laser diodes can be found in Ref. [8], while Ref. [9] is more focused on the operational characteristics of such laser diodes, in particular devices based on AlAs/GaAs. Reference [10] also covers the basics, but new developments such as *vertical cavity surface emitting lasers (VCSEL)* and more advanced processing techniques are presented as well, while the focus is in particular on InGaAsP-based lasers.

The technological relevance of lasers in general is based on their unique characteristics, especially their ability to deliver an *intense beam* of *monochromatic radiation* with a *high coherence length* and *low divergence*. Depending on the application different types of lasers can be used. Gas lasers are used where high optical intensities on the order of several kW are required, e.g. for welding¹. Solid state lasers deliver moderate intensities (on the order of W) with excellent beam profiles and very short pulses (in the fs regime). Semiconductor diode lasers are cheap and small laser sources, ideal for applications in consumer products such as CD players or computer peripherals.

1.1.1 Electromagnetic wave inside a crystal

The three types of interaction of electromagnetic radiation with matter that are common to all types of lasers are: *absorption, spontaneous emission* and *stimulated emission*. These interactions are transitions of the charge carriers in the matter between different energy levels, which are induced by the electromagnetic field, i.e., the photons. In a semiconductor crystal, these energy levels are determined by the band structure and

 $^{^{1}}$ a typical application of CO₂ lasers; at the *Bremer Institut für Angewandte Strahlforschung (BIAS)* up to 10 kW can be obtained from such a system, for instance [11]

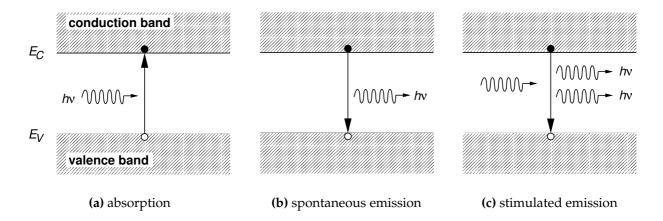


Figure 1.1: Interaction of light with a semiconductor [10].

the properties of the semiconductor material. Figure 1.1 schematically illustrates these processes. The semiconductor is characterized by its band gap energy $E_g = E_C - E_V$, which corresponds to the energy difference between the conduction band E_C and the valence band E_V . If a photon with the energy $E_g = h\nu = \frac{hc}{\lambda}$ is absorbed by the semiconductor, its energy is transferred to the crystal and an electron is excited from the valence band into the conduction band, while leaving a hole in the valence band, as depicted in Fig. 1.1(a). However, this excited state is unstable and the electron will eventually recombine with the hole thus returning into the ground state. During the transition, the energy of E_g is released by emitting a photon with the same energy. This spontaneous emission, shown in Fig. 1.1(b), proceeds on a time scale of 10^{-9} to 10^{-3} s, depending on the semiconductor material and band structure, in particular on the type of band gap: direct (fast) or indirect (slow). The spontaneous emission is a random process and no preferred direction of emission exists for the emitted photon.

A different situation is depicted in Fig. 1.1(c). Again, an electron was excited to the conduction band by external pumping (e.g., by optical excitation or current injection). If a photon of the energy E_g impinges on the excited electron, it can stimulate the recombination of the excited electron with the hole in the valence band, which results in the emission of a second photon. The characteristic feature of the *stimulated emission* is that the emitted photon is *in phase* with the impinging photon, i.e., they have the same energy and propagate in exactly the same direction. Thus, the photon has been amplified and *coherent* light is created. Stimulated emission occurs on a much faster time-scale.

Gain is achieved, as soon as more photons of the energy E_g leave the system than enter it. In this situation the rate of stimulated emission compensate the losses due to absorption and non-radiative recombination. This condition is achieved, when the system is in *inversion*, i.e., more carriers are in the excited state than in the ground state. The point at which inversion is reached is called the *laser threshold*. Below the threshold, spontaneous emission dominates. Directly at threshold the semiconductor is optically transparent, i.e., gain equals loss. Above the threshold stimulated emission dominates, which amplifies the light passing through. Normally, the electron population in the valence band by far exceeds that in the conduction band, such that the absorption dominates over the stimulated emission. The condition for the threshold is obtained from the occupation propabilities of electrons of the energy E_c in the conduction band $f_c(E_c)$

and holes of energy E_v in the valence band $f_v(E_v)$. These probabilities are determined by the *Fermi-Dirac statistics*, with the quasi-Fermi levels E_{fc} and E_{fv} in the conduction band and the valence band, resp. [10],

$$f_c(E_c) = \frac{1}{e^{\frac{E_c - E_{fc}}{k_B T}} + 1}$$
 and $f_v(E_v) = \frac{1}{e^{\frac{E_v - E_{fv}}{k_B T}} + 1}$. (1.1)

If photons of energy $E = h\nu = E_c + E_v + E_g$ impinge on the semiconductor of band gap E_g , they can be absorbed, creating electrons of energy E_c and holes of energy E_v at a rate R_a ,

$$R_a = B[1 - f_c(E_c)][1 - f_v(E_v)]\rho(E). \tag{1.2}$$

Here, B is the transition propability and $\rho(E)$ the density of photons of energy E. The factor $[1 - f_c(E_c)]$ give the propability that the electron state with energy E_c is not occupied, whereas $[1 - f_v(E_v)]$ gives the propability of an free hole state of energy E_v .

Stimulated emission can also occur, at a rate of

$$R_e = Bf_c(E_c)f_v(E_v)\rho(E), \tag{1.3}$$

which represents the fact, that stimulated emission requires an excited electron. Stimulated emission dominates over absorption as soon as

$$R_e > R_a. (1.4)$$

From Eqs. 1.2 and 1.3 follows, that

$$f_c(E_c) + f_v(E_v) > 1,$$
 (1.5)

which can be rewritten by using Eq. 1.1, leading to

$$E_{\rm fc} + E_{\rm fv} > E_c + E_v. \tag{1.6}$$

Adding the band gap energy to both sides results in

$$E_q + E_{fc} + E_{fv} > E_c + E_v + E_q = h\nu > E_q.$$
 (1.7)

Equation 1.7 represents the condition for *optical gain*. In the case of electrical pumping, it implies that the externally applied electric field must result in a separation of the quasi-Fermi energies, that exceeds the photon energy of the stimulated emission and the band gap energy of the semiconductor [10]. The specific absorption and emission rates can be calculated using time-dependent pertubation theory and summing over the available electron and hole states, which depends on the specific band structure of the semiconductor, as well as on the presence of additional confinement effects, as, e.g., in quantum wells or quantum dots.

Lasing, however, is only obtained, if a second requirement is fulfilled: *optical feed-back*. The feedback provides the selectivity for the stimulated emission in terms of direction and wavelength and thus enables the laser oscillation. Optical feedback is usually provided by placing the gain medium between two parallel semi-transparent mirrors, which form a so-called *Fabry-Pérot resonator*.

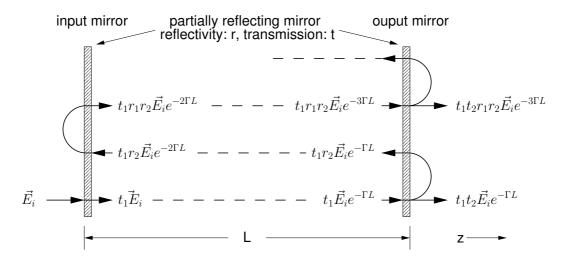


Figure 1.2: A hot cavity: Fabry-Pérot resonator of length L, enclosing an amplifying medium. Only the portion of the light transmitted at the output mirror is considered in the calculation of the lasing condition. $\vec{E_i}$ represents a plane wave, incident onto the input mirror [8].

1.1.2 Fabry-Pérot cavity filled with a gain medium: condition for lasing

A quantitative description of the laser process and in particular of the laser threshold can be obtained from calculation of the optical field inside the Fabry-Pérot cavity [8]: Figure 1.2 shows such a resonator of length L with a gain medium between two partially reflecting mirrors, which have the transmission coefficients t_1 and t_2 and the reflectivities r_1 and r_2 , resp. Using a plane-wave ansatz, it is sufficient to consider only the propagation part of the wave $\vec{E} \, e^{-\Gamma z}$, where Γ is the complex propagation constant, including gain as well as absorption, while the time dependence can be neglected. A wave \vec{E}_i incident onto the input plane z=0 on the left hand side will be partially transmitted into the cavity. Inside the cavity the light will be partially reflected and transmitted everytime it reaches one of the two mirrors. For the calculation of the lasing condition, it is only necessary to consider the part of the wave that leaves the cavity at z=L. Summing up the transmitted fields gives a geometric progression,

$$\vec{E}_{t} = t_{1}t_{2} \vec{E}_{i}e^{-\Gamma L} + r_{1}r_{2} t_{1}t_{2} \vec{E}_{i} e^{-3\Gamma L} + \dots
= \vec{E}_{i} \left[\frac{t_{1}t_{2} e^{-\Gamma L}}{1 - r_{1}r_{2} e^{-2\Gamma L}} \right].$$
(1.8)

The condition for lasing oscillation is, that for an incident wave with vanishing intensity $\vec{E_i}$, a finite transmitted intensity $\vec{E_t}$ is obtained. This is fulfilled, when the denominator of Eq. 1.8 approaches zero, or,

$$r_1 r_2 e^{-2\Gamma L} \stackrel{!}{=} 1.$$
 (1.9)

The complex propagation constant Γ in Eq. 1.9 describes the damping α and the phase $\phi = \frac{2\pi}{\lambda}$ of the wave,

$$\Gamma = \alpha + i \frac{2\pi}{\lambda}.\tag{1.10}$$

Since the cavity is filled with an amplifying medium, Eq. 1.10 can be modified to

$$\Gamma = (\alpha_i - g) + i \frac{2\pi n}{\lambda},\tag{1.11}$$

where α_i represents all internal losses, g the negative damping, i.e., gain, and $\frac{\lambda}{n}$ is the wavelength inside the medium of refractive index n. Combining Eq. 1.11 with the lasing condition of Eq. 1.9 gives,

$$r_1 r_2 e^{(g-\alpha_i)2L} e^{-i2L\frac{2\pi n}{\lambda}} \stackrel{!}{=} 1,$$
 (1.12)

which represents a wave that makes a round trip of 2L inside the cavity and returns to the input mirror with the same amplitude and in-phase.

Threshold current density

In Eq. 1.12 two conditions have to be fulfilled in order to obtain lasing oscillation. The first one concerns the gain,

$$r_1 r_2 e^{(g-\alpha_i)2L} \stackrel{!}{=} 1$$

$$g_{th} = \alpha_i + \frac{1}{2L} \ln \frac{1}{r_1 r_2}, \qquad (1.13)$$

where g_{th} stands for the threshold gain necessary for laser oscillation. Equation 1.13 illustrates that the gain must compensate the losses due to internal absorption (α_i) on the one hand, and the light $\frac{1}{2L} \ln \frac{1}{r_1 r_2}$, leaving the cavity on the other hand, which is also referred to as *mirror losses*. It has to be noted that both – gain and absorption – are in general frequency dependent.

For an electrically pumped laser diode the gain depends on the amount of injected carriers. Experimentally, a quadratic dependence of the gain on the current density was found for conventional III-V laser diodes, whereas for higher gain values (50–400 cm⁻¹) only a linear relation is found. The same results were reported for ZnSe-based laser diodes as well, however, thermal effect can lead to significant deviations [12, 13]. Using the nominal current density $J_{\text{nom}} = \frac{\eta_{ij}}{d}$ and the transparency current J_0^2 , the linear relationship can be written as

$$g = \Gamma \beta (J_{\text{nom}} - J_0), \tag{1.14}$$

In this equation β denotes the gain constant or gain factor. It is a purely phenomenological factor without physical significance, as Casey and Panish point out – but since it is directly related to the material quality, it is a useful figure of merit to compare different laser structures [8]. The nominal current density is the current density j injected into the device, normalized by the thickness d of the active region, i.e., the light producing region, and the internal quantum efficiency η_i . It represents only that portion of the current density, that contributes to the amplification of the light. Furthermore, the optical wave in a semiconductor laser diode does not completely overlap with the gain medium, which makes it necessary to introduce in Eq. 1.14 the confinement factor Γ , defined as the overlap of the optical wave with the gain medium [14].

²also referred to as nominal threshold current density

Using Eq. 1.14 and Eq. 1.13 the *threshold current density* j_{th} can be calculated in dependence on the physical parameters of the cavity,

$$j_{th} = \frac{J_0 d}{\eta_i} + \frac{d}{\beta \eta_i \Gamma} \left(\alpha_i + \frac{1}{2L} \ln \frac{1}{r_1 r_2} \right). \tag{1.15}$$

Equation 1.15 illustrates, that the threshold current density does not only depend on intrinsic parameters, but also on extrinsic parameters, namely cavity length and reflectivity. Thus the threshold current density can still be modified after the growth process.

Longitudinal mode selection

The second lasing condition contained in Eq. 1.12 is related to the phase, which results in the well-known Fabry-Pérot condition,

$$2L\frac{2\pi n}{\lambda} = m 2\pi \text{ with } m = 1, 2, 3, \dots$$

$$m\frac{\lambda}{n} = 2L. \tag{1.16}$$

From Eq. 1.16 the longitudinal mode separation in the cavity is obtained by differentiation and a mode difference of $\Delta m = 1$,

$$\Delta \lambda = \frac{\lambda^2}{2nL\left[1 - \frac{\lambda}{n}\frac{dn}{d\lambda}\right]}.$$
(1.17)

For a small wavelength region the dispersion $\frac{dn}{d\lambda}$ can be neglected, and replacing the refractive index n by an effective refractive index $n_{\rm eff}$ the Eq. 1.17 simplifies to

$$\Delta \lambda \cong \frac{\lambda^2}{2n_{\text{eff}}L}.\tag{1.18}$$

Quantum efficiency

The *quantum efficiency* is another important parameter concerning the operational characteristics of semiconductor laser diodes. It is defined as the ratio of injected carriers to emitted photons. Ideally, each electron is converted into a photon, which corresponds to a quantum efficiency of unity. One has to distinguish between the *internal quantum efficiency* η_i , which describes the efficiency of the stimulated emission, and the *external* or *differential quantum efficiency* η_d which only accounts for the light that escapes from the cavity [10],

$$\eta_d = \frac{e\lambda}{hc} \frac{\Delta P}{\Delta I},\tag{1.19}$$

where P is the total light putput power of the laser³ and I is the driving current. Using Eq. 1.19, one can obtain the external quantum efficiency of a laser diode from the slope of the light output in dependence of the driving current (cf. Section 2.3.4).

³i.e., the light power emitted at both facets

The external quantum efficiency is directly related to the internal quantum efficiency by the escape probability. This escape propability is the ratio of emitted light intensity $P_{\rm ext}$ to the total amount of produced light,

$$\eta_d = \eta_i \frac{P_{\text{ext}}}{P_{\text{ext}} + P_{\text{abs}}}. (1.20)$$

A representation for the light emitted from the facets was given in Eq. 1.13, combining both gives

$$\eta_{d} = \eta_{i} \frac{\frac{1}{2L} \ln \frac{1}{r_{1}r_{2}}}{\alpha_{i} + \frac{1}{2L} \ln \frac{1}{r_{1}r_{2}}} \\
= \frac{\eta_{i}}{1 + \frac{2\alpha_{i}L}{\ln \frac{1}{r_{1}r_{2}}}}$$
(1.21)

Comparing Eq. 1.15 and Eq. 1.21, it follows, that threshold current density and external quantum efficiency are complementary. That implies, that it is not possible, to fabricate a device, that has both, a low threshold current density and a high external quantum efficiency. This fact is most intuitive for the mirror reflectivities: a high-reflectivity coating will reduce the laser threshold significantly, however, only a small amount of light can leave the device in this case.

1.2 Design of a semiconductor laser diode

Any type of laser requires

- a medium with gain
- optical feedback

Both requirements are met in a semiconductor crystal. *Gain* is realized by external pumping of the system through which the carrier inversion is produced. This can be achieved either optically or electrically. In the case of electrical pumping the crystal has to be doped p- and n-type, such that under forward bias current passes through the crystal. In that case electrons and holes are simultaneously present in the region of the pn-junction, such that they can recombine under the emission of a photon with an energy corresponding to the band gap of the semiconductor⁴ as described in Section 1.1.1.

The specific physical mechanisms that produce gain in semiconductors, however, are rather complex and beyond the scope of this thesis. In typical III-V semiconductors, e.g., lasing involves an electron-hole plasma, whereas several different lasing mechanisms have been identified in ZnSe-based laser structures, depending on the samples and the experimental conditions. At low temperatures (below 80 K), excitonic – and even bi-excitonic – lasing occurs [15]. At higher temperatures, a transition to lasing by the recombination of a strongly correlated electron-hole plasma is observed [16]. This was reported for binary ZnSe-wells, as well as for Cd-containing structures. Further details concerning lasing in ZnSe-based structures can be found in Refs. [17, 18, 19].

⁴of course, non-radiative recombination occurs as well

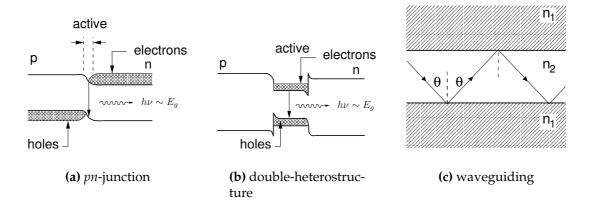


Figure 1.3: Schematic band alignments for different types of laser structures. (a) simple pn-junction – the active region is very small. (b) double heterostructure with band discontinuities for carrier confinement. (c) dielectric wave guiding. The active region (refractive index n_2) is sandwiched into the cladding layers of refractive index n_1 (after Ref. [10]).

Optical feedback is usually provided by placing the gain medium between two parallel semi-transparent mirrors. In some semiconductor crystals, these mirrors can be easily formed by cleaving the crystal along one of its crystallographic axes. The reflectivity of the cleaved facets mainly depends on the refractive index of the semiconductor and is given for the case of normal incidence by [20, 21]

$$R = \frac{(1-n)^2}{(1+n)^2}. (1.22)$$

For ZnSe, which has a refractive index $n \sim 2.7$, a reflectivity of 21% can be expected [22]. By applying dielectric coatings, these reflectivities can be increased beyond 99% (cf. Sec. 4.3).

Indeed, the first electrically pumped lasing in semiconductors has been obtained from such simple diodes. However, the practical use is very limited, since lasing is only realized at low temperatures (77 K) and at current densities on the order of 50 kA/cm^2 [23, 24, 25, 26]⁵. The main problem of these simple structures is that the thickness of the region, where electrons and holes overlap, i.e., the *active region* where light amplification occurs, is only on the order of $0.01 \mu m$, as indicated in Fig. 1.3(a) [10]. Nevertheless, this region can be considerably enlarged by a carrier confining mechanism. In a semiconductor this confinement is achieved by sandwiching the active region between two semiconductors of a higher band gap energy. Thus, the carriers can freely move inside the active region, but cannot escape from it due to the potential barriers resulting from the band gap discontinuities, as shown in Fig. 1.3(b). Such a design is called a *double-heterostructure* (*DH*) and was independently proposed by Kroemer and Alferov and Kazarinov for which they received the Nobel Prize in 2000 [28, 29]. In a double-heterostructure, not only the carriers are confined, at the same time, the band

⁵A collection of the key papers about semiconductor devices, including laser diodes, can be found in Ref. [27].

gap discontinuities give rise to an optical confinement of the wave inside the active region. Since a higher band gap implies a lower refractive index, total reflection occurs at the interface between the *cladding layers* and the active region for angles θ , satisfying,

$$\sin \theta > \frac{n_1}{n_2}.\tag{1.23}$$

Therefore, the cladding layers form a dielectric waveguide for the light inside the active region and efficient amplification is obtained, which leads in turn to a drastic reduction of the laser threshold. A more detailed description of DH laser structures requires the use of Maxwell's equations and can be found in Refs. [8, 10]. The typical thickness of the active region of a DH laser is about 0.1– $0.3~\mu$ m– obviously, such a device is more complex to realize, and in general, epitaxial techniques are necessary to fabricate the desired structure.

Modern edge-emitting semiconductor lasers are based on the DH concept. With the invention of recent epitaxial techniques, such as molecular beam epitaxy or vapor phase epitaxy, which allow a precise composition and thickness control on a nanometer scale, the original DH concept was extended by adding waveguiding layers to the system. Accordingly, two band gap discontinuities exist on each side of the active region. The discontinuities between the active layer and the waveguide are chosen such that efficient carrier confinement is achieved. However, this discontinuity is usually not sufficient for a good optical confinement. This is realized by a larger band gap difference between the waveguide and the cladding layers. In this kind of structure the carriers and the optical wave are separately confined, as shown schematically in Fig. 1.4. Such a structure is called a separate confinement heterostructure (SCH). This design allows lower threshold currents and better emission characteristics [8, 9].

A further reduction of the laser threshold is achieved by reducing the thickness of the active region to a size, where quantum mechanical effects dominate (3–10 nm). In such a system the movement of the carriers normal to the plane of the active region is restricted. As a result the kinetic energy of the carriers is quantized into discrete energy levels. This one-dimensional well is called a *quantum well*. For this thin active region, the overlap of the optical wave with the gain medium is very small,

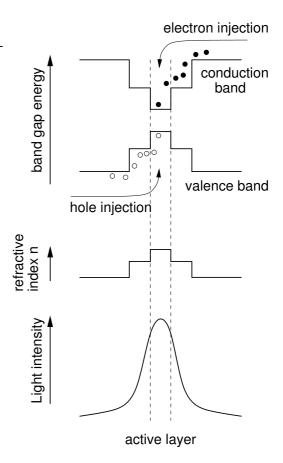


Figure 1.4: Schematic representation of the separate confinement heterostructure (SCH) design. Shown are the profile of the band gap energy, refractive index and the intensity of the optical wave perpendicular to the junction plane (after Ref. [14]).

such that a quantum well as active region is only useful in a SCH laser design. In this

case the confinement factor Γ is in the order of 1–5%, which is large enough for a reasonable threshold current density. Quantum wells as active regions have several advantages, in particular a higher temperature stability and better dynamical characteristics, which is especially relevant in communication applications [30, 7].

All laser structures fabricated in the course of this thesis are based on the SCH concept and utilize quantum wells as active region. For a practical use, it is necessary to reduce the threshold current of the laser diodes to a region, that is accessible by normal lab power sources (0–500 mA). Given a typical threshold current density of 500 A/cm² for ZnSe-baser laser diodes, this requires a pumped area of about 0.001 cm² – an additional *lateral confinement* is necessary. Usually, this is achieved by limiting the current injection region to a small stripe (10 μ m width), and thus an amplification of the wave occurs only in that section of the quantum well, in which carriers are injected. Such a structure is called *gain-guided*. More advanced techniques can provide *index-guiding*, where the wave is confined by a lateral variation of the refractive index. Additional details can be found in the appendix A. Lateral confinement has significant influence on the emission characteristics and the threshold current density of the laser diodes.

Recent novel semiconductor laser devices exploit the quantum mechanical effects even further by employing *quantum dots* as active region. These quantum dots provide a three-dimensional carrier confinement, which in principle results in a further reduced threshold and improved temperature stability [31]. The use of quantum dots, fabricated from the II-VI material system CdSe/ZnSe, in a ZnSe-based laser diode will be presented in Chapter 6.

Clearly, there are more aspects concerning the physics of semiconductor lasers, than presented in this section. For many applications, a careful design of the emission characteristics, e.g., the shape of the far-field pattern, or a single-mode emission are necessary. Other aspects are related to the correct theoretical description of the gain processes or the optimal composition and thickness of each layer in the laser structure. For studies of these topics of ZnSe-based laser diodes, one should refer e.g. to Refs. [32, 17, 33].

1.3 The II-VI material system ZnSe

Semiconductor material systems are classified according to the elements that they are formed of. For opto-electronic applications *compound semiconductors* are commonly used. Most compound semiconductors have direct band gaps, which are the prerequisite for an efficient radiative recombination. Due to the direct band gap, no phonons are necessary to observe the momentum conservation and the recombination rate is much higher, as compared to indirect semiconductors. Compound semiconductors are formed from two elements of complementary groups of the periodic system. As a consequence, the type of binding between the atoms of the semiconductor are not purely covalent, but also exhibit ionic character. However, in the technologically most prominent *III-V semiconductors* – formed of elements of the third and the fifth group, e.g. GaAs, GaP and InP – the covalent binding character dominates. For the *II-VI semiconductor* ZnSe the opposite case is true.

From a commercial point of view, the most important II-VI semiconductors are CdTe, HgTe and their alloys, especially CdHgTe. These materials have a band gap suitable for applications in the infrared region of the spectrum, where these compounds are primar-

Parameter		ZnSe	CdSe	CdS	MgSe	MgS	ZnS	ZnTe	GaAs
Lattice constant a	[Å]	5.6684	6.050	5.832	5.890	5.620	5.409	6.103	5.653
Band gap E_q at 300 K	[eV]	2.69	1.70	2.42	3.59	4.45	3.68	2.26	1.42
Melting point	[°C]	1517	1239	1477			1827	1295	1237
Density	[g/cm ³]	5.42	5.674	4.826			4.079	6.34	5.316
Micro hardness	$[N/mm^2]$	1350	1300	1250			1780	900	7500
Thermal conductivity	[W/(K cm)]	0.19	0.09	0.2			0.251	0.108	0.44
Lin. thermal expansion	$[10^{-6} \text{ 1/K}]$	8.2	3.8	4.7			6.36	8.19	6.4
Eff. electron mass	$[m_e]$	0.134	0.11	0.14			0.20	0.11	0.063
Eff. heavy hole mass [r		0.894	0.44	0.51				0.6	0.35
Ex. binding energy E_X^B	[meV]	20.8					40	12.4	4.2
Dielectric constants	ϵ_0	8.6					8.9	9.4	15.15
	ϵ_{∞}	5.7					5.7	7.28	12.25

Table 1.1: Physical parameters of some of the semiconductors used in this thesis. This table was first complied by H. Wenisch from whose thesis it was taken [34]. The values were verified using the latest edition of the Landolt-Börnstein [36].

ily used in detectors. Another relevant system is CdS, which is particularly suited to study the physics of semiconductors in general. Concerning opto-electronic devices for the visible part of the spectrum, ZnSe is without any doubt the most important II-VI semiconductor, because

- it has a direct band gap with an energy of 2.69 eV at room-temperature.
- it can be doped *n* and *p*-type.
- alloying it with Mg, S and Cd provides material suitable for cladding, waveguiding, and quantum well layers.

Although the technological relevance of ZnSe-based devices cannot be compared to that of the conventional III-V lasers, or even the new GaN-based emitters, the material system is well-established and intensively studied at the Institut für Festkörperphysik. As mentioned before, several Ph.D. thesises dealt with specific aspects of the growth and the physics of ZnSe-based material and devices. It is therefore justified to refer to these works for a more detailed presentation of the ZnSe material system. In particular, Ref. [34] gives a complete overview of the physical properties of ZnSe as well as a description of the different ZnSe-based alloys, whereas in Ref. [35] the problems of the heteroepitaxy and the different types of defects in this material are presented. The following section contains a short summary of both.

1.3.1 Physical properties

The thermodynamically stable crystal structure of ZnSe is the zincblende structure. Only at temperatures above 1425°C the wurtzite structure occurs [37]. The lattice constant of ZnSe along the [001] direction is a=5.6684 Å [36]. Being a cubic crystal, ZnSe can be cleaved along the [110] direction, which is allows a simple fabrication of mirror facets. The melting point of ZnSe is relatively high (1527°C) and in conjunction with the

also relatively high vapor pressure of 0.15 Torr⁶ at the melting point this complicates the fabrication of bulk ZnSe crystals [36]. In fact, ZnSe single crystals with a crystalline quality suitable for device fabrication are rare and usually only available in small sizes. A detailed description of the fabrication of ZnSe single crystals is found in Ref. [38], whereas Ref. [34] deals with the realization of devices, fabricated on ZnSe substrates. Concerning devices, it should also be mentioned that due to the high ionicity of the atomic bonds, the thermal conductivity of ZnSe is relatively low: 0.19 W/(K cm) [36].

The electronic structure of ZnSe at the Γ point allow the parabolic approximation of the energy bands with a good agreement such that the effective mass approximation is valid. The resulting effective masses for the electron and the holes are high, which in turn gives a small exciton Bohr radius a_B . Furthermore, the dielectric constant ϵ of ZnSe is rather small and with

$$E_X^B = \frac{e^2}{8\pi\epsilon\epsilon_0 a_B},\tag{1.24}$$

a high exciton binding energy E_X^B of 20.8 meV follows [21]. Consequently, excitonic effects dominate at low temperatures. The most important physical parameters of ZnSe, as well as that of other semiconductors relevant for this thesis are summarized in Tab. 1.1.

1.3.2 Epitaxy

For the fabrication of SCH laser diodes, it is necessary to deposit thin layers of semi-conductor material with a defined composition and thickness and high crystaline perfection. In such an *epitaxy process*, the semiconductor material is deposited on a seed crystal, the so-called *substrate*. This substrate crystal determines the crystallographic orientation of the deposited layers. All substrates used in this thesis were oriented in the [001] direction, which is therefore the *growth direction*. If the substrate is made from the same material as the deposited layers, i.e., ZnSe layers grown on a ZnSe crystal, a *homoepitaxial* growth process is performed. Since ZnSe crystals are difficult to obtain, most ZnSe layers and devices are grown on a different substrate material, where one has to find a compromise between suitability for the epitaxial growth process on the one hand and the availability, size, cost, and quality of the crystals on the other hand. Alternative substrates found in the literature, are Ge, AlAs, and $In_xGa_{1-x}As$, nevertheless, these are only of small relevance concerning devices [39, 40, 41]. Some research groups focus on unstrained CdZnSe quantum wells – in that case, InP is of particular interest [42, 43].

The most important substrate material for ZnSe-based devices is GaAs. Accordingly, the *heteroepitaxial* growth of ZnSe devices on GaAs is well-established. Since GaAs is not only well-known material system, but also used in many commercial applications, such as laser diodes or high performance transistors, substrates are available in convenient sizes (starting with 2" diameter) and with extremely high quality (less than 100 defects per cm⁻² [44]). However, most important is the relatively small lattice mismatch between ZnSe and GaAs at room-temperature of

$$\frac{a_{\rm ZnSe} - a_{\rm GaAs}}{a_{\rm GaAs}} = 0.27\%. \tag{1.25}$$

⁶1 Torr equals 133.322 Pa. In the vacuum technology – and in particular under MBE growers – it is still common to use Torr instead of the appropriate SI unit Pa. To make comparison with literature values easier, the use of Torr will be retained in the course of this thesis.

Even a small lattice mismatch gives rise to the formation of defects inside the growing crystal. In the case of ZnSe on GaAs, the latter has the smaller lattice. Thus, the ZnSe layer is compressively strained, as indicated on the left-hand side of Fig. 1.5. In this case, the lateral lattice constant of the ZnSe layer equals that of the GaAs substrate and the layer is elongated along the growth direction – the layer is fully strained or pseudomorphic. With increasing layer thickness, the strain energy accumulates, and as soon as the critical thickness is exceeded, the strain is released via the generation of dislocations. Accordingly, the lattice constant of the layer relaxes to its bulk value. Finally, the fully relaxed case is reached and the whole layer has the ZnSe lattice constant, as schematically shown on the right-hand side of Fig. 1.5. The critical thickness does not only depend on the lattice mismatch, but also on the substrate preparation and the growth start procedure. Under the specific growth conditions used in Bremen, a critical thickness of 300 nm is

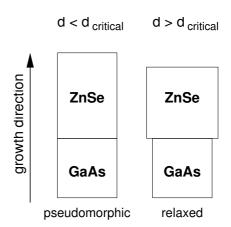


Figure 1.5: Schematic representation of pseudomorphic and relaxed ZnSe grown on GaAs. Relaxation occurs when the layer thickness d exceeds the critical thickness d_{critical}.

typically found, whereas a fully relaxed ZnSe layer on GaAs can be expected for layer thicknesses beyond 1000 nm [45]. It has to be noted, that additional strain is induced due to the different thermal expansion coefficients of GaAs and ZnSe (c.f. Table 1.1), when the sample is cooled down from growth temperature (typically 280°C) to room-temperature. Therefore, a ZnSe layer can be lattice matched to the GaAs substrate at the growth temperature *or* at room-temperature, but never both.

1.3.3 Defects

The degradation of semiconductor devices is directly related to the existence of defects inside the crystal. The different types of crystalline defects in ZnSe-based devices and their influence on the degradation has been studied intensively (e.g. Refs. [46, 47, 48, 49, 50, 51]). It was found that two different types of defects play a major role in this context:

- stacking faults
- misfit dislocations.

Stacking faults (SF) usually nucleate at the GaAs/ZnSe heterointerface. They are directly related to the substrate surface morphology, which is affected by the substrate preparation, the deoxidation process, and the growth start procedure. A stacking fault is created, when the stacking sequence along the [111] direction is broken. Such a SF is bound by partial dislocations, which have a Burgers vector $b = 1/3\langle111\rangle$ in the case of a Frank-type SF, and a Burgers vector $b = 1/6\langle121\rangle$ for a Shockley-type SF [46]. These SF propagate upwards during growth and form a V-shaped defect in cross section, as shown in Fig. 1.6(a). Sometimes, the partial dislocations of a SF can react and form a perfect 60°-dislocation that threads upwards. Such a dissociation process often occurs at a layer interface [46, 47]. The lifetime of a light emitting device depends on the

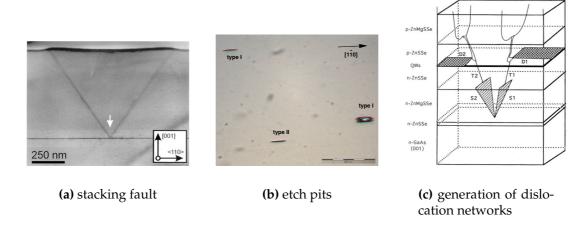


Figure 1.6: Defects in ZnSe-based devices. (a) TEM micrograph of a stacking fault (this particular SF is generated at a highly strained Cd-containing quantum well, but the same type is also observed at the GaAs/ZnSe heterointerface [TEM preparation and micrograph by H. Selke]). (b) At the semiconductor surface, SF are visible as distinct features in [110] direction under an optical microscope after short wet etching. Different types of SF are identified (cf. text). (c) schematic representation of the nucleation of misfit dislocation networks (D) in the quantum well by a stacking fault (S) and its associated threading dislocations (T). The network is generated under current injection (taken from Ref. [47]).

density of SF in the structure, since they are electrically active and act as non-radiative recombination centers [46]. Using an etching technique, these SF are visible in an optical microscope, where they appear as pits of distinctive shape on the surface, as shown in Fig. 1.6(b). In Sec. 2.3.3 this etching technique is used to determined the defect density of laser structures. It is even possible to distinguish different types of stacking faults, as Fig. 1.6(b) also shows. Large, lense-shaped pits (type I) originate from a pair of narrowly separated Shockely partial dislocations, whereas the single small lense shaped pit (type II) stems from a single Shockely-type stacking fault [52]. Paired Frank-type stacking fault are observed in form of narrowly separated pair of small lenses [not shown in Fig. 1.6(b)] [52].

Another negative feature of SF is that they act as nucleation centers for misfit dislocations (MD). Misfit dislocations are generated, when the layer and the substrate do not have the same lattice constant. For ZnSe-based devices, this is especially relevant in the case of Cd-containing quantum wells. When a SF (or its associated threading dislocation) intersects the highly strained quantum well, the dislocation can dissociate and form a MD in the quantum well. Under current injection, these MD can multiply and finally form a network of dislocations as indicated in Fig. 1.6(c) [47, 53]. These networks are responsible for the formation of the so-called *dark defects*, which will be discussed in Sec. 3.2.

1.3.4 Alloys

The fabrication of semiconductor heterostructures – and in particular SCH laser structures – requires the stacking of layers with different band gap energies and refractive indices. Semiconductor alloys allow to vary the band gap energy and consequently the refractive index of the material depending on the composition. By adding an additional element to the binary material, a *ternary alloy* is formed. The additional element should belong to either group of the host system, i.e., in case of ZnSe either a group-II or group-VI element can be used. The composition change mainly influences the lattice constant and the band gap energy of the newly formed crystal A_xB_{1-x} , obeying *Vegard's law* for the lattice constant a(x) [54],

$$a(x) = x a_{AC} + (1 - x) a_{BC}.$$
 (1.26)

However, for the band gap energy $E_g(x)$ the simple linear interpolation is not valid such that often a *bowing parameter* b has to be introduced [55],

$$E_q(x) = x E_{q,AC} + (1 - x) E_{q,BC} - x(1 - x) b.$$
(1.27)

Since both physical properties are directly coupled to the composition x, it is not possible to change only one of the properties individually. Only in the case of the III-V material $Al_xGa_{1-x}As$ this limitation is unproblematic, because the lattice constant difference between AlAs and GaAs is not more than 9×10^{-3} Å, while the bang gap energy differs by 0.85 eV^7 .

This limitation is bypassed by adding a fourth element to the alloy, and with an appropriate choice of elements, the lattice constant and the band gap energy of the *quaternary alloy* $A_xB_{1-x}C_yD_{1-y}$ is independently controlled by the composition x and y – at least to a certain degree. In analogy to Eqs. 1.26 and 1.27 one finds [56]:

$$a(x,y) = xy a_{AC} + (1-x)y a_{BC} + x(1-y) a_{AD} + (1-x)(1-y) a_{BD}$$

$$E_g(x,y) = xy E_{g,AC} + (1-x)y E_{g,BC} + x(1-y) E_{g,AD} + (1-x)(1-y) E_{g,BD}$$

$$-x(1-x) [y b_{ABC} + (1-y) b_{ABD}]$$

$$-y(1-y) [x b_{ACD} - (1-x) b_{BCD}].$$

$$(1.29)$$

It should be noted, that in general not all elements can be mixed to form a ternary or quaternary alloy. A common problem often observed is a miscibility gap, i.e., a certain compositional range is not stable and phase separation occurs (e.g. $In_xGa_{1-x}N$ [57, 58]). Other difficulties are related to different modifications of the binary compound, e.g., zincblende ZnSe and rocksalt MgSe, or a transition from a direct to an indirect band gap.

Although the composition x and y of the alloy determine the physical properties, they are not the relevant parameters for the device fabrication. More important are the resulting properties, i.e., the lattice constant and the band gap energy of the alloy. In fact, for some alloys not all parameters are known with certainty and significant discrepancies are found in literature for important values, e.g. the band gap of one of the binary compounds (cf. the MgZnSSe alloy below). Thus, the band gap and the lattice constant can vary for a given composition, depending on which model and which

⁷This one of main reasons for the success of GaAs-based laser diodes

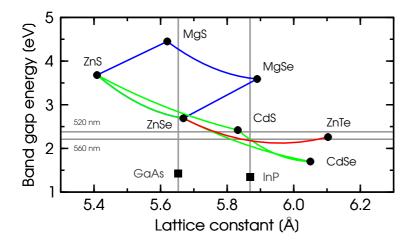


Figure 1.7: Band gap vs. lattice constant for the ZnSebased material system. For the most important alloy systems MgZnSSe, CdZnSSe and ZnTeSe, the bowing of the band gap energy is indicated. GaAs and InP are III-V semiconductors that can be used as substrates for the heteroepitaxy of ZnSe-based compounds.

bowing [eV]	MgZnSSe [56]	CdZnSSe [22]	ZnSSe [56]	ZnTeSe [60]
$b_{\rm ABC} = b_{\rm ABD}$	0	0.47	0.68	1.27
$b_{\rm ACD} = b_{\rm BCD}$	0.68	0.68	_	_

Table 1.2: Bowing parameters for several ZnSe-based quaternary and ternary alloys.

parameters are used. To avoid this problem, compositions itself will not be given in the course of this thesis, but rather the physical properties of the alloys.

In the following, the different for ZnSe-based laser diodes relevant ternary and quaternary alloys will be introduced. For a more detailed description of the ZnSe-based alloy system, cf. Ref. [34].

ZnSSe Probably the most important ternary alloy of the ZnSe-based material system is ZnSSe. In the first ZnSe-based laser diode, ZnSSe was used as cladding layer material [59]. By adding S to ZnSe it is possible to fabricate material lattice matched to GaAs. Thus, the critical thickness is significantly enlarged and layers of several μ m thickness can be grown pseudomorphically, which is a major requirement for laser structures. For that reason ZnSSe was used as cladding layer material in the first ZnSe-based laser diode [59]. A S content of 5.9% is necessary for lattice matching at room-temperature, as derived from Eq. 1.26. This amount is small enough to approximate almost all important physical properties of the lattice matched ternary ZnSSe by the corresponding value for ZnSe. Nevertheless, a strong bowing of the band gap energy of ZnSSe is observed (cf. Tab. 1.2).

However, obtaining lattice matching is not as straightforward as Eq. 1.26 suggests: comparing the linear thermal expansion coefficients α of GaAs and ZnSe in Tab. 1.1, one finds a significant difference. Consequently, with

$$a(T) = a(300 \text{ K}) [1 + \alpha \times (T - 300 \text{ K})],$$
 (1.30)

lattice matching at the typical growth temperature of 280°C is achieved for a S content of 6.9% [61]. Therefore, one has to choose between lattice matching at room-temperature or at growth temperature. This question is further complicated by the fact that the composition control in the MBE system is difficult, since the S sticking coefficient exhibits a

strong temperature dependence [62, 63, 64]. Most samples fabricated during the experimental work of this thesis have a S content between 5.9% and 6.9%.

MgZnSSe In the same way as ZnSSe played a major role for the fabrication of the first ZnSe-based laser diode, the quaternary alloy MgZnSSe played an important role for the realization of the first room-temperature cw-laser diodes [65, 66]. Figure 1.7, in which the lattice constant of some ZnSe-based alloys is plotted vs. the associated band gap energy of the material, nicely illustrates the advantage of the MgZnSSe alloy: it is possible to tune the band gap from 2.7 eV to more than 4.0 eV, while still being lattice matched to GaAs. Thus, waveguiding and cladding layers can be grown using MgZnSSe alloys of different composition⁸. A particularly convenient feature of the MgZnSSe alloy is, that the band gap and the lattice constant can be controlled almost independently, with the Mg content being largely responsible for the band gap, whereas the S content controls the lattice constant. This is mainly related to the different bowing factors of (Mg,Zn)SSe on the one hand and MgZn(S,Se) on the other hand (cf. Tab. 1.2 and Fig. 1.7).

For the quaternary MgZnSSe alloy, the composition control is basically limited by the control of the S incorporation, since Mg has a sticking coefficient of unity, which is in addition not sensitive to temperature [67, 64]. It was first proposed and successfully grown by Okuyama *et al.* and also studied in detail in Bremen [68, 64]. Most structural problems of this alloy are connected to the Mg. Generally, Mg containing materials are hygroscopic and tend to fast oxidation for high Mg contents – apart from the problem, that it has the tendency to grow in rocksalt structure above a layer thickness of a few nm [68, 69]. Especially for the binary compound MgSe, this leads to a considerable variation of the reported room-temperature band gap energy [56, 70]. Furthermore, high-purity Mg is difficult to obtain (typically a purity of 4N, i.e. 99.99%, is offered, which is two orders of magnitude lower compared to the rest of the materials). Consequently, pronounced impurity signals can be found in Mg containing layers [56]. Another problem of the MgZnSSe alloy is related to *p*-type doping and will be reported in Sec. 1.4.3.

For the cladding layers in typical green-emitting ZnSe-based laser diodes with Cd-containing quantum wells, no high Mg contents are necessary and therefore, the structural quality and stability of the cladding layers is not a problem. An effective carrier confinement with a negligible carrier overflow over the quantum well requires a band gap energy difference of more than 0.35 eV [71]. Assuming an emission wavelength around 510 nm, a quantum well with a bandgap of 2.45 eV is necessary, thus, the claddings should have a bandgap energy of at least 2.8 eV. A lower band gap energy difference will result in a drastic increase of the threshold current density, e.g., for a binary ZnSe active layer, a threshold current density of 20 kA/cm² results from the insufficient confinement [72]. In the standard laser structures grown for this thesis, a cladding layer band gap energy of 2.89 eV at room-temperature, resp. an energy of 2.99 eV at 10 K, is targeted, in order to be on the safe side.

CdSSe and **CdZnSSe** The most important layer of a modern semiconductor laser diode is the quantum well, since here the light is produced. The quantum well is formed

⁸For practical reasons the waveguides are usually made of ZnSSe.

from a material of a lower band gap compared to the waveguiding and cladding layers. By adding Cd to Zn(S)Se, a suitable quantum well material is obtained. As Fig. 1.7 indicates, the band gap energy and consequently the emission energy of the quantum well can be tuned over the complete high-energy part of the visible spectrum – just by varying the Cd content⁹.

However, the CdZnSSe alloy system does not provide the composition flexibility as the MgZnSSe system, as Fig. 1.7 reveals as well. For large Cd contents a high lattice mismatch to GaAs occurs, which cannot be compensated by adding S. Thus the quantum well is under high compressive strain, and since the critical thickness for such layers (8–10 nm for 35% Cd) is very small, only moderate amounts of Cd are incorporated in most devices reported in the literature[73]. This is done in order to avoid a relaxation and the massive generation of non-radiative defects connected to it. Typically, Cd contents about 20–30% are found [59, 74, 65, 75]. Since the addition of S cannot improve the lattice matching significantly for a given band gap energy (cf. Fig. 1.7), a ternary CdZnSe alloy is commonly employed as quantum well material. Yet, there exists one report of a quaternary CdZnSe quantum well, where improved lifetimes were found [76].

The degradation of ZnSe laser diodes is directly related to the stability of the active region and in particular to the Cd-containing material, as it will be established in the course of this thesis. The main problem of Cd-containing alloys is the strong diffusion of Cd. Especially in the presence of point defects and *p*-type doping, this diffusion is enhanced, as it was investigated in detail in a co-operation with the *Technische Universität Berlin* [77, 35]. Furthermore, a direct connection to the degradation mechanism was found [78]. Sulphur, on the other hand, is very stable in ZnSSe and CdZnSSe alloys, and consequently, only minimal diffusion is observed [77]. This is one of the main reasons, why ZnSe-based laser structures grown in Bremen employ a quaternary CdZnSSe instead of a ternary quantum well [79].

Due to the high lattice mismatch of about 7% to ZnSe the binary compound CdSe has special significance. The high lattice mismatch can lead to a strain-induced self-organized formation of *quantum dots* [80]. The self-assembled quantum dots have been successfully incorporated as active region in laser diodes in the III-V semiconductor material system – most prominently the material combination InAs/GaAs, which has a similar lattice mismatch as CdSe/ZnSe [81]. CdSe quantum dots were one of the hottest topic in II-VI semiconductors in recent years, although most studies concentrate on structural and optical characterization [82, 83, 84, 85]. First results concerning *electrically pumped lasing* in these structures will be discussed in Chapter 6.

ZnTeSe Concerning band gap energy and lattice constant the ternary alloy system ZnTeSe is an alternative quantum well material for green light-emitting devices. Considering the strong bowing factor of 1.27 eV, the band gap variation with composition is almost identical to the CdZnSSe system (cf. Tab. 1.2 and Fig. 1.7). However, the band alignment of ZnSe and ZnTe leads to a type-II quantum well, where only the holes are confined [86]. Obviously, such a system is not useful for an efficient laser diode, although it has been successfully employed in high-brightness LED structures [87]. In the active region of those LEDs Te acts as an isoelectronic trap for holes, giving rise to

⁹The emission energy of a quantum well is not simply determined by the band gap energy of the material, but also by the quantum well thickness.

very efficient, but spectrally broad, recombination [88]. Furthermore, Te tends to form clusters when incorporated in contents of more than a few percent [89].

The importance of the ZnTeSe alloy for ZnSe-based laser diodes comes from its high p-type dopability [90, 91]. In Sec. 1.4.3 and 1.4.4, the problematic p-type doping of ZnSe and the lack of a low-resistance metal contact to p-ZnSe will be discussed; at this point it should be noted, that these problems make the addition of an epitaxial p-side contact structure necessary for the stable operation of ZnSe-based laser diodes. This can be achieved by using a highly doped p-ZnTeSe alloy structure [92, 93, 60].

Although the full composition range of ZnTeSe can be grown with MBE, the composition control is difficult, since the difference in the sticking coefficients of Te and Se favors the incorporation of Se [94]. By using a *digital alloy*, where the alloy ZnTeSe is grown in form of a ZnTe/ZnSe superlattice and composition control is achieved by varying the thickness ratio of the two binary compounds, this problem can be avoided, which has been investigated in a Diploma thesis prior to the start of this work [95].

1.3.5 Doping

Electrical pumping of laser diodes requires the ability to grown n-type, as well as p-type doped semiconductor material. For ZnSe-based material the halogenide Cl and I are efficient dopants for n-type doping. The donor activation energy of these dopants is in the range of 25–30 meV [20]. Using Cl, a free-carrier concentration of 1×10^{19} cm⁻³, with mobilities in the order of $100 \text{ cm}^2/\text{Vs}$ can easily be obtained [96, 97]. With lower doping, higher mobilities are possible.

In a MBE system, the dopants are usually provided by compound sources (ZnCl₂ and ZnI₂), which allow a precise control of the doping level. The source materials are hygroscopic and special care has to be taken during a chamber opening to avoid the contamination of the source material with water. Other problems are related to the rather low vapor pressure, which leads to high doping level even at moderate cell temperatures¹⁰. Consequently, the maximum bake-out temperature of the chamber is limited to levels, where no excessive contamination of the chamber with Cl occurs¹¹.

The *p*-type doping of ZnSe is considerably more difficult to realize. In fact, it was the invention of an efficient *p*-type doping technique, that started the research on electrically pumped ZnSe-based laser diodes [59]. In the early work on doping of ZnSe, ion implantation techniques were often employed, which lead to the first fabrication of a ZnSe *pn*-junction by Li implantation [98]. Implantation of P even allowed the first observation of electroluminescence [99]. However, the emission was around 590–630 nm and thus corresponds to P-related impurity luminescence. With the implantation of N, first blue emitting ZnSe *pn*-junctions were fabricted [100]. All these results were obtained on ZnSe single crystals.

The first p-type doped epitaxial ZnSe structures were obtained by ion implantation of N on the one hand, and the by the incorporation of O^{12} from a ZnO-source on the other hand [101, 102]. However, neither could a high concentration of free carriers be realized by this techniques, nor were they reliable or reproducible. These requirements

 $^{^{10}}$ In the Bremen system a free-carrier concentration of 1×10^{18} cm $^{-3}$ is obtained at a ZnCl₂-cell temperature of 220°C.

¹¹in Bremen: 115°C

¹²acting as an isoelectric impurity that forms an acceptor level

could be fulfilled for the first time by incorporating Li, although, the doping level was limited below 1×10^{17} cm⁻³, which is too low for devices. In addition, a strong diffusion or electromigration of Li was observed [103, 104]. The breakthrough concerning p-type doping of ZnSe was finally achieved in 1990, when activated N from a plasma source was successfully incorporated into ZnSe, leading to free carrier concentrations in the mid- 10^{17} cm⁻³ [3, 4, 105]. Until today, the N-doping of ZnSe using a RF-plasma cell in a MBE system is the only successful way to obtain a reproducible p-type doping with a sufficiently high free carrier concentration for electronic devices. Neither could a good p-type doping of ZnSe be realized by other epitaxial methods (MOVPE), nor were other doping elements – such as P – successful, although a P-acceptor was clearly identified [106, 107, 108]. A strong self-compensation is identified as main reason for the lack of sufficient p-type conductivity from P [109]. The problems connected to the p-type doping of ZnSe will be discussed in Sec. 1.4.3.

1.4 State of the art and solved problems

1.4.1 History of ZnSe-based laser diodes

Two major ingredients were necessary for the realization of an electrically pumped semiconductor laser diode based on ZnSe:

- a suitable epitaxy process to produce high-quality thin layers
- an efficient *p*-type doping.

The epitaxy of ZnSe-based material by means of MBE proved not to be difficult. Accordingly, optically pumped lasing from ZnCdSe quantum wells was realized first [139]. As mentioned before the work on electrically pumped ZnSe-lasers was started by the invention of a reliable *p*-type doping technique, in 1991 by Haase *et al.* from the *3M* company [59]. In the following years, ZnSe-based lasers became an very actively investigated topic. The exciting history of these research activities is summarized in Tab. 1.3, which list the important milestone papers and the corresponding device parameters.

From this table, some important conclusions can be drawn. First, it is noteworthy that in the early days some important contributions came form university-based research teams. But by 1994, the leading pace was taken over by company-based research, leaving the more "advanced" concepts – such as ridge-waveguide or DBR lasers or novel materials, such as Be containing compounds – to the universities. On the company side, the leading activities were initially done by 3M (USA), Philips (USA) and Sony (Japan), but by mid-1994 Sony started to dominate. In the university-based research, the joint efforts of $Purdue\ University$ and $Brown\ University$ (both USA) was initially most successful, but stopped around 1995. Later, this was taken over by the $Universität\ Würzburg$ and the $Universität\ Bremen$.

Looking through the literature, one counts a total of 9 companies and 5 universities reporting ZnSe-based lasers; from these 14 groups, only 7 obtained cw-operation. It is interesting to note, that the cw-lifetimes of the two university devices is below 1 min at room-temperature, whereas the leading companies achieved operation over at least 1 h. This reflects the different processing technology capabilities. An instructive example

Group	Date	Struc-	QW	Clad-	ZnTe	Type	Facet	Тор-	Op. tem-	Emission	Operation	Threshold	Voltage	Lifetime (cw)	Output	Remark	Ref.
Gloup	Date	ture	num-	ding	Zitte	Турс	coat-	down	perature	[nm]	Орстанон	[A/cm ²]	[V]	Eliculic (cw)	(pulsed)	Kemark	IXCI.
			ber				ing		[K]			L			[mW]		
3M	09/1991	SCH	1	Z	-	G	-	-	77-200	490	pulsed	320*	20		100*	first laser	[59]
Purdue/Brown	12/1991	SCH	3	Z	-	G	-	-	77-250	480-500	pulsed	850*			600*	first university, p-on-n and n-on-p	[110]
Purdue/Brown	04/1992	SCH	6	Z	-	G	-	-	77–273	490-500	pulsed	400*,	30–35	several hours	400*	InGaAs buffer	[111]
Heriot-Watt	08/1992	SCH	4	Z		G			4-100	473.2	pulsed	1500 (RT) 50*		(pulsed)*		first European laser	[112]
Sony	09/1992	DH	6	M	-	G	_	_	77	447	cw*	225*				ECR plasma, first MgZnSSe, first	
Softy	09/1992	DII	U	111	_	G	_	_	11	447	CW	223				Japanese laser, first cw	[113]
Matsushita	10/1992	SCH	1	Z	_	G	_	_	77	490-520	pulsed	160-580*	30		100	Jupanese laser, mot ew	[114]
Purdue/Brown	12/92	SCH	3	Z	x	G	_	-	77-200	490-500	pulsed	2000*	15–17			first ZnTe contact	[92]
North Carolina	01/1993	SCH	1	Z	-	G	-	-	77-200	470	pulsed,	174*-725	12-13		200*		[115]
State University											cw*						
Sony	03/1993	SCH	1	M	x	G	x	x	300-324	507	cw	460	7.9	40 s	30 [†]	first high temperature cw	[65]
3M	05/1993	SCH	1	Z	-	G	x	-	77-300	508-535	pulsed,	1500	9-20	20 min (80 K)	70 [†]	first RT	[116]
						_					cw (80 K)						
Philips	05/1993	SCH	1	M	-	G	-	-	77–394	496–516	pulsed	500	12	5–10 min (pul-	500	first MgZnSSe SCH, high-temp-	[66]
C	08/1993	SCH	1	M		G			300	523.5		1400	11.7	sed)	2†	erature operation first RT cw	[65]
Sony 3M	10/1993	SCH	1	M	-	I	X X	X -	300	523.5	cw pulsed	630-700	11./		2'	first K1 cw first buried ridge-waveguide	[117]
Toshiba	11/1993	SCH	3	Z	_	G	_	_	77	509	pulsed	1750*			600*	n-on-p, InGaP buffer	[117]
Sony	12/1993	SCH	1	M	x	G	x	x	300	490	cw	1500	6.3	1 s	3 [†]	first blue RT cw	[119]
Purdue/Brown	12/1993	SCH	1	M	x	ī	_	-	300	509	cw	600-1100	5.8	20 s	10^{\dagger}	first ridge-waveguide	[74]
Würzburg	01/1994	SCH	1	Z	-	G	_	-	77–250	497	pulsed	570*	0.0	3 h (pulsed)*	50*	first German laser	[120]
Sony	07/1994	SCH	1,3	M	x	G	x	x	300-380	509	cw	638	4.7	3 min (SOW),		cw at 380 K	[71]
,			,											9 min (MQW)			, ,
Purdue/Brown	12/1994	DH	2	M	x	G	-	-	300	462.7	pulsed	4000			1	shortest emission wavelength	[121]
Purdue/Brown	03/1995	SCH	1	M	x	G	-	-	300	508	cw	250		37 s		university record	[63]
Sony	05/1995	SCH	1	M	x	G	-	x	300	517	pulsed,				$30^{\dagger}, 834$	highest output power	[122]
Sony	06/1995	SCH	1	M	x	G	x	x	300	507	cw cw	1300	9	1 h	1†	first lifetime above 1 h	[123]
Eagle-	08/1995	SCH	1	M	Ĥ	G	_	_	77–220	507-517	pulsed,	160*	9	111	1	first on ZnSe substrate	[124]
Pitcher/NCSU	00/1//0	Jen	1	141	-11				77 220	307 317	cw*	100	_			inst on Zhoe substrate	[121]
Tampere Uni-	08/1995	SCH	1	M	-	G	-	-	300	520	pulsed	1200-	20	several min	9	n-on-p at RT	[125]
versity											•	1500		(pulsed)		,	` `
Sony	09/1995	SCH	1	M	x	I	x	-	300	512	pulsed	240			3	structured (channeled) substrate	[126]
Sony	10/1995	SCH	1	M	-	G	-	-	77	473.3	pulsed	900-	13		2	only MOVPE-grown laser	[106]
												1800*					
Würzburg	12/1995	SCH	1	M	x	I	-	-	300	517	pulsed	2300				first DBR laser	[127]
Würzburg	01/1996	SCH	1	В	В	G	-	-	77	530	pulsed	240*	20	2.2.1	70*	Be-containing laser	[128]
3M	02/1996 03/1996	SCH SCH	1	M M	x	I G	_	-	300 300	529 514.7	cw	460 533	4.5 11	3.2 h 101.5 h	20 [†] 3 [†]	CdZnSSe quaternary QW record lifetime, without ZnTe	[76] [75]
Sony 3M/Philips	03/1996	SCH	1	M	x	I	Х	x x	300	514.7	cw cw	470	11	3.6 h	20 [†]	top down study	[129]
NTT	05/1997	SCH	1	M	x	G	x	-	300	517.3	cw	1100	15	3.0 11	1 [†]	first RT cw on ZnSe substrate	[130]
Samsung	05/1997	SCH	1	M	X	G	X	x	300	536.5	cw	1000	8	11 s	40 [†]	first Korean laser	[131]
Sony	02/1998	SCH	1	M	x	G	x	x	300	514	cw	431	5.3	389 h	20 [†]	world record lifetime	[5]
Bremen	02/1998	SCH	1	M	x	G	-	-	300	529	cw	400-500	12	2 s		first European cw	[132]
Sumitomo	03/1998	SCH	1	M	x	G	x	-	300	527.9	cw	222	5.4	74 s	8†	first cw on ZnSe conductive sub-	[133]
																strate	
Bremen	04/1998	SCH	1	M	x	G	-	-	300	512	pulsed	980	14		32	first Bremen on ZnSe substrate	[134]
Sumitomo	06/1998	SCH	1	M	x	G	x	-	300	538	cw	175	3.9	2.1 h	4^{\dagger}	lowest threshold	[135]
Sony	09/1998	SCH	1	M	x	G	x	x	300	500	cw	310	3.5	330 h	3 [†]	lowest voltage	[136]
Sumitomo	09/1998	SCH	1	M	Х	G	х	-	300	517	cw	205	4.5	7.5 h		world record lifetime on ZnSe sub-	[137]
Mingham	10/1998	SCH	1	В	В	G			300-440	521	nules 4	750				strates	[120]
Würzburg	10/1998	SCH	1	D	D	G	_	-	300-440	321	pulsed	750				short-period super lattice wave- guide	[138]
		l														Build	

have been used: cladding material ZnSSe (Z), MgZnSSe (M) or MgZnBeSe (B); ZnTe-(x), HgSe- (H) or BeTe- (B) based p-side contact; gain guided (G) or index guided (I) structure; a "-" stands for not used, "x" for used; * denotes operation at 77 K; † implies cw-operation. publication date of the paper, not the experimental realization. Following abbreviations Table 1.3: History of ZnSe-based laser diodes. The entries are sorted according to the

for this are the results reported by Sony. Almost from the beginning they applied facet coating and performed top-down mounting. Considering the technological difficulties of this processing (cf. Sect. 4.2), the consequent employment of advanced technology is one of the reason for the success. It is also worth mentioning, that the third longest lifetime and the lowest threshold current density was obtained from a device grown on a ZnSe substrate. This illustrates the principle suitability of homoepitaxy for devices.

Using Tab. 1.3 one can distinguish three different phases in the research on ZnSe-based lasers. In the early stage, the principle design had to be found. Different substrates and buffer layers were explored, the optimum number of quantum wells had to be found, and even different configurations (*n*-on-*p* or *p*-on-*n*) were investigated. By mid-1994, the standard design was established as a *p*-on-*n* SQW structure grown on a GaAs buffer layer, which is still the state of the art.

During the second phase, the fundamental material limitations had to be solved. In the beginning, the work was motivated by the need of a new laser light source for the next generation of compact disk and optical data storage systems. Since the data density of such systems scales with the square of the emission wavelength of the laser diode, the main research was aimed at the short-wavelength region, i.e., blue laser emission. However, one major problem in these devices is the insufficient confinement, which was an especially severe problem in the early designs with ternary ZnSSe cladding and ZnSe waveguide layers. Thus, room-temperature operation was difficult to realize. By introducing a new material combination - the quaternary alloy MgZnSSe - this problem was solved (cf. Sec. 1.3.4) and consequently, room-temperature operation was easily achieved, even in cw-mode [65]. Another material problem that had to be solved, was a low-resistive *p*-side contact (cf. below). Here, a ZnTe-based design was first proposed in 1992 [92]. Around end of 1993, such p-side contact structures were successfully incorporated in laser devices, and low operating voltages were obtained. Nevertheless, a very interesting fact is, that in the record laser diode from Sony from the year 1996 – which showed a lifetime of more than 100 h – no special *p*-side contact structure was used [75]. This illustrates again the effectiveness of facet coating and top-down mounting.

The third phase in ZnSe-laser diode research concentrated on the degradation mechanism, since it turned out that a low-ohmic p-contact and an appropriate cladding material does not solve the problem of the short cw-lifetimes. This phase was completely dominated by Sony. The work started with the microscopic characterization of the degradation processes, from which it became evident, that a low stacking fault density is necessary for long lifetimes and to avoid the formation of dark defects in the active region [46, 140, 47, 141]. Consequently, a cw-lifetime of 100 h was achieved by careful optimization of the growth start procedure [75]. For such devices, the lifetime is no longer limited by the existence of the dark defects, but now, a gradual darkening of the active region could be observed, which is attributed to an accumulation of point defects [142, 143]. An optimization of the quantum well growth conditions led to a lifetime improvement to 389 h [5]. Until today, this is the highest lifetime of a ZnSebased laser diode. However, Tab. 1.3 also nicely illustrates, that the limited lifetime of the devices is the only remaining problem concerning ZnSe-based laser diodes. All other parameters are comparable to – or even better than – the that of conventional III-V laser diodes. Low threshold current densities and low operating voltages, suitable for consumer electronics, have been reported. In addition, high output powers were realized, and consequently, CD and DVD-writers with ZnSe-based laser diodes are not only

possible, but have even been demonstrated [144].

In the following sections, some of the main problems will be shortly described. These were already solved prior or at the beginning of this thesis. The remaining issues, such as the quantum well stability, are part of the investigation of the degradation mechanism in ZnSe-based laser diodes and will be covered in Chapter 3.

1.4.2 GaAs/ZnSe heterointerface: growth start

Due to the limited quality, size, and quantity of ZnSe substrates, ZnSe-based structures are commonly grown on GaAs. From an epitaxial point of view, this has some major disadvantages. Being compound semiconductors of different material systems, e.g. the electronic structure at the heterointerface is complex due to unbalanced atomic bonds and electron numbers. The lattice mismatch between ZnSe and GaAs gives rise to strain, and the different thermal expansion coefficients intensify this problem. The biggest epitaxial challenge is the nucleation of a ZnSe layer on GaAs with a minimal generation of defects, i.e., stacking faults. For a long-living device, a defect-free current injection region is mandatory. Given the typical dimensions of a 10 μ m-wide injection stripe and a 1000 μ m long cavity, this implies a defect density below 10^4 cm $^{-2}$. Such a low defect density can only be obtained by a combination of different preparation steps and growth techniques. The literature offers a broad spectrum of different recipes for low-defect ZnSe on GaAs, but these disagree in part. Therefore, M. Behringer investigated this topic in his Ph.D. thesis and identified the following key points [35]:

- thermal deoxidation of the GaAs substrate under As flux
- growth of a GaAs buffer layer and preparation of a 2×4 surface reconstruction
- pre-irridation with Zn before the ZnSe growth start
- no direct nucleation of Se or S on the GaAs substrate
- ZnSe growth start by using migration enhanced epitaxy

The first two points are derived from the well-established substrate preparation of GaAs and produce a crystallographically perfect GaAs surface which improves the reproducibility. In fact, it was the introduction and optimization of the GaAs buffer that enabled defect densities on the order of 10^4 cm⁻² and below reproducibly, and thus device lifetimes above 1 h in cw-mode become possible [145, 123].

The next two steps are directly related to oneother. It was found, that the GaAs surface is sensitive to the presence of Se. Under such conditions, a Ga_2Se_3 layer forms, which has a large lattice mismatch (about 5%) and acts as reservoir for vacancies. These vacancies in turn act as nucleation sites for SF. Furthermore, these point defects play a major role in the degradation process. By performing a Zn pre-irridation, these reactions can be minimized or even be avoided completely [146, 75, 147].

The final step is to initiate the ZnSe growth by using a special MBE growth technique, the *migration enhanced epitaxy* (MEE). In this growth mode, the participating elements are not supplied at the same time (conventional MBE), but are offered alternately instead. Thus, the surface diffusion of the elements is maximized, and ideally, the material is deposited monolayer by monolayer [147]. By using such a technique,

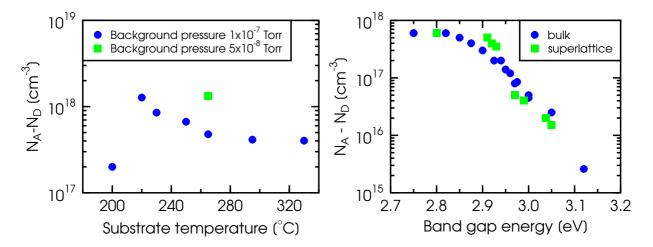


Figure 1.8: p-type doping of ZnSe and MgZnSSe. Left: free carrier concentration $N_A - N_D$ in dependence on the growth temperature [95]. The background pressure in the chamber is directly proportional to the N flux from the plasma cell. Right: maximum doping level in MgZnSSe in dependence on the band gap energy of the material for bulk layers (77 K, taken from Ref. [161]) and superlattices (10 K, taken from Ref. [35]).

a true two-dimensional growth is achieved, avoiding the defect rich three-dimensional growth completely [148].

The above described recipe ensures the required low defect densities in the Bremen epitaxy system. Laser structures grown during this thesis have a defect density of 10^4 cm⁻² or less on average, as determined by X-ray diffraction on the one hand and etch pit counting on the other hand (cf. Sec 2.3.3).

1.4.3 p-type doping

It was mentioned before that, the *p*-type doping of ZnSe and its related alloys proves to be difficult. So far, there is only one known technique for a reliable *p*-type doping: the doping with active N provided by a plasma cell in a MBE system [149, 150]. Other techniques to provide N, e.g. by supplying ammonia (using thermally cracked NO), a high N background pressure or a specially designed ECR plasma source, do not result in a better *p*-type conductivity [151, 152, 153, 154].

Soon it was established, that under normal growth conditions the maximum concentration of free carriers $N_A - N_D$ in p-ZnSe is limited to the lower 10^{18} cm⁻³ region, although N concentrations in the range of 10^{20} cm⁻³ can be realized [155, 156]. The reason for this limitation is a self-compensation process which results in the formation of N-related donors [157]. The onset of the donor formation is rather abrupt, such that a N-activation rate of unity can be maintained up to 1×10^{18} cm⁻³ [158, 159]. Nevertheless, the highest reported free carrier concentration for p-ZnSe in the literature is not more than 2×10^{18} cm⁻³ [160]. In addition to this compensation problem, one has to take into account that with an activation energy around 110 meV only a small fraction of the acceptors is activated at room-temperature [36].

For high current injection levels – as it is necessary for laser oscillation – the resistance of the layers has to be as low as possible. Accordingly, it is necessary to achieve

a doping level as high as possible. Although there are reports in the literature with doping levels around 10^{18} cm⁻³, no experimental details concerning the growth conditions are given. In a preceeding Diploma thesis, the p-type doping of ZnSe was studied and the observed strong dependence of the doping level on the growth temperature is shown on the left-hand part of Fig. 1.8 [95]. The reason for the higher doping level at the reduced temperature is the lower formation energy of the N-acceptor in relation to the N-related donors [157]. For a high doping level, a low growth temperature is necessary. However, the crystalline perfection deteriorates fast at low growth temperatures, thus, this technique is not applicable for the complete p-side of the laser structure and is limited to the p-side contact structure. Beyond the growth temperature dependence, it was also found that the doping level can be increased by reducing the N-flux, as indicated in by the measurement denoted with a square in the left graph of Fig. 1.8 . By reducing the flux, the fraction of active N can be increased 13 and thus a higher doping level is achieved while maintaining a satisfactory crystalline quality in the top layers [95].

Another problem related to the *p*-type doping is illustrated on the right-hand side of Fig. 1.8, where the maximum doping level of quaternary MgZnSSe is plotted against the band gap energy of the material (taken from [161]). It is found, that the doping level is drastically reduced with increasing band gap energy. For band gap energies above 3 eV, the carrier concentration drops below 10¹⁷ cm⁻³, which causes a high serial resistance and leads to an increased heating of the device during current injection. This doping limitation can be explained with the amphoteric native defect model, as demonstrated in Ref. [162]. An alternative to bypass the problem of the limited p-type dopability, the use of ZnSe/MgZnSSe superlattices as cladding layers was proposed [123, 163]. In his Ph.D. thesis, M. Behringer investigated this problem and did indeed achieve a higher doping level for a given band gap energy, as also seen in the right graph of Fig. 1.8 – at least for the relevant band gap energies around 2.9 eV [35]. However, the current transport in such superlattice layers is subject to a strong spreading, which make an effective current path definition by etching, i.e. a ridge-waveguide fabrication, necessary for the device processing. Since this was in Bremen not possible until late 2001, when a suitable etching system was installed, such superlattice claddings are not investigated in this thesis.

1.4.4 p-side contact

When a semiconductor is contacted with a metal a Schottky-barrier is formed (cf. e.g. Refs. [164, 14]). In general, the height of the Schottky-barrier is determined by the work function of the metal on the one hand and the semiconductor's electron affinity on the other hand. Due to its deep valence band, ZnSe has a high electron affinity, such that a metal/p-ZnSe contact always results in a considerable Schottky-barrier height (around 1.2 eV). Furthermore, a strong Fermi-level pinning is observed [165]. The thermionic current transport, i.e., the carrier transport over the barrier, is hindered by the barrier and high operating voltages result (cf. the early reports in Tab. 1.3). Another transport process across the barrier is provided by carrier tunneling, which dominates, if the barrier is small enough. The barrier width, on the other hand, depends only on the doping

¹³the activation is lost as soon as two atoms collide and the propability of such an event decreases with decreasing flux

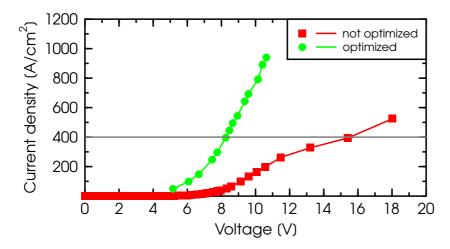


Figure 1.9: J/V characteristics of ZnSe-based laser diodes in comparison. The structures have an identical layer sequence with exception of the p-side contact structure. Both devices are operated in cw-mode at room-temperature.

level in the semiconductor. For high carrier concentrations around 10^{19} cm⁻³, a low resistive contact is possible. In that sense the difficulties to obtain a low-resistive contact to p-type ZnSe are directly connected to its limited p-type dopability.

In 1992 Fan *et al.* proposed an alternative concept for a low-resistive contact to p-ZnSe [92]. They suggested to insert an additional epitaxial semiconductor layer between the p-ZnSe and the metal. The requirements for the additional material are:

- a high *p*-type dopability
- easy fabrication of an ohmic metal contact
- small barrier formation at the interface to the *p*-ZnSe
- compability to MBE and ZnSe-laser structure growth.

Thus it is possible to avoid the metal/p-ZnSe contact and instead to use a contact to a material which it is easier to handle. In the following years, different materials were employed in this scheme, including CdSe, HgSe, BeTe, and Ga₂Se₃, but all with limited success [166, 167, 168, 169, 170]. Up to today, a reliable, low-resistive p-side contact structure always implies the useage of ZnTe as Fan et al. proposed [92]. As described in Sec. 1.3.4, ZnTe has an excellent p-type dopability, which makes ohmic contact fabrication easy [171, 172, 173]. Problematic is the direct deposition of p-ZnTe on p-ZnSe, which leads to significant barrier. Therefore, a ZnTeSe transition layer is inserted between both binary compounds, in which the Te content is gradually varied. Since the composition control in such a grading is difficult, it is experimentally realized in form of a ZnTe/ZnSe superlattice. These gradings come in different flavors (linear, parabolic, numerically optimized, or as resonant tunneling MQW structure), but do not differ much in the experimental realization, as it was shown in a previous work [92, 174, 60, 93, 95]. Using such a ZnTe-based *p*-side contact structure, operating voltages as low as 3.5 V can be obtained [136]. Furthermore, the electrode lifetime exceeds 1000 h at current densities around 500 A/cm² – the *p*-side contact does not limit the lifetime of ZnSe-based laser diodes [175].

The importance of a careful p-side contact optimization is demonstrated in Fig. 1.9, where the j/V characteristics of two laser diodes with different p-contact structures are

compared. Both lasers have the same layer sequence and showed cw-operation at room-temperature. With a cw-lifetime of 16 s the structure with un-optimized p-contact represents the best laser diode available in Bremen at the start of this thesis [35]. By optimizing the contact, the operating voltage at 400 A/cm^2 could be reduced by a factor of 2, down to 8 V. Consequently, the cw-lifetime of this new laser diode, which was the first one grown in the framework of this thesis, could be extended to more than 3 min.

Chapter 2

Experimental techniques and standard devices

A semiconductor laser diode is a very complex structure. It consists of numerous different layers with varying compositions and thicknesses as described in the previous chapter. Each and every single one of those layers must be optimized carefully. But this is not enough – in the end all layers have to fit into the same structure. An optimization that gives a record performance of an individual single layer, but deteriorates the quality of the complete laser structure, is useless. It is therefore natural that the development of the laser structures reported in this thesis is a joint and continuing effort of many people. This holds especially for the subsequent characterization of the structures after growth. Given the complex nature of a laser diode numerous characterization methods can be applied. In the following chapter the most important ones will be introduced as they are part of the *Standard Laser Characterization Scheme* developed during this thesis. Some of these characterizations were done by other members of the group, mostly as part of a different research project. This will be indicated where necessary.

The work on ZnSe-based laser diodes in Bremen started in 1995, long before this thesis was begun. Therefore many basics – in particular the growth start process and the layer sequence – were already developed. In this sense it is necessary to mention the Ph.D. thesises of B. Jobst, M. Behringer, and H. Wenisch, as well as the one of M. Fehrer concerning metalization and processing [64, 35, 34, 176]. The descriptions given in the following will therefore be kept as short as possible, and it is advised to consult the citied references for a more detailed explanation.

2.1 Molecular beam epitaxy

During the research on ZnSe-based structures for light emission in the short-wavelength part of the visible spectrum, it was found that the *Molecular Beam Epitaxy (MBE)* is the only practically relevant epitaxy method to obtain *n*- and in particular *p*-type material, although one electrically pumped ZnSe-laser diode – operating at 77 K – was fabricated by a *Metal Organic Chemical Vapor Deposition (MOCVD)* epitaxy process [106].

2.1.1 Principle of operation

In the MBE-type process of epitaxy the elements that form the semiconductor crystal are evaporated from individual cells containing only one single element. The evaporation process is carried out in an ultra-high-vacuum (UHV) chamber where the pressure is usually on the order of 10^{-11} Torr. Thus it is ensured that the mean free path of the constituents is large compared to the diameter of the chamber – each cell produces a beam of material [177]. These material beams are directed onto the surface of the heated substrate crystal, where a reaction between the different materials occurs and thus the semiconductor crystal grows.

Since the whole process usually is carried out far away from the thermodynamical equilibrium, it is only controlled by the reaction kinetics between the participating elements. Hence, the growth process – and consequently the growth rate and composition – of the crystal can be controlled by the temperatures of the cells on the one hand, and the substrate crystal on the other hand. Typical growth rates are in the order of 300–600 nm/h in the case of ZnSe growth. Each cell is equipped with a shutter which enables the abrupt turn-on and -off of the molecular beam. Given a shutter movement time of 1 s, a layer thickness control on the order of atomic mono-layers is possible. A comprehensive description of MBE can be found e.g. in Refs. [178, 179].

2.1.2 The Bremen MBE system

A detailed description of the MBE system of the Institut für Festkörperphysik of the Universität Bremen is given in Refs. [34, 180]. Nevertheless, the important aspects of the system will be reviewed here since the MBE system is the foundation for all work reported in this thesis.

The Bremen MBE system as shown in Fig. 2.1 was fabricated by the *EPI MBE Products Group* corporation¹. It consists of two EPI930 growth chambers and a *X-ray Photon Spectroscopy (XPS)* analysis chamber, interconnected by an UHV transfer tube. The transfer tube is separated by gate valves and equipped with two degas stations, which allow the pre-degassing of samples and sample holders outside the growth chamber. A separately pumped and heatable load-lock is used to introduce the samples into the UHV system. Both growth chambers are equipped with a pump system consisting of a cryo pump, an ion-getter pump, a Ti-ball sublimation pump, and a liquid-N₂-cooled cryo shroud. Each chamber has 9 cell ports for different materials. One chamber is used for the growth of III-V material, the other one for II-VI material.

The III-V chamber has Knudsen cells for Ga, In, Al, Si, and Mg. Furthermore, it is equipped with a plasma source for N and a valved cracker cell for As. Thus both, GaN-and GaAs-based material can be grown. Silicon (*n*-type) and Mg (*p*-type) are used for doping of the III-V material. The III-V chamber is important for the II-VI activities, since it enables the thermal deoxidation of GaAs substrates under As over-pressure and the growth of undoped and *n*-type doped GaAs buffer layers – measures necessary for high-quality heteroepitaxial ZnSe-laser structures on GaAs.

In the II-VI chamber, the cell ports are occupied by Knudsen cells for Zn, Se, Mg, Cd, Te, and ZnCl₂, two valved-cracker cells for S and Se, and a plasma source for N. There are several peculiarities of this II-VI chamber: the Te cell is a double-filament cell,

¹now Applied Epi Inc. [181]

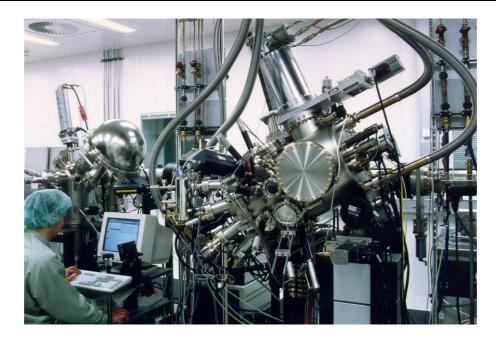


Figure 2.1: Photograph of the MBE system installed at the Universität Bremen with the II-VI epitaxy chamber in the center.

i.e., the top part of the cell's crucible is separately heated. Thus, a clogging of the cell due to condensation of material is avoided. Another modification was applied to the ZnCl₂ dopant cell, which provides *n*-type doping. It is equipped with a valve that seals the crucible from the rest of the chamber and which is only opened when doping is intended. Due to this valve, the material inside the crucible is protected from the air during a chamber opening. Since ZnCl₂ is strongly hygroscopic, it otherwise incorporates large amounts of water from the air-humidity, which in turn significantly increases the backout time after the chamber opening. Furthermore, the valve reduces the contamination of the chamber with Cl, so that a higher background carrier concentration in nominally undoped epilayers is avoided.

Also, the N-plasma source, that provides p-type doping, has a non-standard modification. The source is the RF-plasma source MPD 21 from *Oxford Applied Research*, operating at 13.56 MHz and at powers of 200–500 W [182]. The modification concerns the so-called beam plate that covers the BN-crucible in which the plasma burns. The beam plate used in this source has only one small pinhole of 0.2 mm diameter². Thus the flux of activated nitrogen reaching the substrate is small. It turns out that the degree of self-compensation inside the p-typed doped layers is negligible under standard doping conditions due to this measure [183, 184]. It is also possible to operate the plasma source with H. This is described in Ref. [34].

It should also be mentioned that the S valved cracker cell is not operated in cracking-mode but rather used as a valve-controlled cell, since cracking of the S molecules does not improve the layer quality [64]. The S flux from the cell is directly proportional to the valve opening, and the S composition can easily be changed over a large range within

 $^{^{2}}$ This fact disagrees with the original documentation (4 pinholes), but was verified on a chamber opening on 05/27/2002.

one second while still being absolutely reproducible³. A similar operation mode was intended for the Se cracker, however, cracking of Se occurs at a much lower temperature, such that under standard growth conditions most Se is already cracked [185]. In any case, the flexible flux control is not affected by this.

The transfer system of the MBE system is fully controlled by external magnets and does not have a direct connection to the lab-atmosphere. Thereby, all feed-throughs are stationary, which improves the vacuum stability. To facilitate transfer, the samples are mounted onto molybdenum blocks (Molly block). Since the samples are fixed between two Mo-masks, no gluing with an InGa eutecticum is necessary.

A very useful feature of the MBE system is that it can be controlled by a computer workstation⁴. The software package *Molly* from the machine's manufacturer Applied Epi allows the precisely timed operation of shutters and temperatures. A growth-run is essentially a recipe-controlled operation of the system – enhancing the reproducibility considerably (cf. also Section 2.1.4).

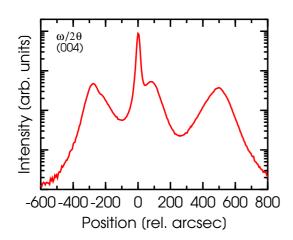
MBE growth is influenced by numerous parameters. Without access to the most basic of them a successful operation in this high-degree, n-dimensional space is impossible. Therefore, the MBE chambers are equipped with several measurement systems. There are e.g. two ionization pressure gauges to keep track of the pressure in the chamber. One of them can be positioned in front of the substrate heater, to monitor the flux coming from the cells (BFM, beam flux monitor) at the exact position, the sample will occupy during growth. A quadrupole mass spectrometer provides leak detection capabilities and residual gas analysis. From an electron gun high-energy electrons can be directed onto the surface of the substrate with a small angle of incidence. The reflection pattern is detected on a phosphor screen. With this Reflection High Energy Electron Diffraction (RHEED) system the surface morphology of the growing crystal can be examined [187, 188]. Similar optical ports allow to measure how the sample changes the polarization vector of light, again, incident under a small angle (ellipsometry). Using ellipsometry data the layer thickness can be calculated [64, 189, 190, 191]. An additional optical port provides access to the substrate in direct reflection. This port is used for pyrometry to measure the substrate temperature and recently also for reflectometry to monitor layer thicknesses during the growth of DBR mirror structures in-situ and in real-time [192, 193, 194, 195].

2.1.3 Calibration of the growth parameters

The calibration of the growth parameters is the most important and most time consuming task that has to be performed by the MBE grower. A complete set of calibration samples is usually grown after a chamber opening. These calibrations have to be verified as long as the chamber is up and running. Typically every 4–6 weeks recalibrations of the most basic parameters are necessary, depending on the growth activities. In Ref. [34] such a calibration procedure is described in detail. However, in the course of this thesis this procedure was modified considerably – in particular with respect to the growth of laser structures, therefore, an updated version will be described in the following.

³The valve position for a valved cracker cell is measured in the manufactures own unit *mil*, which determines the degree of valve opening. The possible range for all cracker cells is 0–300 mil.

⁴SUN SPARCstation 5, with operating system SunOS Release 5.4/Solaris 2.4 [186]



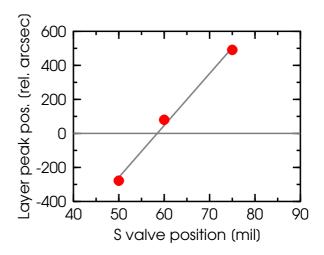
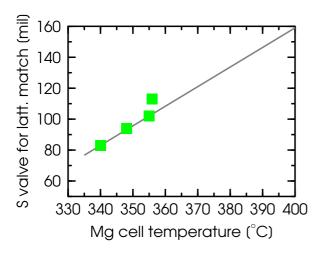


Figure 2.2: Typical ZnSSe calibration procedure. The calibration layer consists of three ZnSSe layers of equal thickness and with different S contents. Left: X-ray diffraction $\omega/2\theta$ scan of the (004) reflex to determine the lattice mismatch of each layer. The most intense peak stems from the GaAs substrate. Right: layer peak position relative to the substrate peak in dependence on the S valve position. For a valve position of 58 mil lattice matching will be obtained.

Flux ratio and growth rate: Starting point of all growth activities is the growth of binary ZnSe. The first sample grown after a chamber opening is a thick ZnSe-layer⁵. During the growth of this sample, the Se cell-temperature and the Zn cell temperature are adjusted so that stoichiometric or slightly Se-rich growth conditions are obtained. This can be detected in the RHEED pattern, where a mixture of a 2×1 (Se-rich) and $c(2 \times 2)$ (Zn-rich) reconstruction is visible under these conditions. Simultaneously, the growth rate is monitored using the ellipsometer. The cell temperatures and, consequently, the fluxes are set such that a growth rate of about 500 nm/h is obtained. The same procedure is also carried out with the Se cracker cell, where the correct flux ratios are much faster obtained due to the valve-controlled operation. Since lately, with the installation of the reflectometer the *in-situ*-growth rate measurement is also simplified. After growth, the photoluminescence spectrum of the sample should be measured to check for residual impurities and other defects (cf. Section 2.3.3).

Ternary and quaternary composition: Next, ZnSSe and MgZnSSe layers are grown. The main focus here is to obtain layers that are lattice matched to the GaAs substrate. To hinder premature relaxation of the calibration layers these samples are grown on GaAs buffer layers. Thus, fully strained layers can even be grown if the chosen growth parameters are not optimal. For these samples the starting procedures and initial layer sequences are identical with the ones used in real laser structures (cf. Section 2.3.1). In the case of a ZnSSe calibration layer, two or three 300–500 nm thick layers with different S contents are deposited. From a high-resolution X-ray diffraction measurement the lattice constants can be determined, which allows to interpolate the peak position versus S valve position (concerning X-ray diffraction see also Sec. 2.3.3). The correct S valve

⁵All calibration samples are grown on a quarter of a 2"-n-type GaAs substrate.



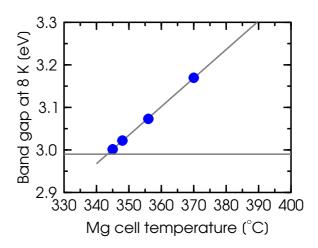


Figure 2.3: Quaternary calibration procedure. Left: from X-ray diffraction measurements the S valve position for lattice matching is obtained in a similar way as for ZnSSe ternary calibration layers. This procedure is done for several Mg cell temperatures. Right: band gap variation of the quaternary MgZnSSe material with Mg cell temperature, i.e., for different Mg contents. In order to serve as a cladding layer material in laser structures a band gap of 2.99 eV at 8 K is desired.

setting for lattice matched ZnSSe is extrapolated as shown in Fig. 2.2.

While keeping the Mg flux constant, the same procedure is used to obtain lattice matched MgZnSSe (Fig. 2.3). Additionally, the band gap energy of the quaternary layers are measured in low-temperature photoluminescence, where a band gap around 2.99 eV is targeted (concerning photoluminescence, cf. Sec. 2.3.3). Using data from older calibration runs, the correct settings can even be extrapolated to a certain degree from failed calibration samples. However, this procedure depends strongly on the grower's experience and is generally dissuaded.

p-side contact: As described in Section 1.4.4, the *p*-side contact is an important and complicated part of ZnSe-laser structures. It turned out that the long-term reproducibility of the standard contact structure is not easily maintained. Therefore, the calibration scheme given in Ref. [34] is not sufficient. Currently, the calibration scheme requires the growth of 1–4 test samples. These samples consist of a *p*-type ZnSe layer grown for 1 h under standard growth conditions and the ZnTe/ZnSe-multi-quantum well *p*-contact structure with a ZnTe cap layer. After the growth, $100 \, \mu \text{m} \, \text{Pd/Au}$ stripe are processed onto the sample, and the contact performance is determined by comparing the I/V-characteristics with older calibration samples. In the design of the *p*-type contact structure the adjustable growth parameters are the growth time of the ZnSe barriers (depending on the growth rate) and especially the ZnTe cap layer growth time. This experience corresponds with results from Sony [175].

"Uncalibrated" parameters: There are some parameters that do not change after a chamber opening and which are very stable over time. One of them is the substrate temperature. In the course of three years of the continuing growth activities of this thesis, the substrate temperature was changed only once.

Also the conditions for doping are rather uncritical. Concerning n-type doping, the free carrier concentration provided by the $ZnCl_2$ cell is very reproducible. Furthermore, the material consumption is very low so that the cell does not need to be refilled. A sort of the same effect simplifies the p-type doping with the N plasma source, since here, the cell is continuously supplied with purified N gas and the flux is regulated by a full-metal micrometer valve.

Usually, there is a certain flexibility concerning the emission wavelength of the laser diodes. Therefore, it is sufficient to measure the Cd flux and adjust the quantum well growth time accordingly. If the emission wavelength of the first laser grown at the end of the calibration period is not in the range of 515–530 nm the Cd flux or the growth time can be changed.

In sum, the complete calibration procedure of the growth parameters after a chamber opening requires at least 4 samples. Normally, this is not enough and typically an average of 8–10 samples are grown. Consequently, the task of a system calibration is not only a joint effort of the growers, but also performed by those members of the group who primarily do *ex-situ* characterization, especially the X-ray diffraction team. The calibration concludes with the growth of a complete and fully doped laser structure. Only after this laser structure shows electrically pumped stimulated emission the calibration is truly finished.

2.1.4 Standardization of the growth process

The MBE facilities are used for a variety of different growth experiments, ranging from studies on the formation of quantum dots to the growth of ZnTe-based material on ZnTe substrates. Keeping that in mind, the *Molly* software with its recipe-controlled operation of the MBE system provides a powerful method to increase the reproducibility of experimental results, because this feature enables computer access to all control elements of the system. Thus, it is possible to create a set of recipes that covers all standard operations connected to the growth of ZnSe-based material on GaAs substrates. Hence, the compability of experimental results by different growers obtained on different kinds of samples is increased. In co-operation with the other MBE users the recipe scheme presented in Tab. 2.1 was developed.

The most important recipes of this set are the ones connected to the ramping of the cell temperatures and the subsequent flux measurements. During the temperature ramping, the cells are heated 10–20°C above the desired values and kept at that elevated temperature for 20 min. Thus, material that condensated on the source material during the standby time is evaporated before the cell is used for growth. By this measure the material quality and purity is increased.

Due to the recipe controlled flux measurement the cells are always measured in the same sequence and for the same time. This is important, since especially the elemental materials used for II-VI growth tend to produce different beam equivalent pressure (BEP) values, depending on the measurement history of the beam flux monitor (BFM) filament [34]. Using the recipe for flux measurements does not solve this problem, but it makes this same systematic error common for *all* MBE users.

Chapter 2: Experimental techniques and standard devices

Recipe	Function	Specials
ramp-all	ramps cells to growth tempera-	temperature overshoot; cracker
	ture	optional
degas	degassing of a substrate on the	versions for 1/4 2" and full 2"
	degas station	wafers
flux-all	flux measurement of all neces-	two cracker valve positions pos-
	sary cells	sible; initial degas of the BFM fil-
		ament
subdeoxy	performs a thermal substrate de-	versions for both Se cells
-	oxidation	
subheat	ramps the substrate to the	wafer size dependent; versions
	growth temperature and per-	for both Se cells
	forms a pre-Zn irridation	
mee-start	performs a growth start in MEE	wafer size dependent; versions
	mode	for both Se cells
rampdown	ramps cells to standby tempera-	short opening of cracker valves
_	tures	
d-block	degasses an etched Molly block	_

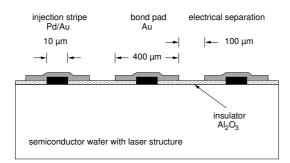
Table 2.1: Set of recipes that enables to perform the standard procedures common to all *ZnSe-based* growth activities computer-controlled.

2.2 Device processing

The technological steps necessary to process a wafer containing a laser structure into an electrically pumped laser diode, were developed by Michael Fehrer in the framework of his Ph. D. thesis [176]. During the last two years of this thesis the laser processing was done by S. Hesselmann and M. Henken. Since device processing is a fundamental part of the laser characterization the procedure, it will be briefly reviewed here, although it was never performed by the author himself.

Starting point for all activities is the epitaxially grown laser structure on the substrate crystal. After growth the wafer is cleaved along the $\langle 110 \rangle$ and $\langle 1\bar{1}0 \rangle$ axes of the crystal. *Gain-guided* laser devices are processed from typically (1×1) cm² pieces. Therefore, current injection stripes have to be applied to the sample. After thermal evaporation of Pd (10 nm) and Au (200 nm) in a vacuum chamber the injection stripes are photolithographically defined using wet chemical etching. Typically, 10 μ m stripes are used, but 20 μ m and 50 μ m are also possible.

The correct placement of the injection stripes is very crucial for the performance of the lasers. Two aspects have to be taken into account. One of them is a careful alignment of the stripes with respect to the cleaving edges. Only if the stripes are perpendicular to the edge they can fulfill their purpose as laser mirror. If there is a small misorientation, the light will not be reflected directly back into the laser cavity and consequently, it can not be amplified, which in turn leads to increased (mirror) losses. Simple geometrical calculations show that for a 1 mm cavity and a 10 μ m stripe the misorientation has to be less than 0.3° [176].



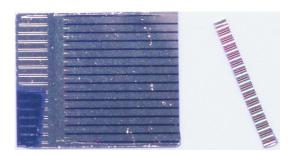


Figure 2.4: Processing of gain-guided laser diodes. Left: schematic side-view of a laser bar. The individual laser diodes are formed by the current injection stripes which are electrically separated by an insulator. For an easier testing, larger contact pads are processed onto the injection stripes (drawing not to scale). Right: photograph of a processed laser structure. The black stripes provide the electrical separation of the laser diodes, the current injection stripes are too fine to be seen. Laser bars are obtained from the processed wafer piece by cleaving.

Furthermore, the stripes should be parallel to the $\langle 110 \rangle$ direction of the crystal. The lifetime of a device is drastically reduced, if stacking faults exist inside the active region, i.e., beneath the injection stripe, since they act as effective non-radiative recombination centers [196, 46]. On the other hand, the typical stacking faults in ZnSe layers have an asymmetric shape which is elongated along the $\langle 110 \rangle$ direction [48]. Thus, the propability to find a stacking fault beneath the stripe is smaller if it is aligned along the $\langle 110 \rangle$ direction.

In principle, the processing could be stopped after the definition of the injection stripe, however, from a practical point of view, $10~\mu m$ metal stripes are difficult to contact with an electrode in order to apply current. To facilitate the contacting larger bond pads are applied onto the injection stripes. Therefore, the next step is to evaporate Al_2O_3 by an electron beam onto the sample (100 nm). Since Al_2O_3 is an insulator it provides electrical separation of the injection stripes. After a lift-off process the injection stripes are recovered. The bond pads are obtained by evaporating another 200–300 nm Au onto the sample. The injection stripes are electrically separated by etching $100~\mu m$ stripes into the bond pads. The final processing step is usually the metalization of the backside of the sample with Pd (10 nm) and AuGe (200 nm), which serves as n-side contact to the GaAs substrate.

The complete processing results into a structure as illustrated in Fig. 2.4. After the processing bars can be cleaved from the sample. These bars then contain on average 10–15 individual laser devices that can be contacted with electrodes (contact needles) or bonded. A further separation of the laser bar into single laser chips is usually not necessary and too time consuming (cf. Section 4.2). For device testing and characterization the laser bars are glued with silver paste onto a small sheet of copper, which acts as heat sink and facilitates handling.

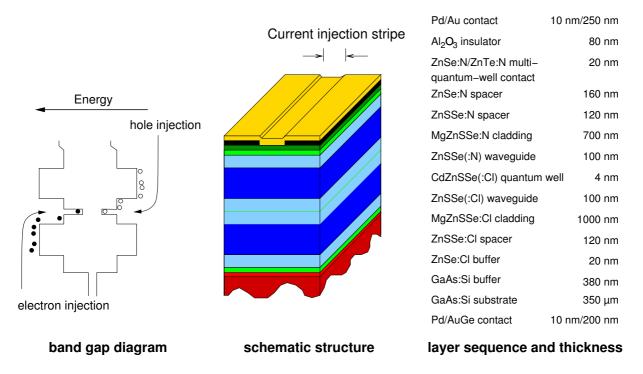


Figure 2.5: Schematic view of a ZnSe-based laser structure including layer sequence and band gap diagram. (Drawings are not to scale, likewise, the band bending has not been taken into account.)

2.3 Standard laser structure and characterization scheme

In the following section the design, the growth, and the characterization of ZnSe-based laser diodes as they are grown and tested in Bremen, will be described. This section should fulfill two purposes: first, it should introduce the samples, second, it is intended as introduction into the various characterization methods employed in this thesis. For a better illustration of the process the full characterization of a real laser structure is presented. Sample no. *S0607* was chosen as example.

2.3.1 Layer sequence

Figure 2.5 shows the standard laser structure used for all laser samples grown in the framework of this thesis. The active region of the lasers consists of one 2–5 nm thick quaternary CdZnSSe quantum well. This single quantum well is embedded into ZnSSe waveguiding layers of higher band gap (*double heterostructure* [DH]). MgZnSSe cladding layers of an even higher band gap surround those waveguides and thus, an additional confinement is provided for the carriers, which is therefore a *separate confinement heterostructure* (*SCH*). The band gap diagram in the left-hand part of Fig. 2.5 illustrates this schematically.

The complete laser structure is grown on a full 2" Si-doped *n*-type GaAs substrate. By adjusting the composition of the ternary and quaternary ZnSSe and MgZnSSe material, it is possible to grow the claddings and the waveguides lattice-matched to the substrate. However, a direct nucleation of the MgZnSSe cladding on the GaAs is not practicable. As reported in Section 1.4.2, the highest layer quality and lowest defect

densities are only obtained when using a sequence of GaAs and ZnSe buffer layers. Therefore, a 180 nm GaAs:Si buffer layer is grown first. The II-VI heteroepitaxy starts with a thin ZnSe:Cl buffer. Since the band gap difference between GaAs and ZnSe is quite large ($\Delta E_g = 1.27$ eV), a barrier for the carriers is built-up at the III-V/II-VI heterointerface. To reduce the effect of this barrier both buffer layers are heavily doped n-type (about 2–5 $\times 10^{18}$ cm⁻³), facilitating carrier tunneling. In the ZnSSe buffer layer on the n-side of the laser structure, the doping level is reduced to values of about 5 $\times 10^{18}$ cm⁻³ in order to maintain a high material quality.

In the n-type MgZnSSe cladding layer (E $_g$ around 2.9 eV at room-temperature) a free carrier concentration of $1–5 \times 10^{18}$ cm $^{-3}$ is targeted. This cladding layer has a thickness of 1000 nm. Thus, it is ensured that the optical wave does not penetrate into the lower buffer layers, where it would not only be effectively guided, but also strong absorption in the GaAs would occur. Such effects would increase the internal losses significantly and in turn raise the threshold current density.

The waveguides have a thickness of 100 nm each. Theoretical calculations and simulations performed in the framework of a Ph.D. thesis from Würzburg showed that such symmetric waveguides exhibit the best characteristics concerning waveguiding, emission pattern, and threshold [33]. The waveguiding layers are only doped half-way. By this measure the carrier overflow over the quantum well is reduced and the internal quantum efficiency is increased. However, some of the structures contain upper waveguides that were not doped at all. Furthermore, the quantum well has routinely been doped n-type with Cl (free carrier concentration below 5×10^{16} cm⁻³). Concerning this doping of the quantum well and the upper waveguide see also Section 3.4.1.

Due to the limited p-type dopability of MgZnSSe and the band gap (i.e. composition) dependence of the free carrier concentration, the design of the upper cladding layer requires special care. On the one hand, a good confinement is desired, therefore, the band gap should be high. Furthermore, the optical wave should not penetrate into the upper transition and contact layers, since strong absorption would occur otherwise. Consequently, the upper cladding layer should be sufficiently thick. But a thick cladding layer with a high band gap will increase the serial resistance significantly. In turn, this will lead to higher operation voltages and an increased heat generation, accelerating the degradation process. As a compromise between those two opposing boundary conditions, the p-side cladding layer has a thickness of 700 nm and a band gap of 2.9 eV at room-temperature, which gives a net acceptor concentration of 0.5– 1×10^{17} cm⁻³.

The top layers of the laser structures consist of ZnSSe and ZnSe transition layers and the ZnTe/ZnSe multi-quantum well contact with a thin ZnTe cap layer, as described in Section 1.4.4. In these layers the doping levels are gradually increased up to 5×10^{19} cm⁻³ in the ZnTe.

The layer thicknesses given in Fig. 2.5, as well as the doping levels, and the material compositions, are only *intended* values. The real values for each laser structure depend on the quality of the preceding calibration. Insofar, most laser structures will show deviations for at least one of these parameters. This problem makes the comparison between different laser structures more difficult – if not impossible sometimes. Yet, the growth of a whole set of laser structures in a row – ideally, with changing only one parameter per sample – is usually not possible, given the amount of time and other resources, necessary for one growth run.

2.3.2 **Growth**

Before the substrate can be introduced into the growth chamber it is degassed on one of the external degas stations of the MBE system. This is done in order to remove residual water and other contaminations from the Molly block and the substrate. Degassing takes roughly 1 h at a temperature of 400° C. As soon as the substrate is cooled down below 200° C 6 it can be transferred into the III-V growth chamber.

The surface of the GaAs substrate crystal is oxidized. These Ga- and As-oxides must be removed prior to the epitaxy process, in order to obtain a perfect single-crystal surface. Usually, a deoxidation is performed by heating the crystal to a temperature above the decomposition temperature of the oxides. In the case of GaAs this leads to a roughening of the surface, since As has a high vapor pressure and therefore escapes from the surface. To prevent this roughening the deoxidation is performed under a constant supply of As from the As cracker. As soon as a 2×4 reconstruction appears, the growth of the GaAs buffer layer can be started, during which the 2×4 reconstruction is maintained. After the buffer layer growth, the substrate is cooled down for transfer – again under As flux to stabilize the 2×4 surface, since it was found that such a 2×4 GaAs surface gives the lowest defect densities in the subsequent ZnSe heteroepitaxy [197, 198].

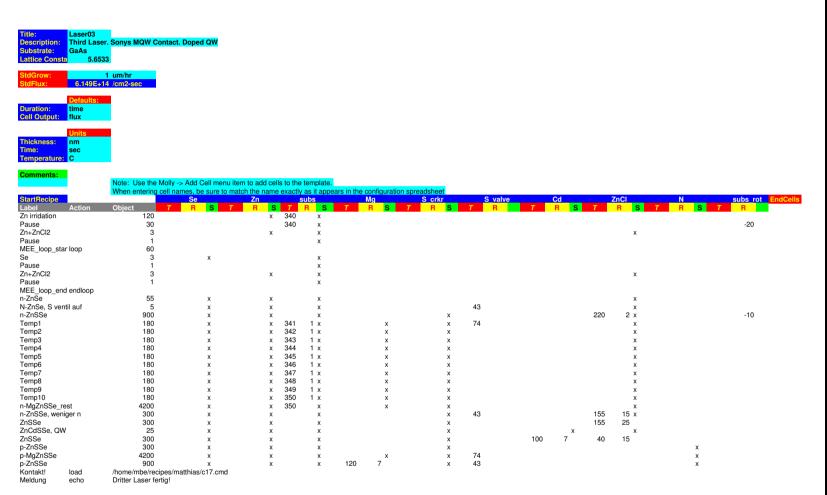
As soon as the substrate temperature permits it, the block is transfered into the II-VI chamber, where it is immediately heated up again. The fast transfer – the substrate is still hot – is necessary to prevent any condensation of rest-gas or other material on the substrate surface. It is a crucial point insofar, as the GaAs/ZnSe-heterointerface is very sensible to such contaminations, which give rise to an increased defect density.

The II-VI epitaxy is initiated in the fashion described in Section 1.4.2 with a 2 min Zn irridation and a subsequent MEE growth start. The following growth steps are determined by the layer sequence described in the previous Sec. 2.5. Figure 2.6 illustrates the typical growth steps necessary to deposit these layers. It shows the molly recipe used to grow laser sample S0607. Concerning the growth of the main layers there is one noteworthy peculiarity: the slow adjustment of the substrate (i.e. growth) temperature during the growth of the lower *n*-type cladding layer⁷. This growth step was developed by M. Behringer in order to compensated the changing temperature characteristic of the sample during the early stage of the growth [35]. It was found that this temperature change is due to a modified emissivity of the sample, caused by the newly grown II-VI layers [63]. Together with the strong temperature dependence of the S sticking coefficient this leads to an unwanted composition drift in the material if no countermeasures are taken [199].

Concerning doping, it should be noted that the $ZnCl_2$ cell temperature is reduced during the growth of the lower waveguide and closed half-way through. However, the quantum well of sample S0607 is doped n-type again. About 1–2 min after the deposition of the quantum well, N is introduced into the chamber and the plasma cell is started, so that stable operation is obtained when the p-type doping of the structure begins. The layer sequence of the p-side contact structure is not shown in Fig. 2.6, since

⁶Mechanical manipulation or transfer of in the UHV environment should always be performed at temperatures below 200°C in order to minimize the stress onto the equipment.

⁷The substrate temperature is measured by the substrate heater temperature, which is not the substrate surface temperature. A substrate thermocouple reading of 350°C corresponds to a substrate temperature of 285°C.



of additional recipe (c17. cmd). manually to the initial growth temperature, the p-side contact structure is defined in an nipulator. temperature (T) and the shutter position (S) of each cell, including the substrate ma-Figure 2.6: Main body of the growth recipe for sample S0607. a cell-temperature change can also be set independently (R). The substrate is heated The duration of each growth step is set in the Object-column. The recipe controls the The velocity

it is saved in a different growth recipe (c17.cmd), which is loaded following the growth of the p-ZnSSe transition layer.

After growth, the sample is cooled down, and as soon as the chamber has been pumped down to tolerable pressures⁸ it is taken out. After the sample has been removed from the UHV system, it is cleaved and several pieces are prepared for the following *exsitu* characterization.

2.3.3 Structural and optical characterization

The structural characterization of the sample serves two different purposes. On the one hand, it is used to verify that the intended sample structure was indeed obtained – especially concerning layer composition. On the other hand, it also determines the crystalline perfection of the sample, which is directly connected to the density of defects in the material.

High-resolution X-ray diffraction

The most important structural characterization method is the *high-resolution X-ray diffraction (HRXRD* or short *XRD)*. These XRD measurements are performed by members of the XRD-team, lead by H. Heinke. During the course of this thesis measurements were routinely done by V. Großmann, T. Passow, and G. Alexe. The Ph.D. thesis of V. Großmann was specially focused on the XRD characterization of ZnSe-based laser diodes and should therefore be referred to for more detailed information [61].

X-ray diffraction is a method based on the interference of photons that are elastically scattered at the electron cores of the atoms forming the sample. In a crystal the atoms are organized in a periodic lattice. Scattering of the incident beam occurs at every lattice plane. At an infinite distance, the scattered beams interfere and a signal is measured if the distance between the lattice planes *d* satisfies the Bragg condition

$$2d\sin\theta = n\lambda \text{ with } n = 1, 2, 3, ...,$$
 (2.1)

where θ is the angle of incidence and λ the wavelength of the incident beam. Using this relation in combination with light of a short wavelength – such as X-rays – a very precise determination of the (local) lattice constant of the sample is possible.

In the reciprocal space, the Bragg condition transforms to the Laue condition for the incoming wave \vec{k} and the scattered wave $\vec{k}\prime$,

$$\Delta \vec{k} = \vec{k}' - \vec{k} = \vec{Q} = \vec{G}. \tag{2.2}$$

Thus, the Laue condition is satisfied, if the scattering vector \vec{Q} equals a reciprocal lattice vector \vec{G} . This is illustrated in the Ewald construction of Fig. 2.7.

In a XRD setup the sample is illuminated with X-rays⁹. The scattered light from the sample is collected in a detector. Both, the sample and the detector can be rotated in this setup. In Fig. 2.7 the typical rotation (i.e. scan) directions are indicated. In a $\omega/2\theta$ scan the sample is rotated around ω , the detector around 2θ . That kind of scan is typically

⁸During *p*-type doping the background pressure in the chamber is about 3×10^{-7} Torr.

 $^{^{9}\}lambda = 1.54056 \text{ Å (Cu K}_{\alpha_{1}} \text{ line)}$

performed on the (004) reflex of the sample. In this configuration the penetration depth of the light is 7.6 μ m and consequently, all epitaxial layers are detectable – even for in a laser structure.

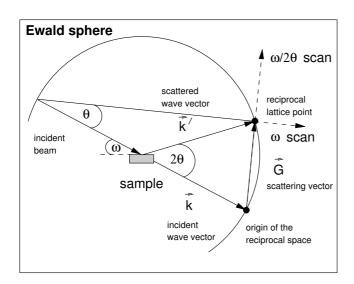


Figure 2.7: *Ewald construction, describing the measurement geometries. The most important XRD measurement directions,* $\omega/2\theta$ *scan and* ω *scan are indicated* [200].

assign the thickness fringes to the correct layer. Finally, for sufficient thick layers the crystalline quality can be judged by measuring the width of the layer peak [178] in ω direction. A typical $\omega/2\theta$ scan of a laser is given in Fig. 2.8(a).

The most intense peak in Fig. 2.8(a) stems from the substrate, because is has the highest scattering volume. With around 0.7–1 μ m thickness each, the cladding layers are the thickest II-VI layers. They can be found near the substrate peak. During the growth of the p-side the plasma cell provides an additional heating of the substrate surface. Since the S sticking coefficient is very sensitive to temperature changes, this additional heating is reflected by a slightly different layer composition of the upper cladding [199]. This layer can be found 60 arcsecs right of the substrate. For the lower cladding the lattice match is perfect, and the layer peak can only be identified as a small shoulder of the substrate peak, as the insert in Fig. 2.8(a) shows. Another possible explanation for the different compositions of the upper and lower cladding layer could be an enhanced Mg incorporation rate in the presence of N [201]. However, by lowering the substrate temperature during the growth of the upper cladding the composition differences can be reduced indicating that the heating effect dominates in the Bremen MBE system.

Roughly 140 arcsecs left of the substrate, the layer peaks from the ZnSSe waveguides can be found. The magnification of this region reveals an high-frequency modulation of the signal. These thickness fringes indicate a high layer quality and smooth interfaces. The oscillation period corresponds to a thickness of 1000 nm and can therefore be attributed to an interference between the interfaces of the lower cladding layer.

The broader peak 800 arcsecs left to the substrate originates from the ZnSe layers of the *p*-side contact region. Its intensity is lower as compared to the ZnSSe waveguides,

The main information that can be extracted from a $\omega/2\theta$ scan is, how perfect the epitaxial layers are lattice matched to the GaAs substrate. Such a scan is therefore not only used for laser structures, but also for the ternary and quaternary calibration layers described in Section 2.1.3. Since the intensity of the scattered light depends on the scattering volume, i.e., the layer thickness, a first rough estimation of the layer thicknesses is also possible. A more precise information concerning the thicknesses can be extrapolated, if the sample contains layers with very smooth interfaces. They give rise to thickness oscillations - socalled fringes – which are observed in form of a high-frequency modulation of the layer signals. However, in a multilayer sample it is difficult to

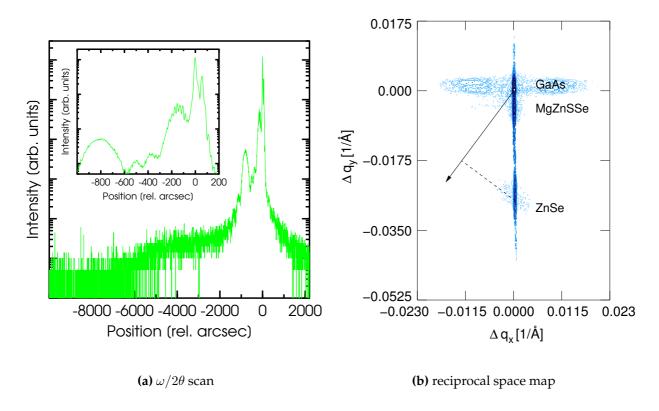


Figure 2.8: $\omega/2\theta$ scan of the (004) reflex of laser S0607 and reciprocal space map of the (224) reflex of the same laser structure. The insert in the graph of the $\omega/2\theta$ scan shows a magnification of the substrate peak region. The arrow in the (224) mapping points into the direction of the origin of the reciprocal space.

since it is considerably thinner (ca. 80 nm as compared to 200 nm). Furthermore, the substrate temperature is reduced during the growth of the p-side contact and therefore, the layer quality is reduced, which is the reason for the increased width of the peak.

Around 4200 arcsecs to the left of the substrate peak another layer signal can be found. However, its intensity is very low, which indicates a very small layer thickness. Also, the lattice mismatch between this layer and the substrate is very high. These facts leave only two layers as possible sources for the signal: the ZnTe layers of the *p*-side contact structure or the CdZnSSe quantum well. From a simple XRD measurement this can not be clarified. For a better identification of the signal source, an etching experiment, in which the ZnTe layers will be removed, followed by a subsequent XRD measurement are necessary.

Further insight into the crystaline quality of a sample is obtained by performing a mapping of the reciprocal space. Such a *reciprocal space map* is obtained by measuring multiple ω scans along the $\omega/2\theta$ direction around a reciprocal lattice point, as indicated in Fig. 2.7. In such a measurement configuration a relaxation of the layers, i.e., an inplane lattice constant that differs from the substrate lattice constant, can easily be detected by a different Δq_x position of the layer peak in a mapping of an asymmetrical reflex, e.g. of the (224) reflex, which is shown in Fig. 2.8(b). Since the layer peak positions are all at the same q_x value of the substrate, i.e., $\Delta q_x = 0$, the structure is fully

strained. The arrow gives the direction to the origin of the reciprocal space. A relaxation of the layer structure would occur perpendicular to this direction, as exemplary indicated by the dashed line for the ZnSe layer signal. In a fully relaxed case the layer peak position would be on the intersection of the direction to the origin and the dashed line. The triangle formed by the substrate peak position, the layer peak position in the fully strained case, and in the fully relaxed case is the so-called *relaxation triangle* [61].

As mentioned before, the layer peak width in ω direction can give an indication about the defect density in the layer. However, since the scattering volume of the defects is small, the full width of half maximum of a layer peak can only indicate defect densities above 10^5 cm $^{-2}$. A good laser diode should have a at least one order of magnitude lower defect densities. For these kind of structures, V. Grossmann developed a method to determine the defect densities from measurements of the diffuse background and a comparison of the 1/1000- and 1/10000-width, which are sensitive to a defect density down to 10^4 cm $^{-2}$ [61]. However, for laser S0607 no significant broadening could be detected, indicating a defect density below 10^4 cm $^{-2}$.

Etch pit density

One of the most important factors that influences the lifetime of electronic devices and ZnSe-based laser diodes in particular, is the number of extended 10 defects present in the device. In order to judge the device performance it is necessary to obtain precise information about the defect density. From XRD measurements, information about defect densities above 10^4 cm $^{-2}$ can be obtained. Another very direct way to aquire information about defects is to perform transmission electron microscopy. But in this case, the lower detection limit is even higher: 10^5 cm $^{-2}$. For a long-living ZnSe laser diode, defect densities on the order of 10^3 cm $^{-2}$ are necessary. A method that provides access to this defect density range is the determination of the *etch pit density* (cf. Sec. 1.3). In this experiment the sample surface is etched. In the region of a defect, the crystal is pertubated and the chemical bonds between the atoms can be broken more easily than for the rest of the crystal. This results in a higher etching rate and consequently, the etching produces a hole – or more precise an etch pit – in the sample at the position of the defect, which can then be counted under a microscope.

The technique for etch pit density measurements was established by A. Isemann and H. Wenisch [202, 34]. A critical point for obtaining clear etch pits is the correct choice of the etchand. For laser structures, best results were obtained with HCl at 60° C [48]. The etching time is typically 20–30 s. The top layers of a doped laser structure consist of the ZnTe-containing p-side contact structure and the ZnSe layer grown at lower temperatures. Due to the high lattice mismatch and the low growth temperature, the layer quality is low and defects are massively generated in this region during growth. However, it was found that these defects do not extend in to the active region of the device, but stay localized in the top layers [51]. Their influence on the device lifetime is therefore limited. In order to count only the relevant defects, the p-contact structure of the doped laser diodes, the entire p-side contact structure¹¹ is removed by etching the sample for 2–3 min in a solution of $K_2Cr_2O_7$ in H_2SO_4 and H_2O^{12} , the usual ZnSe etchand [203].

¹⁰i.e., not point defects, but rather stacking faults and dislocations

¹¹ZnTe cap, ZnTe/ZnSe multi-quantum well structue and the low-temperature ZnSe

¹²1 g K₂Cr₂O₇, 10 ml H₂SO₄, 20 ml H₂O

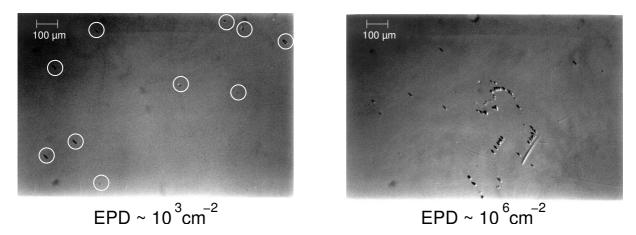


Figure 2.9: Microscope photograph of the sample surface of laser structure S0607 after the removal of the p-side contact structure and subsequent etching with hot HCl for 20 s. Left: sample area (2042 x 1633) μ m², etch pits are circled. Right: section of the sample with a cluster of defects.

Figure 2.9 shows the result of the etching process for laser structure S0607. In the left hand part of Fig. 2.9, on a sample area of (2042 x 1633) μ m², only 10 defects are found, resulting in a very low defect density of less than 300 cm⁻². On the other hand, the photograph on the right of the same figure shows significantly more defects. But these defects are clustered around a scratch, which originates from a sub-optimal wafer handling during the substrate preparation procedure. This indicates that careful wafer handling and processing is crucial for high quality devices – albeit difficult to achieve with manual processing ¹³. It is obvious that these processing deficiencies give rise to an increased scattering of the performance between individual devices. The average defect density of laser S0607 is in the low 10^3 cm⁻².

Photoluminescence

In general, luminescence is a physical process in which a sample emits a photon after an excitation. Depending on the source of excitation one distinguishes between *cathodoluminescence* (CL, electrons), *thermoluminescence* (heat), *sonoluminescence* (sound), *electroluminescence* (EL, current injection), or *photoluminescence* (PL, photons). The PL is the foundation of the optical characterization of semiconductors. Though the principle of operation is rather simple, its results can provide access to numerous physical aspects of the sample, ranging from ultra-fast carrier dynamics to defect characterization.

In a PL measurement the sample is illuminated with photons, typically from a laser. Inside the sample, these photons can excite the electrons of the crystal to a higher state, thus creating a pair of an electron and a hole. The excited carriers then relax back into the ground state. During the transition into the ground state – which is a recombination of an electron with a hole – energy is realeased. The recombination can either be radiative (emission of a photon) or *non-radiative*. Non-radiative recombination usually occurs at defect sites, since defects form electronic states deep in the otherwise forbidden band gap. In this case, the excess energy is released into the crystal lattice by the

 $^{^{13}}$ In commercial device production wafer handling is completely mechanized and performed by robots.

emission of phonons. In both cases, the total recombination energy corresponds to the energy separation between the excited and the final state. In the most simplest (and ideal) case of a radiative recombination in a semiconductor, the transition occurs between the band edges, i.e., the recombination energy exactly corresponds to the band gap energy of the crystal. In a real sample however, more complex mechanisms have to be considered, depending on the sample quality, design, doping, and measurement situation. For instance, especially at low temperatures, it is usually observed that an electron and a hole bind to each other and form an artificial (H-like) atom, a so-called exciton. The energy of the exciton is reduced by the exciton binding energy, and the excitonic recombination results in sharp lines at energies below the band gap. Typically, this excitonic features dominate the luminescence spectra, since the relaxation of free electrons and holes to excitons is a fast and effective process. But the formation of free excitons is not the only possible processes. In real semiconductor samples, many more effects can be observed, e.g. the formation of a bi-exciton, a He-like atom consisting of two excitons. Also charged excitons – a complex of two electrons with one hole or vice versa – have been observed. Finally, the carriers can bind to defects and impurities, e.g. dopants. All these complexes have different formation energies and consequently, give rise to different signals in the PL spectrum. For an complete overview of PL signals in ZnSe, see e.g. Ref. [204].

The line width of the PL emission depends on two factors. One is the lifetime of the excited state which is correlated to the homogeneous line width. In a typical PL measurement many electron-hole pairs are created at once in the sample. The emission energy of the emitted photons strongly depends on the band gap. Since the band gap in the crystal can vary locally due to composition fluctuations or defects for example, the emission is broadend, which gives rise to the inhomogeneous line width. Aside from the band gap of the sample, it is hence possible, to obtain additional information about the structural quality of the layers by measuring the line width of the PL signal(s). Furthermore, the emission line width also depends on the temperature. Therefore, temperature dependent PL measurements can provide further insight – especially concerning localization of carriers. For more detailed description of PL measurements on ZnSe samples and especially the influence of material composition and homogeneity on the PL emission line width cf. e.g. Ref. [205].

Standard-PL measurements are routinely performed on calibration samples as well as on laser samples. These experiments are carried out at low temperatures (around 8 K) in a He-cryostat. A HeCd laser provides the excitation at a wavelength of 325 nm, corresponding to an emission energy of 3.81 eV. This energy is high enough to even measure MgZnSSe layers with a high band gap. The PL spectra from the samples are recorded with a CCD camera, which is cooled by liquid N and that is attached to a grating-monochromator with a spectral resolution of about 0.2 meV. A complete description of the PL setup is given in Ref. [34]. For normal samples, as well as calibration samples, a special sample preparation is not required for PL experiments. However, the emission spectrum of a doped (laser) structure is dominated by luminescence from the *p*-side contact structure, which conceals the signals from the deeper lying layers. This *p*-contact structure has to be removed by etching prior to the PL measurement, in order to obtain information about the rest of the structure. All standard-PL measurements were performed by other members of the group, in particular by K. Leonardi, T. Seedorf, and T. Passow.

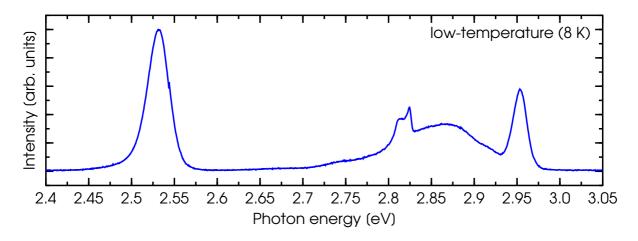


Figure 2.10: Standard-PL spectrum of S0607, recorded at 8 K. The p-side contact has been removed to reveal the signals from the deeper layers.

In Fig. 2.10 the standard low-temperature PL spectrum of S0607 is depicted. It is dominated by the quantum well emission at 2.532 eV, which indicates a Cd content of roughly 20%, using the model given in Ref. [22]. Taking into account the temperature shift of the band gap of CdZn(S)Se, one can expect an emission around 2.43 eV at room-temperature, corresponding to an emission wavelength around 510 nm, which is relatively blue. The full width at half maximum (FWHM) of the quantum well emission is 30 meV (at 8 K). Using the model from Young et al., and assuming a Cd content of 20% and a quantum well width of 3 nm, the inhomogeneous line width due to composition fluctuations should be around 12 meV for a perfectly mixed crystal, which is significantly lower than the measured value [206]. This indicates that the growth conditions for the quantum well were not optimal. In a following chapter, it will be shown that by adjusting the flux conditions during the quantum well growth, the line width, i.e., the material composition fluctuations, can be reduced (cf. Chapter 5). The quantum well emission in Fig. 2.10 has a clear asymmetric shape with an Urbach-tail on the low energy side [207]. This asymmetric shape is a characteristic feature of quantum wells samples and mainly connected to composition fluctuations. For an ideal quantum well this is not expected, since the shape of the emission spectrum is primarily dominated by the carrier scattering (intra-band relaxation) [33, 207]. For an active region with quantum dots, a clear Gaussian-shape of the emission is expected.

Aside from the quantum well emission, signals from the other layers can also be found in Fig. 2.10. The signals from the ZnSSe waveguides and transition layers appear around 2.82 eV. At 2.953 eV, a clear peak from the cladding layer is visible. The band gap of the cladding is lower than the desired value of 2.99 eV (at 8 K). Although the band offset ΔE_g between quantum well and cladding is with 0.421 eV still larger than the necessary 0.35 eV introduced in Sec. 1.3.4, a slightly increased threshold current density must be expected for the laser diodes processed from this structure.

Finally, it should be mentioned that the intensity ratio between cladding layer and quantum well emission is also an indication for the structural quality. During the excitation of the sample with the laser, the electron-hole pairs are created in the upper layers. Ideally, most carriers relax into the quantum well, where they recombine radiatively. In

a real sample there are always defects (point defect, but also extended defects) present, that provide efficient non-radiative recombination centers. The defect density determines how many carriers can reach the quantum well. Thus, in a high-quality structure most electron-hole pairs contribute to the quantum well emission and as a result the quantum well dominates the PL spectrum. In that sense, the laser structure shown in Fig. 2.10 has a good structural quality.

To shortly summerize, the results of the structural characterization of sample S0607 indicate a high quality. With a very low stacking fault density in the order of $10^3 \, \rm cm^{-2}$ the device lifetime should not be limited by extended defects. Furthermore, a very good lattice matching of the cladding and the waveguiding layers was achieved. From optical characterization an emission around 510 nm with good efficiency can be expected. However, a slightly increased threshold current density is possible. In the next section it will be investigated, in how far these results transfer into good operational characteristics under current injection.

2.3.4 Electrical and electro-optical characterization

In this section the electrical characteristics of the lasers are determined. Contrary to the structural characterization, it is mostly concerned with *devices*. The main focus lies on the operational characteristics, i.e., what happens during current injection.

The experimental setups for the different electro-optical tests were developed before this thesis was begun, in particular, the first versions of the measurement software were created by A. Isemann during his Diploma thesis work [202]. However, most of these programs have been improved, partly rewritten, or even newly created since then.

Electro-chemical capacitance-voltage profiling

Although XRD and PL measurements can provide a detailed insight in the sample structure and quality, there is at least one important aspect that can not be accessed: doping. Without doping efficient current injection into the device is impossible. The doping levels in the different layers of the structure determine the resistance and thus the amount of heat that is generated during operation. Hence, doping is also crucial for the device stability and lifetime. An important part of the standard laser characterization is therefore the measurement of the doping levels in the device. This can be performed by *electro-chemical capacitance-voltage profiling (ECV)*.

An ECV measurement is an extension of the conventional *capacitance-voltage* (*C/V*) concept: when a semiconductor is contacted with a metal, the Fermi levels in both elements align by an exchange of carriers. This exchange process results in a depletion region at the contact interface and thereby a so-called *Schottky barrier* is formed. The height of the barrier is determined by the different work functions of metal and semiconductor. Since the free carrier density in the metal is high as compared to the semiconductor, the depletion layer is essentially located in the semiconductor. Its width – and consequently the Schottky barrier width – depends on the free carrier density, i.e., the doping level. By applying an external voltage the carrier density in the semiconductor and the depletion layer width can be manipulated. On the other hand, the depletion layer can be considered as a simple capacitor, whose capacity does only depend on the free carrier density and the layer width. By measuring the capacitance of the contact in

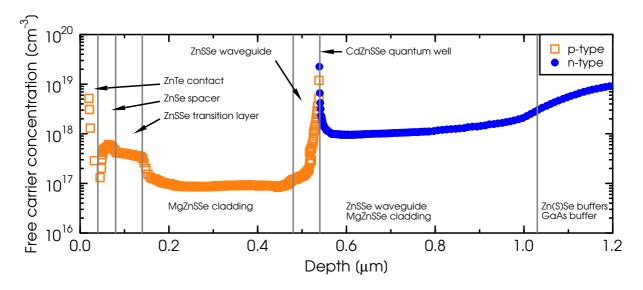


Figure 2.11: Doping profile of sample S0607 obtained by an ECV profiling experiment. The positions of the different layers of the laser structure are marked.

dependence on the external voltage, the free carrier density in the semiconductor can be extracted. For a more detailed description, cf. Ref. [208].

The measurement-depth of a C/V experiment depends on the applied voltage. At a high bias (i.e. large depletion layer thicknesses), the measurement becomes difficult; practical measurement-depths are limited to 200–600 nm. The ECV concept circumvents this limitation. Here, the Schottky contact is not formed by a metal but an electrolyte¹⁴. The electrolyte is also used to etch the semiconductor. Thus, a doping profile is obtained by performing an alternating sequence of C/V measurement and etching. Further information can be found in Ref. [209].

ECV measurements were performed in a commercial setup (ECV-Profiler PN 4300) from *Bio-Rad Semiconductor Systems*¹⁵ [210]. A technical description of the system is given in [211]. Conventional C/V measurements were done on calibration samples in a self-designed setup [208].

In Fig. 2.11 the doping profile of sample S0607 obtained by an ECV measurement is shown. The profile starts at the sample surface, where the *p*-side contact is located. Due to the Schottky contact and the depletion layer the, first point is taken at a depth of 20 nm. It has to be noted that generally the depth-scale of the ECV experiments is not calibrated and should therefore be taken rather qualitatively than quantitatively.

Figure 2.11 reveals a satisfactory doping level in the ZnTe-containing p-type contact. The free hole concentration drops significantly directly beneath the ZnTe layers, caused by the high lattice mismatch of the ZnTe [175]. At the interface between the ZnSe and ZnSSe transition layers an increase of the doping level can be seen. This is related to a growth temperature reduction during the deposition of the ZnSe layer. The doping level in the ZnSSe transition layer is $3-4\times10^{17}$ cm $^{-3}$, which is the normal value that can be achieved by standard MBE growth. In the p-type cladding layer the doping level drops down below 1×10^{17} cm $^{-3}$ as expected. The upper half of the upper ZnSSe waveguide is

 $^{^{14}}$ 1 M NaOH, 1 M Na₂SO₃ in H₂O

¹⁵now Accent Opto Technologies, Inc.

sample micro lens

Si–power head
ILX OMH–6701B

optical multimeter
ILX OMM–6810B

current source
ILX LDP–3811

voltmeter
KI 197

Figure 2.12: Schematic view of the electro-optical test setup. The sample can be placed in front of the optical multimeter for integrated intensity measurements (position a) or in front of the spectrometer for spectrally resolved measurements (position b).

also doped and consequently, a carrier concentration increase is found.

In the region of the pn-junction the simple model on which the C/V measurements are based, is not valid and accordingly, the measured doping level in the quantum well region is only a measurement artefact. However, its position can be seen clearly. The different doping levels in the lower waveguide and cladding layer are not as structured as on the p-side and the interfaces can not be identified clearly. With 1×10^{18} cm⁻³, the doping level is higher than on the p-side. The heterointerface between ZnSe and GaAs is identified by a very high carrier concentration of about 1×10^{19} cm⁻³. In sum, the doping levels of laser S0607 are fine and good electrical characteristics can be expected.

Current injection

The lasing process inside a laser diode is controlled via the density of carriers inside the active region of the device. Thus, current injection plays the most important role in the characterization – and naturally the operation – of such devices. The critical parameter of electrical operation is the *current density* inside that active region. Given the non-linear characteristics of diode-like devices, it is desireable to provide the current injection by a power supply that is *current-controlled*. Taking also into account that the device lifetime of ZnSe-based laser diodes without any advanced processing is limited to a few minutes in *continuous wave* (*cw-*) *mode*, an operation in *pulsed-mode* enables a better characterization of the laser. Therefore, the electro-optical characterization setup, as it is depicted in Fig. 2.12, uses the *precision pulsed-current source* LDP-3811 from *ILX Lightwave Inc.* [212].

The pulsing conditions of the applied current can be varied concerning *pulse width* (0.1 μ s–6.5 ms) and the delay between the individual current pulses. A useful representation of the repetition rate is given by the *duty cycle*, which is defined as the ratio of the pulse width and total pulse duration as defined in Eq. 2.3

$$duty cycle[\%] = \frac{pulse \ width}{pulse \ width + delay} \times 100.$$
 (2.3)

The current source allows a duty cycle variation between 0.01% and 100% (cw-mode). Using the duty cycle, the output power of a device measured in pulsed-mode can be

extrapolated to cw-mode, by

$$L_{cw} = \frac{L_{pulsed}}{\text{duty cycle}} \times 100. \tag{2.4}$$

Under pulsed driving conditions, it is also possible to study the degradation mechanism and its driving forces in more detail. This will be discussed in Section 3.4. However, to compare the performance of different laser structures, all standard test should be carried out under the same conditions. To ensure that even sub-optimal structures can be evaluated, the standard pulsing conditions were chosen to be 0.1% duty cycle and $1~\mu s$ pulse width for all tests with current injection. Since the cavity length also has a strong influence on the lasing parameters, a standard laser bar has a length of $1000~\mu m$.

One problem connected with the pulsed current injection is that one has to take high-frequency effects into account. In particular, the devices under test act not as simple ohmic resistors in the electrical circuit, but they also exhibit a non-constant capacitance, which is connected to the space charge regions and depletion layers in the device (e.g. at the pn-junction). Therefore, effects similar to the charging of a capacitor with a RC time-constant, can be expected. For the devices tested here, the RC time-constant is in the order of 100 ns and cannot be neglected.

Current-voltage characteristics

The electrical characteristics of a laser structure basically determine the device stability. If the high current levels necessary for lasing operation can only be achieved at high voltages, excessive heat is generated in the device and the degradation process is accelerated. The operating voltage of the structure is determined by several factors. In a ZnSe-based laser diode the most important factors are the doping level in the upper *p*-type cladding and the quality of the *p*-side contact. Contributions of these two factors to the operating voltage can be identified in *current-voltage* (*I/V*) measurements ¹⁶. The *p*-side contact forms a barrier for the current transport in the same way as the *pn*-junction does. Only if the voltage is high enough can the current flow – the barriers determine the *turn-on voltage* of the current flow. A *pn*-diode exhibits an exponential I/V characteristic, however, at higher operating voltages the serial resistance in the device limits the current transport, which then manifests itself as a linear I/V characteristic. The physics of current transport through barriers and *pn*-junctions is discussed in detail in Ref. [14]. For a simulation of the current transport in ZnSe-base laser diodes, cf. Ref. [33, 95].

In Fig. 2.13 the j/V characteristic of laser S0607 is depicted. The curve was acquired under DC current injection. The voltage was measured with the voltmeter KI 197 from *Keithly Instruments* [213]. From the linear regression at higher operating voltages the turn-on voltage and the serial resistance of the laser structure are estimated. The turn-on is slightly below 4 V. Subtracting the 2.4 V that drop at the pn-junction containing the quantum well, not more than 1.5 V drop at the p-side contact. This is a very good value for a ZnSe-based laser diode. The same linear regression gives a serial resistance of 13 Ω , which is acceptable for such a device. Consequently, stable operation can be expected from laser S0607.

¹⁶ actually it should be carried out as the more relevant *current-density vs. voltage* measurement (j/V)

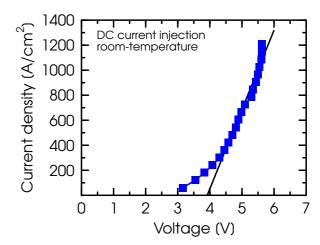


Figure 2.13: Current density vs. voltage characteristic of laser S0607, measured in DC-mode. Also shown is a linear regression to extrapolate the turn-on voltage and the serial resistance.

Electroluminescence and lasing spectra

One of the most important characteristic of a laser diode is its emission wavelength, which is determined by the composition of the material of the active region, i.e., the band gap of the quantum well material and its thickness. Although low-temperature PL measurements can give a hint about the spectral region, in which a device will emit light, it is still necessary to measure the emission spectrum under electrical current injection to obtain the precise wavelength. Furthermore, it is possible to characterize the gain process in the laser structure from the emission spectrum. Using different current injection conditions it is also possible to study heating effects in the device. Finally, the degradation mechanism can be studied in long-term measurements.

Electroluminescence spectra from a laser diode can be recorded using the same experimental setup depicted in Fig. 2.12. Placing the sample at position (b) in Fig. 2.12, the light coming from the device is focused by a system of lenses on the entrance slit of the spectrometer J.Y. 38 from *Jobin-Yvon* [214]. Due to a long focal length of 1 m, the spectral resolution of the spectrometer is 0.0073 nm at a wavelength of 520 nm [215]. Thus, it is ensured that the Fabry-Perot modes of the laser can be resolved clearly. The system is fully computer controlled using a software package from the spectrometer manufacturer. A more detailed description of the setup and the procedure can be found in Refs. [202, 216].

The typical electroluminescence and lasing emission spectra of laser S0607 are shown on the left hand of Fig. 2.14. At low current injection levels the device operates in LED-mode. For a current density of 20 A/cm² the emission maximum is centered around 512.5 nm with a FWHM of 8.5 nm, which corresponds to about 40 meV. The emission has a clear asymmetrical shape, which can be explained by (re-)absorption of the light in the device leading to an increased emission intensity on the low-energy side [8].

With increasing injection levels, the maximum of the LED emission shifts to shorter wavelengths, i.e., to the blue. This blue-shift can be explained with renormalization of the band structure and band filling [217]. Another striking feature already visible in LED-mode, is the high-frequency modulation of the EL signal. This modulation comes from the Fabry-Perot modes of the cavity. The cavity of this laser has a length of 475 μ m, the average mode separation is $\Delta\lambda=0.076$ nm – using Eq. 1.18 one can calculate the effective refractive index of $n_{\rm eff}=3.59$. This corresponds to the value H. Wenisch found for a homoepitaxial laser diode emitting in the same spectral region and which lies in

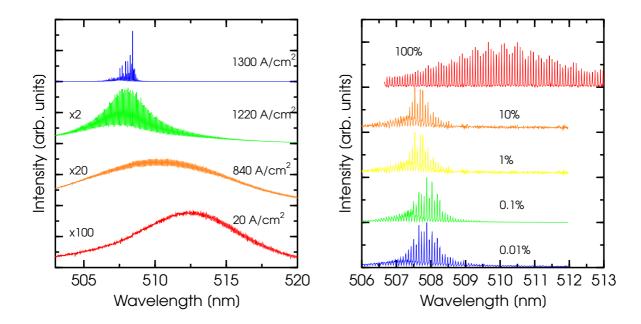


Figure 2.14: Electroluminescence and lasing spectra of the sample laser. Left: operation below (20 A/cm^2 and 840 A/cm^2) and above the laser threshold (1220 A/cm^2 and 1300 A/cm^2). The spectra are recorded in pulsed-mode with 0.1% duty cycle and $1 \mu \text{s}$ pulse width, the cavity length is only $475 \mu \text{m}$. Right: lasing operation in pulsed- and cw-mode ($1 \mu \text{s}$ pulse width). Between 10% duty cycle and cw-mode a red shift occurs due to an increased heat load.

the typical range reported in the literature [34, 59, 218]. Due to dispersion, this value deviates from the refractive index of pure ZnSe of 2.76.

A further increase of the driving current puts the device over the threshold and lasing occurs. To precisely determine the lasing threshold from the EL spectrum, it is necessary to check the difference between neighboring intensity maximum I_+ and minimum I_- in the mode spectrum, as derived by Hakki and Paoli [219]. Similar to Eq. 1.14 they obtained

$$\Gamma g - \alpha_i = \frac{1}{2L} \ln \frac{1}{r_1 r_2} \ln \frac{\sqrt{I_+} - \sqrt{I_-}}{\sqrt{I_+} + \sqrt{I_-}}.$$
 (2.5)

For equal mirrors with a reflectivity of 20% one can calculate the intensity difference necessary for lasing from Eq. 2.5,

$$I_{+} > 2.25 \times I_{-}.$$
 (2.6)

In Fig. 2.14 this point is reached at a threshold current density of 1220 A/cm², since here the intensity difference is more than 3 for the dominating mode at 508.1 nm. However, this mode dominates the spectrum not completely yet. This changes with increasing current density, as can be seen from the spectrum taken at 1300 A/cm².

The spectra in the right-hand part of Fig. 2.14 are all taken well above threshold and from the same device. However, different driving conditions – in particular different duty cycles – were used. The first spectrum is taken at a very low duty cycle of 0.01%. Under such conditions heating effects can be neglected. The laser emission occurs at

507.9 nm. With increasing duty cycle, no significant shift of the lasing wavelength is noted up to a duty cycle of 10%.

Under DC current injection, i.e., in cw-operation, the heating effects can not be neglected any longer and a shift of the emission wavelength occurs. Different physical effects contribute to this wavelength shift. The most important effect is the temperature dependence of the quantum well material, which of course depends also on the material composition itself. Furthermore, one has to include the fact that the active region consists of a quantum confined system. Other effects are related to the strain in the quantum well and the thermal expansion of the crystal, as well as band edge renormalization and band filling [217]. Thus, the temperature dependence of the emission wavelength strongly depends on the particular sample structure and quality.

As a starting point for the calculation of the temperature rise inside the active region, based on the shift of the emission wavelength, one can use the model from Lunz et~al., which describes the temperature dependence of the band gap of $Cd_xZn_{1-x}Se$ [22]. In the relevant spectral region of 506–536 nm, the temperature coefficient is in the range of 0.107–0.113 nm/K. A better way to determine the temperature coefficient, is to operate the laser diode in a temperature stabilized environment, while simultaneously monitoring the emission shift with temperature. In such a measurement, band filling or renormalization effects are excluded. For this kind of experiment, Sony reported a coefficient of 0.071 nm/K for encapsulated LEDs with triple CdZnSe quantum wells, embedded into ZnSSe and MgZnSSe barriers, which emit at 513 nm at 25°C [220]. On the other hand, Philips found a temperature coefficient of 0.096 nm/K for gain-guided CdZnSe quantum well laser diodes [221].

The experimental setup used for electro-optical characterization does not allow a temperature-stabilized operation of the devices, therefore, the temperature in the active region can only be estimated. For this, a temperature coefficient of 0.1 nm/K will be used. In Fig. 2.14 the red-shift between the "cold" device and the "heated" device is $\Delta\lambda=1.78$ nm, which consequently corresponds to a temperature rise of 17.8°C in the active region. However, since this estimation cannot account for band filling (which leads to a blue-shift) the actual temperature rise inside the device could be higher. In any case, the obtained temperature increase is low compared to older laser structures grown and processed in Bremen, where a shift around 30-100°C was found [35, 132]. The main difference between the older laser structures and structure S0607 is an improved epitaxial p-side contact. Thus, Fig. 2.14 illustrates the importance of a thorough contact optimization.

Light output vs. current characteristic

Determining the threshold from the emission spectrum of the device using Eq. 2.6 is rather tedious and not always precise. A better extrapolation of the threshold is obtained by measuring the *light output vs. current* (*L/I*), resp. the *light output vs. current density* (*L/j*) *characteristic* of the device. In LED-mode only spontaneous emission comes from the device – the light output increases linearly, but with a low efficiency. At threshold, stimulated emission sets in and the quantum efficiency increases drastically. This is reflected in a steep increase in light output with driving current, once the threshold has been reached.

From a typical L/j characteristic, the threshold current density and the external

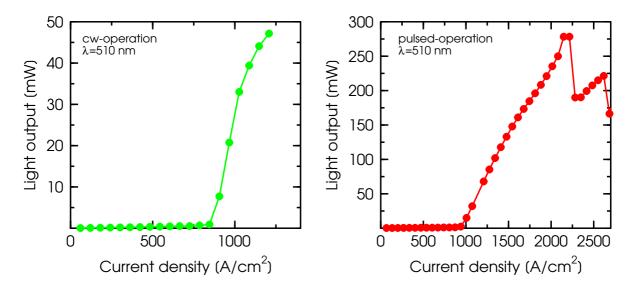


Figure 2.15: L/j characteristics of S0607. Left: cw-operation. The cavity length of this device is 1200 μ m.. Right: pulsed-mode (0.01% duty cycle, 1 μ s pulse width) with high driving current, here the cavity is 745 μ m long.

quantum efficiency of the laser can be extracted using a simple linear regression in the lasing part of the L/j curve and Eq. 1.19.

The experimental setup for L/j measurements is shown in Fig. 2.12 (position a). Current injection is provided by the precision pulsed-current source, the light coming from the device is focused by a micro lense on the entrance hole of the Si power head OMH-6701B of the optical multimeter OMM-6710B, both from *ILX Lightwave Inc.* [212]. In pulsed-mode, the integrated output power that the optical multimeter measures, can be converted into the output power of the single current pulse by using Eq. 2.4. It has to be noted that the power head is designed as an *integrating sphere* (*Ulbricht sphere*), thus, it is ensured that all light that enters through the entrance hole contributes to the measurement. However, only the light coming from one facet can be collected, accordingly, for uncoated facets the measured value has to be multiplied by 2 to obtain the total light output of the device. In the literature, it is common to report the *total output power during the current pulse*, therefore, all light output values given in this thesis have been re-evaluated to comply with this standard, unless otherwise stated.

Typical L/j measurements of laser S0607 are shown in the left-hand part of Fig. 2.15. As already noted, the quality of the laser is high and cw-operation is possible, which is shown in the left-hand part of Fig. 2.15. This device has a threshold current density of 870 A/cm² and the external differential quantum efficiency is 72%. A light output of more than 45 mW is achieved. This is among the highest output powers ever reported for ZnSe-based laser diodes operating in cw-mode. For uncoated facet, the record is 20 mW, whereas for a one-facet-coated device 30 mW were reported [5, 53]¹⁷. The threshold current density obtained from the L/j characteristics does not correspond with the value from the lasing spectra. This is due to the fact that the devices were taken from different laser bars with different cavity lengths. The laser bar used in Fig. 2.14 has

¹⁷On the Kyoto Conference on II-VI compounds S. Itoh from Sony showed a transparency with 87 mW, but details were not given [222].

a length of only 475 μ m. In Section 1.1.2 it was shown that the threshold current density is proportional to 1/L (Eq. 1.15), i.e., for shorter resonators higher thresholds result, since the mirror losses dominate the laser performance. For the 1200 μ m long device used for the cw-test in Fig. 2.15, the contribution of the mirror losses to the threshold is less significant.

In the right-hand part of Fig. 2.15 a L/j characteristic recorded in pulsed-mode is shown. To minimize the stress on the device a very low duty cycle of 0.01% at a pulse width of 1 μ s was chosen. Thus, it is possible to operate the device with high driving current. With 745 μ m the cavity of the device is somewhat shorter than that used for the cw-tests, consequently, a slightly higher threshold current density is found: 895 A/cm². Also, the external quantum efficiency of 60% is lower. A maximum light output of more than 275 mW is measured at a current density of 2200 A/cm². A further increase of the driving current results in a drastic decrease of the light output. This effect is related to a very fast degradation of the laser facets and is known as a *catastrophic optical damage* (COD). It will be discussed in more detail in Section 3.6.

Lifetime

The most important parameter and characteristic of a laser diode is its lifetime. Without a sufficiently high lifetime the commercialization is impossible¹⁸. A lifetime measurement is a very simple test: the device is set at a certain light output power and the current is adjusted such that the light output remains constant. Such a test is normally performed in cw-mode. When the device can not deliver the desired light output any longer the test ends. However, for commercial laser diodes with lifetimes exceeding several 10,000 h, this is not a practical criterion. For such devices, the lifetime tests are carried out at elevated temperatures in order to accelerate the degradation. Even then the *end of life (EOL)* is seldomly reached. The EOL has to be extrapolated from the change in operating current over time. Usually, the EOL is defined as the time when the operating current has increased by 50%. The main parameters determing the lifetime of a semiconductor laser diode are: operating current (being the combination of threshold current and efficiency), light output power level, and operating temperature.

In the framework of this thesis no elevated temperatures or EOL extrapolations were necessary, since the degradation velocity in the tested devices is high enough to actually reach the end of the device's life. For the tests, the same experimental setup as for the L/j characterization was used (position a in Fig. 2.12). Although the lifetimes found in the literature are always reported for operation in cw-mode, tests were also carried out in pulsed-mode, since cw-operation was not always possible. It is emphasized, that it is generally not possible to calculate the "cw"-lifetime of a device from a "pulsed"-lifetime in a similar fashion as for the light output using Eq. 2.4.

The left-hand part of Fig. 2.16 shows a lifetime measurement of laser S0607 in cw-mode. For this test the light output was kept constant at 2 mW. After about 70 s this output power could no longer be sustained, and the measurement was stopped. One of the problems connected with lifetime measurements in cw-mode using the setup from Fig. 2.12 is obvious in Fig. 2.16: the efficiency of the device is very high – a small change in driving current leads to a drastic change in light output. One the other hand,

 $^{^{18}}$ The "magical" lifetime barrier for the commercialization of semiconductor laser diodes is 10,000 h – just about one year.

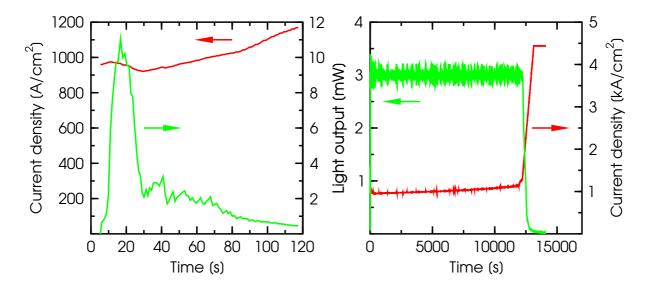


Figure 2.16: Lifetime measurements of S0607. Left: cw-operation at a constant light output of 2 mW. Right: pulsed-mode operation with 10% duty cycle and a pulse width of 1 μ s at a constant light output of integrated 3 mW, i.e., 30 mW light output per pulse.

the experimental setup is not very fast, since a cycle of measuring and adjusting takes about 0.8 s. Finally, the degradation in the device is a rapid process. The result is that the setup has difficulties to keep the light output constant and, as a result, stresses the device too much (initially the light output is more than 6 times of the desired value!).

Although the lifetime of 70 s in cw-mode is almost twice of the best value ever reported from an university based research team (37 s), it is still far below the best values from Sony of a few hundred hours [63, 5]. This is surprising insofar, as that all parameters reported for laser structure S0607 were good enough to promise a long-living device. The possible explanations for the limited lifetimes and the related degradation mechanisms will be discussed in Chapter 3.

A first hint about the underlying processes can already be seen in the right-hand part of Fig. 2.16. Here, a lifetime measurement in pulsed-mode is shown. The driving current was pulsed with a duty cycle of 10%. It has to be noted, that the light output for this measurement was set to be 30 mW per pulse – scaled with the duty cycle that gives an integrated light output of 3 mW. Therefore, both devices in Fig. 2.16 produce the same amount of light. Nevertheless, in pulsed-mode the device lives 180 times longer than in cw-mode! Taking into account that for these devices a temperature induced emission wavelength shift was only found for a duty cycle above 10%, this result indicates that the generation of heat plays a major role in the degradation process.

2.3.5 Reproducibility

The degradation of ZnSe-based laser diodes plays a central role in this thesis. Degradation mainly occurs under current injection. Thus, the electro-optical characterization methods introduced in the previous sections play a major role. To compare different laser structures it is necessary to obtain reliable results from such measurements. This is achieved by testing not only one device, but several and by using well-established statistical methods. For commercialization, semiconductor laser diodes are typically

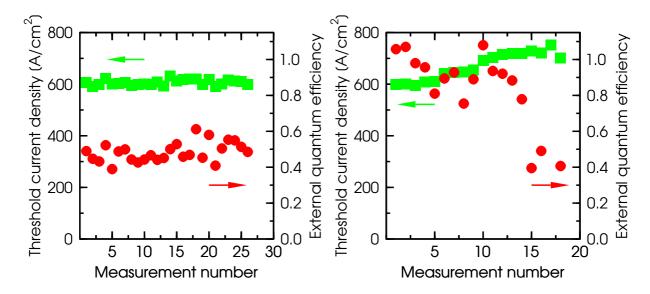


Figure 2.17: Reproducibility of L/j measurements. Shown are the threshold current density (marked by squares) and the external quantum efficiency (circles) obtained from repeated measurements of the same device. The pulse width is $3 \mu s$ in all measurements. Left: pulsed-mode with 1% duty cycle. Right: pulsed-mode with 10% duty cycle.

tested in lots of 15–20 devices under different conditions, namely output power and operating temperature. For example, a typical production qualification test for a 1.3 μ m laser diode at *Siemens/OSRAM Opto semiconductors* consists of a total of 8 test lots with 15–20 devices each, operated under 4 different conditions [223].

Such tests require multiple electro-optical characterization setups, which are usually not found in a basic-research-oriented university institute. Furthermore, the number of devices is limited: usually only one (1×1) cm² piece of the laser wafer is processed at a time. From this piece, about 8 laser bars can be cleaved, each containing 8–15 individual devices. It is therefore necessary to limit the tests to a manageable number, but still being able to obtain significant results.

The reproducibility and simultaneously the influence of the degradation onto the electro-optical measurements were partly investigated by J. Müller in a Student Paper (*Studienarbeit*), whose results will be presented in the following [216]. In particular, two important questions have to be answered: how reproducible is a single measurement and how strong is the scattering between individual devices. Whereas the first question is directly related to the influence of the degradation, the second one concerns the homogeneity of the epitaxial growth as well as the *ex-situ* processing and handling.

Reproducibility of single-shot measurements

Given a cw-lifetime on the order of a few minutes, it is obvious that severe degradation occurs under DC current injection right from the start of the experiment. Therefore, it is not expected that, for instance, a repeated L/j measurement in cw-mode will produce the same curve. However, sometimes it is necessary to perform a L/j measurement first, in order to find the start values for a subsequent measurement. Thus, pulsed-operation is necessary, and the pulsing condition have to be chosen carefully. This is illustrated in Fig. 2.17, where repeated measurements on a single device are shown. The left-hand

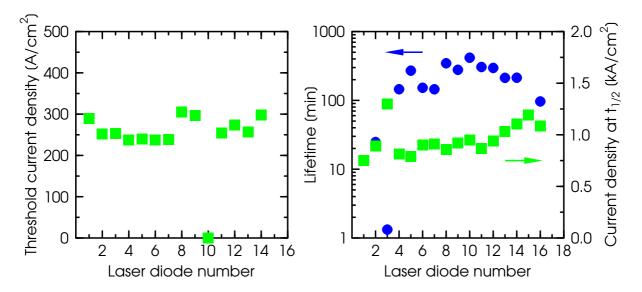


Figure 2.18: Performance variation over a laser bar. Left: scattering of the threshold current density (pulsed-mode, 1% duty cycle 1 μ s). Right: device lifetime and operating current density at half-lifetime $t_{1/2}$ in pulsed-mode at a light output power of 30 mW (0.1% duty cycle, 1 μ s).

part shows the results of L/j measurements performed at a duty cycle of 1%. During the 26 single measurements no significant change in the threshold current density of the device is found. The same is true for the external quantum efficiency, however, due to experimental limitations of the optical multimeter, the evaluation of the quantum efficiency shows generally a stronger scattering – especially for L/j characteristics with only a few measurement points. Nevertheless, degradation can be neglected. On the other hand, the same measurement performed at 10% duty cycle, as shown in the right-hand part of Fig. 2.17, results in a threshold increase after the 4th measurement, and after 17 measurements the threshold has increased by 25%. This threshold increase is accompanied by a reduced quantum efficiency – the sample is degrading. The overall higher quantum efficiency at 10% duty cycle can be explained by an additional thermal index guiding, as described in Refs. [202, 12].

It has to be mentioned that the sample tested in Fig. 2.17 is not processed from the same wafer as the devices characterized in the preceding section, where no drastic influence of the degradation was found at a duty cycle of 10%. Again, this emphasizes that the pulsing conditions have to be chosen carefully depending on the particular sample. The standard pulsing condition of 1 μ s pulse width at a duty cycle of 0.1% were derived from this demand. Hence, a L/j characteristic measured under standard conditions is a *non-destructive* test.

Uniformity of a laser bar

The reproducibility of single-shot measurements can be controlled to a certain degree by the testing conditions. Under these conditions, test results obtained from different devices of the same laser bar should be comparable. However, Fig. 2.18 shows that this is not necessarily the case. In the left-hand part, the threshold current density of individual laser diodes is plotted over their position on the bar. Clearly seen is that the devices

at the edges of the bar (#1 and #14) have a 20% higher threshold. The reason for the increase is connected to the device processing and handling. During the processing the sample is coated with photo-resist several times. This resist is applied to the sample by a spin-coater. Thus, the resist's thickness is higher at the edges of the sample piece. This gives rise to a sub-optimal processing at the edges, which is reflected in the increased threshold. Furthermore, the bar is handled using tweezers. In order not to damage the facets of the laser bar, it is grabbed at the outer edges. Since ZnSe-based material is soft, even this handling can introduce defects in the sample, which deteriorates the performance further. Meaningful results can therefore only be obtained from devices, which were not taken from the edge of the laser bar. However, Fig. 2.18 also shows that even devices taken from the middle can exhibit mediocre performance. Here, the explanation is not as straight forward. One reason for the increased threshold of devices #8, #9 and #10 (no lasing!) can be a damaged mirror facet or a processing problem. From the left-hand part of Fig. 2.18 one can conclude that all measurements should be performed at least more than once for each bar and certainly not on devices from the edge.

The right-hand part of Fig. 2.18 shows the scattering of the device lifetime over a complete bar. For this test the same laser piece as on the left-hand part was used, but a new bar was cleaved from it. Furthermore, on the second y-axis the operating current density of the device is plotted. To exclude initial defect annealing and terminal degradation processes, the operating current was taken after half of the device's total lifetime was reached. Again, the problematic edge-devices show a poor performance (or even no performance at all). But even for the devices from the middle, the lifetime scatters quite drastically. In addition, the lifetimes cannot be related directly to the operating current. One reason for the strong scattering can be the existence of extended defects in the device, i.e., of stacking faults underneath the injection stripe. This can also explain that the lifetime is not directly correlated to the operating current. However, typical defect densities in the tested laser structures are on the order of 10⁴ cm⁻² or better, thus, they should not play a significant role. In any case, it is safe to assume that the strong scattering is basically a manifestation of the non-professional experimental techniques and processing.

Figure 2.18 shows that it is sometimes difficult to obtain reliable results from just a few or even single-shot measurements. One has to make a compromise between the available sample material and the significance of the results. Once more, this illustrates the fact that a semiconductor laser diode is a highly complex system, whose performance is determined by numerous parameters, that are not all necessarily directly accessible. In the course of the following chapters it has been ensured that the findings presented are not single "lucky shots" but representative results.

Chapter 3

Degradation in ZnSe-based laser diodes

The most serious problem of ZnSe-based laser diodes is the insufficient short lifetime. Starting from some initial observations this degradation process will be characterized in the following chapter. It will focus on "conventional" ZnSe-based devices, i.e., lasers that emit around 510–530 nm. The degradation process – being the primary limitation of ZnSe-based devices concerning practical use – will not only be investigated with respect to the microscopical nature, but also concerning the major parameters that drive it. Based on these result, novel approaches to improve the reliability will be developed and tested.

3.1 Initial observations

Figure 3.1 shows the best cw-characteristics ever obtained from a standard laser diode grown and processed in Bremen. On the left-hand side, the combined L/j and j/V characteristics are shown. Despite no facet coating was applied, a threshold current density of only 600 A/cm² is necessary for lasing. When lasing occurs the initial differential quantum efficiency is almost unity. A record output power of 75 mW is obtained. This implies a quantum well with a high structural and optical quality. On the other hand, the operating voltage at threshold is about 9 V. Although this is higher than for other structures grown in Bremen, it is still tolerable, considering, that Sony's record laser diode from 1996 lased for more than 101 h in cw-mode with an operating voltage of 11 V and a threshold current density of 533 A/cm² (cf. Tab. 1.3) [75].

Nevertheless, the right-hand side of Fig. 3.1 reveals that such high stability is not the case for the Bremen laser diode. Here, a typical lifetime measurement of the same laser structure at a nominally constant output power is depicted. The light output from the device shows a strong oscillation, which derives from the slow test setup on the one hand and from the relatively high quantum efficiency of the device otherwise, as mentioned before. This is verified by the evolution of the driving current necessary to maintain the desired output power: only small oscillations are visible (the current adjustment was perfromed in 0.2 mA steps). In order to keep the device over the threshold for the entire lifetime test, this device's output power was kept constant around 4 mW, thus the device is operated above threshold – even if the current adjustment is not performed fast enough. It should be kept in mind that most devices found in the literature are usually tested at an output power of only 1 mW. Under such conditions and with

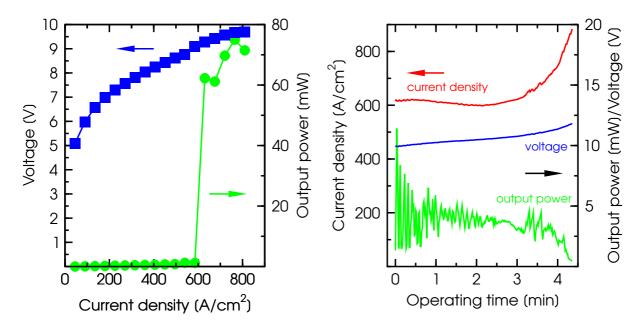


Figure 3.1: Best cw-characteristics obtained from a laser diode grown and processed in Bremen (sample S0728). Left: L/j and j/V characteristics. Right: lifetime measurement of the same structure. The light output was kept constant at 4 mW, the operating voltage and current density are also depicted.

a better test setup, a higher lifetime can be expected surely, yet, it will remain well below Sony's record. The current density curve also shows that only in the last quarter of the experiment a significant increase in operating current is necessary, nevertheless, the current increase is a continuous process. It should be realized that the increase in driving current is caused by a gradual decrease of the quantum efficiency: *the device becomes darker* if no current adjustment is performed. Even after the lasing mode cannot be sustained any further, spontaneous emission is still detected.

Considering the operating voltage evolution, one can conclude that degradation of the electrical characteristics does not occur during the aging test. The increase in operating voltage simply reflects the increased driving current required to deliver the constant light output. Two important findings should be noted from this aging experiment:

- A decreasing quantum efficiency causes the device's failure.
- The lifetime is 4 min in cw-mode.

Obviously, it is necessary to investigate and to understand which mechanisms cause the decrease of the quantum efficiency. This is a topic of general interest and has been discussed intensively in the literature, as it will be presented later on. Apart from the general significance of understanding the underlying degradation process, it should also be possible to reproduce the results reported in the literature – or at least to obtain lifetimes of the same order. In that sense the second point is troubling. Although the initial device characteristics are absolutely comparable to the literature values, the lifetime of structures grown in Bremen is still three orders of magnitude lower! Identifying the

¹Yet, they are the best values ever obtained from a university based reseach group.

reason for this difference is naturally important for the research work in Bremen, but can also help to gain insight in the nature of the degradation process.

For the work presented in the rest of this chapter, the following two questions represent the leitmotiv:

- 1. Why does the light go out?
- 2. Why is the degradation in Sony's devices slower?

3.2 Dark defects

3.2.1 Experimental observations

There are several experimental methods to investigate the mechanisms behind the (gradual) darkening of light emitting devices. Starting from a quantitative approach to determine the dynamics of the process by monitoring the light output over time – ideally under various driving conditions, such as ambient temperature or operating current – down to a microscopical investigation of the degraded samples using transmission electron microscopy (TEM), the full spectrum of experimental techniques can be used. But the most direct approach is to monitor the light emission process in the active region during operation. In such a *topography* measurement, free carriers are produced in the device either by current injection (*electroluminescence*), optical excitation (*photoluminescence*), or electron-beam excitation (*cathodoluminescence*), while the emission from the device is monitored spatially resolved – typically in an optical microscope. All three types have been performed on ZnSe-based light emitting structures, however, in terms of device relevance clearly the EL topography is most important, even though it requires the preparation of samples with a transparent top contact [140, 63, 46].

Figure 3.2 shows a sequence of photographs taken at different times during such an experiment. For this test special devices with a 50 nm thin top Au-contact were prepared and the device was operated at 20 A/cm² in DC-mode in an optical microscope equipped with a camera. The first photograph is taken directly after turn-on. It reveals some darker features labelled I–IV. Scanning through the other photographs, it is found that these features do not grow or change their shape in time². It can therefore be concluded that these features originate from dust on the sample-surface or on the lenses in the optical path.

However, after 2 min of operation, two clusters of dark regions are clearly visible (A and B) and 4 additional dark spots (1–4) can be seen. It is interesting to note that at the beginning of the experiment no dark feature is seen at the location of the later appearing clusters A and B. The same holds true for the dark spots.

From the clusters dark lines extend. These lines are oriented along the $\langle 100 \rangle$ and the $\langle 010 \rangle$ directions. Due to limitations of the test setup, it cannot be ruled out that these lines are inclined at a small angle to these directions. From the sequence of photographs, it seems that the dark lines are mostly nucleated at a dark spot during current injection. The dark lines at the edge of the photographs are nucleated in the current injection region outside of the photographed area. During operation, the dark lines grow along their directions and form a network. Only at the later stages of the experiments (25 min),

²The gradual intensity increase in the undegraded areas is caused by the increasing exposure time.

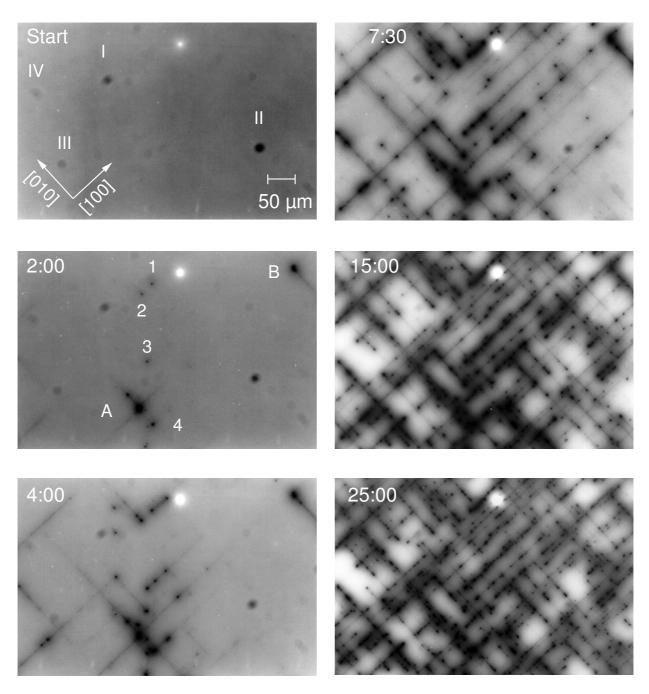


Figure 3.2: Electroluminescence topography on a ZnSe-based laser diode, operated at $20~A/cm^2$ in DC-mode at room-temperature. The area shown in these photographs is $(360\times540)~\mu\text{m}^2$. One single defect in this area corresponds to a defect density of $5\times10^2~c\text{m}^{-3}$. It should be noted that the current injection area was much larger: $(1000\times1000)~\mu\text{m}^2$. During the experiment the exposure time was increased to obtain a sufficient contrast.

it can be identified, that the dark lines actually contain many dark spots. In particular, it turns out, that the dark clusters A and B are an area with a high density of dark spots. Most dark spots appear in the vicinity of an already existing dark area. Also visible is that the dark spots all grow to roughly the same size of 5–6 μ m after initial nucleation. Similar values are reported in the literature [49]. Last but not least, it is noticeable that the dark features are homogeneously distributed over the complete current injection area [176].

In sum, the EL topography gives a first answer how the quantum efficiency of the devices is reduced: through the generation of dark defects during operation. Furthermore, two types of dark defects – *dark spot defects* (*DSD*) and *dark line defects* (*DLD*) – are identified.

3.2.2 Microscopic nature and generation of new defects

Dark defects are well-know features commonly found in degraded opto-electronic devices [9]. They have been identified as main cause of degradation in conventional III-V lasers. For ZnSe-based lasers they have first been mentioned by Haase *et al.* as early as 1993, followed by a first microstructural characterization using TEM [117, 140]. In the following years, the combination of one kind of topography measurement and subsequent TEM characterization proved to be most successfull to understand the degradation process in these devices. However, due to limited TEM resources such combined experiments could not be performed in Bremen, and consequently, the following description of the microstructure of these defects has to be limited to results reported in the literature.

Dark spot defects

Already in the first studies, it was observed that the initial DSD seen directly after turn-on of the current, are nucleated at the site of a pre-existing defect, usually a stacking fault [140, 47, 224]. Furthermore, the defects responsible for the reduced light emission are confined to the active region [47]. During operation, these dark defects grow in number and form a network of triangular shape³, as shown in Fig. 3.3. They consist of dislocation dipoles and dislocation loops with a density of the order of 10¹⁰ cm⁻² at the final stage [140]. There are some discrepancies concerning the Burgers vectors of these defects: Whereas Guha *et al.* reported vectors

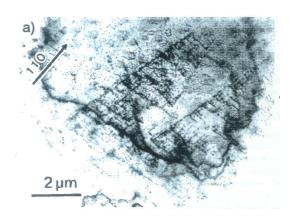


Figure 3.3: Network of dislocations that forms a DSD (TEM micrograph, taken from Ref. [53]).

of the type $(a/2)\langle 110\rangle$ lying in the (100) junction plane, Hua *et al.* reported that the dislocation dipoles are oriented along the $\langle 430\rangle$ directions [140, 47]. Tomiya *et al.* from Sony found networks involving dislocation dipoles with Burgers vectors of $(a/2)\langle 011\rangle$ in-

³The magnification used in the photographs in Fig. 3.2 is too low to reveal this aspect, cf. e.g. Ref. [225].

clined at 45° to the (001) junction plane in degraded structures [224]. Such type of Burgers vector corresponds to the one found for the $\langle 100 \rangle$ DLD in AlGaAs optical devices, although the dislocation dipoles lie in the (001) junction plane in that case, whereas for the ZnSe-based devices they are in the {111} plane [224]. The reason for the discrepancies between the different reports on ZnSe-based devices is unclear, but may be attributed to different growth conditions and sample preparation techniques [226].

Dark line defects

Concerning the DLD, one has to distinguish between two different types of DLD which are related to different type of defects. The first type of DLD is aligned in the $\langle 110 \rangle$ direction and correlates to misfit dislocations in the quantum well [46]. Under current injection these lines do not grow significantly and consequently, are only of limited significance for the degradation process [224]. They indicate a (partly) relaxed quantum well, as it could also be verified using samples grown in Bremen [34].

The second type of DLD is oriented along $\langle 100 \rangle$ and $\langle 010 \rangle$ as seen in Fig. 3.2. This type of DLD is usually not seen in topography experiments initially, rather, it is formed during the degradation experiment, i.e., under current injection or optical excitation, which stresses their importance for the degradation process. In the same fashion as the SF act as nucleation site for the DSD, the DSD act as nucleation site for the DLD. Qualitatively, one observes that the DLD are actually DSD growing along the above mentioned directions [49]. There are some reports in the literature that mention the observation of a highly mobile defect preceding the formation of a DLD. This mobile defect, ejected from a DSD, travels along $\langle 100 \rangle$ and in its trace a DLD forms [227, 228, 146]. However, this could not be observed in Fig. 3.2 nor in similar experiments in Bremen.

Generation of dark defects

An important fact of the DLD (and also the DSD) formation is that it is directly related to the recombination of carriers in the quantum well: in optical degradation experiments with variable excitation energies, it was found that dark features could only be produced when the excitation energy was at least as high as the band gap energy of the quantum well barrier [225].

The early TEM investigations on DLD showed that the defects responsible for the DLD are located in the quantum well, but it could not be correlated to the presence of a dense network of dislocations as in the case of the DSD [229]. In fact, no specific microscopic feature could be identified and based on this observation it was proposed that *point defects* – acting as non-radiative recombination centers – are responsible for the formation of the DLD. Later studies confirmed that the DLD are composed of a series of small aligned dislocations and dislocation loops [146].

Combining the two findings above, it is possible to develop a model of how the DLD (and also the DSD) grow under current injection [230]: when carriers are injected into the system, some of them recombine non-radiatively at a defect site (point defect or microscopic defect). The absorbed energy is released into the crystal lattice via the generation of phonons, which leads to a local heating and a strong vibration of the defect atoms. Thus, the barrier for the motion of the defect is reduced which in turn

can enable the migration of the defect or even the generation of a new defect. Such a recombination-enhanced defect reaction (REDR) is a well-known degradation mechanism for conventional III-V opto-electronic devices [231, 9]. There are different types of defect reactions. For the generation and growth of the dark defects in ZnSe-based devices, two types of mechanisms were found to be important. Whereas for the expansion of the defects in $\langle 110 \rangle$ a recombination-enhanced dislocation glide (REDG) is responsible, the formation of the $\langle 100 \rangle$ -DLD occurs via a dislocation climb (REDC) process [232, 49]. It is interesting to note that for a REDG process no point defects are necessary, contrary to the REDC, which requires such defects to maintain growth [196]. Degradation of ZnSebased lasers is caused by a combination of both processes [232]. Deviations of the DLD from the exact crystallographic axes can occur (angles up to 20°), which are caused by different growth conditions and surface morphologies [233].

In most of the cited literature reports, the DSD/DLD were nucleated at a site of a preexisting defect, usually a SF. Consequently, most groups concentrated on the reduction of these defects, i.e., on the substrate preparation and the growth start procedure to obtain a low initial defect density, such that no defect is present in the active region of the device ($< 10^4 \text{ cm}^{-2}$). In this case the lifetime is no longer limited by the SF defect density [123]. Indeed, the lifetime of ZnSe laser diodes could be extended by these measures, however, although the SF act as nucleation site for the dark defects, they do not play an active role in the degradation process itself [75, 49]. This observation is very important, because it indicates, that the degradation processes is facilitated and accelerated by the presence of SF, but degradation takes places just the same, even when SF are absent. This facilitation of the degradation by SF is reflected in different activation energies for the degradation process, as it was obtained from temperature-dependent lifetime test. In the case of a high SF density (10^7 cm⁻²) an activation energy of 0.3 eV was found, whereas for defect free devices (10³ cm⁻²) an energy of 1 eV results. In the first case, the formation of DLD are observed, whereas the second case is purely REDR [234]. These two cases therefore represent the outer limits. Due to the limitations of the experimental setup, no temperature dependent lifetime test could be performed on the samples grown during the experimental work of this thesis, however, it is safe to assume that the activation energy is between 0.3 eV and 1 eV.

In the same sense it is not surprising that no dark spots are seen in Fig. 3.2 initially, but then appear after a few min of operation. Similar observations are reported by other groups [235, 78]. For very low defect densities and optimized growth conditions, no dark features are observed, and the degradation manifests itself only in a gradual darkening of the active area [142]. Still, this gradual darkening process is caused by REDR [49, 232]. In the absence of SF, this REDR process causes the diffusion of the point defects in the material. The activation energy for this process depends primarily on the type and density of the point defects, as well as the specific diffusion mechanism. Both of these aspects can be influenced by the growth conditions and the layer design. Concerning the nature of the point defects, several candidates have been proposed, including vacancies, interstitials, and doping related defects [236, 237]. For a N-acceptor-decomposition related Se vacancy, a strong diffusion has been proposed and calculated, but only for a Zn interstitial a recombination-enhanced migration was experimentally observered and explained [238, 239, 240]. This aspect is still under investigation and discussion, and more work is necessary.

3.3 Dynamics of recombination enhanced defect reaction

Knowing the mechanism behind the generation of the dark defects, it is possible to develop a model for the quantitative description of the process, as shown by Chuang *et al.* [143, 230]. Using this model it is possible to explain the long-term behavior of light-emitting devices under current injection and thus, gain further insight in the degradation dynamics. In conjunction with *constant current degradation experiments*, this model is particularly useful and therefore, it will be described in the following sections.

The starting point is the basic carrier continuity equation for the carrier concentration n(t) in the quantum well at a given time t,

$$\frac{dn(t)}{dt} = \frac{j}{ed} - B \, n(t)^2 - A \, N_d(t) \, n(t),\tag{3.1}$$

with j as constant current density, d the quantum well thickness, B the radiative recombination coefficient, A the non-radiative recombination coefficient and $N_d(t)$ as defect density in the active region.

In Eq. 3.1 it is explicitly assumed that the non-radiative carrier recombination related to *A* occurs at a defect site. Furthermore, it is legitimate to assume that the carrier density reaches its equilibrium value on a much faster timescale than defect generation occurs, thus Eq. 3.1 can be set equal to zero (quasi-static). The long-term behavior is of special interest, however, after a sufficiently long operation time, no significant radiative recombination can be expected any longer and only the first and the last term contribute to Eq. 3.1. Thus, one obtains for the carrier density in the active region,

$$n(t) \approx \frac{(j/ed)}{A N_D(t)}$$
 for large t . (3.2)

This form indicates that the long-term behavior of the device is determined by the time-dependence of the defect density $N_D(t)$.

3.3.1 Defect generation mechanisms and long-term behavior

The time-dependence of the defect density depends on the mechanism that generates the defects during current injection. In Fig. 3.4 several types of these defect reactions are schematically depicted. Type (a) represents radiative recombination which does not produce a defect. Type (b) is the direct generation of a defect D due to an electron-hole

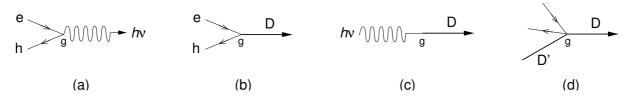


Figure 3.4: Diagrams of carrier recombination and defect reaction processes. e and h denote electron and hole, resp., D and D' are defects and $h\nu$ represents a photon. The recombination couples to the defect with a coupling constant g. For the description of the different processes cf. text [196].

recombination. Such a process was first found in Si solar cells and is known as silicon weak-bond-breaking (SWB) [241]. For such a process the following defect generation rate⁴ can be assumed [230],

$$\frac{dN_D(t)}{dt} = K \, n(t)p(t) = K \, n(t)^2,\tag{3.3}$$

with K as defect generation coefficient and using the fact that the active region is undoped, i.e., n(t) = p(t). Replacing n(t) in Eq. 3.3 with Eq. 3.2 and separating the variables one obtains

$$N_D(t)^2 dN_D(t) = K \left(\frac{j}{edA}\right)^2 dt.$$
 (3.4)

This can be integrated, and the time-dependence of the defect density in the case of a SWB-like process is given by

$$N_D(t) = \left[3K\left(\frac{j}{edA}\right)^2\right]^{\frac{1}{3}}t^{\frac{1}{3}}.$$
(3.5)

Plugging this time-dependence back into Eq. 3.2, it is found that for long times t the carrier density n(t) in the device is proportional to $t^{-\frac{1}{3}}$. Since the light output P is proportional to $n(t)^2$, the long-term behavior of the light output of the device under constant current injection is in the case of a SWB-like defect generation mechanism proportional to

$$P_{\text{SWB}} \sim t^{-\frac{2}{3}}$$
. (3.6)

In Fig. 3.4, case (c) essentially represents the same defect generation mechanism, except that the defect is directly created by a photon (which was first created by a radiative recombination).

Defect creation mechanisms (b) and (c) are the most simple processes possible in semiconductors. The next simplest process is shown in diagram (d): here a new defect D is generated again by carrier recombination – but at a side of an already existing defect D'. Thus, in the defect generation rate equation, the defect density $N_D(t)$ has to appear explicitly,

$$\frac{dN_D(t)}{dt} = K \, n(t)p(t) \, N_D(t) = K \, n(t)^2 \, N_D(t). \tag{3.7}$$

Following the same procedure as before, one obtains for the long-term dependence of the light output in case of a REDR-based degradation process,

$$P_{\text{REDR}} \sim t^{-1}.\tag{3.8}$$

3.3.2 Experimental verification

From the above discussion it can be deduced that the time-dependence of the light output for long times reveals the dominating defect generation process present in the device. In such a measurement the device is operated at a constant current injection level, as shown on the left-hand side of Fig. 3.5. Almost no degradation occurs in the first hour

⁴defect annealing is neglected in the following discussion

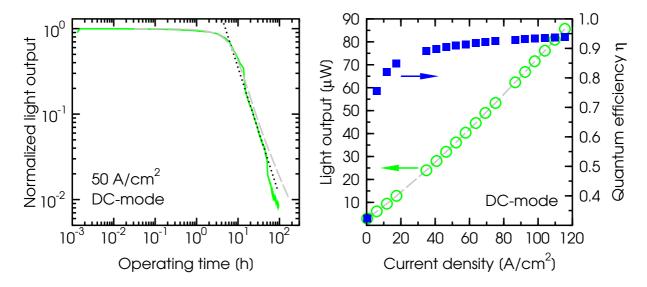


Figure 3.5: Left: constant current degradation of a ZnSe-based laser diode. Plotted is the light output normalized to its initial value over the operating time. The device was operated below threshold. A first evaluation using a simple power law leads to a long-term behavior $\sim t^{-1.5}$ as indicated by the doted line. The dashed line represents a theoretical calculation based on the more detailed analysis of the dynamics presented in Sec. 3.3.3 (initial quantum efficiency: 90%). Right: L/I characteristic of the same sample prior to the lifetime test. The curve has been fitted using Eq. 3.10 (dashed line). With the results of this fit, the initial quantum efficiency η has been calculated using Eq. 3.11.

and after 10 h the device still emits 50% of the initial light output. Concentrating on the long-term behavior of the output, one finds that the intensity decreases with $t^{-1.5}$ for operating times around 15–45 h . Although this value is closer to the time-dependence expected for the REDR- than for a SWB-based process, it still differs significantly. However, for operating times beyond 70 h a t^{-1} dependence is visible. A longer measurement time would have been desireable for this experiment, but one should take into consideration the logarithmic scaling of the time axis.

Figure 3.5 hints that the major defect generation mechanism is REDR with a t^{-1} long-term behavior of the output power. However, to verify this, a more detailed study of the light output evolution determined by Eq. 3.1 and Eq. 3.7 is necessary.

3.3.3 Analytical solution

The complete procedure to obtain an analytical solution for the light output evolution under constant current degradation in the case of a REDR-based degradation mechanism is described in Ref. [230], only the result will be presented in the following.

Using the normalized operation time $\tau=K\,n(0)^2\,t$ and the initial radiative quantum efficiency $\eta=\frac{Bn(0)^2}{(j/ed)}$, the following relation between operating time τ and the normalized output power $P=\frac{Bn(t)}{Bn(0)}$ is found,

$$\tau = \eta \ln \left[\frac{1 - \eta P}{(1 - \eta)P} \right] + \frac{1}{2} \left(\frac{1}{P} - 1 \right). \tag{3.9}$$

By calculating τ for the normalized output power range $0 < P \le 1$ and a subsequently plotting of P vs. τ , general constant current degradation curves are obtained in which the quantum efficiency is the only adjustable input parameter. η determines the curvature of the degradation curve.

The initial radiative quantum efficiency can be extracted from L/I characteristics performed prior to the degradation experiment. Setting Eq. 3.1 equal zero and solving for n(t), resp. for $n(t)^2$, in order to obtain the output power [$\sim n(t)^2$], one obtains,

$$P = C\left(I + Y - Y\sqrt{1 + \frac{2I}{Y}}\right),\tag{3.10}$$

with C as optical coupling coefficient, current I, and the term $Y = \frac{eSd(AN_D)^2}{2B}$, in which the current injection area is given by S. In this form, the light output does only depend on the current I and the parameter Y, which can be obtained by fitting Eq. 3.10 to the L/I characteristic. Furthermore the intrinsic quantum efficiency is given by

$$\eta = 1 + \frac{Y}{I} - \sqrt{\left(1 + \frac{Y}{I}\right)^2 - 1}.$$
(3.11)

Thus, the initial quantum efficiency can be calculated using the value of Y obtained by the fitting procedure.

A complete analysis of constant current degradation curves involves the recording of the L/I characteristics prior to the experiment. Using the quantum efficiency η obtained from this test, universal degradation curves can be plotted using Eq. 3.9. These curves differ from the experimentally obtained one only by a scaling factor of the time axis, since $\tau = K \, n(0)^2 \, t$. By comparing theoretical and experimental curves, the scaling factor $K \, n(0)^2$ can be obtained. In Eq. 3.7 K was introduced as defect generation coefficient, thus this scaling factor $K \, n(0)^2$ is related to the initial defect density, as well as it depends on the precise physical defect reaction mechanism and operating temperature. Since these aspects differ between different samples, one can not simply calculate the initial defect density [143]. However, it can still be used as a figure of merrit for the comparison of different structures.

Based on this procedure a theoretical curve for the constant current degradation shown in Fig. 3.5 has been calculated. On the right-hand side of Fig. 3.5, the initial L/I characteristic of the device is shown. This curve has been fitted using Eq. 3.10, and the initial radiative quantum efficiency η was calculated. Using an efficiency of 90.2%, the theoretical $P(\tau)$ curve has been calculated and by comparing it to the experimental curve a scaling factor $K \, n(0)^2 \sim 3$ is obtained. The good agreement of theoretical and experimental curve also reveals that the main degradation process is indeed REDR based, and that a t^{-1} behavior can only be expected for very long operating times.

Constant current degradation experiments are a useful tool to test the stability of opto-electronic devices. A complete fitting procedure is not alway necessary – for a qualitative comparison the experimental curves are sufficient, if obtained under the same conditions.

Another interesting feature of the REDR-based model of defect creation developed by Chuang *et al.* is that with minor additions it can also be used to explain defect annealing, e.g. the recovery and improvement of quantum well luminescence under optical excitation [242, 243].

3.4 Driving forces of the degradation mechanism

Once the primary degradation mechanism is identified, the next important question is which physical parameters influence the process. In a opto-electronic semiconductor device, there are several critical parameters which can act as driving force. In the following section some of them will be investigated in more detail, in order to develop new approaches to improve the laser diode stability.

3.4.1 p-type doping

Recombination-enhanced defect reactions are related to the diffusion of point defects. Their generation and type is mainly determind in the growth process. An additional complication occurs when doping is present. It was described before that p-type doping is difficult in the case of ZnSe-based material, and that it can act as source for point defects – especially in the case of highly compensated material. In fact, a drastic reduction of the free hole concentration in the p-type doped layers of a laser diode was found after long-time operation [244]. Furthermore, it is reported that during optical degradation of doped ZnSe-laser structures, the quantum well emission decreases, which correlates with the occurrence and intensification of a defect related emission originating in the waveguides. For not-p-type doped structures, such a behavior is not observed - in particular, no decrease of the quantum well emission intensity is found [237]. A strong influence of the N doping was concluded from this experiment. In addition, Gundel et al. calculated that p-type doping with N not only provides free acceptors in the semiconductor material, but is also accompanied by the formation of a very stable threefold-positively-charged interstitial N-complex [245]. Under current injection or optical pumping, N-acceptors can transform into this charged complex, which is naturally subject to migration in the presence of an electrical field. Under forward bias, the complex will migrate to the *n*-side due to its positive charge, thus, not only the effective carrier concentration on the p-side is reduced, but also the density of point defects in the quantum well is increased. On the other hand, other groups reported the generation of dark line defects and gradual darkening of the active area also for undoped structures [227].

One reason for the discrepancies between these reports is related to the different experimental configurations used – namely the plasma cells that provide the N-dopants. The ratio of activated N strongly depends on the individual cell (cf. e.g. data cited in Ref. [246]). Fact is, that the N-doping or at least the *p*-type doping does exhibit a tendency to migrate, however, it is not clear if the lifetime of the laser diodes is limited by the stability of the *p*-type doping [247, 248].

To investigate the situation for samples grown in Bremen, the same experiment as in Ref. [237] was performed by J. Müller [216]. Fully doped laser structures were optically excited with a laser emitting at 441 nm. For such laser light, the claddings are transparent and excitation occurs only in the waveguides and the quantum well. Furthermore, the laser was focused to a spot diameter of about $10~\mu\text{m}$, resulting in an excitation energy of roughly $50~\text{kW/cm}^2$, which is about twice of the energy used in Ref. [237].

Figure 3.6 shows the results of this experiment. On the left-hand side, the evolution of the quantum well emission intensity is plotted vs. the operating time for two different laser structures. For the laser structure with undoped quantum well, a fast decrease

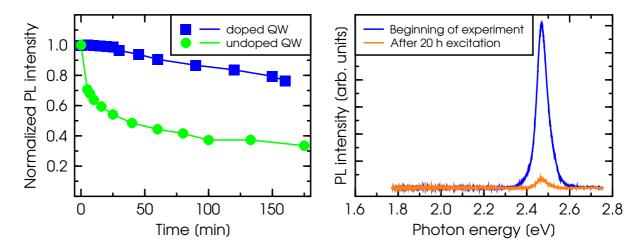


Figure 3.6: Left: time-dependence of the room-temperature quantum well PL signal of fully doped laser structures under optical excitation. One laser contains a Cl-doped quantum well. The excitation wavelength is 441 nm, the laser spot is focused to a diameter of $10 \,\mu\text{m}$, and the excitation energy is $50 \,\text{kW/cm}^2$. The intensity has been normalized to the initial value. Right: exemplary PL spectra of the laser with doped quantum well taken at the beginning and the end of the same experiment [216].

down to 70% of the initial emission intensity is found after a few minutes of operation. But the decrease slows down, and after 180 min the emission intensity is still more than 30%. In Ref. [237], a significantly faster degradation was observed for a comparable laser structure (30% after 2 min), despite the lower excitation intensity. Since the excitation spot is in both cases only 10 μ m wide, one can rule out the existence of a SF in the excited region – the emission degradation is purely related to point defects.

The second laser structure tested in Fig. 3.6 contains a Cl-doped quantum well. For this structure, no degradation is observed in the first 30 min; after that, the intensity decreases slowly. Since the doped quantum well is the only difference between both structures, the slowed-down degradation has to be related to this quantum well doping. The precise mechanism behind this stabilization remains to be investigated. But the fact that *n*-type doping leads to a stabilization, fits to the observation that Cd exhibits an increased diffusion tendency in the presence of p-type doping [249, 77]. This would imply that Cd diffusion plays an important role in the degradation process, and that this diffusion can be slowed down by *n*-type doping of the quantum well. If the degradation on the other hand would be dominated by the stability of the N-acceptor and the proposed charged interstitial complex, one would – if anything – expect an acceleration of the degradation and migration due to the quantum well doping. Since this is not the case, one can at least conclude that the stability of the quantum well is more important, such that the positive effects of it's *n*-type doping predominate. This is supported by the data shown on the right-hand side of Fig. 3.6, where the emission spectra of the doped-quantum well structure at the beginning of the experiment and after 20 h excitation are depicted. These spectra are representative for all tested samples. No deep defect-related emission is observed around 2.2 eV, contrary to the report in Ref. [237]. Furthermore, no shift of the emission energy occurs.

From the experimental results it follows that the degradation process in the laser

samples from Bremen is different from that reported in Ref. [237]. Although an influence of the *p*-type doping is seen, it is of different nature and strength. By low *n*-type doping of the quantum well the stability of the devices can be improved. These findings most probably reflect the different experimental realizations of the doping with N.

3.4.2 Strained quantum well and Cd diffusion

The active region of a typical ZnSe laser diode consists of a CdZn(S)Se quantum well with Cd contents up to 40%. Such a quantum well is highly compressively strained. It was mentioned before that a relaxed quantum well gives rise to $\langle 110 \rangle$ -dark lines in topography experiments. Therefore, one can expect that the strained quantum well plays a major role in the degradation process. Furtheron, the REDR mechanism is based on the diffusion of point defects. Although the carrier-recombination *stimulates* the diffusion, an intrinsic driving force is still required to enable the diffusion process. In that sense, the non-radiative recombination provides the energy to surpass the diffusion barrier. The strained quantum well is obviously a potential candidate for such a driving force – all the more since the dark defects are confined to the active region. On the other hand, in conventional III-V laser diodes a compressively strained quantum well has positive effects on the stability of the devices, since it supresses the climb of $\langle 100 \rangle$ -dark lines defects [250].

Additionally, the strong tendency of Cd to diffuse – in particular in the presence of *p*-type doping – is well known [77, 249]. A noteworthy observation of these temperature-dependent annealing experiments is that the diffusion starts from the GaAs/ZnSe heterointerface, which acts as reservoir for point defects [132, 251, 252]. Similarly, it was found that the temperature stability of the PL emission of CdZnSe quantum wells depends on the distance from the heterointerface – obviously point defects play a vital role for the Cd diffusion process [253].

Figure 3.7 shows the results of constant current degradation experiments with different light emitting structures. Although the samples differ in several points, the graph gives a first hint of the influence of the strain, resp. the Cd diffusion, on the degradation velocity. First, one should note that the shortest lifetime is measured for a homoepitaxial multi-quantum well (MQW) LED with Cd-containing quantum wells (grown by H. Wenisch [34]). Due to a not optimized substrate preparation and deoxidation process, the defect density in homoepitaxially grown samples is roughly two orders of magnitude higher than for heteroepitaxy [34]. This explains the higher lifetime of the hetero-MQW LED. Both devices show a decrease of the output power as expected for a REDR-based degradation. In the case of the short-lived homo-LED, the shape of the curve is considerably rounder than for the hetero-LED. Based on Eq. 3.10 this indicates a lower initial quantum efficiency, caused by the higher defect density.

One the other hand, the heteroepitaxially grown single-quantum well laser diode has a higher lifetime than both Cd-containing MQW LEDs. Since the substrate preparation for LED and laser structures is different in heteroepitaxy, this reflects again a different defect density [35]. Another reason is a possible lattice hardening due to the addition of S (alloy hardening) [76]. In any case surprising is the behavior of the homoepitaxial MQW LED structure without any Cd in the quantum wells. Here, binary (and consequently unstrained) ZnSe quantum wells form the active region. Although the device is operated at a 10 times higher current density, it lives at least one order

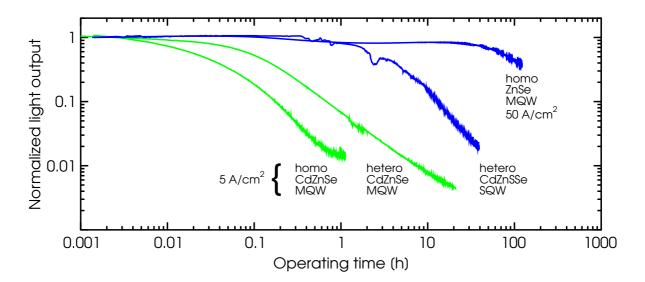


Figure 3.7: Constant current degradation experiments on different homo- and heteroepitaxially grown LED structures with multi-quantum wells (MQW) and single-quantum well (SQW) laser structures. The homoepitaxial samples were grown by H. Wenisch [34], the heteroepitaxial MQW-LED is from Ref. [95], whereas the SQW-LD was grown in the framework of this thesis.

of magnitude longer than any other sample, despite the fact that the defect density of this structure is comparable to that of the other homo-LED. This strongly suggests that a strained quantum well and/or Cd diffusion are major driving forces for the point defect diffusion-based degradation.

In this context it is interesting to investigate, whether the generation of dark defects based on the REDR process modifies the quantum well region aside of the massive generation of non-radiative recombination centers. One way to access this information is to perform CL mappings of the degraded active regions with μ m-resolution. In such investigations, it was found that inside a dark spot the emission energy is blue-shifted [254, 78]. On the other, along a $\langle 100 \rangle$ -DLD, starting at a DSD, a blue-shift was observed. With increasing distance to the DSD, an increasing red-shift is superimposed [254]. Other groups observed a red-shift in DLD formed outside of the current-injection region [78]. These emission shifts can be explained by two individual effects taking place at the same time. Concerning the blue-shift, an out-diffusion of Cd is responsible. Due to this out-diffusion, the band gap energy of the quantum well material is enlarged and a higher emission energy results. This out-diffusion is driven by non-radiative carrier recombination – Cd is subject to a strong *recombination-enhanced interdiffusion* [78]. Similar diffusion related degradation accompanied by an emission blue-shift has been observed in conventional III-V laser diodes under current injection [255].

The red-shift, on the other hand, can be explained by a relaxation of strain. In the presence of an in-plane strain, the band edges shift relative to each other and the strain-induced variation of the band gap energy is given by

$$\Delta E_g(\epsilon) = 2a \left[\frac{C_{11} - C_{12}}{C_{11}} \right] \epsilon - b \left[\frac{C_{11} + C_{12}}{C_{11}} \right] \epsilon$$
 (3.12)

where a is the hydrostatic deformation potential, b the shear deformation potential, C_{11} ,

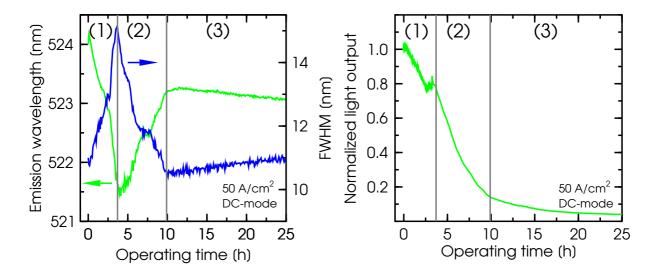


Figure 3.8: Change of emission wavelength, sharpness (left), and integrated emission intensity (right) during a typical constant current degradation experiment at 50 A/cm² in DC-mode. Spectra have been recorded every 5 min. Three different phases of the degradation can be identified (1)–(3).

 C_{12} the elastic stiffness constants and ϵ represents the in-plane strain, which is $\epsilon < 0$ for compression and $\epsilon > 0$ for tension [256, 254]. Values for the different parameters can be found in Refs. [257, 258, 259, 260]. Plugging those numerical values into Eq. 3.12 gives

$$\Delta E_g(\Delta \epsilon) = (-1761 \text{ meV}) \Delta \epsilon.$$
 (3.13)

If strain is relaxed, i.e., ϵ becomes smaller, then $\Delta \epsilon > 0$ and with Eq. 3.13 a lower band gap energy results.

Performing μ m-CL mappings requires not only a special experimental setup, but also the changes of the emission cannot be observed in real-time [254, 78]. Therefore, a different experimental approach was used to investigate the influence of strain and Cd diffusion: during a constant current degradation experiment, the light output from the device is not only monitored by the optical multimeter, but also one part of the emission is focused on the entrance slit of the spectrometer, using a beam-splitter and lenses. Thus, emission spectra can be recorded at different stages of the experiment.

The results of such an experiment are exemplary shown in Fig. 3.8. On the left-hand side of Fig. 3.8, the spectral position of the emission maximum (left axis) and the FWHM (right axis) is plotted vs. the operating time. One can distinguish three different phases during the course of this experiment. In the first 4 hours corresponding to phase (1), a distinct, almost linear, blue-shift of the emission by about 3 nm is observed, which is comparable to the values reported in Refs. [254, 78]. Using Eq. 1.28 and the parameters for CdZnSSe as well as an initial Cd content of 23.7%, one can estimate a Cd content reduction by roughly 1% in the quantum well. The emission blue-shift is accompanied by an increasing FWHM, indicating a broadening of the emission. Several structural parameters influence the emission broadness, with the main factors being composition fluctuation, interface roughness, and thickness fluctuation. Without a microscopic analysis of the sample, e.g. by high-resolution TEM, it is difficult to name the responsible

effect. One possible explanation is an increased composition fluctuation in the quantum well due to an inhomogeneous diffusion. In the specific experimental setup used for this test, the recorded spectra always represent the integrated emission of the device, i.e., a spatially resolved recording of the spectra – as it can be performed in μ m-CL mappings – is not possible. Thus, the spectra always contain emission from degraded and undegraded regions of the device. Taking into account that the degradation for these samples involves the generation of dark defects, the origin of the inhomogeneous diffusion can be identified: the diffusion is strongest in the dark defects, such that initially, a broadening of the emission is observed. With continuing degradation, more dark defects are generated and the degree of inhomogeneity should reduce, resulting in a narrowing of the emission.

Indeed, the second phase (2) of the degradation, which sets in after 4 hours and last until 10 h of operation, is not only characterized by a linear red-shift of about 2 nm, but is also accompanied by a narrowing of the emission. The red-shift cannot be caused by an additional heating of the device, since the experimental conditions ensure that the sample is always in the thermal equilibrium. Also, an increase of the operating voltage, which would cause an additional resistive heating, is not observed. On the other hand, if this red-shift is caused by a partial relaxation of the strain in the quantum well, one can estimate a strain reduction of $\Delta\epsilon = 0.45\%$ by using Eq. 3.13. Assuming an initial strain of $\epsilon = -1.87\%$ for 23.7% Cd, this value is relatively high, but again comparable to those reported in the literature [254].

The final phase (3) is achieved after about 10 h of operation. Now a blue-shift is observed again. However, the shift velocity is significantly lower than before. And similar to phase (1) the blue-shift is characterized by a broadening of the emission. A striking feature of the dynamic of the emission shift broadness is that both are complementary through-out the complete experiment. The fact that the shift velocity is reduced in phase (3) as compared to phase (1) hints that this process is – at least in part – driven by the strain: after the strain has been relaxed in phase (2) the driving force for the diffusion is reduced.

On the other hand, the sudden occurrence of the red-shift cannot be so easily explained. One possibility is that there exists a threshold for the strain relaxation. If the relaxation process requires the presence of point defects, for instance, then this threshold would be a certain density of these defects. During operation, the point defects accumulate in the quantum well and, once the relaxation threshold is reached, relaxation occurs.

To verify the given hypothesises, additional experiments are necessary. A more detailed investigation should be carried out as a combined study of electro-optical experiments, high-resolution XRD, and high-resolution TEM. Starting point for these experiments should be a constant current degradation experiment with parallel recording of the emission spectra, followed by a XRD-measurement, in order to determine the strain state of the quantum well, and a concluding TEM investigation to reveal the microscopic structural change. In a more advanced setup, one should try to monitor the emitted light not only spectrally, but also spatially resolved, e.g. in the the region of a dark defect and in an undegraded area. Concerning the tested devices, one should investigate samples with different quantum well compositions, so that the effects of Cd diffusion and strain relaxation can be separated better. Due to lack of time and resources, such tests could not be performed during this thesis.

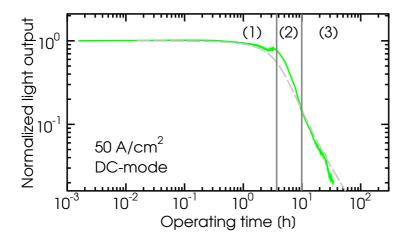


Figure 3.9: Electroluminescence intensity change from Fig. 3.8, re-plotted with double-logarithmic axis scaling. A theoretical curve based on the REDR model is also shown (dashed). The different phases (1)–(3) are the ones defined in Fig. 3.8.

In any case, both phases (1) and (2) are accompanied by a continuous decrease of the emission intensity as shown on the right-hand side of Fig. 3.8. Here, the significantly different degradation processes are obviously not reflected. However, in phase (3) the luminescence intensity reduction is slowed down. In order to compare this experiment with the typical constant current degradation test, the intensity evolution from Fig. 3.8 has been re-plotted in the usual double-logarithmic axis scaling in Fig. 3.9. The rescaling reveals that the complete degradation process is well described using the REDR model.

The evolution of the spectral emission strongly suggests that the degradation process modifies the structural properties of the active region. Cd diffusion and the strain in the active region drive the process together – they are the two faces of the same coin. For a separation of both effects, a better developed microscopic degradation model is necessary. Such a model should concentrate on point defects and in particular on how the point defects can provide mechanisms for diffusion and relaxation. The results from Fig. 3.8 show that the Cd diffusion dominates during most of the time. In constant current degradation experiments, as well as in lifetime measurements (constant output power) – both carried out in pulsed- and cw-mode, with current levels above and below the laser threshold – the same blue-shift was found for most structures [216, 202]. A similar blue-shift during lifetime test is also reported in the literature for a highly-strained CdSe-based active region [261]. Finally, it is important to note that the fuel of the degradation process is the recombination of free carriers in the quantum well – they provide the energy. This observation is consistent with optical pumping experiments with different excitation energies, where a degradation was only observed for excitation above the quantum well band gap [262].

3.4.3 Current injection and accumulation of heat

So far, the driving forces of the degradation process have been investigated from a structural point of view. However, for a device under operation there is at least one additional aspect that drives the degradation: heat – generated during current injection. To study the influence of heat onto the device, pulsed-operation under varying pulsing conditions is an useful tool⁵. In Fig. 3.10 lifetime tests at constant output powers of different laser structures and under different pulsing conditions are shown. The time-

⁵The following results have been published in Refs. [263, 264].

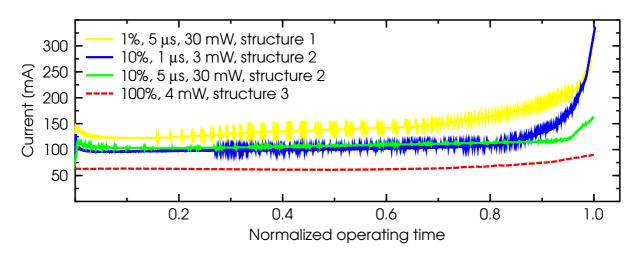


Figure 3.10: Lifetime tests at constant output power for different laser structures and different pulsing conditions, including cw-operation. The time scale has been normalized to the total lifetime of each device.

evolution of the driving current reflects the degradation dynamics. In order to visualize the general course of degradation, the time axis has been normalized to the maximum operating time of each device.

During all tests the time evolution is the same. After an initial drop of the operating current, a slow increase is found, which is attributed to defect annealing processes [265, 249, 242]. Only in the last 10% of the operating time a drastic increase is observed. Taking into account that some of the devices were operated well above threshold – with output powers as high as 30 mW per pulse – this indicates that the heat generated during current injection does not alter the degradation process itself, but rather influences the degradation velocity. Accordingly, the REDR model is also valid at high current injection levels and thus, represents the fundamental degradation mechanism of these devices.

Heat also influences the threshold current density, since it intrinsically depends on the operating temperature [8, 66]. In devices which exhibit extensive heat generation during current injection, an additional extrinsic effect is observed. For such devices, the heat leads to a temperature increase inside the current injection path, which in turn decreases the band gap energy of the semiconductor in the pumped region. Thus, a band gap discontinuity is created between injection stripe and surrounding material, which gives rise to an additional lateral confinement, and consequently a reduced threshold [12, 13, 266]. In ZnSe-based devices the low-doped p-side and especially a poor performing p-side contact were identified as source of such kind of massive heat generation [202]. The effect shows a strong dependence on the applied current pulse width [12]. In lifetime tests a strong dependence on the pulse width is therefore expected. However, the right-hand side of Fig. 3.11 shows that this is not the case. An extensive heat generation does not take place during operation, even for high output powers. Nevertheless, the same graph also shows a strong lifetime variation between different laser bars, which is caused by an inhomogeneous distribution of defects as shown before in Fig. 2.9.

A better insight how the generation of heat accelerates the degradation process can be gained from the right-hand side of Fig. 3.11. Here, the lifetime of different devices

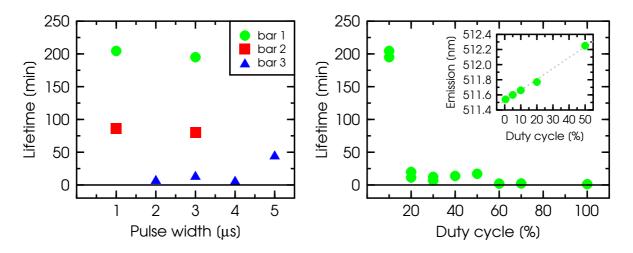


Figure 3.11: Influence of driving conditions on the lifetime of laser diodes. Dashed lines represent guides to the eye. Left: dependence on the pulse width. Three different bars of the same laser structure were tested under a duty cycle of 10% and a constant output power of 30 mW. Right: lifetime vs. duty cycle for the same laser structure. The pulse width was set to 1 μ s and the integrated output power was kept constant at 3 mW. The insert shows the shift of emission wavelength with increasing duty cycle.

of the same structure is plotted vs. the duty cycle during the test. At a duty cycle of 10%, a lifetime of 200 min is measured. But at 20% duty cycle the device lasted only 20 min. From 20% to 100% duty cycle the decrease is less pronounced. It is important to note that for these tests the *integrated* output power was kept constant at 3 mW, therefore, the output power of the devices emitted during a current pulse decreases with increasing duty cycle, obeying Eq. 2.4. This implies that with increasing duty cycle less operating current is needed to provide the required output power. Yet, this positive effect is not reflected in the experimental results. The strong dependence of the lifetime on the duty cycle implies that the accumulation of heat primarily determines the degradation velocity. If the recovery time between the current pulses is long enough, such that all heat can be dissipated before the next pulse arrives – i.e., at a low duty cycle - the device degrades slowly. With increasing duty cycle the heat cannot be removed completely, and it accumulates in the device, which in turn accelerates the degradation process. This argument is supported by the insert of the right-hand graph of Fig. 3.11, which shows the shift of the emission wavelength with increasing duty cycle. From the temperature dependence of the band gap energy of CdZnSSe given in Sec. 2.3.4 follows that the lower bound for the temperature increase between 10% and 20% duty cycle is about 1 K (0.11 nm shift).

Consequently, for a stable operation an effective heat dissipation is necessary, e.g. by mounting the device with the epi-side down onto a heat sink, as discussed in Sect. 4.2. On the other hand, for carefully chosen operation conditions – namely an adequate duty cycle – stable operation can be expected, even at high current injection levels or high output powers, resp. In fact, the thorough optimization of the operating conditions is a key requirement for stable operation. Whereas in pulsed-mode the pulsing conditions have to be optimized, for cw-operation an optimization of the cavity length and stripe width is similar necessary, as reported in Ref. [267].

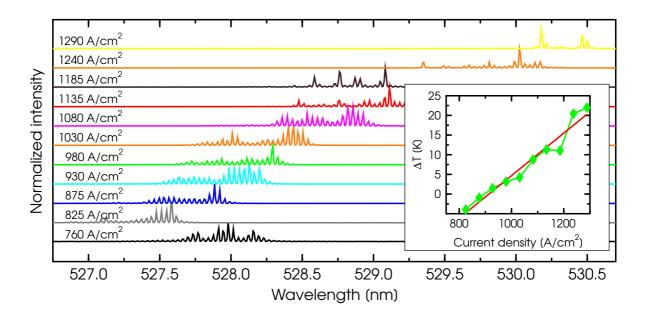


Figure 3.12: Lasing spectra in cw-mode for different current injection levels. The insert shows the temperature increase of the active region extracted from the shift of the emission wavelength.

That ZnSe-based laser diodes are indeed capable to sustain high current injection levels is shown in Fig. 3.12. For this test the very same laser stripe was operated with increasing current levels in cw-mode, and the emission spectrum of the device was recorded, which took about 2 s. The threshold current density of this particular device is 600 A/cm^2 . Lasing operation up to almost 1300 A/cm^2 is obtained, which is more that twice of the threshold current density. During this test only a moderate temperature increase occurs. Based upon the shift of the emission wavelength with increasing driving current, a temperature increase of 22 K between $750-1300 \text{ A/cm}^2$ is calculated, corresponding to a slope of $0.04 \text{ K/(A/cm}^2)$. Further details concerning the high-power operation of ZnSe-based laser diodes are given in Sec. 3.6.

3.5 Improving the quantum well stability

Once the substrate preparation and growth start procedure has been optimized, such that the pre-existing (SF) defect density is in the order of 10^3 – 10^4 cm⁻², the degradation of a ZnSe-based laser diode is primarily dominated by the density of point defects and the stability of the active region. Thus, the first approach to improve the lifetime of these devices naturally implies the optimization of the active region, i.e., the quantum well. In the course of this thesis several new approaches have been investigated and tested in fully-functional laser diodes. Unfortunately, these tests were only of limited success, therefore, they will only be described briefly.

3.5.1 Alternative growth modes

Typically, ZnSe-based laser diodes employ a CdZnSe quantum well as active region, which is grown in a conventional MBE growth mode, i.e., all elements are supplied simultaneously. From the optimization of the growth start of ZnSe on GaAs it is known that an initial MEE growth mode improves the layer quality and reduces the defect density (cf. Sec. 1.4.2). In this MEE growth mode, the constituents are supplied alternately, which gives rise to an increased surface diffusion and in turn improves the structural layer quality [179]. Since a high surface diffusion is also a key requirement for growing self-organized quantum dots, the MEE growth was also successfully employed to grow CdSe quantum dots [31, 180]. The question, whether a MEE growth technique is useful for growing CdZnSe⁶ quantum wells, was investigated by T. Seedorf in his Diploma thesis [205]. In the following investigation of laser structures, the motivation is to increase the quantum well stability by improving the structural quality of the material, i.e., the density of non-radiative recombination centers is minimized by reducing crystalline imperfections.

In a first approach the quantum well was grown by alternating between group-VI (Se) and group-II (Cd+Zn) supply. It was found that in this case the amount of Cd incorporated into the material is significantly lower than in conventional MBE growth, and the Cd content remains limited to below 20% [268]. The decreased Cd incorporation results from a different vapor pressure of Cd and Zn. Since Cd has a higher vapor pressure, its desorption coefficient is also higher, thus Zn incorporation is preferred, if both species are offered simultaneously [269, 270].

The structural properties of the quantum wells were investigated using low-temperature PL and high-resolution TEM, which was performed by M. Cornelißen during his Diploma thesis [271]. Using a MEE growth mode the structural properties are slightly improved. However, a Cd content of 12.5% is rather low and results in emission wavelengths below 500 nm. Such laser structures have the problem that either the *p*-claddings suffer from a low carrier concentration and, hence, a high serial resistance, or the confinement is too low, which gives rise to significant current overflow and a likewise increased threshold current density.

To raise the Cd content in the material it is obviously necessary to avoid offering Zn and Cd simultaneously. Thus, in a modified MEE growth mode a CdZnSe *digital alloy (DA)* was grown. Such a DA consists of alternating layers of CdSe and ZnSe of sub-monolayer thickness [272]. Due to the sub-monolayer thickness of the individual layers, the superlattice can be treated as a ternary alloy and the average Cd content is controlled via the thickness ratio [205]. Comparing the PL emission width of MBE-and MEE-DA-grown Cd_{23%}Zn_{77%}Se a reduction by 40% is found [268]. High-resolution TEM investigations confirm that this optical improvement is due to a structural improvement, namely a reduced composition fluctuation in the MEE-DA and a decreased interface roughness.

Figure 3.13 demonstrates the feasibility of a CdZnSe quantum well grown as MEE-DA as active region for an electrically pumped laser diode. On the left of Fig. 3.13 the emission spectrum of the laser diode in pulsed-mode is depicted. Clear laser emission occurs around 531 nm, which is a relative long emission wavelength for a ZnSe-based laser diode. On the right-hand side of Fig. 3.13 the L/j characteristic of this laser diode

⁶For sake of simplicity the growth mode experiments were conducted on ternary quantum wells.

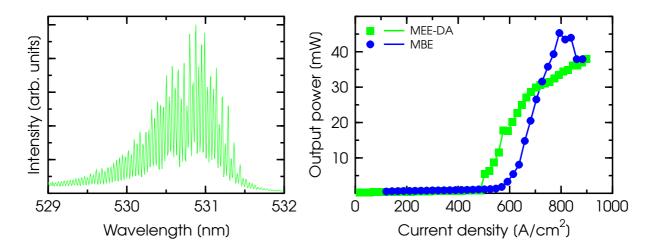


Figure 3.13: Operational characteristics of a laser diode with a CdZnSe quantum well grown as MEE-DA. Left: emission spectrum at room-temperature above threshold, obtained in pulsed-mode (0.1%, 1 μ s). Right: L/j characteristics in comparison to a laser diode with MBE-grown CdZnSSe quantum well (pulsed: 0.1%, 2 μ s).

is shown. For comparison an identical laser structure with a conventional CdZnSSe-MBE quantum well was grown, too. The L/j characteristic of that device, which has an emission wavelength of 526 nm, is also shown in the figure. Although the MEE-DA laser diode has a lower threshold current density, a higher external quantum efficiency was obtained for the conventional device. From this observation follows that the better structural quality of the quantum well is not reflected in better device characteristics. This is supported by tests in cw-mode: the lifetime of the MEE-DA laser is about 40 s, whereas the MBE-grown laser lasts for more than 240 s. Similarly, in cw-mode a maximum output power of 75 mW was obtained for the MBE laser, whereas only 20 mW could be extracted from the MEE-DA laser (cw-results not shown). One possible reason for the inferior device characteristics of the MEE-DA laser is a partly relaxation of the quantum well due to a too high Cd content, however, this could not be verified using high-resolution XRD.

In this context it is interesting to note that temperature-dependent PL measurements on those structures show that the superior optical quality of the MEE-DA quantum well at low-temperatures does not carry over to room-temperature – at least concerning the sharp emission [273].

3.5.2 Low-temperature growth

Besides the growth mode, other parameters of the MBE growth process can influence the structural and optical properties of the material as well. One of these parameters is the growth temperature. In the literature, there are only few reports on how the growth temperature during the quantum well growth influences the device performance – nevertheless, some reports suggest better characteristics when the active region is grown at low temperatures [160, 272, 117]. The results of Fig. 3.14 support these observation. In this graph the integrated quantum well emission of single CdZnSSe quantum wells embedded into ZnSe barriers is plotted vs. the growth temperature. To better visualize

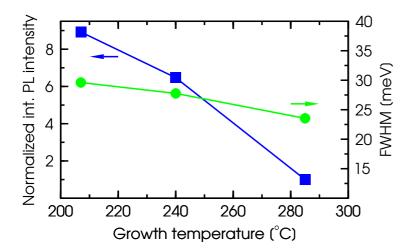


Figure 3.14: Low-temperature PL results from single quantum wells grown at different substrate temperatures. Shown is the integrated emission intensity, normalized to the value obtained from standard growth conditions (285 °C), and the emission width.

the effect of the reduced growth temperature, the intensity has been normalized to the value obtained under standard growth conditions at 285°C. A clear increase in emission intensity is found for a decreasing growth temperature. At 207°C the PL intensity has increased by more than a factor of 8. Since a higher intensity implies a better radiative recombination efficiency and/or a reduced number of non-radiative recombination center, a lower growth temperature may offer some potential for improving the laser diodes.

However, Fig. 3.14 also shows that the emission width increases with lower growth temperature indicating a stronger composition fluctuation. One countermeasure against this broadening effect is to use the MEE growth mode for such quantum wells. Indeed, employing MEE-DA quantum wells, grown at low temperatures (LT-DA), as active region in LED structures resulted in an improved efficiency as compared to conventional MBE quantum wells [274]. But the overall quantum efficiency for the complete series of LED structures was relatively low, thus, a concluding judgment can not be made based on these LED results alone.

The next step is therefore to incorporate such quantum wells into fully-doped laser structures, which is shown in Fig. 3.15. Again, an identical laser structure with a standard-MBE-grown quantum well was fabricated as reference for the comparison. Concentrating on the low-temperature PL spectra on the left first, one observes that the LT-DA laser has a higher optical quality, since the emission is not only sharper (11 meV instead of 17 meV), but also stronger and more efficient as derived from the intensity ratio of the quantum well emission around 2.5 eV and the ZnSSe waveguide layer emission at 2.83 eV. Despite better optical characteristics, the device characteristics of the LT-DA laser are far below that of the standard-MBE laser. In fact, no lasing could be realized for the LT-DA laser diode, as shown in the L/j characteristics of Fig. 3.15.

Several additional laser structures have been grown following these first results shown in Fig. 3.15. From a total of 5 laser structures with an active region grown at a lower temperature, none showed electrically pumped lasing at room-temperature. In these structures MEE-DA as well as regular MBE-grown quantum wells were employed. It was also checked whether the device failure is connected to the growth interruption – which is necessary to change the substrate temperature – or the lower growth temperature itself. These experiments revealed that a growth interruption is not detrimental and the lower growth temperature must be responsible. Yet, the mechanism

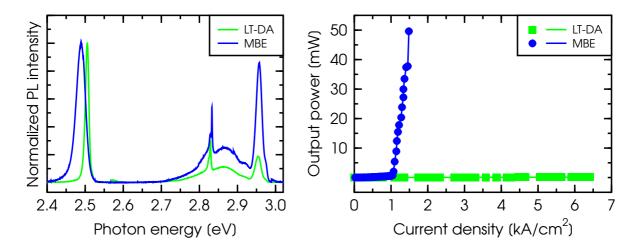


Figure 3.15: Characterization of a laser diode with quantum well grown as MEE-DA at low temperature (220°C, LT-DA) in comparison to a conventionally grown laser structure (285°C, MBE). Left: low-temperature PL. Right: L/j characteristics in pulsed-mode. Only weak spontaneous emission is detected from the LT-DA laser.

that prevents electrically pumped lasing remains unclear. One possible source of failure could be the thin ZnSe cap that is also grown at low temperature (growth time 10–30 s). However, this question was not further investigated.

3.5.3 Strain reduction in the active region

In Sec. 3.4.2 it was shown that the high compressive strain built into the CdZnSSe quantum well acts as driving force for the degradation process. A reduced strain in the quantum well can eventually improve the device stability. The most simple approach to achieve a strain reduction is obviously to reduce the amount of Cd in the quantum well. But this leads to a higher band gap energy, which in turn results in a less effective carrier confinement and a higher threshold current density. Also, increasing the S content in the quantum well provides no solution, since this rises the band gap energy of the quantum well accordingly, as seen in Fig. 1.7. Only, by growing on a different substrate, such as InP, unstrained CdZnSe quantum wells can easily be fabricated. However, changing the substrate was not an option in this work.

On the other hand, by using a MBE growth technique, it is possible to control layer thicknesses and compositions on a monolayer scale. This allows the fabrication of superlattices in which the main parameters – such as band gap energy and lattice constant – are determined by the composition and thickness ratio of the individual layers. A superlattice can be treated as an alloy, but it allows – to some extend – access to material compositions and thickness combinations that cannot be grown as regular alloy. Other advantages are an improved stability against defect formation or higher doping levels [275, 123]. Superlattices have successfully been employed in ZnSe-based laser diodes and distributed Bragg reflectors (DBR) [35, 194]. In particular, superlattices provide the means to realize *strain compensation*, which has been successfully employed to reduce the stacking fault formation in CdSe quantum dot stacks, as will be shown in Chapter 6 [85]. Generally, the design and growth of superlattices with no net strain is a

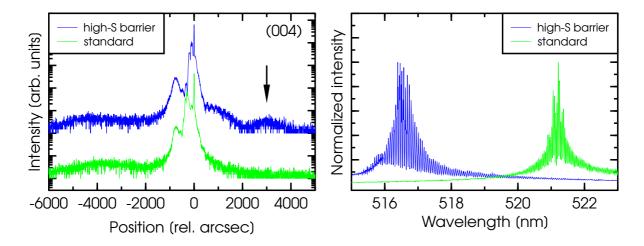


Figure 3.16: Laser structure with tensile strained ZnSSe barriers embedding the CdZnSSe quantum well. The barriers and the quantum well are 4 nm thick each. The whole system is embedded into lattice matched ZnSSe waveguide layers. For comparison, the results from a reference laser structure without strain compensation are also depicted. Left: $\omega/2\theta$ scan of the (004) reflex. The position of the high S-containing ZnSSe layers is marked by an arrow. Right: emission spectra of both laser structures in pulsed-mode above threshold (0.1%, 1 μ s).

complex task and has to take into account several factors, such as defect formation with different types of defects, the individual critical thickness of each layer, and the total critical thickness, as well as the situation during growth where for a short time, each individual layer is naturally not embedded into the strain compensating structure, i.e., during its deposition [276]. However, in a simple approximation the net strain is given by the sum of the strain of each individual layer, scaled with its layer thickness [35].

Therefore, a concept was developed, which applies the superlattice concept of strain compensation to the single CdZnSSe quantum well of a ZnSe-laser diode. For the strain compensation, the quantum well has to be embedded into tensile strained layers. Accordingly, this system consists of only three layers in the simplest case: the quantum well and the surrounding barriers. However, it is questionable whether such a simple system really can be treated as superlattice. This question has to be investigated.

Putting the question of applicability aside, one can calculate the necessary S content in the tensile strained barriers by using [35]

$$\sum_{i} \frac{\Delta a_{i}}{a_{\text{GaAs}}} t_{i} = \frac{\Delta a_{\text{ZnSSe}}}{a_{\text{GaAs}}} t_{\text{ZnSSe}} + \frac{\Delta a_{\text{CdZnSSe}}}{a_{\text{GaAs}}} t_{\text{CdZnSSe}} + \frac{\Delta a_{\text{ZnSSe}}}{a_{\text{GaAs}}} t_{\text{ZnSSe}} \stackrel{!}{=} 0,$$
(3.14)

where $\Delta a_{\rm ZnSSe}$ denotes the lattice mismatch of the ZnSSe barriers and $\Delta a_{\rm CdZnSSe}$ that of the quantum well, likewise the t_i are the individual layer thicknesses. For simplicity the layer thickness is set to 4 nm each, and, consequently, for a CdZnSSe quantum well with 25% Cd and 6% S, a S content of 25% is necessary in the ZnSSe strain compensating barriers.

In Fig. 3.16 such a laser diode with strain compensating ZnSSe barriers is compared with a standard laser structure. The $\omega/2\theta$ scan of the (004) reflex shows an additional layer signal around 3000 arcsec right from the substrate for the strain compensated laser

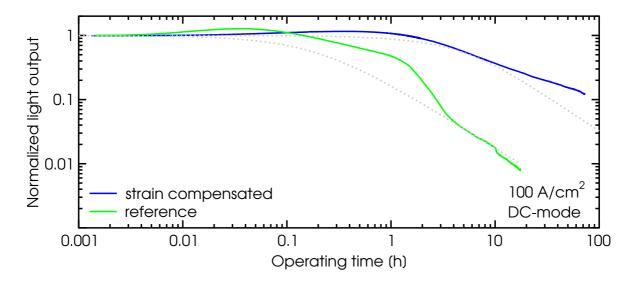


Figure 3.17: Constant current degradation at 100 A/cm² of the laser structure with strain compensating barriers and the reference laser for comparison. The dashed lines are theoretical curves with an initial quantum efficiency of 44.5% for the modified laser and 44.1% for the reference laser.

structure. This signal stems from the thin tensile strained barriers, and a S content of 28% is estimated, which is a little bit more than the intended value. But since the S valve settings was calculated based on the ZnSSe calibration layers with low S contents (5–8%), such a deviation is acceptable. The emission spectra of both lasers above threshold show clear lasing emission around 520 nm, with the emission of the modified laser being blue-shifted by 4 nm. The blue-shift is systematically observed when using strain compensated barriers for quantum well laser structures. It originates from the higher S content in the barriers, that leads to a higher band gap energy and a better confinement of the quantum well, causing the blue-shift. Another effect that cannot be ruled out completely is a reduced Cd incorporation in the quantum well, caused by the tensile strain state of the lower barrier.

Comparing the operational characteristics no significant differences are found. Both structures have a threshold current density of 1.2 kA/cm^2 , which is relatively high. They are part of a series of five laser structures (S0823–S0827, cf. Tab. B.1 in the appendix) grown on consecutive days, and which are all characterized by a relatively high threshold and low quantum efficiency, which implies a systematic growth problem during that periode (cf. also Ref. [185]). Furthermore, the p-side contact is less stable against current injection and has a higher operating voltage. Due to these problems, the lifetimes of the laser structures are far below the usual values, and consequently, a positive effect of the strain compensation is in part hidden by them. Nevertheless, in constant current degradation experiments a significant stability improvement is found as shown in Fig. 3.17.

The tests in Fig. 3.17 were carried out at a current density of 100 A/cm². Both curves show a less abrupt decrease of the emission intensity and a rather soft curvature. As mentioned before, this is caused by a low initial quantum efficiency of about 44% in both cases – for comparison, the device in Fig. 3.5 had over 90% initial efficiency. Additionally, a strong defect annealing is seen for the reference laser, indicating non-optimized

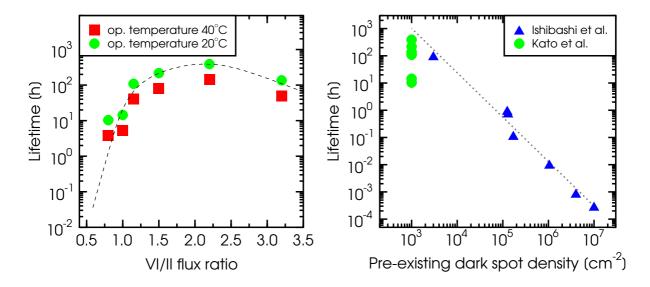


Figure 3.18: Left: lifetime dependence on the VI/II flux ratio during quantum well growth (values marked by the squares are taken from Ref. [5], lifetimes for 20°C operating temperature have been extrapolated). The dashed line is a guide to the eye. Right: lifetime at 20°C vs. pre-existing dark spot density, taken from Ref. [196]; the values from Ref. [5] are added.

growth conditions. The modified laser is also subject to defect annealing, albeit less pronounced and over a longer time-scale. The output power of the reference laser after about 20 h of operation is less than 1% of the initial value. In comparision, the output power of the modified laser after about 80 h of operation is still more than 10% of the starting value. This higher stability is reflected in different scaling factors $K n(0)^2$ for both structures, where the one of the laser with strain compensating barriers is by more than one order of magnitude higher $(K n(0)^2 \sim 6)$. In fact, this laser structure exhibits an even higher stability than the cw-record laser structure which was shown in Fig. 3.5 – despite a 2 times higher driving current density of 100 A/cm^2 .

Since the reference and the modified laser structure stem both from the same growth period and have an identical layer sequence, the improved stability under low current injection levels can be attributed to the strain compensating ZnSSe barriers. The fact that it does not fully transfer to lifetime tests above threshold is caused by the growth problems mentioned before. Therefore, a concluding statement concerning the effectiveness of this measure cannot be made at present. Nevertheless, under low current injection levels – where the effects of the low stability and the heating by the poor *p*-side contact do not limit the device performance – a higher stability is observed. This promising result was obtained despite the fact, that the quantum well growth conditions were group-II rich and consequently unfavorable, as will be shown next.

3.5.4 Sony's approach

After it became obvious that the stability of the quantum well region is directly related to the existence of point defects, Sony's research activities concentrated on reducing the point defect density. Point defects are always present in real semiconductor crystals due

Cell	Zn	Mg	Cd	Se	S_{ZnSSe}	$S_{MgZnSSe}$
Flux in BEP [Torr]	4.5×10^{-7}	2×10^{-8}	2.5×10^{-7}	1×10^{-6}	2×10^{-7}	4×10^{-7}

Table 3.1: Typical cell fluxes used for growing ZnSe-based material. S_{ZnSSe} , denotes the S flux, necessary for lattice matched ternary ZnSSe, which is also the S flux used for growing the quaternary CdZnSSe quantum well, whereas $S_{MgZnSSe}$ stands for the flux required for lattice matched quaternary MgZnSSe.

to thermodynamical reasons [277]. They are naturally formed during the growth process, consequently, several parameters, such as growth temperature, growth mode, and flux ratios, determine their density. Indeed, the so far described approaches represent nothing else but efforts to control the point defect density in the active region – albeit with limited success.

The ansatz to optimize the *flux ratios during quantum well growth* proved to be more successful [5]. Normalizing the VI/II flux ratio for stoichiometric growth to unity, the highest lifetime was obtained for a VI/II flux ratio of 2.2, i.e., group-VI rich conditions, as shown on the left of Fig. 3.18. It should be noted that the device characteristics such as threshold current density or L/j characteristics do not exhibit a similar dependence on the flux ratio [267]. In case of such optimized growth conditions, no generation of dark lines or dark spots is observed [232]. This underlines once again that the formation of dark defects is related to point defects, incorporated under group-II rich conditions, e.g. Se vacancies or Zn interstitials, and that the Cd diffusion proceeds in the group-II sub-lattice of the crystal [77]. By growing group-VI rich, a high density of group-II vacancies is generated, which allows the Cd to diffuse inside the quantum well, i.e. an out-diffusion is inhibited or at least reduced. Furthermore, the high density of point defects also reduces the diffusion of point defects from outside of the quantum well into the quantum well.

Obviously, the optimization of the growth conditions provided the means to realized stable cw-operation over several hundreds of hours, as proven by the world record lifetime of 389 h. However, it is instructive to compare the lifetimes given by Kato $et\ al.$ in Ref. [5] with the ones reported two years earlier by Ishibashi $et\ al.$ in Ref. [196], as it is shown on the right of Fig. 3.18. Despite the growth optimization and the fact, that for a pre-existing defect density below $10^4\ cm^{-2}$ no defect is present in the active region of the device, the lifetime still follows the trend. In fact, samples grown under inappropriate flux conditions have lower lifetimes than the record laser from 1996 [75]. Based on this observation, it is save to assume that Sony performed the flux ratio optimization much earlier than 1998.

Finally, it has to be mentioned that most laser structures grown in the course of this thesis contain quantum well material that was grown under group-II rich – and hence unfavorable – conditions. However, one has to keep in mind that providing Se-rich growth conditions during the quantum well growth poses some experimental difficulties. As described in Sec. 2.1.3, the flux conditions for regular growth are set to be slightly group-VI rich for ZnSe growth. In Tab. 3.1 typical flux values for the main elements are given. These fluxes are recorded in *beam equivalent pressure* (BEP), which does not take into account the sticking coefficients on the substrate surface. With a BEP-ratio of [Se]/[Zn] ~ 2 stoichiometric growth is obtained, as it is determined from the surface

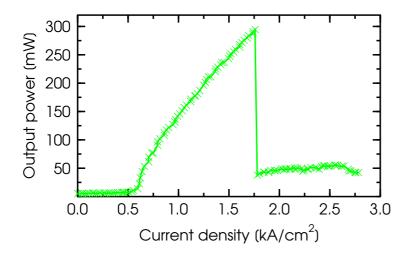


Figure 3.19: High-power operation of a ZnSe-based laser diode emitting at 520 nm. The device is operated in pulsed-mode with 0.01% duty cycle and 1 μ s pulse width.

reconstructions revealed by RHEED. From the values listed in Tab. 3.1, it is apparent that the addition of S and Mg do not change the flux conditions much, thus ZnSSe and MgZnSSe growth is also stoichiometric, resp. slightly group-VI rich. However, using the standard fluxes for Zn, S_{ZnSSe}, and Se the CdZnSSe quantum well growth will automatically be group-II rich, since the Cd and the Zn fluxes are of the same magnitude. Providing group-VI rich conditions, hence requires the drastic change of the Se flux within a short time. In a MBE system – where the elements are supplied by simple thermal evaporation – this is not possible and requires a growth interruption of about 10–30 min, in order to raise the Se cell temperature. Such a growth interruption is not desireable, since it leaves the interface between lower waveguide and quantum well exposed to the chamber environment, increasing the possibility to incorporate impurities at a very sensitive position. Furtheron, a surface roughening can be expected due to desorption of Se or Zn. The only way to avoid the growth interruption is to immediately increase the Se flux during the CdZnSSe growth, either by using a second Se Knudsen cell or by using a valved cracker cell. Such experimental conditions, namely a fully functioning Se valved cracker cell, were only given during the last part of this thesis.

Due to these experimental limitations most laser samples were grown under flux ratios corresponding to a value below 0.5 in Fig. 3.18. Extrapolating the lifetime dependence to these values gives lifetimes around few minutes, which coincidences nicely with the record values obtained for laser diodes grown in Bremen.

3.6 High-power operation

In Sec. 3.4.3 it was shown that with careful choice of the driving conditions, ZnSe-based laser diodes are in principle able to sustain high current injection levels without rapid degradation. Thus, high output powers can in principle be delivered over a long time. So far there are only very few reports concerning high-power operation of ZnSe-based laser diodes. In fact, only Sony reported such operation conditions where they obtained a maximum output power of 834 mW – yet, no further details concerning pulsing conditions or lifetime at such high output power are given [122].

In the following the influence of very high current injection levels on the degrada-

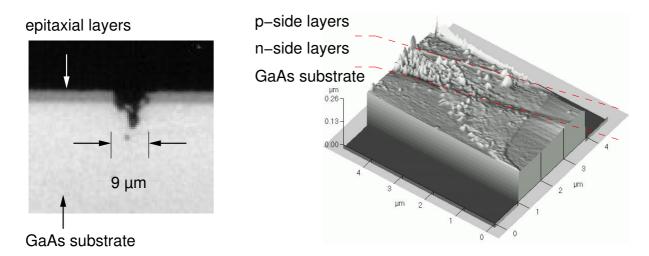


Figure 3.20: Left: microscope photograph of the mirror facet of a ZnSe-laser diode after occurrence of COD. Underneath the current stripe material degradation can be seen. The degraded region extends into the GaAs substrate. The metal contact of the device does not exhibit any signs of degradation (not shown). Right: atomic force microscopy image of a facet destroyed by COD (AFM topography measured by S. Figge).

tion of ZnSe-based device will be investigated⁷. For these tests the driving conditions are chosen such that the accumulation of heat is minimized, i.e., low duty cycles are used. Figure 3.19 shows a typical high-power L/j characteristic obtained under these conditions. The threshold current density in this case is 500 A/cm², with an external differential quantum efficiency close to unity. Up to 1.6 kA/cm² the light output increases linearly to almost 300 mW. A further increase of the output power results in a drastic drop of the emission intensity down to 40 mW. Although the device still exhibits lasing emission, the external quantum efficiency is now less than 8% of the initial lasing efficiency. After this sharp drop, the current density can be increased up to about 2.5 kA/cm², still the output does not exceed 55 mW. This effect of an abrupt decrease of the output power is a clear sign of a *catastrophic optical damage (COD)*. COD is not only a well-known degradation mechanism of conventional III-V high-power laser diodes, but it is also the lifetime-limiting factor for those devices at present [9, 278, 279, 280].

The COD process is directly related to the stability of the mirror facets that form the laser cavity. The facets – being cleaved edges of the semiconductor crystal – give rise to a surface space-charge region, immediately adjacent to the mirror in which absorption occurs. This non-radiative recombination gives rise to local heating, which is dissipated at the surface. However, due to the heat, the temperature rises locally, which leads to a band gap reduction and consequently a higher absorption. This process can result in a thermal runaway process, during which the surface absorption is drastically enhanced, and finally a melting of the semiconductor material occurs, destroying the crystalline perfection. Since the reflectivity strongly relies on a high crystalline perfection, the mirror quality is severely degraded under these circumstances, and in turn the threshold current is increased, resp. the light output is reduced [278]. This runaway process explains not only the abrupt intensity drop in Fig. 3.19, but also the reduced quantum efficiency afterwards. In Fig. 3.19, COD occurs at a total output power of 300 mW, i.e.,

⁷The following results have been published in Ref. [264].

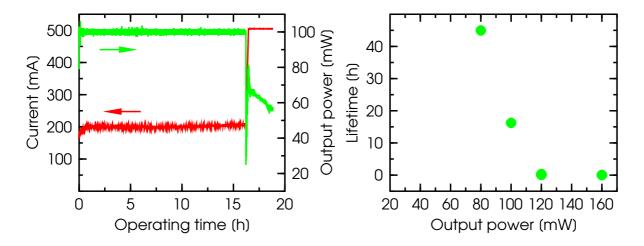


Figure 3.21: Left: typical lifetime measurement limited by COD. For this test the device was set to an output power level of 100 mW at 0.01% duty cycle and 0.6 μ s pulse width. Right: dependence of the lifetime on the output power for the same pulsing conditions.

150 mW per facet. Assuming that the light wave is localized in the waveguides (complete thickness 200 nm) and limited to the current injection region of 10 μ m width, a COD threshold level of 7.5 MW/cm² is calculated. This corresponds to threshold levels obtained for contemporary AlGaAs/GaAs and InGaAs/InGaP laser diodes grown on GaAs [281, 282]. It is emphasized that the thermal runaway process does not require the existence of defects at the mirror surface in order to be initiated – even a perfectly cleaved facet is subject to COD (although the presence of defects surely lowers the COD threshold) [278].

To verify that the process observed in Fig. 3.19 is indeed related to a change of the facet, the cleaved edge of a laser bar after operation and occurrence of COD was examined using an optical microscope and an atomic force microscope (AFM). These pictures are shown in Fig. 3.20. The microscope photograph clearly reveals that underneath the injection stripe a material change occurred. Furthermore, a reduced reflectivity in comparison to the surrounding material is indicated by the black contrast of the degraded region, which extends well into the GaAs substrate. In the AFM topography measurement the formation of droplets in the area of the current injection is observed. It can therefore be concluded that indeed a COD process occurred. Such type of degradation has not been reported for ZnSe-based laser diodes before.

Under high-power operation, the occurrence of COD is the lifetime limiting factor, when operated in pulsed-mode, as shown in Fig. 3.21. The left-hand side shows a typical lifetime measurement under these conditions. Here, an output power level of 100 mW was chosen. After an initial operating current increase within the first hour, it increases only by 5% during the rest of the test. However, after 16 h of operation the light output decreases from 100 mW down to 20 mW within one second due to COD. Based on the change in operating current alone, one would expect a 4 times higher lifetime. However, since COD is based on a thermal runaway process there is no simple approach to predict the occurrence of COD during a lifetime test. In fact, why should COD occur at all, if the output power remains below the COD threshold? The answer is that the COD threshold level decreases with operating time, mainly due to a point

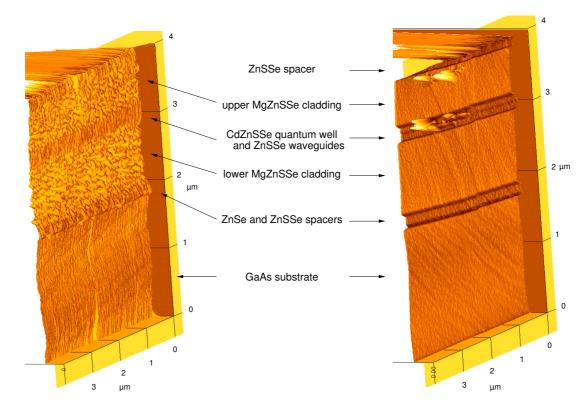


Figure 3.22: AFM topography of laser facets. The rms-roughness values are 4.73 Å and 1.4 Å, resp. (etching of the facets was performed by C. Petter, the AFM topography was recorded by S. Figge) Left: untreated cleaved facet. Right: facet after 2 min plasma etching in an Ar-atmosphere at 200 W [285].

defect accumulation at the facet, as well as a progressing facet oxidation during aging time [283].

The right-hand side of Fig. 3.21 gives the dependence of the lifetime on the output power. All devices tested during this experiment were taken from the same laser bar in order to ensure a comparable facet quality. At a light output power of 40 mW, no increase of the operating current was found after 24 h. Due to limited time resources, the test was stopped at that point. At 80 mW, the lifetime exceeds 45 h before COD occurs. The graph indicates that beyond an output power of 120 mW the devices can only be operated for a short time (a few min) – the intrinsic stability of the uncoated laser facet seems to be limited to about 100 mW. Performing the same experiments on different laser bars of different laser structures revealed, that the COD threshold mainly depends on the facet quality and not so much on the current injection level – at least when performing a manual cleaving technique as in this case.

From the III-V devices it is known that the occurrence of COD also depends on the pulse width [9]. For short pulses the damage threshold increases. Thus a record output power of 1.55 W at 520 nm was recently obtained from a ZnSe-based laser diode grown in Bremen by using 125 ns short pulses [284].

Finally, it should be noted that the occurrence of COD is less dramatic than it seems on first sight. Indeed, since COD is a well-studied problem in conventional III-V laser diodes, several countermeasures have been developed, which can in principle be ap-

plied to ZnSe-based devices, too. One of the most effective countermeasure is a facet coating in combination with a facet passivation [286, 287]. Since none of the devices reported so far were subject to such a coating, significant improvements are expected. First results from an ongoing Diploma thesis work are shown in Fig. 3.22 [285]. In this figure an untreated and a plasma-etched laser facets are shown. Whereas the as-cleaved facet shows a clear corrugation of the surface, these features are completely removed after etching. Since the corrugation is most pronounced in the region of the Mg-containing cladding layers, it is attributed to oxidation. The rms-roughness value of the as-cleaved facet is 4.73 Å, after etching this is reduced to 1.4 Å. The surface oxidation gives rise to an additional absorption at the facets and, consequently, a reduced COD threshold [283]. Thus, by removing these oxides an improved stability under high power operation will result.

Other approaches to improve the stability against COD are, for instance, based on optimized layer designs [288]. Further insight into this degradation mechanism requires more advanced techniques, such as TEM, to clarify the microscopic nature [289, 290]. Furthermore, an investigation of the temperature rise at the facets compared to the rest of the active region, e.g. by electroluminescence or photothermal deflection, is helpful [291, 292, 293].

3.7 Summary

It was shown that the degradation of ZnSe-based laser diodes is directly related to the stability of the active region, namely the quantum well. During operation, non-radiative recombination centers are increasingly formed, giving rise to "dark areas" in the quantum well. The formation of these dark defects is influenced by pre-existing defects in the sample, as well as by the strain accumulated in the highly lattice mismatched quantum well and the presence of point defects. This degradation process is not catastrophic, but gradual and is accompanied by a structural change of the active region by Cd diffusion and strain relaxation. Heat accelerates the degradation, which is a further indication that the process is based on diffusion. Improving the stability of the devices requires an optimization of the quantum well growth. Using low-temperature growth or a MEE-DA growth mode is only of limited success, however, an electrically pumped laser diode with a MEE-grown digital alloy quantum well was realized for the first time. Another, more promising approach is to embed the compressively strained CdZnSSe quantum well into tensile strained ZnSSe barrier layers, in order to compensate the strain in the active region. For such devices an improved stability under low current injection levels was found. In conjunction with optimized growth conditions – in particular for the quantum well – this higher stability is expected to carry over into operation above the laser threshold. Furthermore, it was found that under carefully chosen driving conditions stable operation of ZnSe-based laser diodes can be realized in pulsed-mode – even at a high current injection level and light output power. Under these conditions, catastrophic optical damage is identified as new dominating degradation mechanism, which was so far unknown for ZnSe-based devices.

Chapter 4

Advanced processing technologies

In the last chapter the degradation of ZnSe laser diodes was investigated. The results have been obtained from devices which do not resemble much commercially available laser diodes. In fact, only a very basic processing technology was applied to the wafers. In this chapter some more advanced – so called "front-end" and "back-end" processing technologies – will be introduced. Although the principles of these technologies are commonly know, so far only little work has been done – and even less been published – about how they can be transfered to II-VI laser diode devices.

4.1 Overview

The starting point for all semiconductor laser diodes is the epitaxial growth of a laser structure on a substrate crystal. To obtain laser light from such a structure numerous processing steps are necessary after the growth process itself. This is the starting point of the so-called *front-end* technology. One of the most important steps obviously is to metalize the wafer, so that current can be applied. However, stable room-temperature lasing operation requires at least two additional measures: lateral confinement and optical feedback. The lateral confinement is required to lower the threshold current density to a practical value. In the simplest case one can achieve lateral confinement with a thin metal current injection stripe (gain guiding). Optical feedback is provided by cleaving the wafer perpendicular to the injection stripes. The result is a bar which contains several individual laser diodes. Next, the individual laser diodes have to be separated into single laser chips, this process is called *pelletizing*. These chips are then mounted onto a heat sink holder. Finally, a collimator lense is attached to the system and the package is sealed.

These are the most basic processes necessary to process a single laser diode from the original wafer. Additional processing steps can be incorporated, depending on the intended application of the device. In general, one can distinguish between measures which help to slow down the degradation of the laser on the one hand and such, which improve particular device characteristics, otherwise.

One of the most important aspects for improving the lifetime of laser diodes is to minimize the generation and the influence of heat onto the device. This can be achieved by applying a *facet coating* and by mounting the device with the epitaxial side facing downwards onto the heat sink (*top-down mounting*). Facet coating is also a useful tool to

improve the stability of the laser facet against high light powers and, therefore, necessary for high-power light output applications.

Both of these techniques have been investigated and transfered to ZnSe-based laser diodes here in Bremen, as it will be presented in the following. However, in co-operation with external research teams, other processing techniques and device concepts have also been successfully realized with laser structures grown in the framework of this thesis. These concepts include the fabrication of *ridge waveguide lasers*, novel *p*-side contact metalization schemes, and *distributed feedback lasers*. Since the fabrication and the characterization of these structures was mainly done by the co-operation partners, they will be presented in Appendix A.

4.2 Top-down mounting

From Sec. 3.4.3 it becomes clear that one key measure to improve the lifetime of the laser diodes is a better heat management. In the device, heat is primarily generated on the p-side due to the limited p-type dopability of ZnSe and especially MgZnSSe on the one hand, and the limited hole mobility, on the other hand. Thus, the serial resistance in the p-type layers of the laser diode structure is significantly higher than in the n-type layers. Furthermore, even after optimization, there is still a significant barrier at the p-side semiconductor-metal interface. An effective heat management therefore has to concentrate on the p-side.

4.2.1 Idea and background

In a mounting configuration, where the laser chip is glued with the substrate side down ("epi-side up") onto the heat sink/holder, the heat generated on the p-side has to be dissipated through the complete device, including the active region and the substrate crystal. This method of heat dissipation is not optimal. First, naturally the active region itself is heated. Since the generation of non-radiative recombination centers is driven by heat, this leads to an accelerated degradation. Secondly, the dissipation through the substrate crystal is ineffective. In the case of heteroepitaxially grown ZnSe-laser diodes, GaAs is used as substrate material. Although the thermal conductivity of GaAs [0.44 W/(K cm)] is more than twice than that of ZnSe [0.19 W/(K cm)], it is still one order of magnitude lower than that of copper [3.8 W/(K cm)]. Furthermore, the substrate is quite thick (around 300–400 μ m). It is therefore desireable to minimize the dissipation length through the substrate. This can either be achieved by polishing the substrate down to a smaller thickness (typically around 100 μ m) or avoiding this dissipation path completely by mounting the chip with the epitaxial side facing down onto the heat sink. In this "top-down" mounting configuration, the heat generated on the p-side is directly dissipated into the heat sink.

Although the intuitive principle of top-down mounting sounds simple, its technological implications are difficult. This is illustrated by the fact that there is only one report in the literature concerning the top-down mounting of ZnSe-based laser diodes. By this measure a lifetime improvement by a factor of two was achieved [129]. However, no details on the mounting procedure are given. Similarly, in almost all reports

on ZnSe-based laser diodes by Sony the tested devices were mounted top-down, yet, information on the mounting procedure was never published¹.

The technological problems with top-down mounting arise predominantly from the small size of the laser chip. Whereas a laser bar usually has a size of ($10 \times 1 \times 0.4$) mm³, a single laser chip is only about ($0.4 \times 1 \times 0.4$) mm³. These chips can only be handled with a pair of high-precision tweezers. Furthermore, the mounting procedure must ensure that no short-circuits are created on the chip. With the *pn*-junction being only $1-2~\mu$ m away from the surface and exposed at the side facets of the chips, this is a major challenge.

Nevertheless, top-down mounting is a standard procedure for conventional III-V laser diodes. In principle, all necessary steps and technologies have already been developed and the required equipment for such a process is commercially available, although not all procedures can be directly applied to ZnSe-based laser diodes. This hold especially true for the mounting procedure itself, where a suitable solder has to be found. Furthermore, the costs for such tools are in a range, where the investment pays only under extreme mass production conditions². This is not accessible for a purely university-based research.

Therefore, a top-down mounting procedure for ZnSe-based laser diodes was developed in a co-operation between the *Institut für Festkörperphysik* (IFP) and a partner from industry, *Kranz & Nägele*³, Bremen. The project was supported by the *Land Bremen* via the *Bremer Innovationsagentur* (BIA). In this project the development of an optimized metalization procedure, as well as the pelletizing of the laser bars into single chips was done at the IFP. The heat sink and the mounting procedure was developed by Kranz & Nägele, in particular by C. Falldorf. Testing and characterization of the mounted devices was again done at the IFP⁴.

4.2.2 Pelletizing of laser bars

In principle, two methods can be used to achieve a controlled separation of a GaAs wafer in smaller units: sawing and cleaving. The latter method is normally used to separate a processed wafer into laser bars. When a wafer is cleaved it ideally breaks along a crystallographic axis, which leads to a very smooth and even surface with a roughness on the order of mono-atomic steps (cf. e.g. Fig. 3.22). This is the preferred method to obtain mirror facets. However, for a controlled cleavage it is necessary to have a "seed", which is usually produced by scribing with a diamond scriber an indention on the edge of the wafer at the desired position. Then, the wafer is turned over and pressure is locally applied at the position of the indention – the wafer breaks [9]. With most of the tested laser bars in this thesis the indentions were placed manually. For better-defined cavity lengths a skip scriber which is equipped with a microscope and a micrometer screw was used ⁵.

¹According to A. Ishisbashi, former project lead of the blue laser diode project of Sony, Sony regards this technology as one of its "key competences".

²Pelletizing, mounting, and packaging of optoelectronic chips is usually done in so-called *foundries* in the far east.

³now Optoprecision, Bremen [294]

⁴The results of the BIA project are documented in Ref. [295].

⁵courtesy of Prof. Gutowski, AG Halbleiteroptik

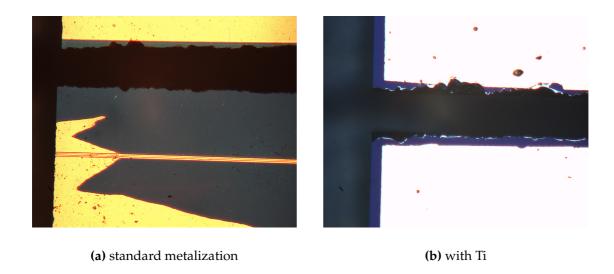


Figure 4.1: Top-view on the sawing edges of laser bars, photographed through an optical microscope. Two different metalization schemes were used.

One disadvantage of the cleaving technique is that the placement of the indention requires special care. For an ideally cleaved edge it has to be oriented exactly along a crystallographic main axis, otherwise, only small pieces will break out, or the edge will be heavily stepped (cf. e.g. Fig. 10.11 in Ref. [176]). Especially if one tries to separate the individual laser diodes of a laser bar into single chips, this becomes troublesome. Here, each mark has to be placed into the 100 μ m-wide stripe which provides the electrical isolation between the different laser diodes of the bar (cf. Fig. 2.4). For these purposes sawing of the bar is better suited. Since GaAs is a rather soft semiconductor, it can be sawed relatively easy with a diamond-powder-coated dicing disk. Sawing has the further advantage that it produces rough edges as compared to cleaved ones, which inhibits the formation of modes perpendicular to the cavity. The sawing is done under a constant supply of water to remove the sawdust as well as to cool the dicing disk and the semiconductor. By fixing the wafer onto a self-adherent plastic foil it is ensured that the laser chips are not flushed away. These sawing experiments were carried out with the dicing machine from the *Institut für Mikrosysteme*, -aktuatoren und -sensoren (IMSAS) which is specially designed to automatically separate complete wafers into single chips.

The sawing experiments revealed that the standard laser processing technology developed by M. Fehrer in the framework of his Ph.D. thesis has to be adjusted to this new processing step [176]. Figure 4.1(a) shows that during the sawing process the top gold bond pad is pealed off from the chip. To avoid this peal-off the adherence between the gold of the metal contact and the Al_2O_3 -insulator has to be improved. This is usually achieved by inserting a thin layer of Ti or Cr [9].

Figure 4.1(b) demonstrates the feasibility of this measure. In this case a thin layer of Ti (5 nm) was inserted between Al_2O_3 and Au. Furthermore, no influence of the modified metal layer sequence on the electrical characteristics of the devices was observed. In fact, the additional Ti layer provides also an improved reproducibility concerning the metalization process in general, which leads to more stable contacts. Therefore, it became part of the standard laser processing technology for ZnSe-based laser diodes.

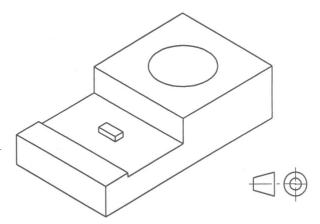


Figure 4.2: Technical drawing of the K&N heat sink design. The laser diode chip is soldered onto the small socket in the center [295].

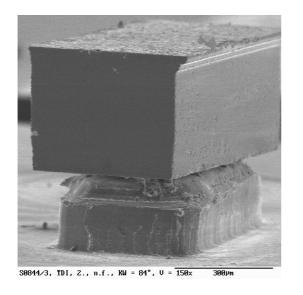
4.2.3 Design of the heat sink

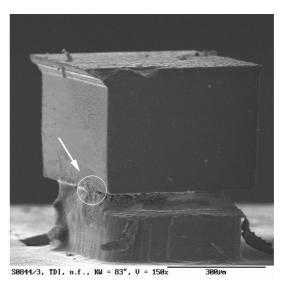
Heat sinks for semiconductor laser diodes are commercially available in a variety of different shapes, materials, and prices, cf. e.g. Ref. [296]. It depends on the desired application of the laser diode which design is chosen. Expecially, for high-power and telecommunication application an efficient heat dissipation is mandatory. Whereas in high-power systems the excessive generation of heat leads to an accelerated degradation, in telecommunication its influence on the emission characteristics – such as lasing wavelength and mode stability – is extremely critical. For these purposes commonly diamond heat sinks are used, since diamond has the highest know thermal conductivity [30 W/(K cm)][297]. However, for the devices reported in this thesis such an expensive material is not necessary. As mentioned earlier, even a simple copper heat sink should significantly improve the device stability. Given the technological experience of Kranz & Nägele concerning micro-precision engineering of metal components, it lay at hand to use a specially self-designed and manufactured copper heat sink. Thus, the design could be fully adjusted to the special requirements of the ZnSe-laser chips fabricated by the IFP.

The size of the heat sink was chosen so that it enables convenient handling of the complete laser unit. Furthermore, it should provide easy mounting of the unit, e.g. in a laser pointer. Most important for the design of the mounting system is, however, that the possibility of a short-circuit of the *pn*-junction at the facets due to excess solder is reduced. In the actual design, this requirement is met by milling a socket of a size, smaller than the typical laser chip, out of the heat sink. A 2.2 mm drill hole simplifies the mounting of the complete unit. The full design, developed by Kranz & Nägele in cooperation with the IFP, is shown in Fig. 4.2. The heat sink has a size of $(2 \times 4 \times 7.5)$ mm³ with a laser chip mounting socket area of (0.75×0.35) mm². For the mounting tests, laser chips of $(1.2 \times 0.4 \times 0.35)$ mm³ were used. In conjunction with the rounded edges of the mounting socket it is therefore ensured that eventual excess solder will flow away from the chip.

4.2.4 Solder

The growth temperature of ZnSe-based material is typically around 285°C. This is significantly lower than the usual temperatures used to grow and process conventional III-V semiconductors. Thus, special care has to be taken with respect to the melting





(a) working device

(b) short-circuited

Figure 4.3: SEM photographs of top-down mounted laser chips. A short-circuit is marked by an arrow (photographs taken by E. Meyer).

point of the solder for the mounting of the laser chips. High-resolution XRD experiments on single ZnSe layers show that at temperatures above 250°C, formation of thermally induced stacking faults occurs [45]. Furthermore, the *p*-type doping level will be influenced by increased temperatures [95]. It is therefore mandatory that the melting point of the solder is lower than 250°C. To minimize the heat load onto the device during the soldering process, as much as possible solders with melting points between 120 and 160°C were considered. Potential candidates in this particular temperature region are the PbSn alloys, commonly used in electronics [298]. Their melting point is around 180°C, but with the addition of Bi it can be reduced to the desired lower value.

Another requirement concerning the solder is that it wets the whole surface of the copper socket on the one hand, and the Au metal contact of the chip, on the other hand. Using the PbSn alloys, this limits the useful melting point range to 125° C, since further addition of Bi deteriorates the wetting characteristics [298]. As optimal alloy the following composition with an melting point at 125° C was used: $Pb_{39.5\%}Sn_{20.3\%}Bi_{40.2\%}$.

The wetting characteristics of the solder and the electrical characteristic of the contact depend not only on the composition of the solder alloy, but also on the cleanness of the involved parts. Especially, residual oxides on the copper surface degrade the performance [298]. Therefore, the copper socket is polished and treated with solder grease before the mounting process, which is done in a special preparation chamber under an Ar atmosphere.

The actual solder process is a two-step process. First, the solder is applied to the heat sink. Thus, the excess solder can be remove from the socket, before the chip is mounted. Furthermore, a complete wetting of the copper socket requires the use of the solder grease, that needs to be activated at elevated temperatures around 450°C. After the appropriate amount of solder is deposited and the heat sink is heated up to 160°C,

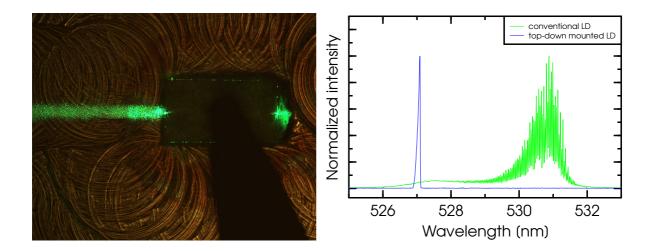


Figure 4.4: Left: microscope photograph of a top-down mounted laser chip under current injection. Clear lasing emission is seen. Right: lasing spectra of a top-down mounted laser and a conventionally processed laser diode of the same wafer.

the laser chip is placed epi-side facing downwards onto the socket. This placement process is done manually, however, due to the special design of the sink and the surface tension of the solder between chip and socket, this process is self-centering. This is illustrated in Fig. 4.3, which shows an scanning electron microscope (SEM) photographs of such top-down mounted ZnSe-laser chips. Although both laser chips in Fig. 4.3 are larger than the socket, only the chip in part (a) is a functioning device. The chip shown in Fig. 4.3(b) has some solder at the edge (marked by the arrow) which leads to a short-circuit.

4.2.5 Results and outlook

Figure 4.4 shows one of the first top-down mounted ZnSe-laser diodes from Bremen. Clear laser emission from the device is visible. On the right-hand part of Fig. 4.4 the lasing spectrum of this device just above threshold is shown. Lasing occurs at a wavelength of 527 nm. Due to the limited dynamic of the CCD camera of the spectrometer, two filters were necessary to damp the laser signal (total transmission coefficient: $T = 6.25 \times 10^{-6}$). Thus, only the lasing mode, but no side-modes are visible. Also depicted in this figure is the typical emission spectrum of a conventionally processed device of the same laser wafer. The two devices differ by more than 4 nm in emission wavelength. In Chapter 3 it was described that heat has a significant influence on the emission wavelength of the laser diodes. Taking into account that the emission wavelength of a laser structure typically changes by not more than 1 nm across the full wafer, one can attribute the blue shift of the emission wavelength to a decreased heat load in the device. Using the standard estimation for the temperature induced wavelengthshift, a difference of 40 K between the temperatures of the active regions of both devices is calculated. This nicely illustrates the improved heat management due to the topdown mounting.

Although special care was taken to avoid short circuits in the mounted system, it

turned out that most of the devices could not be operated due to precisely this problem. The reason for this could not be clarified completely. Some of the devices could at least be operated in LED-mode. This indicates that the mounting procedure is in principle OK. However, when the current level is increased a short circuit is generated. One explanation for this effect is that the heat generated at the *p*-side contact is high enough to melt the solder so that it can reach the facet of the chip. Here, solders with higher melting points might solve the problem. Another source of the short circuit can be a metalization of the facets by condensed metal vapor deposited during the soldering process.

Before the top-down mounting of the lasers, the single chips were electro-optically characterized epi-side up without any problem. Thus, a failure of the devices due to the sawing process can definitely be ruled out. The best solution for the short-circuit problem is obviously a passivation of all four laser chip facets. Then, the pn-junction is not exposed to the solder and a short circuit is avoided. Additionally, it would be helpfull to take the pn-junction further away from the surface. This could be done by inserting a thicker spacer layer on the p-side. In fact, most laser structures reported by Sony have an 1.8 μ m thick p-ZnSSe spacer, which facilitates top-down mounting [122].

Although the realization of the top-down mounting of the laser diodes is a success by itself, the potential improvements concerning the stability of ZnSe-lasers could not be verified. This results from the fact, that the first mounted devices were obtained at the end of the project. Due to the described short-circuit problems, only few devices could actually be tested. Here, more work is necessary.

4.3 High-reflectivity facet coating

Facet coating is the standard measure to reduce the threshold current density of semi-conductor laser diode and well-established for III-V devices. Even most of the results concerning electrical pumping of ZnSe-laser diodes reported in literature, are obtained from coated lasers, yet, the experimental realization of coating requires the development and optimization of a reproducible process for the individual machine used for the deposition of the coatings. Namely, a precise thickness control of the deposited material is necessary. This work was done by C. Petter in the framework of his Diploma thesis [285]. Some of his result will be presented in the following.

4.3.1 Dielectric mirrors

Dielectric mirrors are formed by a periodic variation of the refractive index, which is also called a *Bragg mirror*. Such an index variation is usually obtained by alternately depositing two materials with different refractive index. The degree of reflectivity depends on the number of mirror pairs, whereas the frequency selection is given by the mirror period, i.e., the layer thicknesses.

The principle of operation of such dielectric mirrors is simple: at every refractive index step, one part of the wave is reflected, the rest is transmitted, and a phase shift occurs. If the layer thicknesses are chosen so that the optical path between the interfaces is exactly $\lambda/4$, these phase shifts give rise to constructive interference for the light of the wavelength λ . The reflectivity r of such a mirror with N pairs of layers with refractive

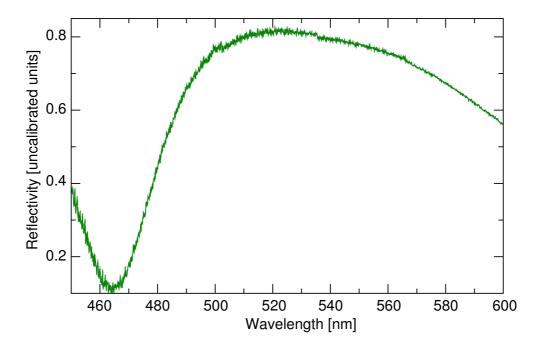


Figure 4.5: Reflectivity spectrum of a dielectric mirror with 4 pairs, deposited onto a laser facet (taken from Ref. [300]). Due to experimental difficulties, the absolute values of the reflectivity are not calibrated, however, the maximum reflectivity is surely above 80%.

indices n_1 and n_2 on a substrate with reflective index n_s is given by [299, 285]

$$r = \tanh^2 \left(\ln \frac{n_1}{n_2} + \frac{1}{2N} \ln n_s \right). \tag{4.1}$$

A more detailed description of the problem can be found in Ref. [299].

For a high reflectivity with only a few mirror pairs, the refractive index contrast between the two materials has to be high. Commonly, oxides – such as SiO_2 , TiO_2 of HfO_2 – are used. It is not necessary to deposit the materials as single crystals, therefore, they are usually obtained from plasma sputtering. The sputter system in Bremen is operated with an Ar plasma and provides two targets with SiO_2 ($n_1 = 1.5$) and TiO_2 ($n_2 = 2.6$). A description of the system, as well as the technical difficulties – such as operation of the machine, mounting of the samples, and reproducible deposition rates – can be found in Ref. [285].

Figure 4.5 shows a typical reflectivity spectrum of a mirror with 4 pairs of SiO₂ and TiO₂ layers, measured using a white lamp and a spectrometer. The layer thicknesses are 87 nm and 50 nm, resp., to obtain a reflectivity maximum at 520 nm. As the graph shows, the desired wavelength was obtained, indicating a satisfactory thickness control. Since the mirror was directly deposited onto the facet of a laser bar, no calibration of the absolute reflectivity is possible, because the measurement spot of 1 mm is larger than the facet length of 350 μ m. However, it is safe to assume that the absolute reflectivity in the maximum is above 80%.

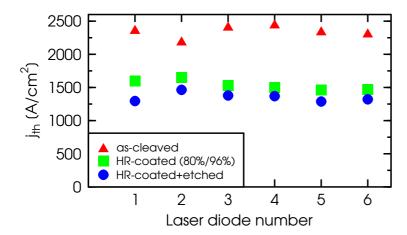


Figure 4.6: Effect of high-reflectivity (HR) coatings on the threshold current densities j_{th} of ZnSe-laser diodes. Three different bars of comparable length were cleaved from the same laser wafer. In order to remove oxides from the facet, one laser bar has been etched in an Ar plasma before coating (from Ref. [300]).

4.3.2 Influence on the threshold current density

The mirror shown in Fig. 4.5 is suitable as a coating for a ZnSe-laser diode. However, it is not useful to apply coatings with identical reflectivities on both laser facets, because that would reduce the light output from the device significantly. Commonly, an asymmetric coating is used, where one side has a reflectivity above 95%. The other facet is coated with 40–60%, depending on the desired purpose (high lifetime vs. high output power) [116, 131, 267].

From Eq. 1.15 the influence of a high-reflectivity facet coating can be calculated. Using typical laser parameters for ZnSe-based laser diodes, given in Refs. [301, 34], and a cavity length of 700 μ m, one can expect a threshold current density reduction by a factor of 2 for a reflectivity combination of 40%/95% as compared to the as-cleaved facet with only 20% reflectivity [300]. This is confirmed in Fig. 4.6, where the threshold current density of different laser bars are shown for the coated and the uncoated case. Although the absolute threshold current density of all devices is quite high⁶ (more than 2 kA/cm² for the uncoated devices), a significant reduction for the coated devices is seen. Here, a combination of 6 and 2 mirror pairs was used, resulting in a reflectivity of about 96% and 80%. On average, the threshold current density is reduced by 35% for the unetched facet.

In Sec. 3.6 it was shown that as-cleaved facets suffer from an oxidation of the semi-conductor material. Therefore, an additional bar of the same laser structure was coated in the same fashion, but before the coating the facet was etched for 30 s in an Ar plasma. Thus, the threshold could be reduced by 43% as compared to the as-cleaved, uncoated facet.

In summary, facet coating is a effective method to reduce the threshold current density of the laser diodes. Due to the reduced operating current, less heat is generated and a higher lifetime can be expected. However, this expectation remains to be demonstrated, since the appropriate tests are currently being performed. These results will be reported in Ref. [285].

⁶due to problems during the laser processing prior to the coating

4.4 Summary

The work presented in this chapter was motivated by the desire to improve the reliability of ZnSe-baser laser diodes by improving the *ex-situ processing*, not the growth itself. In co-operation with others, top-down mounting and high-reflectivity facet coating was developed and successfully realized for these devices. The technological difficulties connected to both processes and the additional degree of complexity, however, oppose an inclusion in the standard laser diode processing sequence. Nevertheless, the feasibility of the techniques could be demonstrated. Therefore, such advanced processing will rather be reserved for special purposes, e.g. where high lifetimes are desired, or where the standard process only results in mediocre performance.

Chapter 5

Exploring the limits and possibilities of Cd-rich quantum wells

The work presented so far was focused on ZnSe-based laser diodes emitting around 510–530 nm. In the following chapter it will be shown that such devices are not limited to these emission wavelengths. Since wavelengths below 500 nm have already been realized by other groups, devices operating at long wavelengths around 560 nm will be investigated – developing new possibilities while simultaneously exploring the limits of very high compressively strained quaternary CdZnSSe quantum well.

5.1 Motivation

The question whether the emission wavelength of ZnSe-based laser diodes can be tuned beyond 530 nm is not a pure academic question to demonstrate what degree of material perfection is possible. Aside this aspect there exists a very attractive application for such devices that has not been considered so far: as light source for optical data communication systems employing plastic optical fibers (POFs) as transmission medium. Optical data communication is the backbone of today's communication age. The reason is obvious: the data is transmitted at the speed of light¹. Using different transmission wavelengths, several data channels can be transmitted via the same fiber simultaneously [302]. Furthermore, light is not susceptible to electro-magnetic interferences. For large-scale networks – such as intercontinental connects – doped silica fibers are used as transmission medium due to their very low transmission losses. However, such fibers are not only expensive but also brittle. For short and medium transmission ranges cheaper types of optical fibers are used: POFs. The most common and simplest type of POF is a fiber with a polymethyl methacrylate (PMMA) core. PMMA is a general purpose plastic and hence cheap and easy to fabricate. Other types of POF employ a multiply layers of plastic layers with different refractive indices, so-called graded index fibers (GOF). All types of plastic fibers in common is their advantage over the silica fibers, which are a higher flexibility, a larger diameter, which facilitates the connection mechanisms to light sources and receivers, and a lower sensitivity against vibrations. Especially, the last point – in conjunction with the insensitivity against electro-magnetic

¹to be more precise, at the speed of light v in the transmission medium $v = \frac{c}{n}$, with n as refractive index of the medium

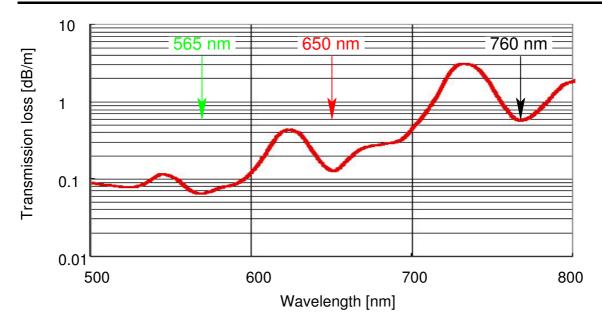


Figure 5.1: Typical transmission loss spectrum of a plastic optical fiber with a PMMA core [306].

interference – makes them most attractive for the automobil and aircraft industry [303]. Whereas the multimedia – and recently also the safety communication backbones – in most modern cars are based on POF, the use in aircrafts is not yet fully developed, mainly due to the limited transmission range. Although using a specially designed GOF, a transmission range of 990 m at a data speed of 1.25 GBit/s could recently be demonstrated, this range needs to be extended [304]. The main obstacle here are the high transmission losses in the POF [305]. Figure 5.1 shows, how ZnSe-based laser diodes may provide a solution to overcome this range limitation.

The typical PMMA-POF transmission loss spectrum shown in Fig. 5.1 is characterized by several local minima. In most POF-based systems a laser or light-emitting diode operating around 650 nm or 760 nm which match those loss minima are employed. For such devices mostly AlGaInP-based laser structures grown on GaAs substrates are used [307, 308]. Based on Fig. 5.1, devices emitting around 650 nm should be preferred concerning longer ranges, since here the transmission losses are about 0.13 dB/m. However, by using a light source emitting around 560–570 nm, these losses could be reduced to 0.06 dB/m, i.e., by more than 50%. But so far no electrically pumped semiconductor laser diode with an emission around 565 nm has been fabricated. In fact, there exists no obvious material combination that provides access to this particular spectral region. Concerning the conventional III-V laser diodes, the before mentioned AlGaInPbased devices have shown the shortest emission wavelength around 615 nm [309, 310]. These devices could only be realized employing an advanced layer design, such as multi-quantum well barriers, as well as an advanced processing technology such as ridge-waveguide fabrication [309]. Other problems involved in the growth of Al-rich AlGaInP alloys are an increased tendency to show spontaneous alloy ordering and a reduced *p*-type dopability [311]. Finally, a strong increase in the threshold current density is observed for emission wavelengths shorter than 620 nm [310].

Since no conventional III-V material system provides access to the desired emis-

sion wavelength region, other material systems have to be considered. Here, only the II-VI system with devices based on the ZnSe alloy system is a suitable candidate. Such devices are the only ones, that have shown electrically pumped lasing at roomtemperature. Emission wavelengths up to 536 nm were realized on GaAs substrates, while an even longer wavelength was obtained on ZnSe substrates: 538 nm [131, 274, 135]. Extending the emission beyond 560 nm requires the growth of quantum wells with Cd contents around 40–45%, which leads to a highly strained quantum well when using GaAs or ZnSe as substrate. Since it is questionable, whether these highly strained quantum wells can be grown in device-quality, several research groups focus on the realization of devices on alternative substrates such as ZnTe and InP [312, 43, 42, 313]. However, under electrical pumping, only spontaneous emission – sometimes even only at low-temperature (77 K) - was reported so far. Concerning stimulated emission, all these alternative approaches lack the availability of a suitable cladding material with a high band gap energy and a good dopability (p-type when growing CdZnSe-based material, resp. *n*-type in the case of ZnTe-based structures). Furthermore, the substrate preparation and growth start procedures are not as well established, resulting in higher defect densities.

Due to the well-established growth and experience with ZnSe-based structures on GaAs, and the difficulties with alternative substrates, the growth of Cd-rich quantum wells on GaAs with high structural and optical quality will be investigated in the following sections – in order to incorporate them in fully functioning laser diodes². It has to be clarified whether the highly mismatched quantum well can degrade the structural perfection of the rest of the structure and how it influences the operational device characteristics. The main question, nevertheless, is, whether laser emission around 560–570 nm can be realized.

5.2 Growth optimization

The first step to obtain laser emission around 560 nm is to grow material with the appropriate band gap energy. A quaternary CdZnSSe alloy with a high Cd content is such a suitable material. Using a quaternary composition with S is a key point, since an alloy hardening is expected [196, 76]. In order to obtain high quality material several growth parameters can be optimized. An important guideline for this optimization process is composition control. In Sec. 3.5.1 it was mentioned that the Cd incorporation in a ternary CdZnSe ternary is limited to about 20% Cd when growing in the MEE growth mode. Only by fabricating a CdSe/ZnSe sub-monolayer superlattice (digital alloy, DA) a higher Cd content can be realized. But a DA cannot provide access to the full composition range, because that would require the growth of individual CdSe layers with thicknesses above the critical thickness of 2 ML. Then, quantum dot formation – accompanied by massive stacking fault generation – occurs, which is neither intendend nor desired in this case [180, 316]. A MEE growth mode is not suitable for the growth of high Cd-containing CdZnSSe layers.

The limited Cd incorporation derives from the high vapor pressure of Cd. In investigations on the growth mode of CdZnSe by using a mass spectrometer, Okuyama *et al.* found that the sticking coefficient of Cd depends drastically on the flux ratios of Cd to

²Parts of the results reported in this chapter have been published in Refs. [314, 315].

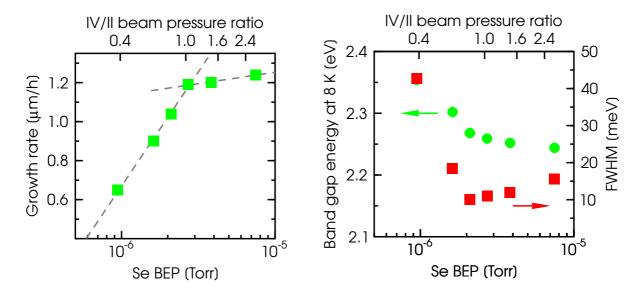


Figure 5.2: Influence of the Se flux on the growth of quaternary CdZnSSe. During the growth of the single layers the Cd, Zn, and S flux were kept constant. The upper x-axis gives the normalized IV/II beam pressure ratio, calculated with Eq. 5.1. Left: growth rate calculated from the layer thickness which was measured with a profilometer. The dashed lines are guides to the eye. Right: optical characteristics of the single layer: band gap energy as obtained from low-temperature PL and corresponding FWHM of the emission.

Zn on the one hand, and of group-II to group-VI on the other hand [56]. Therefore, the flux conditions during growth will have a significant influence on the layer composition. Only the conventional MBE growth mode gives access to this particular parameter and, hence, CdZnSSe material with high Cd contents are grown in MBE mode. As a positive side-effect, the MBE growth mode also allows to perform an optimization concerning point defects, as reported in Sec. 3.5.4.

The main boundary condition for the growth parameters is that they should be applicable to the growth of a full laser structure. As mentioned before, the standard flux conditions for laser growth are set so that the ZnSe, ZnSSe, and MgZnSSe growth is stoichiometric – consequently the CdZnSSe quantum well growth will be group-II rich. Since the flux ratio between group-II and group-VI will have the strongest influence, it was decided to keep all cell fluxes constant, except that of the Se cell. Thus, later also a point defect optimization can be performed.

In order to obtain the correct flux settings for the quantum well growth first, single CdZnSSe bulk layers were grown. Due to technical problems with the Se valved cracker cell, all samples – including the laser structures – were grown with the Se knudsen cell. The thickness of the single CdZnSSe layers is $0.6-1.2~\mu m$, i.e., the layers are relaxed.

Figure 5.2 shows the influence of the Se flux on the material growth. On the left-hand side, the evolution of the growth rate with increasing Se flux is shown. The starting point for the sample series is at a Se flux of a beam equivalent pressure (BEP) of about 1×10^{-6} Torr, which corresponds to the standard Se flux for stoichiometric ZnSe growth. For Se fluxes below 3×10^{-6} Torr the growth rate increases monotonically with the Se supply. This reflects the group-II rich growth conditions, during which the growth rate does only depend on the amount of group-VI elements available for incorporation.

Above 3×10^{-6} Torr the growth rate is likewise limited by the combined supply of Cd and Zn. Stoichiometric growth is obtained at a Se flux of about $2.5 - 3 \times 10^{-6}$ Torr. These findings are supported by the change in the RHEED pattern, where under group-II rich conditions a $c(2 \times 2)$ reconstruction of the growing surface is observed. Under group-VI rich condition this changes to a 2×1 reconstruction and for the growth at a Se flux of 2.7×10^{-6} Torr a mixture of both types is detected.

The optical characterization by low-temperature PL is shown on the right-hand side of Fig. 5.2. Here, a strong band gap energy decrease from 2.35 eV down to 2.26 eV is found, when going from group-II rich to stoichiometric growth conditions, which reflects an increasing Cd incorporation. Under group-VI rich conditions, a further reduction of the band gap energy is observed, but it is not as strong as before. This further reduction is caused by a diminishing S content in the quaternary material: only the Se flux is varied, therefore, the flux ratio between S and Se changes accordingly. However, since the average S content under standard conditions (at a Se flux of 1×10^{-6} Torr) is 6%, the reduced S content caused by the flux change has only a small effect.

The smallest FWHM of the PL emission is obtained from the layer grown at a Se flux of 2.7×10^{-6} Torr, i.e., under stoichiometric conditions. Generally, the linewidth of the emission depends on several factors, such as interface roughness, impurities, and composition homogeneity [317]. Since the samples in Fig. 5.2 are all bulk samples with layer thicknesses above 600 nm, interface roughness can be neglected. Nevertheless, for group-II rich growth conditions a surface roughening is reported, which results into the formation of periodic elongated corrugations aligned in the [110] direction in the material [318]. Such corrugations lead to a broadening of the emission. Besides their negative influence on the emission width, they also contribute to the formation of dark defects [233].

Since the samples were grown as one series within 2 days, the impurity concentrations should be the same in all layers. Consequently, the sharp emission for the stoichiometrically grown sample indicates a reduced composition fluctuation and a better ordered alloy, i.e., no corrugations were formed. Similar findings are reported in the literature [319].

For all samples reported in this chapter the same nominal cell settings for Cd, Zn, and S were used. The VI/II beam pressure ratio (BPR) of group-VI and group-II elements with the individual BEPs f [Cd, Zn, S,Se] is given by

$$IV/II BPR = \frac{f[S] + f[Se]}{f[Cd] + f[Zn]}.$$
(5.1)

Based on the results of Fig. 5.2, it is possible to normalize the flux ratio Eq. 5.1 such that stoichiometric conditions are described by a VI/II flux ratio of unity. The upper x-axes of the graphs in Fig. 5.2 give the II/VI ratio according to such a normalization. Under group-II rich conditions the flux ratio is below unity, whereas group-VI rich conditions are characterized by a flux ratio of more than unity. The same procedure was used by Kato *et al.* for the investigation on the optimal flux ratio concerning point defects [5].

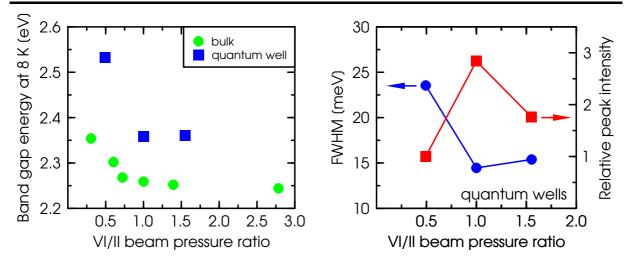


Figure 5.3: Optical characterization of CdZnSSe quantum wells grown under different VI/II ratios. Left: band gap energy. For comparison the data from Fig. **5.2** obtained for bulk layers is also shown. Right: evolution of the FWHM and the integrated PL emission intensity, normalized to the value for standard growth conditions.

5.3 Quantum wells

By changing the Se flux – and therefore the VI/II ratio – CdZnSSe with a band gap energy suitable for long-wavelength³ emission can be grown. The next step is to investigate whether high-quality quantum wells can be fabricated from it. Similar to the procedure in the previous section, CdZnSSe quantum wells were grown with varying Se cell temperatures, while all other parameters were kept constant. The quantum wells are embedded into ZnSe barrier layers, where the lower barrier has a thickness of 43 nm and the upper barrier is 22 nm thick, as determined from high-resolution XRD. The quantum wells themself are 5–6 nm thick.

In Fig. 5.3 the low-temperature PL results of the samples are summarized. The left-hand graph shows the change in emission energy. Again, an increased Cd incorporation with higher VI/II ratios is observed. For comparison the data for bulk layers from Fig. 5.2 has been added. The reasons for the higher emission energy of the quantum well as compared to the single layers are a 10% higher Cd flux on the one hand, and the additional confinement energy due to the quantum confined system on the other hand. Here, the confinement overcompensates the reduced band gap energy related to the higher Cd flux.

Similar to the results on single layers, a reduction of the emission half-width is observed for the quantum wells when grown under stoichiometric conditions. At an emission energy of 2.36 eV, a FWHM of 14.5 meV is measured. This value is close to the theoretical values expected for a perfectly mixed alloy of CdZnSSe with 43% Cd and 4% S [206]. In the same graph, the integrated PL emission intensity, normalized to the standard fluxes, is also plotted. An emission enhancement by almost a factor of 3 is observed for the stoichiometrically grown quantum well. Both parameters – emission sharpness and intensity – indicate a high morphological and optical quality. Such quantum wells are suitable for electrically pumped laser diodes – from an optical point of view.

³In the following, long-wavelength emission implies an emission around 560 nm.

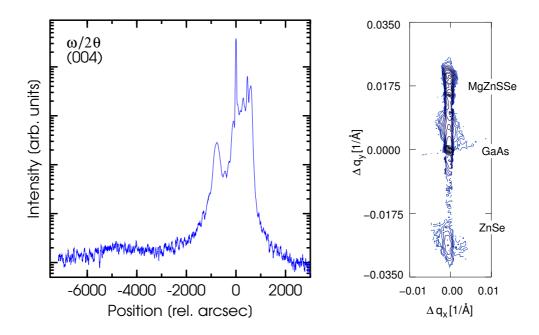


Figure 5.4: High-resolution XRD characterization of a laser structure with a quantum well optimized for long-wavelength emission. Left: $\omega/2\theta$ -scan of the (004) reflex. Right: reciprocal space map of the (224) reflex.

5.4 First laser diodes emitting at 560 nm

The optimization of the CdZnSSe growth based on a change in VI/II flux ratio produces quantum wells with high optical quality. Yet, it remains to be clarified whether the structural quality of a complete laser structure is not deteriorated by such a highly lattice-mismatched layer. Since the quantum well grown under a stoichiometric flux ratio yielded the highest optical quality, it was decided to use these conditions for the first laser structure – despite the fact that a Se-rich growth improves the stability under current injection. The standard laser structure and growth procedure described in Sec. 2.3 was used. However, in order to raise the Se cell to the temperature necessary for the CdZnSSe stoichiometric growth conditions, a growth interruption of 20 min each (heat up and cool down) was performed. During this growth interruption the sample is kept at the regular growth temperature, but under a Se flux exposure.

Figure 5.4 reveals that the optimized growth conditions provide not only the means for the fabrication of high Cd-containing CdZnSSe quantum wells with high optical quality, but also with a good structural perfection. On the left-hand side of Fig. 5.4 the usual $\omega/2\theta$ scan of the (004) reflex is shown. About 500 arcsec to the right of the substrate peak the signal from the MgZnSSe cladding layers is found. This rather large lattice mismatch is still tolerable. As mentioned in Sec. 2.3 the plasma cell operated during the growth of the *p*-side gives rise to an additional heating of the substrate and thus, a reduced S content in the *p*-cladding layer. In order to compensate this additional heating, the growth temperature was lowered, however, the $\omega/2\theta$ scan indicates that the temperature change was too drastic so that an overcompensation occurred. The waveguide layers are better lattice matched to the substrate, and the layer signal can be

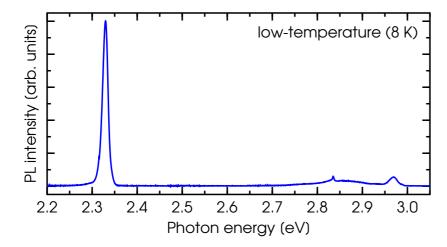


Figure 5.5: Lowtemperature PL form a laser structure with optimized quantum well growth conditions.

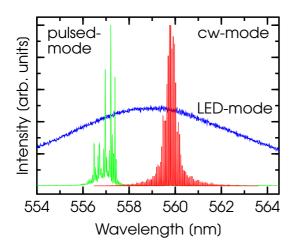
found 100 arcsec to the left.

The weak quantum well signal is found around 5000 arcsec left of the substrate. From a simple $\omega/2\theta$ scan of a symmetric reflex, it cannot be clarified whether the structure is fully strained or a (partial) relaxation has occurred. Here, a mapping of an asymmetrical reflex is required, as it is shown on the right-hand side part of Fig. 5.4. In this mapping of the (224) reflex all layer signals are found at $\Delta q_x = 0$, indicating a fully strained structure. Electrically pumped lasing can be expected from this device.

The high structural quality of the laser structure is also reflected in the low-temperature PL characterization shown in Fig. 5.5. The PL spectrum of the device is dominated by the quantum well emission at 2.33 eV. With a FWHM of less than 14 meV, again, a perfectly mixed alloy with smooth and homogenous interfaces is obtained. At 2.84 eV a weak signal from the ZnSSe waveguides is detected, likewise, the cladding layers show up at 2.96 eV. No other PL spectrum from a ZnSe-based laser diode grown in Bremen exhibits such a dominating quantum well emission as the one shown on Fig. 5.5. This visualizes how important the flux conditions during the growth of the active region are on the luminescence efficiency – not only for the growth of long-wavelength devices.

Figure 5.6 gives the results of the electro-optical characterization. On the left-hand side electroluminescence spectra in pulsed-mode as well as in cw-operation are shown. The spontaneous (LED) emission of the device is centered around 559 nm, corresponding to an emission energy of 2.22 eV, as expected from the low-temperature PL measurement and based on the temperature dependence of the band gap energy of CdZnSSe. Above the threshold of 730 A/cm² clear lasing emission at 557 nm is detected in pulsed-mode. Since the device was operated at a low duty cycle of 0.1%, heating effects can be neglected in this case. Under DC current injection, this is no longer the case and the emission red-shifts by 3 nm resulting in a cw-lasing wavelength of 560 nm. The red-shift corresponds to a temperature increase of 30 K, which is comparable to the conventional ZnSe-based laser diodes⁴ grown in Bremen. This laser emission around 560 nm is not only the longest wavelength ever reported for a ZnSe-based laser diode, but also the first time that electrically pumped lasing from a semiconductor laser diode has been realized in this particular spectral region. Above that, the device could directly be operated in

⁴Laser diodes with an emission around 510–530 nm and with no optimized quantum well growth conditions.



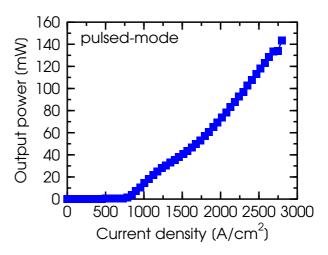


Figure 5.6: Electro-optical characterization of the laser structure with a high Cd content in the quantum well. Left: electroluminescence and lasing spectra, obtained in pulsed-operation, as well as in cw-mode. Right: L/j characteristics measured in pulsed-mode under standard conditions (1 μ s pulse width, 0.1% duty cycle).

cw-mode, indicating a very high material quality and stability.

In Fig. 5.6 the standard L/j characteristics of this device is also shown. A steep increase of the light output power is seen above the threshold current density of 750 A/cm², at which the operating voltage is 6 V. A maximum output power of 150 mW is obtained from this particular device under these conditions. The differential quantum efficiency during lasing operation is 69%. Around 1.25 kA/cm²– corresponding to an output power of about 40 mW – a slight non-linearity of the L/j characteristic is observed. Such a kink is typically associated with a change of the optical mode within the laser cavity [10]. In this case a transition to a higher mode is the most probable explanation. However, the occurrence of such an optical mode change is commonly observed – especially under high current injection – and not related to the longer emission wavelength.

5.5 Operational characteristics in comparison: 500 nm vs. 560 nm emission

Figure 5.7 nicely illustrates the potential of ZnSe-based laser diodes with CdZnSSe quantum wells. It shows the emission of different laser diodes operated above threshold. The only difference between the devices is a varying quantum well composition. By this variation – namely of the Cd content – it is possible to tune the emission wavelength within the full blue-green part of the visible spectrum, ranging from 500 nm to 560 nm. By using binary ZnSe quantum wells, also true blue emission is possible [119]. Thus, the tuning range spans almost 100 nm. In the following it will be investigated, in how far the different emission wavelengths influence the operational characteristics. The focus of this comparison will be on the devices grown under standard growth conditions, resulting in emission wavelength around 500–530 nm on the one hand, and with optimized quantum well growth conditions, emitting at 560 nm, on the other hand.

First, the L/j characteristics are compared, as shown in Fig. 5.8. Here, the devices

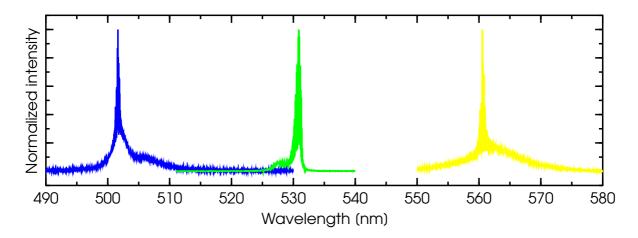


Figure 5.7: Emission spectra of different ZnSe-based laser diodes in comparison. The only difference between the structures is a different Cd composition of the quantum well material.

have been operated in pulsed-mode and at a low duty cycle, in order to obtain high optical output powers. Although the device emitting at 505 nm and that one emitting at 560 nm have a comparable threshold current density, a higher maximum output power is obtained from the long-wavelength device. A record output power of more than 1000 mW is measured. This is among the highest output powers ever obtained from ZnSe-based laser diodes. On the other hand, the output power at 505 nm is limited to 350 mW. But Fig. 5.8 clearly indicates that this limitation is related to the occurrence of COD. Since an output power of 600 mW – limited only by the power supply – was reported for a laser diode emitting at 495 nm, we attribute the occurrence of COD to the device processing alone and not to the shorter emission wavelength [320]. Comparing the slopes of both characteristics a reduced external quantum efficiency of the 505 nmlaser is observed. In sum, the comparison of the L/j characteristics under high current injection levels reveals, that the main difference between both types of quantum wells are not related to the different emission wavelength, but rather to the different optical qualities. An optimization of the quantum well growth conditions for devices emitting in the short-wavelength region will therefore result in better operational characteristics,

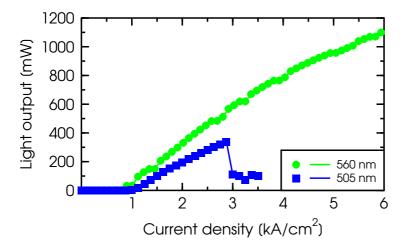


Figure 5.8: High-power operation of ZnSe-based laser diodes with different quantum well material. For these tests the devices were operated at a low duty cycle of 0.01% and a pulse width of $1 \mu s$.

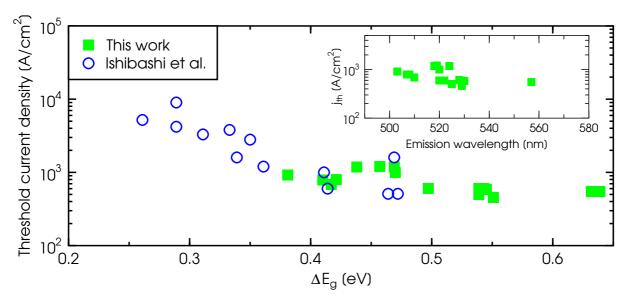


Figure 5.9: Threshold current density (j_{th}) dependence on the band gap energy difference ΔE_g between cladding layers and quantum well. The data points of this graph stem from laser structures grown in the course of this thesis (filled symbols) and from Sony (open circles) [123]. The devices have been tested under comparable operating conditions, i.e., 0.1% duty cycle, 2–5 μ s pulse width and a cavity length of 1 mm. All facets are uncoated. In the insert, the threshold current density is plotted vs. the emission wavelength of the devices (only Bremen samples).

which will be comparable to the ones, at present only obtained for the long-wavelength-devices.

The band gap energy of the MgZnSSe cladding layers of most laser structures grown in the course of this thesis was set to about 2.9 eV at room-temperature - regardless of the band gap energy of the quantum well. Thus, the laser structures exhibit different degrees of confinement. In Fig. 5.9 the influence of these different confinement strengths – expressed in terms of band gap energy difference between cladding layers and quantum well ΔE_q – on the threshold current density is depicted. Generally, a better confinement leads to a reduced current overflow and, hence, a lower threshold current density. As mentioned in Sec. 1.3.4, below a band gap difference of 0.35 eV an increased current overflow will be the result [71]. This is confirmed in Fig. 5.9 (data from Sony has been added to extend the graph into the region of low band gap energy differences [123]). A clear threshold current density increase is seen for ΔE_q below 0.35–0.4 eV. However, even for a better confinement with large ΔE_g , the threshold current density does not drop below 500 A/cm². A drastic threshold reduction – as theoretically predicted for such good confinement – is not observed [321]. In fact, the threshold of these laser structures is dominated by the mirror losses, since the internal absorption in ZnSe-based laser structures is small [322, 301]. Taking into account that the reflectivity of the uncoated facets is only 20%, one can expect significant reduction in threshold current for highreflectivity coated devices. Thus, the operating current can be reduced and less heat is produced, which – based on the results of Sec. 3.11 – will lead to a higher stability.

Another important conclusion can be drawn from the insert of Fig. 5.9, which shows the threshold current density variation with the emission wavelength of the devices. Since the threshold does not benefit much from a high cladding material band gap en-

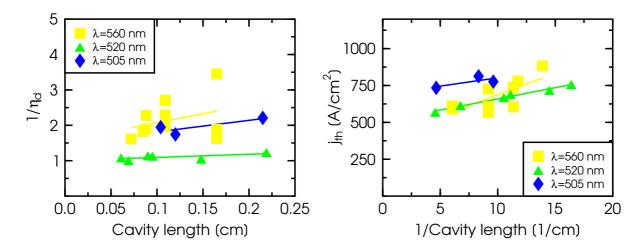


Figure 5.10: Dependence of the laser characteristics on the length of the laser cavity for different laser structures. The devices have been operated in pulsed-mode and with standard driving conditions. Left: reciprocal external quantum efficiency $1/\eta_d$ vs. cavity length L. Right: threshold current density j_{th} plotted vs. the reciprocal cavity length 1/L.

ergy, it can be reduced for laser diodes operating in the spectral region around 560 nm. This would lead to a higher net acceptor concentration in the *p*-doped MgZnSSe and, thus, to a reduced serial resistance of the device [161]. Again, this will improve the reliability due to less heat load.

In order to get better insight in the lasing process, cavity dependent L/j measurements have been performed with the different structures. Based on the theory of lasing in a Fabry-Pérot cavity presented in Sec. 1.1.2, it is possible to extract some figures of merrit often used to compare semiconductor lasers – namely the internal quantum efficiency η_i , the absorption coefficient α_i , the gain constant β , and the nominal current density J_0 . By taking the reciprocal of Eq. 1.21, one obtains a linear dependence of $1/\eta_D$ on the cavity length L, where the intercept is given by the reciprocal internal quantum efficiency and the slope is determined by the mirror losses and the internal absorption and efficiency. Plugging the result from such analysis into Eq. 1.15, it is possible to obtain the nominal threshold current density J_0 and the gain constant β from linear regression of the dependence of the threshold current density on the reciprocal cavity length 1/L. The resulting equations are,

$$\frac{1}{\eta_d} = \frac{1}{\eta_i} + \frac{\eta_i \alpha}{\ln \frac{1}{r_1 r_2}} \times L \tag{5.2}$$

$$j_{\text{th}} = \left(\frac{J_0 d}{\eta_i} + \frac{d \alpha}{\eta_i \beta \Gamma}\right) + \frac{d \ln \frac{1}{r_1 r_2}}{\eta_i \beta \Gamma} \times \frac{1}{L}. \tag{5.3}$$

Figure 5.10 shows the results of the cavity length dependent experiments for three different laser structures, emitting at 505 nm, 520 nm, and 560 nm. The differences between the lasers are small, when comparing 505 nm emission with 560 nm. But the laser diode operating around 520 nm exhibits the best characteristics. However, since that device also shows a higher operating voltage, an additional thermal index guiding, which leads to a seemingly higher quantum efficiency and lower threshold, cannot be ruled out [12]. Especially, the high internal quantum efficiency of 99% together with the very

Laser wavelength [nm]	η_i [%]	α_i [1/cm]	$\frac{\beta}{[(\text{cm} \times \mu\text{m})/\text{kA}]}$	
505	67	3.5	21.3	148.8
520	99	1.4	10.6	163.9
560	64	5.1	15.3	55.3
GaAs	65	12	50	4.5

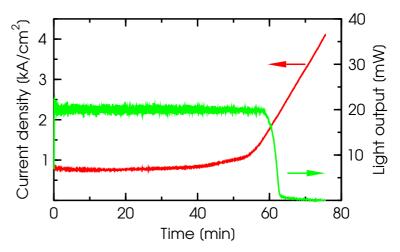
Table 5.1: Laser parameters obtained from Fig. 1.2 and typical values for GaAs/AlGaAs lasers, taken from Ref. [9].

low internal absorption of only 1.4 cm⁻¹ supports this presumption. Also, it should be noted that the the quantum efficiency is generally subject to a strong scattering, due to the limitations of the experimental setup. Nevertheless, the laser parameters obtained for all ZnSe-based lasers are comparable to those obtained for conventional III-V laser, as Tab. 5.1 shows. It also reveals that the highly lattice mismatch quantum well, in case of the 560 nm emission, does not degrade the principle laser design quality. On the other hand, the higher optical quality of the device is not reflected as well. This indicates that the laser parameters itself, listed in Tab. 5.1, mainly depend on the design of the structure, i.e., layer thicknesses and band gap differences, and at the present stage of experimental capabilities they do not depend much on the material quality. They indeed only serve as a figure of merrit for the *principle design*. The influence of the *material quality* on these parameters can only be detected in large-scale tests, i.e., when many devices – fabricated with reproducible processing technology and tested under identical conditions – are characterized and evaluated statistically. With single-shot measurements on a few devices, this is not possible.

5.6 Degradation

In the last section of this chapter the stability of laser diodes with an emission around 560 nm is investigated. An exemplary lifetime measurement of such device in pulsed-

Figure 5.11: Lifetime measurement of a laser diode with a quantum well, optimized for an emission around 560 nm, in pulsed-mode at a constant output power of 20 mW. The pulse width is 1 μ s at a duty cycle of 0.1%.



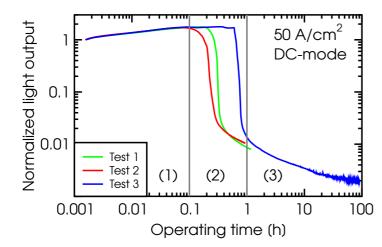


Figure 5.12: Constant current degradation tests of lasers with emission wavelengths around 560 nm. The different devices were all operated at 50 A/cm². For the three different stages (1)–(3) of the experiment, cf. text.

mode is shown in Fig. 5.11. Despite the low duty cycle of 0.1% and the high quality of the laser structure established in Sec. 5.4, the device lives only just about 1 h. This – for the long-wavelength devices typical – short lifetime is far below that of the conventional laser diodes (cf. e.g. Fig. 2.18). Based on the results of Sec. 5.4, the most serious problems of ZnSe-based laser diodes in terms of lifetime limitation can be ruled out: the threshold current density, the p-side contact performance, and quantum well efficiency are all satisfactory. This singles out the highly strained quantum well as primary reason for the fast degradation.

In order to investigate the influence of the strained quantum well in more detail, constant current experiments were performed as shown in Fig. 5.12. The time-evolution of the emission intensity can be divided into three different phases. All curves in common, is an initial increase of the emission intensity by almost a factor of 2 in phase (1) – presumably due to defect annealing [265, 230]. This phase of increasing intensity directly goes over to a drastic decrease of intensity in the second stage, phase (2). Such a change can occur rather abruptly, as seen for the first measurement in Fig. 5.12. In phase (2) the output power drops within a few minutes of operation by almost two orders of magnitude. Such behavior is not expected for a purely REDR-based degradation mechanism, as described in Chapter 3. At the end of this phase the device still emits light. Now, the degradation process moves on to the third phase (3), during which the intensity decreases only slowly with a time constant of less than t^{-1} .

One possible explanation for the unusual time-evolution of the output power is a relaxation of the highly strained quantum well. As described in Sec. 3.4.2, a red-shift of the emission is expected in this case. Therefore, in a second experiment the light output was also spectrally resolved.

Figure 5.13 shows the result of this experiment. On the left-hand side the uncommon three-staged time-evolution is reproduced, on the right-hand part of the figure the position of the maximum intensity of the emission spectrum is depicted. During phase (1) a small red-shift of the emission wavelength is observed. The transition into phase (2) is characterized by a strong blue-shift of the emission. At the end of phase (2) the blue-shift amounts to about 4 nm. In phase (3) the blue shift seems to continue, however, the signal strength is quite low and the emission spectra become noisy.

From Fig. 5.13 one can conclude that the intensity does not decrease due to a direct relaxation of the strain in the quantum well, but rather due to a strong out-diffusion of

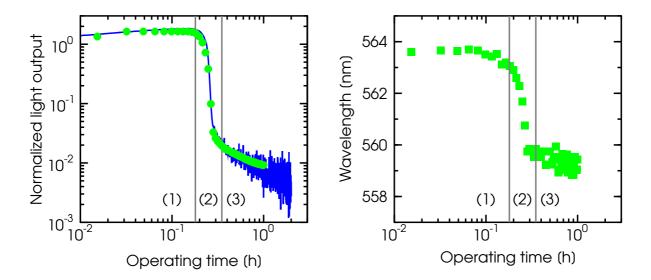


Figure 5.13: Change in light output intensity and emission wavelength during a constant current test, conducted on a laser diode with a highly strained quantum well. Left: emission intensity. The straight line is the recording of the optical multimeter, the symbols represent the integrated intensity of the emission spectrum. Right: wavelength position of the maximum intensity.

Cd. It should be noted, that the degree of blue-shift is comparable with the one observed in the similar experiment on a conventional laser diode, described in Sec. 3.4.2. The results of both experiments together indicate that the addition of S to the quantum well material indeed stabilizes the crystal lattice, since no significant red-shift of the emission wavelength – which would be a sign of relaxation – is observed. However, this interpretation has to be verified by other experimental techniques. Here, high-resolution XRD measurements could be an appropriate method. Secondly, one has to state that the strain in the quantum well is removed by an out-diffusion of Cd. A potential countermeasure against this diffusion process can be the use of strain-compensating ZnSSe barriers with high S content, as described in Sec. 3.5.3.

5.7 Summary

The optimization of the growth conditions of CdZnSSe enables the fabrication of quantum wells with high Cd contents, and good optical and morphological quality. These quantum wells are suitable as active region in ZnSe-based laser structures and do not deteriorate the structural integrity of the device – despite a high lattice mismatch to the GaAs substrate. Thus, electrically pumped laser emission in the spectral region around 560 nm from a semiconductor laser diode was realized for the first time. Due to the growth optimization, the devices exhibit superior optical quality, which results in a record output power of more than 1.1 W in pulsed-mode. Operation in cw-mode was also verified. The design of the laser structures has not been optimized yet, and offers potential for improvement. From a high-reflectivity facet coating a reduced threshold current density can be expected, whereas a lower band gap of the cladding layer material can reduce the serial resistance in the device. Thus, lower operating voltages and

Chapter 5: Exploring the limits and possibilities of Cd-rich quantum wells

a reduced heat load is possible. By using strain compensating ZnSSe barrier layers the out-diffusion of the Cd – which at present limits the device stability – can eventually be slowed down. This measure should increase the reliability significantly. Meanwhile, a further investigation on the degradation process is necessary, in order to clarify the mechanism of the fast degradation. Here, a combination of serval experimental techniques, including XRD topography, PL, and TEM should be used to characterize the out-diffusion process. Also, in an EL topography experiment, it should be checked, whether the generation of dark defects occurs and if there are differences as compared to the conventional structures.

Chapter 6

An alternative approach: CdSe quantum dots

The research on ZnSe-based heterostructures at the *Institut für Festkörperphysik der Uni*versität Bremen is not limited to quantum well laser diodes presented in this thesis so far. Right from the installation of the semiconductor heteroepitaxy group, investigations on the fabrication and growth mechanisms of self-organized CdSe quantum dots have been a second key activity. The motivation for the research is to develop a new active region for ZnSe-based laser diodes which is less susceptible to defects and exhibits a higher stability under current injection – quantum dots offer such an alternative. However, the experimental realization of self-organized grown CdSe quantum dots proves to be difficult as K. Leonardi has documented in his Ph.D. thesis [180]. A key problem that prevents the use of these quantum dots in electrically pumped laser diodes is the massive generation of stacking faults. This problem was systematically investigated by T. Passow, and by optimizing the growth conditions as well as by designing an appropriate barrier material, laser diodes with CdSe quantum dots become possible [6]. This chapter is focused on the electro-optical characterization and device properties of such a laser structure¹. The credit for the design and growth of the active region of this device mainly belongs to T. Passow, whereas the rest of the laser structure corresponds to the standard laser structure investigated so far. Thus, it is possible to directly compare the characteristics of quantum well and quantum dot lasers. But before these results will be reported, a short overview over quantum dot lasers in general and the growth of CdSe quantum dots in particular and the problems connected herewith will be given.

6.1 Quantum dot laser

The active region of modern semiconductor laser diodes consists of light producing material with only a few nanometer thickness, embedded into material of higher band gap energies². Due to this heterostructure design, the carriers are not only confined to the active region but also restricted in their movement. In a quantum well this restriction occurs perpendicular to the junction plane – a two-dimensional system is created. A

¹Part of the results presented in this chapter have been published in Refs. [323, 324, 325].

²High-power laser diodes are an exception, since their special purpose requires a large volume of active material and consequently thicker active regions.

quantum dot is a system which also restricts the carrier movement inside the junction plane, i.e., in all spatial directions. Such a system is called a *zero-dimensional* system – ideally, the carriers are fully localized in the quantum dot. This complete confinement gives rise to a spectrum of discrete energy levels and sharp optical transitions – hence, a quantum dot is also called an *artificial atom* [326]. Due to these discrete energy levels the density of states is small – in an ideal case delta-function-like. Also, such a system has a small gain spectrum and together these effects result in a laser threshold that does not depend on the temperature [31]. Other advantages are a lower threshold current density, mainly due to a reduced lateral carrier diffusion, higher gain, and better operational characteristics under signal modulation, i.e., in pulsed operation, necessary in communication electronics [327]. Finally, it is expected that an active region of quantum dots is less susceptible to defects due to a simple consideration: if a defect crosses a quantum well, the whole quantum well is affected, but if it hits a quantum dot, only that one is affected – the other dots remain undisturbed.

Without the development of a suitable semiconductor epitaxy technology, the advantages of quantum dots would have remained purely theoretical or at best subject of basic research. Given their extremely small size of a few nm³, many quantum dots are necessary to fabricate a useful device. In order to exploit the superior operational characteristics of a quantum-dot-active region, these dots must all have the same size and form. Also, the fabrication process has to be simple and mass-production capable. Thus, quantum dot fabrication processes based on lithography and subsequent etching are ruled out. The epitaxial growth of semiconductor material with different lattice constants provides the solution. For certain material combinations, a self-organized growth of quantum dots is observed [80]. With a moderate lattice mismatch between substrate and layer, the layer growth is first nucleated in a two-dimensional growth. Above a critical thickness of a few ML, three-dimensional island formation sets in. In a certain layer thickness regime, the strain in these islands is relaxed without the formation of crystal defects. Furthermore, the islands exhibit only a small size fluctuation and lateral ordering to a certain degree. Such a growth mode is referred to as Stranski-Krastanov. If the band gap of the layer material is lower than that of the substrate, a carrier confinement occurs in the islands – the islands form quantum dots. On the other hand, if the lattice mismatch between layer and substrate is too high, a complete three-dimensional growth is observed (Volmer-Weber) – usually accompanied by massive defect generation. A more detailed description of the different growth modes can be found in Refs. [31, 180].

Using a Stranski-Krastanov-like growth mode, it is relatively easy to fabricate structures with a high density of quantum dots and a low size fluctuation, which makes the realization of a quantum dot laser possible. In the case of conventional III-V semiconductors, quantum dots based on the material combination InAs/GaAs are well established. Most theoretically predicted advantages of quantum dot lasers could be verified in this system. An instructive overview of the self-organized growth of such InAs/GaAs quantum dots and their application to laser diodes the can be found in Ref. [328].

6.2 Self-organized growth of CdSe quantum dots

In the II-VI material system the combination CdSe/ZnSe has some similarities to the III-V material system InAs/GaAs, as Fig. 6.1 illustrates. Namely, both material combinations have a similar lattice mismatch of about 7% and a comparable band gap energy difference. Furthermore, the band alignment gives a type-I discontinuity, i.e., both – electrons and holes – are confined. But whereas in the III-V material system InAs/GaAs the growth of quantum dots is well established, a similar standard fabrication process for II-VI quantum dots based on CdSe/ZnSe yet remains to be developed. Several groups report different experimental approaches, such as growth on (110) oriented GaAs substrates, thermal activation during a growth interruption, or low-temperature deposition by MEE with subsequent thermal annealing [329, 330, 331]. It was found that one key element of the formation of CdSe quantum dots is a sufficient surface migration, thus the MEE growth mode was chosen in Bremen, since this growth mode offers the highest flexibility concerning surface migration [332].

Despite the similarities to the InAs/GaAs system, no Stranski-Krastanov growth mode is observed during the deposition of CdSe on ZnSe [180]. Surface diffusion coefficients and bond strengths – parameters which also affect the growth – are different and lead to differences in the quantum dot formation. A transition from a two-dimensional to a three-dimensional growth is indeed observed above a critical thickness of about 2–2.5 ML, but it is accompanied by a strong stacking fault formation, indicating that no quantum dot formation by the Stranski-Krastanov growth mode occurs [333, 334, 335]. Nevertheless, quantum dot formation without defect generation can be obtained by segregation enhanced CdSe reorganization. Here, the CdSe must be overgrown by Zn(S)Se using MEE, where Zn and Se (and S) are deposited alternately [336]. This leads to a low growth rate and alternately ex-

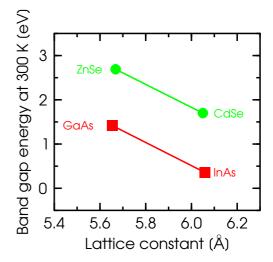


Figure 6.1: Bandgap energy vs. lattice constant diagram to illustrate the similarities between the material combinations InAs/GaAs and CdSe/ZnSe.

tremely group-II and group-VI rich conditions, which stimulates the quantum dot formation [337]. During this process, CdSe intermixes with ZnSe, so that the quantum dots always consist of ternary CdZnSe with a high Cd concentration and are embedded in ternary CdZnSe with a lower Cd concentration. The height and width of the quantum dots were found to be about 1.2 nm and 7 nm, resp., by high-resolution TEM [338]. The typical density of dots obtained by this growth process is on the order of $10^{10} - 10^{11}$ cm⁻² [339, 180].

That such structures indeed provide a three-dimensional localization, could be verified in PL measurements on structured samples. In standard PL experiments always many quantum dots are probed. Due to the size fluctuation of the dots, the single sharp emission lines from the individual dots have slightly different emission energies and typically a broad PL signal is obtained. By reducing the size of the excited area, less

dots are probed and it becomes possible to resolve the individual signals. For etched mesa structures of 60 nm side length, single localized excitons are visible – giving evidence for quantum dot formation. The width of such a single line is below 0.4 meV (limited by the experimental setup) [339, 180]. An additional confirmation of the quantum dot formation is obtained from time-resolved measurements of the PL emission of such structures, where a greatly enhanced decay time of the emission intensity, caused by the three-dimensional confinement, was found [337].

6.3 CdSe quantum dot stacks as active region

When incorporating CdSe quantum dots into a laser diode structure, the design of the active region containing the quantum dots requires special attention. It is mandatory to obey the boundary conditions for device-quality material – otherwise the laser diode will not work. The most important point is that the active region and its growth process does not degrade the rest of the structure. It was shown in Sec. 3.5.1 that the MEE growth mode is suited for a laser structure intended to produce a real device. However, strain relaxation via generation of stacking faults easily occurs for CdSe/ZnSe quantum dots as mentioned above. This problem is aggravated by the fact that a single sheet of quantum dots does not contain enough luminescence centers required for an efficient laser diode – the confinement factor (describing overlap between optical wave and gain medium) is too small. Therefore, a stacking of quantum dot sheets is required, through which the density of dots in the active region can be increased. By itself, the stacking of quantum dots increases the complexity of the structure and the growth – with the high tendency of CdSe to relax the strain by stacking faults, it becomes impossible without additional measures [328, 85].

Since the high lattice mismatch and the accumulation of strain is the main driving force for the stacking fault generation, a solution of this problem is provided by strain-compensating barrier layers [316, 85]: the CdSe quantum dot sheets are embedded into ZnSSe spacer layers with a high S content. Thus the spacers are tensile strained, and in principle a net strain-free system of quantum dots and spacers can be realized [340]. A more detailed description of the problem of stacking fault generation during the growth of CdSe quantum dots, and the experimental technique of strain compensation to avoid this formation, as well as an in-depth investigation on the mechanisms of CdSe quantum dot formation itself, can be found in Ref. [6].

6.3.1 Design of the active area and structural characterization

The active region of the quantum dot laser structure reported in this chapter consists of a fivefold quantum dot stack, containing nominally 1.9 monolayer CdSe per sheet embedded into 3.5 nm thick strain compensating ZnSSe layers to prevent the formation of stacking faults. This active region as a whole is embedded into the well-known conventional ZnSe-based laser structure introduced in Chapter 2.

No significant differences between the quantum dot laser structure and quantum well laser structures were found in those tests of the standard characterization scheme, which are not directly influenced by the active region. This observation holds in particular for the electrical characteristics, i.e. ECV and j/V. Nevertheless, the XRD mea-

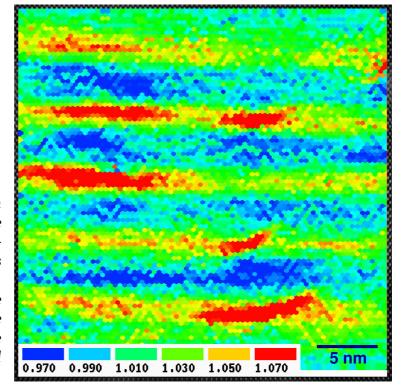


Figure 6.2: High-resolution TEM micrograph of the quantum dot stack. The superimposed DALI image reveals composition fluctuations. Bright (dark) areas indicate a high Cd (S) content. The key denotes the relative lattice constant (TEM image and DALI analysis by R. Kröger).

surement reveals, that this is not entirely true for the crystalline perfection. Although the structure is still fully strained, a significant diffuse background, that indicates the presence of misfit dislocations in the structure, is observed around the layer signals – the structure exhibits signs of a beginning relaxation, caused by the quantum dot stack. Despite this observation an EPD of only 560 cm⁻² was counted.

In order to verify the formation of quantum dots as well as the presence of structural defects in the sample, a piece was investigated by high-resolution TEM. The samples were prepared by R. Kröger using mechanical grinding followed by Xe ion-milling to electron transparency. A Philips CM20/UT operating at 200 kV with a point resolution of 0.19 nm was used for these investigations. Since this high resolution enables the imaging of the crystal lattice on an atomic scale, a *digital analysis of the lattice image* (*DALI*), was performed after the recording of the micrographs. Thus the positions of single atoms³ on the crystal lattice are visible. A comparison of the atomic positions in the region of the quantum well/quantum dot layer with the atomic positions of the barrier material by means of a reference lattice allows the calculation of the local lattice constant, which is directly related to the local composition by Vegard's law⁴ (Eq. 1.26 in Sec. 1.3.4). Thus, composition variations can be visualized on an atomic scale. Details concerning this method can be found in Refs. [342, 338, 271].

Figure 6.2 shows a filtered cross sectional lattice image of the quantum dot stack of the laser diode with the resulting DALI image superimposed. It indicates the variation of the local lattice parameter due to the composition fluctuation by color-coding. The bright contrast originates from the CdSe layers. The fivefold stack is clearly visible.

³or better atom rods in the direction of the electron beam

⁴However, such a TEM sample has to be extremely thin. Therefore an elastic relaxation can occur during sample preparation, thus, an exact calculation of the composition is not possible – DALI can only give an estimation [341].

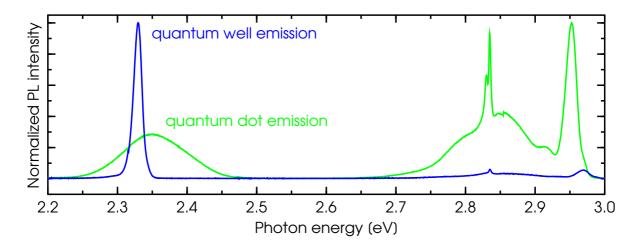


Figure 6.3: Low-temperature PL from the quantum dot laser. The PL spectrum of a quantum well laser emitting in the same spectral region is also shown for comparison. Both lasers emit around 2.3 eV. The signals from the spacer layers and the cladding layers in the range between 2.8–3.0 eV are also shown.

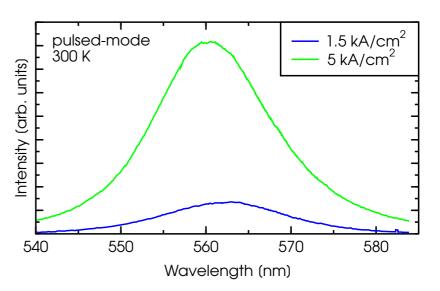
Within each layer composition fluctuations can be seen, resulting in areas of strong localization. The diameter and hight of these quantum dots is 5–10 nm and 1 nm, resp., indicating a rather strong size fluctuation. An estimation of the Cd content from the relative lattice constants yields at least 49% Cd in the quantum dots itself and at least 6% in the sourrounding quantum well. The average S content in the spacer layers is at least 20%. The TEM investigation together with the DALI analysis confirms the formation of CdSe quantum dots in the stack.

In the course of the TEM investigations no intrinsic structural defects were found, which confirms, that the diffuse background of the XRD mapping is indeed not caused by a full (or partial) relaxation of the structure, but rather just by the onset of it.

In Fig. 6.3 the low-temperature PL spectrum of the quantum dot laser (in the following referred to as *dot laser*) is shown. The emission is around 2.34 eV at 8 K, which corresponds to an emission around 560 nm at room-temperature. As mentioned before, the only difference of the dot laser is the active region. Thus, it is possible to study the effects of the additional confinement by comparing its characteristics with that of a conventional quantum well laser diode. Given an expected emission around 560 nm, the devices introduced in the previous chapter are the natural choice for this comparison. Accordingly, the characteristics of the dot laser will be compared to that of those quantum well lasers (short: *well laser*) in the following. Hence, the PL spectrum first shown in Fig. 5.5, is again plotted in Fig. 6.3, confirming that both structures emit at the same energetic position. In contrast to the sharp emission from the well laser, the emission from the quantum dots is broader (110 meV) and of gaussian shape. This is once more a sign of the quantum dot formation – albeit with a rather strong size fluctuation.

The quantum dot laser was also characterized in optical pumping experiments by K. Sebald of the *Semiconductor Optics* group of the Institut für Festkörperphysik (Prof. Gutowski). Above an excitation energy of 70 kW/cm² an enhancement of the PL intensity was found at low temperatures (10 K) [343]. The maximum modal gain of 400 cm⁻¹ at this temperature was obtained at a pump power of 960 kW/cm². Up to 100 K the dot

Figure 6.4: Electroluminescence spectra from the dot laser under pulsed current injection at room-temperature (0.1%, 100 ns). This is the first time that electroluminescence is obtained from CdSe quantum dots.



laser exhibits only a weak temperature dependence of the laser threshold. Typically, the threshold j_{th} of a semiconductor laser diode varies with the temperature T according to [10]

$$j_{th} = j_0 e^{\frac{T}{T_0}}. (6.1)$$

Thus, the temperature stability of the laser structure can be expressed in terms of the characteristic temperature T_0 , where higher values of T_0 indicate a lower temperature sensitivity. In the before mentioned optical pumping experiments a T_0 of 1260 K was measured up to 100 K and 95 K for higher temperatures [343]. These values are comparable or even higher than those of III-V quantum dot lasers and indicate a strong localization of the carriers in the quantum dots – at least for low temperatures [31, 328].

6.3.2 Electroluminescence

Most papers concerning CdSe quantum dots motivate the work with the idea to use such dots as active region in a device emitting in the green spectral region. Despite this key motivation – and the meanwhile advanced optical characterization of CdSe quantum dots – electroluminescence has not been reported so far [344, 345, 346]. There exists only one report in the literature that comes close to this, however, in that particular paper fractional-monolayers of CdSe were studied as active region [261, 347]. This fractional-monolayers form large CdSe-based islands (15–40 nm), but they are not yet quantum dots. More adequately, this system is described as a quantum well with strong thickness and composition fluctuations [348, 347].

Consequently, Fig. 6.4 shows the first electroluminescence spectrum from a light emitting structure based on CdSe quantum dots [340]. Clear emission around 560 nm at room-temperature is measured as predicted. For these test the device is operated in pulsed-mode, however, DC current injection is also possible. It should be noted that the devices were operated at a high current injection level in order to record the spectra. These high driving currents are necessary because the emission intensity from the device – and therefore the efficiency – is low. Hence, no lasing could be realized with the standard pulsed current source, which has an upper current limit of 500 mA.

Even below threshold, the dot laser exhibits some unusual characteristics. First, a blue-shift of the emission with increasing driving current is observed in Fig. 6.4. Since the effect is reversible, it cannot be connected to degradation, e.g., a Cd outdiffusion or other structural changes. In general, a shift of the emission wavelength with increasing current density can be explained by a change of the carrier density inside the active region. At low injection levels, i.e., at a low density of carriers, a renormalization of the band edges due to carrier interaction dominates. This leads to an emission red-shift [7]. With increasing carrier density in the active region, higher energy states are filled, which results in a blue-shift of the emission [217]. Whereas these processes explain the emission characteristics of quantum well laser diodes quite satisfactory, it is not so obvious, if these concepts can be directly transferred to quantum dot laser diodes [202]. First, it is questionable whether the concept of band edges is justified for such structures, since only discrete energy levels are allowed in a three-dimensional confined system. Assuming the easiest model of a quantum dot, i.e., a particle in a box of side-length L_z and with infinitely high barriers, the quantum mechanical treatment allows the calculation of the discrete energy levels,

$$E_n = \frac{\hbar^2}{2m^*} \left(\frac{n\pi}{L_z}\right)^2$$
 with: $n = 1, 2, 3, ...$ (6.2)

Therefore, the energetic position of the ground state inside the dot primarily depends on the size L_z . In a real system, the energetic position of the states obviously depends also on the barrier height, i.e., on the dot/barrier system. Since the distance between individual dots is larger than the dot size itself, one would not expect a strong interaction between the different dots, and thus a change of the ground state energy and the observation of a band edge renormalization is rather unlikely. Secondly, the existence of higher energetic states inside a CdSe quantum dot could not been proven directly so far in PL experiments. Only indirect signatures of such higher states were observed in photoluminescence excitation (PLE) experiments [349, 345]. Hence, also band filling, resp. dot filling processes are questionable.

Another explanation for the blue shift is based on the rather broad size distribution of the dots inside the laser structure. Obeying Eq. 6.2, larger dots have a lower ground state energy. Accordingly, one can assume that those dots are filled first. With increasing current density more carriers are injected into the system and smaller dots will be filled. Thus, the emission shifts to higher energies, i.e., a blue shift is observed.

The emission characteristics of the dot laser do not only depend on the injection current level. Additionally, a strong dependence on the pulse width of the applied current is found, which is illustrated in Fig. 6.5. On the left-hand side of the figure, the change of the emission wavelength is plotted vs. the driving current. For 100 ns-short pulses, the above described blue-shift of the emission occurs. However, with increasing pulse width the degree of blue-shift is reduced and finally a red-shift occurs. Both shift-effects act independently, and both effects cancel each other at a pulse width of 400 ns, resulting in a nearly constant emission energy in the accessible current range. Given the high current densities necessary to measure the spectra, it is justified to explain the red-shift by local heating in the device – even at the low duty cycle of 0.1%. This assumption is supported by the fact, that the degree of red-shift scales with the pulse width, as indicated by the increasingly longer emission wavelength with longer pulses for a given current density, which can also be seen on the left-hand side of Fig. 6.5.

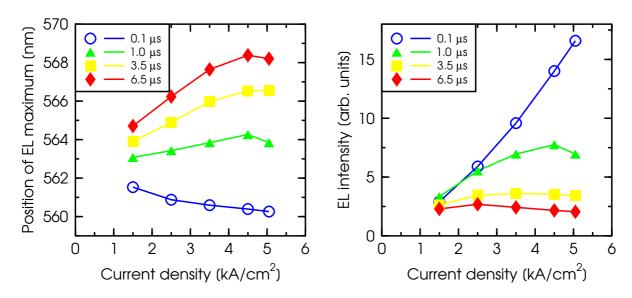


Figure 6.5: Influence of the driving conditions on the electroluminescence of the quantum dot laser (duty cycle 0.1%). Left: shift of the emission wavelength with driving current for various pulse widths. Right: integrated intensity of the emission maximum for the same measurements.

The right-hand part of Fig. 6.5 shows the change of the emission intensity during these measurements. Only for the short pulses (100 ns) a monotonous increase of the intensity with driving current is detected. This is accompanied by a decrease of the emission width. However, for longer pulses this effect is reversed. Here, the intensity increases only weakly, and even decreases at high current level – only the emission FWHM increases monotonously. In fact, the total light output of the device for longer pulse widths is less than for short pulses. Again, the underlying mechanism for this effect is not fully understood at present. A widely discussed problem concerning quantum dot lasers and their dynamics is the so-called *phonon bottleneck* [350, 351, 352]. This problem arises from the question, if the carrier relaxation into the discrete ground state of the quantum dot is slowed down due to the lack of phonons that are needed in order to satisfy the energy conservation rule. In that case, the efficiency of the laser is severely degraded, and the problem manifests itself stronger for higher carrier densities inside the active region. Accordingly, the decreasing efficiency of the dot laser with increasing pulse width and current density might be an indication of such a phonon bottle neck problem. However, that would indicate that the time scale of the phonon bottleneck problem is on the order of a few hundred ns, which is too high for usual carrier dynamics [353]. A more plausible reason for the decreased efficiency – and accordingly decreased emission intensity – is the massive local heating which fits to the observed red-shift.

Although the underlying physical mechanisms and processes that give rise to the unusual emission dynamics and driving current dependency are not yet fully clarified and understood, one important conclusion can already be drawn: electrically pumped lasing from this device can only be realized with high driving currents above $5~\rm kA/cm^2$ due to the overall low efficiency and for short pulses – preferably below 100 ns.

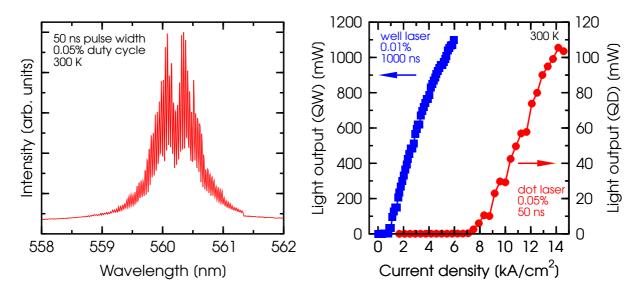


Figure 6.6: Lasing characteristics of the quantum dot laser. Left: laser spectrum recorded in pulsed-mode. Right: L/j-characteristics for quantum dot and quantum well laser (pulsed-mode; well: 1 μ s, 0.01%; dot: 50 ns, 0.05%).

6.4 Lasing operation

Using a current source with a higher current limit, an *Agilent* 8114A, electrically pumped lasing form the CdSe quantum dot laser is possible, which is shown in Fig. 6.6 [354]. On the left-hand part of the figure the lasing spectrum of the device is depicted. Special driving conditions are necessary, typically, lasing of the dot laser is obtained for pulse widths around 30–90 ns, here 50 ns were chosen. As for comparison, lasing of the well laser is obtained in the full possible pulse width range from 9 ns to cw-operation. The emission wavelength of the dot laser is around 560 nm with a threshold current density of 7.5 kA/cm².

A typical L/j characteristic is shown on the right hand part of Fig. 6.6. The comparison with the well laser shows that the threshold current density is one order of magnitude higher. Despite this high threshold, a maximum output power of more than 100 mW per pulse can be obtained from the dot laser. The device in Fig. 6.6 can be operated with up to 14 kA/cm², other devices with higher thresholds sustained even more than 20 kA/cm². In general, the threshold current density of the dot laser varies quite drastically across the processed wafer, ranging from 7 to 14 kA/cm² and is accompanied by a rather low external quantum efficiency of 8–15%.

By itself, the high threshold current density is not exactly a satisfying result, however, the fact that these devices could be operated under such high current densities at all is promising. In fact, such high injection levels have never been reported before for ZnSe-based devices operated at room-temperature (cf. Tab. 1.3). This indicates a surprising stability of the ZnSe-based material against high current injections, and gives hope for devices with a long lifetime – if the threshold current density can be reduced to the typical values of quantum well lasers.

The unusual dynamical behavior found in Sec. 6.3.2 is also present in operation above threshold as shown in Fig. 6.7. Here, the pulse width dependence of the light output of the dot and the well laser are compared under identical pulsing conditions

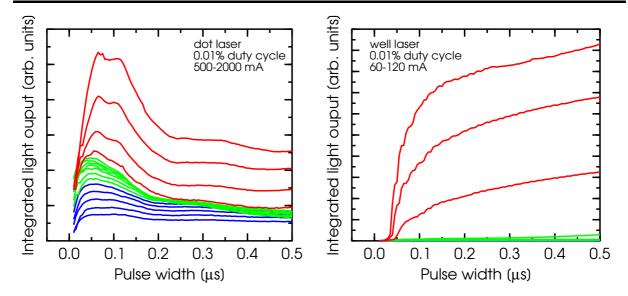


Figure 6.7: Pulse width dependence of the light output of quantum dot (left) and quantum well laser (right) under different driving currents at a fixed duty cycle. For the dot laser operation with more than 1700 mA implies lasing (upper four curves), the well laser threshold is around 90 mA (upper three curves show lasing).

and at the same constant duty cycle. The experiment is conducted at different driving current levels, below and above threshold. It is clearly seen that the dot laser provides a high light output – and in particular lasing – only at the short pulse widths between 50–150 ns. Again, it has been verified that these effects are not related to degradation. Furthermore, the curve exhibits a double-peak structure in lasing mode. In how far this is an indication of a sort of resonance remains to be investigated.

The well laser shows a different dynamical characteristic, where an intensity increase is seen after an initial delay of about 10 to 20 ns. This delay is well know from III-V and also ZnSe-based laser diodes and is attributed to internal Q-switching[355, 9, 12]. The monotonous increase with increasing pulse width may be due to an increased conversion efficiency caused by an additional refractive index step along the current path, induced by heat[12, 266].

Obviously, the dynamical behavior and the high threshold current density are the most serious problems of the dot laser. An improvement of the structure should concentrate on improving the efficiency. A simple calculation reveals a possible ansatz for this: the density of dots per sheet is on the order of 10^{11} cm $^{-2}$; given a diameter of 10 nm per dot and a stacking of 5 sheets, the percentage of the total area covered with active material is: 10^{11} cm $^{-2} \times \pi \left(\frac{10}{2} \times 10^{-7} \text{ cm}\right)^2 \times 5 = 0.39$, i.e. less than 40% of the current injection area produces light. Consequently, the overlap between optical wave and active material is also smaller, giving rise to a higher lasing threshold. However, the factor of 5, introduced into the calculation due to the dot stacking, is an upper limit, that only takes effect in case of a perfectly anti-correlated positioning of the dots in vertical direction. On the other hand, the high-resolution TEM micrograph of Fig. 6.2 clearly shows, that the vertical position of the dots is correlated to a certain degree, i.e., the dots tend to be formed on top of each other. Consequently, in the actual laser structure, significantly less than the calculated 39% of the pumped area contains active material. Thus,

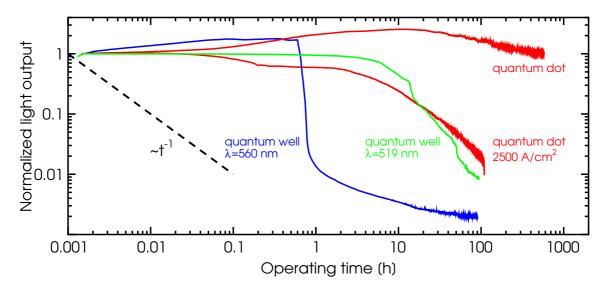


Figure 6.8: Constant current degradation experiment performed on well and dot laser structures under DC current injection. Standard operation is at 50 A/cm^2 . In order to achieve comparable light output powers, the quantum dot laser was also operated at a current density of 2.5 kA/cm^2 . To avoid the problem of a highly strained quantum well and a premature degradation related to that, a degradation experiment on a conventional well laser emitting at 519 nm is also shown.

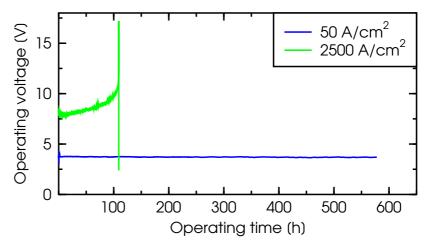
increasing the volume of active material – either by inserting more CdSe sheets or by increasing the dot density in the individual sheet – should lead to a threshold reduction. A further threshold lowering can be expected form a device with a smaller quantum dot size distribution. Last but not least, it should be recalled, that the XRD characterization revealed the onset of a relaxation in the structure. Although no increased defect density was observed by EPD counting or TEM studies, misfit dislocations are present in the structure. These defects give rise to an increased non-radiative recombination which also contributes to the increased laser threshold. Again, improvements of the design and the growth of the quantum-dot-active region are necessary.

6.5 Degradation

Due to the high threshold current density, the lifetime of the dot laser in pulsed-operation above threshold is limited to a few minutes. A comparison with the well lasers is hence not very meaningful at this stage. It is more useful to compare the degradation behavior below threshold and under constant current injection. The result of such an experiment at different current levels, together with the result from the quantum well laser emitting around 560 nm are shown in Fig. 6.8.

Under a low injection current density of 50 A/cm² the dot laser exhibits an astonishing stability. In fact, after a pronounced increase of the light output, the intensity just started to drop after 20 h, but even after more than 500 h, the initial light output was not yet reached. The test was stopped at that point, since a further blocking of lab was not tolerable. Compared to the well laser, it lives at least more than two orders of magnitude longer at this current density. However, it was described before that the well laser

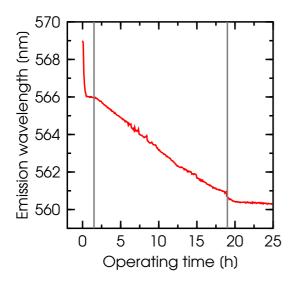
Figure 6.9: Evolution of the operating voltage of the quantum dot laser during the constant current degradation experiments shown in Fig. 6.8. The devices were operated in DC-mode.



emitting around 560 nm suffers from the highly strained quantum well. Therefore, the degradation curve from a conventional quantum well laser at 50 A/cm² is also shown in Fig. 6.8. Even compared to that device the lifetime of the dot laser is significantly higher. In fact, from the shape of the curve it is obvious, that at the end of the test, the long-term behavior at 50 A/cm² has not set-in for the dot laser, yet. In order to verify, whether the dot laser is subject to a different degradation mechanism, i.e., not based on a REDR process, an additional test was performed at a significantly higher current density. This higher injection level was chosen according to two requirements: a) a comparable light output, since at 50 A/cm² the output power of the dot laser is two orders of magnitude lower as compared to the well lasers, and b) a faster degradation, so that the long-term behavior can be investigated. Both boundary conditions are observed at a current density of 2.5 kA/cm², and the result is also shown in Fig. 6.8. First, it is observed that the long-term behavior is indeed now recorded. It follows the t^{-1} -like behavior, that is characteristic for the REDR-based degradation, thus, one can conclude that the CdSe quantum dots are also subject to point-defect-related degradation. Despite the extremely high current density of 2.5 kA/cm² in DC-mode, the device lives for more than 100 h. This result by itself is surprising and has not been thought possible for ZnSe-based devices before. Furthermore, although initially a fast decrease of the emission intensity is observed, in the long-run the device lives even longer, resp. has a higher light output, than the conventional quantum well laser.

Finally, Fig. 6.9, where the operating voltage during these times is plotted vs. the time, reveals that the degradation of the dot laser at this high current density is at least partly related to the degradation of the electrical characteristics – namely the p-side contact. Whereas at 50 A/cm^2 no change in operating voltage is noticeable during the entire experiment span of almost 600 h, at 2.5 kA/cm^2 the voltage increases slowly in the first 3/4 of the test. In the last part this increase accelerates drastically and, finally, the device cannot sustain the massive heat generation any longer. This indicates that the contacts in principle are stable enough to support even high current injection levels, however, under such conditions the long-term stability needs to be improved. At low injection levels the p-side electrodes are not the lifetime limiting factors (at least up to 600 h of operation).

A spectrally resolved constant current experiment was also performed on the dot laser. For the test shown in Fig. 6.10, the device was operated at 2 kA/cm². On the left-



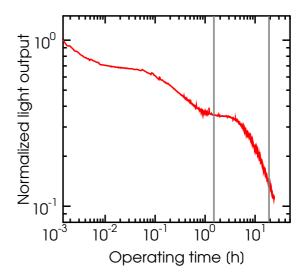


Figure 6.10: Spectrally resolved constant current degradation experiment of the dot laser, conducted at 2 kA/cm^2 . Left: evolution of the emission wavelength during the test. Right: normalized intensity vs. time with double-logarithmic scaled axes. For a better comparison of both graphs, two times have been marked by a line.

hand side of the figure, the shift of the emission wavelength during the course of the measurement is depicted. After an strong blue shift during the first hour of operation, the wavelength shift goes over into a linear blue shift between 2 h and almost 20 h. During the whole experiment, the emission shifts by about 9 nm, which is quite high as compared to the similar measurements reported in Chapter 3. On first sight, this hints to a strong Cd diffusion inside the structure. However, in case of quantum dots, this is not the only possible explanation for an emission wavelength shift. Since the emission energy of the quantum dots depends on the dot size, a shift can also occur, if the radiative recombination occurs in dots of a different size. This would imply, that the dots degrade during current injection, so that different dots start to dominate the emission, or that the dot size itself is changed. Both effects are not necessarily related Cd out-diffusion. To clarify this question, a TEM investigation on a sample before and after operation is highly desireable.

The right-hand side of Fig. 6.10 shows the evolution of the normalized light output. Again, a t^{-1} -like behavior is observed. In Fig. 6.10 the linear blue-shift of the emission cannot be directly related to a similar change of the emission intensity evolution. Furthermore, both test under high current injection (Fig. 6.8 and 6.10) exhibit pronounced steps of the intensity-decrease. The reason for this is unclear at the moment. From Fig. 6.10, one can only conclude that it is connected to a different blue-shift velocity, i.e., a different Cd diffusion coefficient. In that sense, this behavior is similar to that of the quantum well lasers with highly strained quantum wells, shown in Fig. 5.13.

6.6 Outlook

The realization of the first electrically pumped quantum dot laser based on CdSe quantum dots leads to a variety of new and interesting questions. Since this lasing was only

realized close to the end of the experimental work of this thesis, those questions can merely be posed now. The answers have to be developed in following projects. Nevertheless, some important conclusions can already be drawn at this point.

First, electrically pumped lasing is possible. It occurs at an emission wavelength around 560 nm for this particular structure. But in principle, other emission wavelengths should be possible, too. The main factor here is the size of the quantum dots and the amount of deposited CdSe. In fact, most of the published work on CdSe quantum dots covers emission energies around 2.4 eV at low temperatures, giving rise to room-temperature emission wavelengths around 540 nm.

So far, the devices suffer from a high threshold current density. An improvement is expected from several different measures, which are mainly connected to the growth process. Especially, a higher density of dots in the device and a smaller size distribution is necessary. Also, the XRD measurements indicate, that the structural quality can be improved further. Under these circumstances, the unusual dynamics of the dot laser under pulsed current injection might by identified as purely caused by massive local heating. Otherwise, the underlying physical mechanisms have to be identified, in order to also achieve lasing at longer pulses or even in cw-mode.

The surprisingly high stability of the dot laser – especially under high current injection levels – justifies the hope, that more reliable laser diodes based on ZnSe are possible. If the threshold current density can be reduced to the values common for quantum well lasers, fascinating new possibilities arise, and degradation studies might become less important. In the meantime however, it is important to investigate this degradation process in more detail. The first tests indicate – again – a dominating role of Cd and its tendency to diffuse.

Summary and conclusion

The foundation of this work are semiconductor laser diodes fabricated from the II-VI material system based on ZnSe. In these structures, an extremely thin layer of the quaternary alloy CdZnSSe – the quantum well – forms the light producing region. It is the design of this active region, that primarily determines the characteristics of the device – in particular the emission wavelength. Using CdZnSSe with varying compositions, it is possible to tune the emission wavelength of the laser diodes within the full blue-green region of the visible spectrum.

The research on electrically pumped ZnSe-based laser diodes started in 1990, after the development of a reliable *p*-type doping technique. In Bremen, at the Institut für Festkörperphysik, the work on these devices started in 1996 with the installation of the MBE system. By the time this thesis was begun, the most basic problems connected to the growth and the design of such devices were already solved in the framework of several Ph.D. thesises. However, reliable operation – especially in cw-mode – was still rather a question of luck than of careful growth parameter calibration. Here, the establishment of a standard procedure to calibrate the growth parameters, together with the development of a set of standard growth recipes for all common MBE-growth-procedures, proved to be a successful measure for improving the reproducibility of experimental results.

In the same fashion, a standard laser structure and characterization scheme was developed. Given the enormous complexity of a SCH laser structure (a double heterostructure with separate confinement for carriers and optical wave), only a complete characterization of the structural, optical, electrical, and opto-electrical properties of the laser structure allows the correlation of measured effects with design parameters. Especially, for the operation above the laser threshold, the choice of a suitable set of driving conditions requires special care, since several boundary conditions must be observed, in order to ensure a good comparability – even between record-performing and mediocre samples. This standardization process illustrates that the research on ZnSebased devices has left the initial stage of a mere "prove of concept", but has now entered a phase, where detailed studies of material properties, layer design, or new processing technologies become possible – using the laser structure as an experimental tool. Concerning this aspect, it is also instructive to study the appendix of this thesis, where the results of some external co-operation partners – obtained from laser structures grown in the framework of this thesis – are reported.

The major topic that imbues all chapters is the limited stability of the devices under current injection. In the investigations on the degradation process, it was found that this instability is directly related to the stability of the active region, i.e., the CdZnSSe quantum well. During operation, one observes a decreasing efficiency of the device, which is

caused by the generation of dark defects inside the quantum well. Whereas it was not possible to investigate the specific microscopic structure of these dark defects directly, the major degradation mechanism could still be identified. It turned out that the degradation is promoted via recombination enhanced defect reactions (REDR) – processes in which defects are activated, resp. produced, by the non-radiative recombination of carriers at the site of an already existing defect. In these processes, point defects play a major role, but pre-existing extended defects, such as stacking faults, greatly enhance the generation velocity. Using constant current degradation test – conducted under DC current injection and below the laser threshold – it could be confirmed that the recombination of an electron and a hole does not directly create a defect. Furthermore, by monitoring the light output with a spectrometer, it was also found that Cd plays a major role in the REDR-based degradation. It is the strong tendency of Cd to diffuse, that limits the quantum well stability.

In investigations on the driving forces of the degradation process, no significant contribution of the *p*-type doping was observed – contrary to some literature reports. On the other hand, the compressive strain of the Cd-containing quantum well, resp. the high Cd amount itself, has a much stronger influence. Without additional experiments, it is not possible to name which of both factors is responsible – at present, Cd diffusion and high strain resemble the two different faces of the same coin. Based on these findings, several approaches to improve the stability of the active region were investigated. Whereas different growth techniques – such as a MEE growth mode or a low-temperature growth – did not produce a better device stability, a different layer design led to some promising results. Here, the CdZnSSe quantum well was sandwiched between two tensile strained ZnSSe layers with a high S content, in order to produce a three-layer-system which is on average strain-free. Although a general growth problem prevented a new record cw-lifetime, a drastically increased stability was observed during constant current degradation experiments.

Besides these structural driving forces, a third – extrinsic – one could be identified. Since the degradation mechanism exhibits a diffusion-like character, it is not surprising that it is significantly accelerated by heat. Massive generation – or just the accumulation – of heat reduces the lifetime drastically. On the other hand, by a careful optimization of the driving conditions – namely pulse width and duty cycle – the influence of the heat can be minimized, thus enabling operation with high output-powers and relatively high lifetimes. Under these conditions a new degradation mechanism was observed: the occurrence of catastrophic optical damage (COD) at the laser facets. This process is related to a destruction of the facets during a thermal-runaway process, caused by a high light output power. Whereas COD is a well-know degradation mechanism in conventional III-V laser diodes (and at present their lifetime limiting factor), such process has not been reported for ZnSe-based laser diodes before.

The intrinsic parameters – and especially the density of point defects – of the laser structure are determined during growth. In order to improve the device stability by external measures, more advanced processing technologies were developed in co-operation with external partners. One major task was to develop a better heat management for the device. Under current injection, most of the heat is generated in the *p*-side of the structure. An efficient heat management has to by-pass the active region for the heat removal. The standard technique to achieve this is to mount the device with the epitaxial side facing downwards onto the heat sink. Such a top-down mounting tech-

nique was developed and successfully tested, however, the experimental difficulties connected to it inhibited that top-down mounting became part of the standard device processing sequence. Here, the main problems are connected to the small size of the laser chip on the one hand, and the problem to avoid a short-circuit, on the other hand. Nevertheless, an improved metalization scheme including a Ti intermediate layer, as well as a reproducible technique for pelletizing a laser bar into single chips, were obtained as by-product of the top-down mounting development. Similarly, a method for facet coating was developed in the framework of a Diploma thesis. The results obtained from that work led to a reduction of the threshold current density of the devices by roughly 30–40%, which in turn should give a better lifetime due to a reduced operating current.

In the last part of the thesis, the potential and limits of CdZnSSe as active material in laser diodes was explored in terms of maximum Cd content and emission wavelength. This particular research was motivated by the idea to fabricate a suitable light source for optical data communication networks which employ plastic plastic optical fibers (POF) as transmission medium. Since these POFs have their transmission loss minimum around 560–570 nm, the transmission range of such fibers could be improved by using a light source that matches those characteristics. Although the fabrication of a CdZnSSe alloy with the appropriate Cd content is not a problem per se, it was a priori not clear, whether such highly lattice mismatched material can be employed in a laser structure without degrading the structural quality. It turned out that the optimization of the growth conditions is the key point for the fabrication of such lasers. Only by providing stoichiometric growth conditions, it is possible to incorporate the necessary Cd amount. These growth conditions also lead to a very high optical quality with sharp emission and high efficiency. Due to the optimization process, laser diodes emitting at 560 nm could be fabricated. This is not only the first time that laser light in this particular region was obtained from an electrically pumped semiconductor, but the devices could also be directly operated in cw-mode. In addition, a record output power of more than 1.1 W was obtained in pulsed-mode – among the highest output powers ever obtained from a ZnSe-based laser diode. Unfortunately, the stability of the devices seem to be limited by the highly strained quantum well, giving rise to a fast degradation during operation. The maximum possible Cd content is reached in those structures.

Finally, in close co-operation between the individual research projects of the working group, a completely new approach for the active region of ZnSe-based laser diodes could successfully be realized. The development of a growth technique to deposit stacks of CdSe quantum dots without the massive generation of stacking faults – in the framework of a different Ph.D. thesis – enabled the fabrication of the first electrically pumped quantum dot laser based on the II-VI material system. Again, an emission around 560 nm was obtained. However, being the first device ever to show electroluminescence at all, many questions arise from this new design. First, one has to note a relatively low efficiency, that gives rise to extremely high threshold current densities on the order of several kA/cm². This might be caused by the rather small total volume of active material. Also, these high operating currents give rise to massive local heating. This might explain an unusual dependence of the electroluminescence – in terms of wavelength and intensity – on the pulsing conditions, namely the pulse width. Whereas the high threshold current densities prevent a long lifetime – and even lasing with pulses longer than 100 ns – a surprisingly high stability of the device is observed in constant current

degradation experiments below threshold. In fact, under comparable current injection levels, the quantum dot laser lives at least two orders of magnitude longer than the quantum well laser. At a 50 times higher current level – which is necessary for a comparable light output – the quantum dot laser is still more stable. Actually, under these extreme operating conditions (current density $2.5 \, \text{kA/cm}^2$ in DC-mode) the *p*-contact is the stability-limiting factor.

Investigating ZnSe-based laser diodes, one is often faced with the question, whether such work is still necessary and useful, given the overwheeling success of GaN-based light emitters and laser diodes. In fact, the results from this thesis quite obviously demonstrate, that the lifetime of ZnSe-based devices is the crucial problem. Nevertheless, it also shows that the lifetime is the *only* problem. More precise, with exception of the lifetime, each and every single parameter of the devices is at least comparable – sometimes even better – than for conventional III-V laser diodes and definitely much better than for GaN-based laser diodes (especially concerning threshold and operating voltage). Furthermore, one should keep in mind that only ZnSe-based lasers have successfully produced laser light in the green region of the visible spectrum. Achieving this with alternative semiconductor material systems will be difficult. Therefore, as soon as true-blue emitting semiconductor lasers become available, the interest in ZnSe-based lasers will resparkle – enabling the realization of flat-panel, laser TV screens, and monitors. Therefore, it is definitely sensible and even mandatory to conserve the knowledge on ZnSe-laser obtained so far.

In addition to that, open questions still remain. First of all, more detailed studies on the precise degradation mechanism, as well as the role and type of the involved point defects, are needed. Here, the combination of electroluminescence, XRD topography, PL measurements, and a concluding TEM investigation is highly desireable. Given the experimental possibilities available at the Institut für Festkörperphysik, the Universität Bremen can extend its competence and consolidate its leading position in this field of research. Such studies should especially concentrate on the role of Cd and the Cd diffusion. Thus, it might be possible to develop new experimental approaches to inhibit, resp. slow down, this diffusion. Here, the use of strain compensating barriers definitely needs more attention. In connection with an optimization of the growth conditions – namely the flux ratios during quantum well growth, as Sony reported – the stability should improve significantly.

On the other hand, it will be difficult to push the cw-lifetime record into new regions⁵. The processing experience and possibilities in Bremen are not developed enough for this – after all, it is still an university-based research. For this, co-operations with external industrial partners are necessary.

Finally, a lot of work remains to be done on the quantum dot lasers with CdSe. The most pressing problem is obviously to reduce the threshold current density of the device. Then, it can be judged, whether such a device is indeed more stable and the usual dynamics can be investigated in more detail – if they are not purely related to the strong heating. Further improvements can also be expected from an advanced processing, such as ridge-waveguide, coated facets, and top-down mounting. Nevertheless, the first results are not only very promising, but even give hope, that a commercial laser diode based on ZnSe will be possible.

⁵... which is not necessarily convenient. Concerning the every-day research, it is definitely easier and much more practical to test devices with cw-lifetimes on the order of several hours.

Appendix A

Externally processed devices

Some of the laser structures grown during the experimental work of this thesis were also made available to external research groups. The technological experience and possibilities of these co-operation partners allowed to apply novel processing technologies or device processing concepts to ZnSe-based laser structures, as it will be described in this appendix.

A.1 Ridge waveguide by ion implantation

The experiments and results reported in the following two sections were obtained in a collaboration with the Institut für Festkörperphysik of the Technische Universität Berlin. The collaboration partner of Prof. Bimberg's group were M. Straßburg and O. Schulz. In the framework of this thesis the TU Berlin was supplied with unprocessed wafers containing laser structures, as well as with single layers for calibration purposes. Processing and characterization of the devices was carried out in Berlin. The people involved were: M. Straßburg, O. Schulz, U. Pohl, and Prof. D. Bimberg.

A.1.1 Lateral index guiding

In Sec. 1.1 the basic theory of semiconductor lasers was introduced. Optical gain in laser diodes is provided by the carriers in the active region. Since the optical gain determines the optical mode distribution, the emission characteristics of these lasers depend on the carrier distribution in the active region. They are therefore called *gain-guided*. Gain-guiding is usually achieved by limiting the region of current injection in the device. In the simplest case this is done by defining an injection stripe on the surface of the laser diode. Most of the reported ZnSe-based laser diodes were fabricated this way. One disadvantage of this technology is that the current path is only defined at the very top of the device. Due to the sheet resistance of the semiconductor material and carrier diffusion in the active region, the current path is widened perpendicular to the injection direction. Thus, the apparent threshold current density is higher than the actual threshold, since more than the assumed active volume is pumped. This is schematically indicated in Fig. A.1(a).

The emission characteristics and beam profile of a gain-guided laser depend on the driving current. With an increasing current density in the device, the lateral confine-

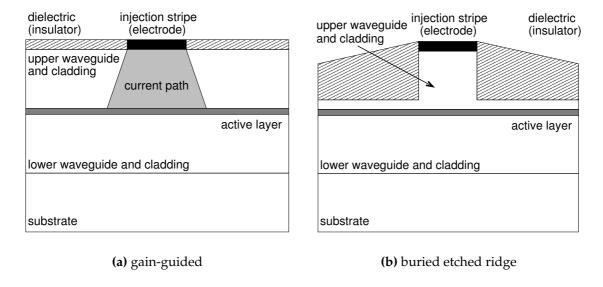


Figure A.1: Schematic cross section of conventional gain-guided (a) and buried ridge-waveguide (b) laser structures. In the gain-guided laser current spreading occurs as indicated by the shaded area.

ment changes and higher optical modes can be excited. For most applications this behavior is undesired. This problem can be avoided if a lateral *index-guiding* is introduced. In this case the lateral guiding of the optical wave is achieved by creating an additional step in refractive index along the current injection path. Since this index step is independent of the driving current, the emission characteristics of the device is less sensitive to varying injection conditions. Furthermore, the index-guiding is usually more efficient than gain-guiding and, thus, the overlap between optical wave and active region is increased. In general, a change in refractive index is realized by changing the material properties next to the injection region, e.g. by depositing a different material. It lies at hand to use an insulating material for this purpose, since so the current spreading in the device is drastically reduced. In this case, the threshold current density of the laser benefits not only from the improved lateral confinement, but also from the reduced current spreading.

There exist several different concepts to achieve index-guiding in semiconductor laser diodes. The most important one is the so-called *ridge-waveguide* structure. In the simplest case of an index-guided laser structure the current injection stripe is etched down to the *p*-type waveguide. Here, the index step occurs at the edges of the mesa, i.e., between the semiconductor and the surrounding air. Such a structure is called *etched ridge-waveguide*. A precise control of the etching process is required for a good performance of this simple structure. If the process is stopped too early, no efficient lateral guiding occurs. On the other hand, etching below the quantum well gives rise to parasitic currents across the *pn*-junction at the sidewalls [10]. Furthermore, such a structure is not planar anymore, which is disadvantageous for subsequent device processing. Therefore, the etched ridge is usually buried, as illustrated in Fig. A.1(b). In such a typical *buried-ridge* laser structure, material of a lower refractive index than the semi-conductor is deposited next to the etched ridge. ZnSe-based buried-ridge waveguide

laser diodes have been successfully realized first by the 3M research group, exhibiting a threshold current as low as 2.5 mA [117]. In this case, polycrystaline ZnS was used as burying material. However, the threshold current density was 700 A/cm^2 . Optimization of the laser structure led to a threshold current density of 460 A/cm^2 (23 mA) in cw-operation [76]. Continuous-wave-operation was also realized by the joint effort of the Purdue and Brown Universities with a threshold current density of 310 A/cm^2 [356].

More advanced variations of ridge-waveguide devices exchange the poly-crystalline burying material with single-crystalline semiconductor material. In that case, the index step - and consequently the lateral guiding - can be increased. By doping the new semiconductor with the appropriate conduction type, efficient current blocking can be maintained. The formation of such an etched-mesa buried heterostructure laser involves a complicating re-growth process for the burying material after the etching of the mesa structure. Especially, for ZnSe-based semiconductor material such a process is difficult to realize, since surface oxides have to be removed before the re-growth process is started. Whereas Se oxides are relatively easy to decompose, the Zn oxides are thermally very stable and can only be effectively removed by a hydrogen plasma treatment. This particular problem has been investigated in detail at the IFP in the framework of a Ph.D. thesis [34]. To avoid the problem of the re-growth of ZnSe-based material, Sony developed a process to grow the laser structures on pre-patterned GaAs substrates. These substrates contain a complete GaAs-pn-diode structure, where the p-type layer acts as current blocking layer for the II-VI-heterostructure. Lateral guiding is achieved by etching stripes into the p-GaAs layer, so that only the n-type GaAs remains. The threshold current density of these channelled-substrate laser diodes is 350 A/cm² without and 240 A/cm² with facet coating [126].

Other approaches to achieve lateral index guiding use different geometric structures (terraced, v-grooved, crescent) or vary the waveguide layer thicknesses. A description of the most relevant concepts can be found in Ref. [10]. However, none of them has been applied to ZnSe-based devices so far.

A.1.2 Implantation-induced disordering

So far, only methods involving mesa-etching have been presented as realizations of lateral index-guiding in laser structures. A completely different approach is to specifically modify the local material properties of the semiconductor structure so that an additional refractive-index step is obtained. Such a method avoids the etching process, thus simplifying the process technology. One way to achieve this modification is to use implantation-induced intermixing of crystals. In this method the sample is bombarded with high-energetic ions, which changes the diffusivity of the material components inside the crystal - an intermixing of the crystal takes place. Implantation is well-established for III-V semiconductor devices, where it is e.g. used for intermixing of quantum wells or super-lattices [357]. In general, intermixing leads to a different band gap energy of the material. It has therefore two main effects on quantum wells: a change in carrier confinement and in refractive index. With a laterally-structured intermixing, very effective lateral optical guiding and carrier confinement is achieved, as illustrated in Fig. A.2. The carrier confinement is further enhanced by the fact that the implantation process usually leads to semi-insulating material [77]. Apart from ion-implantation, intermixing can also be achieved by annealing in appropriate atmospheres. However,

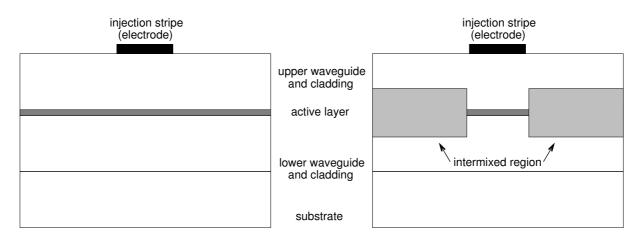


Figure A.2: Principle of lateral index guiding by ion-induced disordering. Left: standard laser structure. Right: structure after ion-implantation, which causes disordering of the quantum well region in the unprotected areas (after Ref. [77]).

the temperatures required for an effective intermixing are usually too high and lateral pattering is difficult to realize.

In the case of ZnSe-based semiconductor lasers, only few attempts have been made to obtain lateral index-guiding by intermixing. In the framework of an earlier collaboration between the TU Berlin and the Universität Bremen, diffusion-induced intermixing of II-VI heterostructures were investigated in detail, therefore, only the main points will be presented here. For further information the corresponding references should be consulted [77, 35]. It turns out, that the generation of vacancies is the main effect responsible for the crystal intermixing, since these vacancies strongly enhance the diffusion coefficient of Cd in Zn(Mg,Cd,S)Se structures [251]. It is accordingly perfectly suited for quantum well intermixing in ZnSe-based laser diodes. Although ion-implantation is an effective method to generate vacancies in the II-VI crystal, under normal implantation conditions no perfect intermixing is achieved, yet, the change in refractive index is sufficiently high for lateral index-guiding [358, 359].

A.1.3 Technological realization

Implantation-induced disordering is a fully planar process and therefore an attractive method to fabricate index-guided laser diodes. Still, some technological difficulties have to be solved. The biggest problems are obviously connected to the implantation process itself. A precise control of the implantation region is necessary in order to avoid damaging the rest of the structure. Especially, the implantation depth has to be chosen carefully. If the defects are generated in the region of the III-V/II-VI heterointerface, the device performance is drastically reduced [196]. On the other hand, efficient index guiding can only occur, if the maximum amount of vacancies is created in the direct vicinity of the quantum well such that the intermixing is as concentrated as possible. The implantation depth is controlled by the energy of the accelerated ions. For the here used low-to-moderate implantation energies, the elastic scattering of the ions at the target atoms is the main physical process. A precise calculation of the implantation depth requires a Monto-Carlo-simulation of the process, as it is exemplary shown in Fig. A.3.

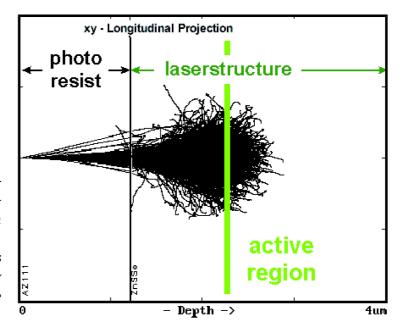


Figure A.3: Typical Monte-Carlo-simulation of an ion-implantation process. Shown are the trajectories of Ar⁺ ions inside the sample. This simulation was done by O. Schulz using the software SRIM2000 [360, 361].

In this figure the trajectories of the implanted ions inside the crystal are shown. To concentrate the disordering of the crystal in the active region, an implantation energy of 2.5 MeV for Ar $^+$ ions at a dose of 5×10^{14} cm $^{-2}$ is necessary. Ions of such energy and sufficient dose are usually not available from lab-size ion sources. Therefore, all presented implantations were carried out at the *Hahn-Meitner-Institut Berlin*.

In the experimental realization of the implantation process, the depth control by direct variation of the implantation energy is difficult. Furthermore, the required energies for the process are at the lower limit of the implantation machine [362]. Therefore, M. Straßburg and O. Schulz developed a multi-layer lithography process, where an exposed negative photo-resist layer acts as initial brake for the ions. On this photo-resist coating, the normal positive resist for defining the lateral structure is applied [360]. After the implantation process, the photo-resist layers are partly carbonized due to outgasing of the lighter resist components (in particular hydrogen). Since these layers can not be completely removed by conventional organic solvents, the resist is ashed in an oxygen plasma. During this process one has to ensure that no excessive heating of the sample occurs.

A.1.4 Results

For lateral index-guided laser structures a reduced threshold current density as compared to gain guided devices is expected. In Fig. A.4(a) the L/j-characteristics of an implanted and a conventional gain-guided device, processed from the same laser structure, are compared. For the unimplanted device the threshold current density is about $450~\rm A/cm^2$, with a differential quantum efficiency of 4.1% (20 μ m stripe width). This threshold current density is already among the best values obtained for the conventional CdZnSSe quantum well lasers reported in this work. After implantation, the threshold even decreases to $153~\rm A/cm^2$, which is only one third of the original value. Accordingly, the external quantum efficiency almost doubles to 9.6%. It has to be noted that the external quantum efficiencies for both devices are low. Whether this is due to

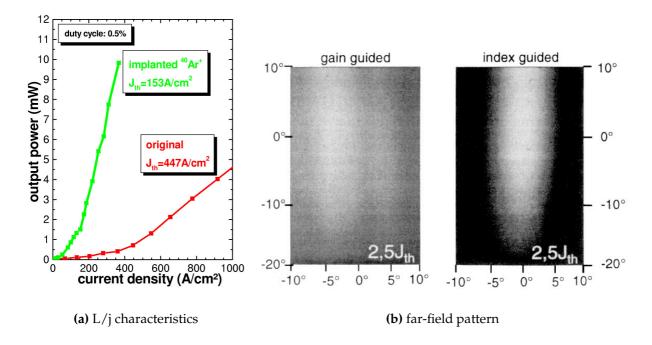


Figure A.4: (a) Comparison of the L/j-characteristics of conventional and implanted ZnSe-based laser diodes. (b) Far field pattern of the laser emission for the unimplanted and the implanted device (20 μ m stripes; graphs taken from Ref. [358]).

an not-optimized experimental setup, or related to the laser structure itself, is not clear. For laser devices from the same wafer, but fabricated in Bremen, significantly higher differential quantum efficiencies were obtained. Nevertheless, careful cross-checking of the equipment did not reveal any obvious differences of the experimental setups in Bremen and Berlin. The results reported here therefore lie in the responsibility of the Berlin group.

In any case, the same process was also applied to laser structures from Sony, here, a reduction to one third of the as-grown structure was obtained similarly, with a threshold current density of 96 A/cm² for the implanted structures [360]. Due to the reduced threshold current density the operating current of the devices is lowered and, thus, the heat load in the device decreases. Consequently, the lifetime of these laser diodes increased by a factor of two for the Sony structures and a factor of five for the structures from Bremen. It has to be noted, that for all tested devices the facets were uncoated. Therefore, even further improvements can be expected.

The positive effects of lateral index-guiding can also be found in the far-field pattern of the laser emission, as seen in Fig. A.4(b). These patterns were recorded with a CCD camera. For the unimplanted device a higher mode appears in the pattern, which is indicated by two spatially separated regions of high intensity. With increasing driving current, more modes are excited and additional stripes appear in the far-field pattern (not shown). The index-guided laser shows only one region of high intensity, which can be attributed to the fundamental TEM_{00} mode. This mode is stable and independent of the driving current as expected for index-guided devices [53].

A.2 Novel ex-situ p-side contacts

Parallel to the fabrication of the index-guided ZnSe-based laser diodes by ion-implantation, the group from the TU Berlin developed a new metalization scheme for the *p*-side electrode. As it was reported in Sec. 1.4.4, obtaining a low-resistive ohmic contact to *p*-type ZnSe is difficult. Therefore, a special epitaxial contact structure – usually a ZnTe/ZnSe multi-quantum-well – is usually deposited on-top of the laser structure. A good ohmic contact is then realized by using a Pd-containing metal contact (Pd/Au in Bremen, PdSn/Au in Berlin).

A.2.1 Idea

ZnTe – which is generally employed for the epitaxially p-side contact structure – can be highly doped p-type [90, 91]. However, this is not the case for ZnSe (cf. Sec.1.4.3) [160]. Furthermore, it was found that in contact structures containing a p-typed doped ZnTe cap-layer, the carrier concentration in the p-type ZnSe is drastically reduced [363, 364]. Whereas the early reports suspect a nitrogen diffusion to cause the carrier concentration reduction, it turned out that the main driving force is the strain, induced by the highly lattice-mismatched ZnTe cap [175, 95]. Even after optimization of the growth process and the layer sequence, the free carrier concentration on the p-side of the laser structure remains low. If the concentration can be increased, significant improvements are expected.

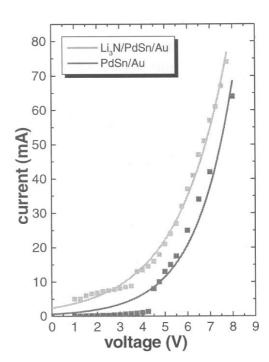


Figure A.5: *I/V-characteristics* of Li_3N -containing and conventional metal contacts (taken from Ref. [358]).

Since there are only limited possibilities to increase the carrier concentration by an *in-situ* process, one has to develop an *ex-situ* process. For this process Li is an attractive candidate. Since it is an element of the first group of the periodic table, it forms an acceptor in II-VI material. In fact, electrical characterization of *p*-type ZnSe was first realized on Li-doped ZnSe [103]. Lithium is a small atom and thus, can diffuse easily. In

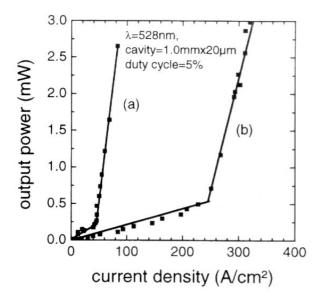


Figure A.6: *L/j-characteristics of a laser diode with Li-containing contact (a) in comparison to a conventionally processed device (b) [366].*

case of Li-doping during an epitaxial growth process, this behavior is unwanted, since it hinders the fabrication of abrupt *pn*-junctions [104]. On the other hand, the strong diffusion enables the conversion from nominally undoped ZnSe to *p*-type doped ZnSe by subsequent thermal annealing, when applied externally [365].

A.2.2 Results and discussion

For the new *ex-situ* contact, Li₃N was chosen as Li source, since pure Li is difficult to handle. Being the conventional *p*-type dopand for ZnSe, the addition of N should not have any negative influence. Furthermore, this material can be evaporated thermally, and it is compatible with the standard laser lithography process. The only difference to the standard laser process therefore is the insertion of a thin Li₃N layer between the PdSn layer and the semiconductor.

In Fig. A.5 the I/V-characteristics of laser diodes with conventional and with Li₃N-containing contacts are compared. The insertion of the Li₃N layer leads to a by ca. 1 V lower turn-on voltage, whereas the serial resistance does not change. Since the turn-on voltage is directly connected to the specific contact resistance, this indicates an improved metal-semiconductor contact, which can be attributed to either a higher doping level in the semiconductor or a lower Schottky-barrier height. To clarify this aspect, transmission-line measurements (TLM) are necessary, but these measurements require specially designed samples, which were not available.

In any case, due to the reduced operating voltage, less heat is generated in the device and a higher lifetime can be expected. It turns out, that the modified contact metalization scheme has an even more dramatic and less expected influence on the threshold current density. This is illustrated in Fig. A.6, which shows the L/j-characteristics of a conventional device and one with Li-contact. Due to the novel contact, the threshold current density is reduced by a factor of 6 from 235 A/cm² down to only 42 A/cm². The same effect was also observed for laser structures from Sony, here, a threshold current density of 30 A/cm² is measured [366]. These threshold current densities are among the best values ever obtained for semiconductor laser diodes, including conventional III-V

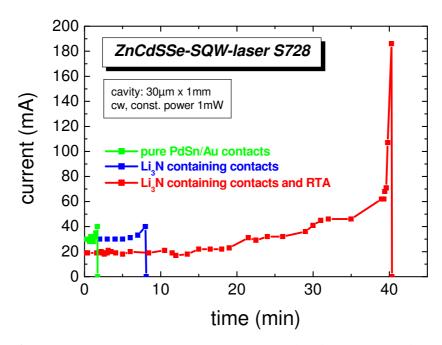


Figure A.7: Lifetime measurement in cw-operation. The devices were kept at a constant output power of 1 mW per facet. RTA indicates a rapid thermal annealing process, performed after contact deposition (graph provided by M. Straßburg).

devices, quantum dot laser diodes, and vertical cavity surface emitting laser diodes (VCSEL) – and this without facet coating or lateral index-guiding.

Naturally, the reduced threshold current density and contact resistance improves the lifetime of the devices in cw-operation considerably, as shown in Fig. A.7. Whereas the conventional metal contact gives a lifetime of less than 2 min, the Li-containing contact leads to a lifetime of more than 8 min. An annealing of the contact for 3 min at 225 $^{\circ}$ C improves the lifetime even further to more than 40 min. This is the longest lifetime ever obtained for a ZnSe-based laser diode fabricated by an university-based research team. Again, the same degree of improvement was also observed for the Sony structures (from 13 min to 9.5 h).

The remaining question is, how a new contact metalization scheme reduces the threshold current density of the laser diodes. In principle, one could argue that the reduced contact resistance leads to a reduced heat generation in the *p*-side. Since the bandgap of a semiconductor depends on the temperature, less heat would give a higher bandgap of the cladding material and, thus, an improved confinement. However, for such an effect a voltage reduction from typically 8 V down to 7 V is not enough.

The fact that the lifetime improves further after annealing gives the first indication of the mechanism, through which the threshold current density is so drastically reduced. It seems plausible that mechanism is connected to the in-diffusion of Li. This is supported by p-type doping experiments with Li $_3$ N performed by Honda et al., where an annealing step at $470\,^{\circ}$ C was employed, in order to obtain p-type conductivity [365]. Indeed, in secondary ion mass spectroscopy (SIMS) depth profiling experiments it was found that Li diffuses deep into the laser structure. But also the N concentration increases as compared to the as-grown sample. Generally, this would lead to an increased compensation of the acceptor since both – Li and N – tend to strong self-compensation [367, 157]. How-

ever, since no degradation of the electrical characteristics is found, such compensation can be ruled out. On the contrary, the improved characteristics suggest the formation of a stable Li-N complex which acts as an acceptor. In conjunction with the strong diffusion, this leads to a region of lower resistivity underneath the contact stripe and thus, an additional current guiding is realized – the structure becomes weakly index-guided, much like the well-known thermal index-guiding effect [366, 202].

A.3 Distributed feedback laser

The devices reported in this section originate from a collaboration with the Universität Würzburg. At the Institut für Technische Physik of Prof. Forchel the laser wafers were processed by M. Legge and distributed feedback lasers were fabricated. Once again, all characterization was done by the collaboration partners. The people involved were: M. Legge, G. Bacher, and Prof. A. Forchel.

A.3.1 Longitudinal mode control

For all lasers reported so far, the feedback necessary for the lasing process is realized by reflection at the cleaved facets of the laser cavity that forms a Fabry-Perot resonator. Since the cavity length is large in comparison to the wavelength of the reflected light, many longitudinal modes exist inside the cavity, and they are all subject to amplification. Such devices therefore usually do not exhibit longitudinal single-mode emission. A control of the longitudinal modes inside the laser can be achieved by modifying the feedback mechanism, e.g. by applying a frequency-selective coating to the cleaved facets. In the simplest case, this is just a high-reflectivity coating as described in Sec. 4.3, which has a broad reflectivity spectrum and does not provide single-mode control. Single-mode control can be achieved by using a *distributed Bragg-reflectors* (DBR). In such DBR lasers the Bragg reflector is realized by an periodic grating applied to the semiconductor at the two ends of the pumped region. Here, accurate wavelength control is obtained. But the use of DBR for laser diodes is not limited to this special device type. Since the degree of reflectivity only depends on the number of mirror pairs, very high reflectivities can be realized (more than 99%). Together with its high frequency selectivity, this makes DBR the primary choice to form microcavities and subsequently vertical cavity surface emitting lasers (VCSEL).

The only ZnSe-based DBR lasers reported so far were fabricated by the group from the Universität Würzburg [127, 368]. However, here single-mode emission was only obtained for short cavities and gratings with a narrow reflection band that leads to an increased threshold current density [32].

In a different concept, the modification of the feedback mechanism in the laser structure is achieved by applying the Bragg grating along the cavity. Thus, amplification and reflection of the optical wave is no longer separated in space – the feedback is distributed along the cavity length. Such a device is therefore referred to as a *Distributed Feedback* (*DFB*) laser. The emission characteristics of a DFB laser depends on the degree and the mode of coupling between grating and light wave. Since the Bragg grating provides a modulation of the complex refractive index, one can distinguish two cases of coupling: one, where the modulation of the real part of the refractive index dom-

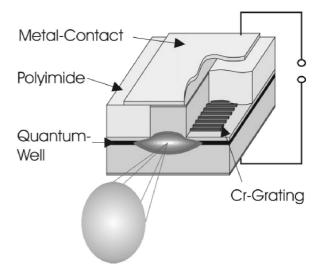


Figure A.8: Schematic view of a laterally-coupled DFB laser. The grating is applied next to etched ridge, where current injection occurs. It is burried in polymide, which is used to planarize the process (graph taken from Ref. [32]).

inates and one, where the modulation of the imaginary part dominates. In case of a real-part modulation, an *index-coupling* is obtained. Theoretical calculations reveal that with such kind of coupling, two modes with the same lowest threshold gain exist for the Bragg wavelength, which is related to the formation of the stop band [10]. Therefore, single-mode emission cannot be expected from index-coupled DFB lasers. A dominating modulation of the imaginary part of the refractive index results in *gain-coupling*. Here, the lowest threshold mode lies exactly at the center of the stop band and, thus, single-mode emission is obtained.

Fabrication of pure index- or gain-coupled DFB lasers is difficult. For example, for gain-coupling, a direct structuring (e.g. etching or implantation) of the active region is necessary, which increases the density of non-radiative recombination centers. Therefore, DFB lasers usually exhibit a mixture of both types of coupling.

Whereas DFB lasers are well-established device structures for III-V semiconductors, so far, only optically pumped ZnSe-based DFB lasers have been demonstarted [369, 370].

A.3.2 DFB laser fabrication

In a DFB laser, a periodic variation of the complex refractive index is achieved by applying a Bragg grating onto the structure along the laser cavity. Since the light wave should couple to the grating, it has to be placed so that they overlap, i.e., in the region of the waveguide or the cladding layers. In conventional III-V DFB lasers, this is realized by a two-step growth process, where first the laser structure is grown up to the layer, where the grating will be placed, then the grating is defined by etching, and finally the rest of the structure is grown. However, as mentioned earlier, for ZnSe-based devices this process is not applicable. M. Legge and his colleagues therefore concentrated on the realization of *laterally-coupled* DFB lasers [371]. In laterally-coupled DFB lasers, the grating is placed next to a ridge-waveguide [372, 373]. As indicated in Fig. A.8, the optical wave is not fully concentrated inside and beneath the ridge. In fact, the wave is very close to the transition point from the ridge to the etched part of the structure. Thus, it can couple to the Cr-Bragg grating placed onto the etched semiconductor region. Since

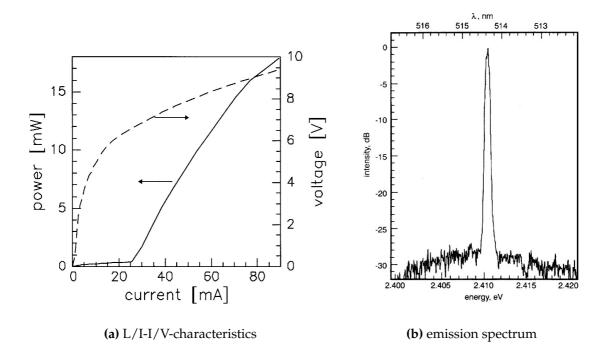


Figure A.9: Electro-optical characterization of a ZnSe-based DFB laser (graphs taken from Refs. [371, 374]).

the ridges are only 1.5 μ m small, the whole structure is filled with polyamide to protect it, and also to facilitate the fabrication of the metal contact. One clear advantage of laterally-coupled over conventional DFB lasers is, that it combines two successful concepts (ridge-waveguide and DFB) – providing a light source with lateral *and* longitudinal single-mode emission.

The performance of the DFB laser essentially depends on two parameters. First, the etch depth for the ridge fabrication has to be chosen carefully. If the etch process is stopped too early, the optical wave does not couple effectively to the grating, similar to what was reported in Section A.1.1. Another important parameter is the period of the grating. Since the grating provides the feedback for the lasing mechanism, the emission wavelength can be tuned by varying the period. However, most of the technological difficulties are connected to the grating. The Bragg condition for constructive interference – and thus the grating period Λ – is

$$\Lambda = m \frac{\lambda}{2 \, n_{\text{eff}}},\tag{A.1}$$

with m=1,2,... being the order of the grating, λ the wavelength of the laser light and $n_{\rm eff}$ the effective refractive index. For a typical ZnSe-based laser diode emitting at 510 nm, a grating period of 96 nm is necessary ($n_{\rm eff}=2.66$) [32]. Furthermore, the fingers of the grating itself have to be even smaller than the period. Such small structures can not be fabricated by conventional photolithography, instead high-resolution electron beam lithography is required.

In the actual technological realization, M. Legge used the following processing steps: first the ridge is prepared by reactive ion etching in a gas mixture of Ar and BCl₃. The

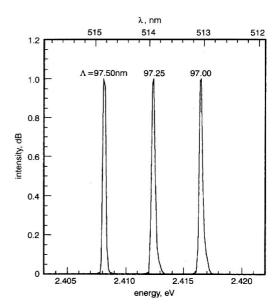


Figure A.10: Emission spectra of DFB lasers with different grating periods Λ (taken from Ref. [32]).

etching is stopped 110 nm above the upper waveguide layer to ensure effective coupling of the wave to the grating. Then a Cr grating with 15 nm-wide fingers and periods around 96 nm is applied on both sides of the ridge, by using the electron beam lithography and a lift-off technique.

A.3.3 Characterization

Figure A.9(a) shows typical L/I- and I/V-characteristics of the ZnSe-DFB laser in pulsed-operation (0.1% duty cycle and 1 μ s pulse width). From the L/I-curve a threshold current of 25 mA can be extrapolated. Up to 17 mW light output power is obtained. Considering that only a small volume is electrically pumped (1.5 μ m ridge and 840 μ m cavity length), this is a relatively high value. The quantum efficiency of the device is 29%. At threshold the operating voltage is 6.5 V. All values are comparable to ridge-waveguide devices fabricated from the same wafer. One can therefore conclude that the numerous processing steps necessary for the DFB laser do not degrade the performance of the laser structure. This is also reflected in lifetime measurements performed in cw-mode. A lifetime of 4.6 min was obtained, which is the higher than the lifetime obtained for devices processed from the same wafer in Bremen (cf. Fig. 2.16). Noteworthy for the lifetime measurement of the DFB laser is that during the test the operating voltage was below 5.12 V, which is the maximum voltage the test setup can deliver. Thereby, this structure has one of the lowest operating voltages of all laser structures grown in Bremen.

The emission spectrum of the same device above threshold ($I=1.5\times I_{\rm th}$) is shown in Fig. A.9(b). Clear single-mode emission at a wavelength of 514.4 nm for a grating period $\Lambda=97.25$ nm is visible. The appearance of only one longitudinal mode implies that the Cr grating provides predominantly a variation of the imaginary part of the refractive index – the wave is gain-coupled to the grating. The spectrum is plotted on a logarithmic intensity scale to illustrate the effective side-mode suppression characteristic for all DFB lasers. The suppression is more than 26 dB¹, which is comparable to values obtained for DBR lasers, but lower than for laterally-coupled III-V-DFB lasers [368, 373]. Here, an

¹limited by the test setup [371]

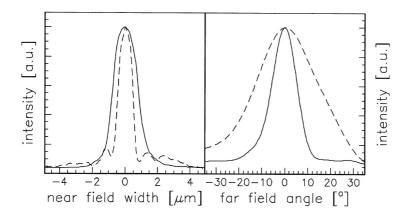


Figure A.11: Near and far field of the DFB laser in horizontal (full) and vertical (dashed) direction (graph taken from Ref. [32]).

optimization of the etch depth can lead to better coupling and thus improved side-band suppression.

In Fig. A.10 the emission spectra of different DFB laser fabricated from the same laser wafer are shown. The only difference between the devices is the period of the grating. It is clearly seen that the emission wavelength of the laser can be precisely chosen by setting the grating period to the appropriate value. Still, single-mode emission is maintained. This holds not only for first-order gratings (m = 1 in Eq. A.1), but also for second-order gratings (m = 2). For this particular laser structure the emission wavelength could be varied from 507.5 to 515 nm, which corresponds to emission energy tuning range of 36 meV. The tuning range is essentially determind by the width of the gain curve of the structure, which in turn depends primarily on the emission width of the quantum well. For this structure the full width at half maximum in low-temperature photoluminescence was about 30 meV, which fits to the tuning range for the laser wavelength.

Another attractive feature of DFB lasers is the beam quality of the laser emission. Especially, for laterally-coupled lasers a lateral single-mode emission is expected. That this is indeed the case, is illustrated in Fig. A.11 where the near- and far-field pattern of the device in horizontal and vertical direction is plotted. The width of the near-field in vertical direction is determined by the thickness of the active area and the waveguides, which is less than 250 nm. Such a small width can not be resolved with the measurement setup, the lower limit is 1 μ m. In the far-field pattern strong guiding of the wave in the waveguides leads to an increased emission angle of 35°.

In the horizontal direction the near-field has a width of 2 μ m. This is wider than the ridge itself, therefore, the wave also overlaps into the region of the grating, which is necessary for lateral coupling and the proper functioning of the DFB laser. Consequently, the far-field in horizontal direction is smaller and has an opening angle of 15°. Finally, the Gaussian shape of the field profiles indicate a lateral single-mode emission.

A.4 Short summary and outlook

The experimental results presented in this appendix nicely illustrate the potential of ZnSe-based laser diodes. More advanced device concepts can relatively easily be applied to these structures, and the expected improvements in the device characteristics are verified. Thus, a special tailoring of the device properties with respect to an specific

application is possible at an expense, comparable to conventional III-V semiconductor lasers. This observation confirms the basic result of this thesis, the only problem of ZnSe-based laser diodes is the limited device lifetime.

Concerning the insufficient stability, some new approaches were tested. Here, the development of Li_3N -containing p-side electrodes could provide an improvement. Although the underlying physical mechanism still remains to be clarified, the results obtained so far are promising. The next step now has to be the combination of all improved processing techniques. The ultimative ZnSe-based laser diode should be processed as ridge-waveguide – or even better as DFB laser – structure, with Li_3 -containing p-side electrodes, mounted epi-side down onto a special heat sink, and with high-reflectivity coating on the facets. This all – together with optimized growth conditions for the CdZnSSe quantum well – raises the hope that a stable ZnSe-based laser diode can be possible.

Appendix B

Index of laser structures

In the framework of this thesis, a total of 39 laser structures were grown. Although all reported results are obtained from lasers grown on GaAs, also 3 homoepitaxial laser diodes were fabricated. Furthermore, 4 lasers were grown as service samples for cooperation partners in Bremen, as well as for external partners. From the 39 structures, 7 were intended purely for optical experiments and are consequently undoped. The active region of most structures consists of quaternary CdZnSe quantum wells, but there are also 3 ternary CdZnSe quantum well lasers. A total of 6 quantum dot laser were grown, but only 4 different designs were tried (all fully doped). For comparison, 2 of those structures were also grown without doping. Not all of the laser samples contributed to this thesis. Table B.1 on the following page lists the relevant structures, together with some important parameters of these structures.

A complete listing of all structures can be found on the data server¹ of the Institut für Festkörperphysik . The results of all characterization measurements, as well as the growth recipes used to fabricate the samples are also stored on this server.

¹at present: mbe07.ifp.uni-bremen.de (only accessible from inside of the institute's computer network)

•	Sample	Date	λ [nm]	$E_{g,clad}$ [eV]	$E_{g,QW}$ [eV]	$j_{th}[A/cm^2]$	EPD [cm ⁻²]	Comment
	S0572	07/02/98	518	3.00	2.50	550	_	cw-lifetime 3 min
	S0599	10/05/98	503	2.94	2.56	920	320	
•	S0607	10/21/98	508	2.95	2.53	800	240	first with doped QW
	S0614	11/05/98	507	2.95	2.53	1600		-
	S0631	02/03/99	n/a	2.98	2.33	n/a		calibration laser
	S0666	05/03/99	525	3.01	2.47	500	_	calibration laser
	S0703	06/10/99	528	2.99	2.45	605	_	calibration laser
•	S0710	06/17/99	529	3.02	2.47	454	_	first with undoped
								<i>p</i> -wave guide
	S0728	07/20/99	520	3.02	2.48	600		cw-lifetime 4.5 min
	S0736	08/10/99	530	3.01	2.48	580		MEE-DA QW
	S0775	01/31/00	518	2.96	2.52	1186		calibration laser
	S0787	02/10/00	507	2.96	2.55	782		
•	S0823	03/27/00	524	2.96	2.49	1179	490	Reference for series
								S0823-S0827
,	S0824	03/28/00	520	2.96	2.49	1000	390	layer thicknesses as
								in [5] (Sony)
	S0825	03/29/00	532	2.96	2.51	n/a		LT-MEE DA
	S0826	03/30/00	519	2.96	2.50	1200	260	strain-compensating
•								ZnSSe barriers
S	S0827	03/31/00	525	2.96	2.48	n/a		LT-MEE DA, strain
								compensating ZnSSe
	S0844	05/11/00	522	2.99	2.49	600		calibration laser
	S0876	07/13/00	560	2.90	2.32	2900		Se-cracker, longest
								emission wavelength
	S0924	11/22/00	560	2.95	2.35	7300	560	quantum dot laser
	S0930	11/28/00	510	2.93	2.52	680		calibration laser
	S0939	12/13/00	557	2.97	2.33	550	1860	stoichiometric QW
	S0940	12/15/00	557	2.97	2.33	550	840	stoichiometric QW

date of growth, the lasing, resp. most intense electroluminescence wavelength λ , the band gap energy of the cladding layers $E_{g,clad}$ and quantum well $E_{g,QW}$, the threshold current density j_{th} , and the etch pit density EPD. If no electroluminescence, resp. lasing, could be obtained from the device, this is indicated by "n/a". determined for each structure. Table B.1: List of laser structures grown in the framework of this thesis. Given are the The EPD was not

Appendix C

Publications

Published papers as first author

- M. Klude, M. Fehrer, V. Großmann, D. Hommel:
 Influence of driving conditions on the stability of ZnSe-based cw-laser diodes
 Journal of Crystal Growth 214/215 (2000) 1040.

 9th International Conference of II-VI-Compound Semiconductors, Kyoto (Japan), November 1–5, 1999.
- M. Klude, M. Fehrer, D. Hommel: High-Power Operation of ZnSe-Based cw-Laser Diodes physica status solidi (a) 180 (2000) 21 3rd International Symposium on Blue Laser and Light Emitting Diodes, Zeuthen/ Berlin (Germany), March 6–10, 2000.
- 3. M. Klude, T. Passow, R. Kröger, D. Hommel: *Electrically pumped lasing from CdSe quantum dots* Electronics Letters **37** (2001) 1119.
- 4. M. Klude, D. Hommel: 560-nm-continuous wave laser emission from ZnSe-based laser diodes on GaAs Applied Physics Letters **79** (2001) 2523.
- 5. M. Klude, G. Alexe, C. Kruse, T. Passow, H. Heinke, D. Hommel: 500–560 nm Laser Emission from Quaternary CdZnSSe Quantum Wells physica status solidi (b) **229** (2002) 935. 10th International Conference of II-VI-Compound Semiconductors, Bremen (Germany), September 9–14, 2001.
- M. Klude, T. Passow, H. Heinke, D. Hommel: Electro-Optical Characterization of CdSe Quantum Dot Laser Diodes physica status solidi (b) 229 (2002) 1029. 10th International Conference of II-VI-Compound Semiconductors, Bremen (Germany), September 9–14, 2001.
- 7. M. Klude, T. Passow, G. Alexe, H. Heinke, D. Hommel:

 New laser sources for plastic optical fibers: ZnSe-based quantum well and quantum dot

laser diodes with 560 nm emission

Proceedings of SPIE 4594 (2001) 260.

SPIE Photonics and Applications Symposium 2001: Design, Fabrication and Characterization of Photonic Devices II, Singapore (Indonesia), November 27–30, 2001.

Published papers as co-author

1. H. Wenisch, A. Isemann, M. Fehrer, V. Großmann, H. Heinke, M. Klude, K. Ohkawa, D. Hommel, H. Selke:

Homoepitaxial green laser diodes grown on conducting and insulating ZnSe substrates Journal of Crystal Growth **201-202** (1999) 933.

10th International Conference on Molecular Beam Epitaxy, Cannes (Frankreich), August 31–September 4, 1998.

2. H. Wenisch, D. Hommel, A. Isemann, M. Fehrer, V. Großmann, H. Heinke, M. Klude, K. Ohkawa, H. Selke:

CW Room temperature operation of homoepitaxial ZnSe laser diodes

Proceedings 2nd International Symposium on Blue Laser and Light Emitting Diodes, Chiba (Japan), September 29–October 2, 1998.

3. M. Behringer, H. Wenisch, M. Fehrer, V. Großmann, A. Isemann, M. Klude, H. Heinke, K. Ohkawa, D. Hommel:

Growth and Characterization of II-VI Semiconductor Lasers

Festkörperprobleme/Advances in Solid State Physics 38 (1999) 47.

4. H. Wenisch, M. Behringer, M. Fehrer, M. Klude, A. Isemann, K. Ohkawa, D. Hommel:

Device Properties of Homo- and Heteroepitaxial ZnSe-based Laser Diodes Japanese Journal of Applied Physics **38** (1999) 2590.

5. M. Legge, G. Bacher, A. Forchel, M. Klude, M. Fehrer, D. Hommel: *Green emitting DFB laser diodes based on ZnSe*

Electronics Letters 35 (1999) 718.

6. H. Wenisch, M. Fehrer, M. Klude, K. Ohkawa, D. Hommel:

Internal Photoluminescence ion ZnSe Homoepitaxy and Application in Blue-Green-Orange Mixed-Color Light-Emitting Diodes

Journal of Crystal Growth 214/215 (2000) 1075.

9th International Conference of II-VI-Compound Semiconductors, Kyoto (Japan), November 1–5, 1999.

7. S. Strauf, P. Michler, J. Gutowski, M. Klude, D. Hommel:

Shallow donors in ultrathin nitrogen doped ZnSe layers - a novel or a disregarded compensation mechanism in II-VI device structures?

Journal of Crystal Growth 214/215 (2000) 497.

9th International Conference of II-VI-Compound Semiconductors, Kyoto (Japan), November 1–5, 1999.

- 8. H. Wenisch, V. Großmann, M. Klude, H. Heinke, D. Hommel: Homoepitaxial ZnSe Laser diodes: A Comparison to the Heteroepitaxial Approach 9th International Conference of II-VI-Compound Semiconductors, Kyoto (Japan), November 1–5, 1999.
- M. Straßburg, O. Schluz, U. W. Pohl, D. Bimberg, M. Klude, D. Hommel: *Lateral index guided ZnCdSSe lasers* Journal of Crystal Growth, 214/215 (2000) 1054.

 9th International Conference of II-VI-Compound Semiconductors, Kyoto (Japan), November 1–5, 1999.
- Low Threshold II-VI Laser Diodes with Transversal and Longitudinal Single Mode Emission
 Journal of Crystal Growth, **214/215** (2000) 1045.
 9th International Conference of II-VI-Compound Semiconductors, Kyoto (Japan), November 1–5, 1999.

10. M. Legge, G. Bacher, A. Forchel, M. Klude, M. Fehrer, D. Hommel:

11. O. Schluz, M. Straßburg, U. W. Pohl, D. Bimberg, S. Itoh, K. Nakano, A. Ishibashi, M. Klude, D. Hommel:

Optimized implantation induced disordering for lowering of the threshold current density of II-VI laser diodes

physica status solidi (a) 180 (2000) 213.

Berlin (Germany), March 6–10, 2000.

3rd International Symposium on Blue Laser and Light Emitting Diodes, Zeuthen/Berlin (Germany), March 6–10, 2000.

12. M. Straßburg, O. Schluz, U. W. Pohl, D. Bimberg, S. Itoh, K. Nakano, A. Ishibashi, M. Klude, D. Hommel:

Lowest threshold current densities and lifetime extension for II-VI lasers

3rd International Symposium on Blue Laser and Light Emitting Diodes, Zeuthen/

13. K. Sebald, O. homburg, P. Michler, J. Gutowski, M. Klude, H. Wenisch, D. Hommel:

Magnetooptics of trions in ZnSe/(Zn,Mg)(S,Se) single quantum wells Proceedings 25th International Conference on Physics of Semiconductors (ICPS), Osaka (Japan), September 17–22, 2000.

14. T. Passow, M. Klude, K. Leonardi, D. Hommel:

Investigations on CdSe/ZnSe Quantum Dot Stacks for the Application in Green Emitting Laser Diodes

Proceedings 25th International Conference on Physics of Semiconductors (ICPS), Osaka (Japan), September 17–22, 2000.

15. M. Straßburg, O. Schluz, U. W. Pohl, D. Bimberg, M. Klude, D. Hommel: Low threshold current densities for II-VI lasers
Electronics Letters **36** (2000) 878.

16. O. Schluz, M. Straßburg, U. W. Pohl, D. Bimberg, S. Itoh, K. Nakano, A. Ishibashi, M. Klude, D. Hommel:

Novel Contact System for II-VI Laser Diodes

42nd Electronic Materials Conference, Denver (USA), June 21–23, 2000.

17. M. Straßburg, O. Schulz, U. W. Pohl, D. Bimberg, S. Itoh, K. Nakano, A. Ishibashi, M. Klude, D. Hommel:

Index Guided II-VI Lasers with Low Threshold Current Densities 42nd Electronic Materials Conference, Denver (USA), June 21–23, 2000.

18. J. J. Davies, D. Wolverson, S. Strauf, P. Michler, J. Gutowski, M. Klude, K. Ohkawa, D. Hommel, E. Tournié and J.-P. Faurie: *Direct evidence for the trigonal symmetry of shallow phosphorus acceptors in ZnSe* Physical Review B **64** (2001) 205206.

 S. Strauf, P. Michler, J. Gutowski, M. Klude, D. Hommel, D. Wolverson, J. J. Davies: *Negatively Charged Donor Centers in Ultrathin ZnSe:N Layers* physica status solidi (b) 229 (2002) 245.
 10th International Conference of II-VI-Compound Semiconductors, Bremen (Germany), September 9–14, 2001.

20. D. Wolverson, J. J. Davies, S. Strauf, P. Michler, J. Gutowski, M. Klude, D. Hommel, H. Heinke, D. Hommel, E. Tournié, J.-P. Faurie: Displaced Substitutional Phosphorous Acceptors in Zinc Selenide physica status solidi (b) 229 (2002) 257. 10th International Conference of II-VI-Compound Semiconductors, Bremen (Germany), September 9–14, 2001.

21. J. Gutowski, K. Sebald, C. Roder, M. Klude, H. Wenisch, D. Hommel: Interplay of the Trion Singlet and Triplet State Transitions in Magnetooptical and Time-Resolved Investigations of ZnSe/Zn(Mg)SSe Single Quantum Wells physica status solidi (b) 229 (2002) 653. 10th International Conference of II-VI-Compound Semiconductors, Bremen (Germany), September 9–14, 2001.

22. G. Alexe, L. Haase, H. Heinke, M. Klude, V. Kaganer, D. Hommel: Studies of Misfit Dislocation Densities in II-VI Heterostructures by Diffuse X-Ray Scattering

physica status solidi (b) 229 (2002) 193.

10th International Conference of II-VI-Compound Semiconductors, Bremen (Germany), September 9–14, 2001.

23. C. Kruse, G. Alexe, M. Klude, H. Heinke, D. Hommel:

High-reflectivity p-type doped distributed Bragg reflector mirrors using ZnSe/MgS superlattices

physica status solidi (b) 229 (2002) 111.

10th International Conference of II-VI-Compound Semiconductors, Bremen (Germany), September 9–14, 2001.

24. M. Straßburg, O. Schulz, T. Rissom, U. W. Pohl, D. Bimberg, M. Klude, D. Hommel, K. Sato:

Characterization of Li_3N -Containing Contacts on ZnCdSSe-based Laser Diodes 10th International Conference of II-VI-Compound Semiconductors, Bremen (Germany), September 9–14, 2001.

25. O. Schulz, M. Straßburg, T. Rissom, S. Rodt, L. Reissmann, U. W. Pohl, D. Bimberg, M. Klude, D. Hommel, S. Itoh, K. Nakano, A. Ishibashi:

Operation and Catastrophic Optical Degradation of II-VI Laser Diodes at Output Powers Larger than 1 W

physica status solidi (b) 229 (2002) 943.

10th International Conference of II-VI-Compound Semiconductors, Bremen (Germany), September 9–14, 2001.

- 26. S. Strauf, P. Michler, M. Klude, D. Hommel, G. Bacher, and A. Forchel: *Single photons from individual nitrogen atoms in a semiconductor* Physical Review Letters, submitted (2002).
- 27. T. Passow, M. Klude, C. Kruse, K. Leonardi, R. Kröger, G. Alexe, K. Sebald, S. Ulrich, P. Michler, J. Gutowski, and D. Hommel:

 On the Way to the II-VI Quantum Dot VCSEL

 Festkörperprobleme/Advances in Solid State Physics, submitted (2002).

Other publications related to this work

- 1. M. Nägele, D. Hommel, M. Klude, C. Falldorf: Bericht zum Kooperationsprojekt Aufbau- und Verbindungstechnologie für Laserdioden March 5, 2001.
- 2. D. Hommel, S. Figge, M. Klude: Lichtquellen für das 21. Jahrhundert Impulse aus der Forschung, Universität Bremen, Nr. 2/2001.
- 3. *Germany: Green CdSe laser is electrically pumped* Opto & Laser Europe 10/2001, p5.
- 4. *Semiconductor Lasers: Zinc selenide diodes go into the green* Opto & Laser Europe 11/2001, p15.
- 5. *Emitters match plastic optical fiber* Laser Focus World 12/2001, p20.

Presentations

1. M. Klude, H. Wenisch, M. Fehrer, V. Großmann, K. Ohkawa, D. Hommel: *Optimierung von Kontakten zu p-ZnSe*Oral presentation at the 62. Physikertagung der Deutsche Physikalischen Gesellschaft, Regensburg (Germany), March 23–27, 1998.

2. M. Klude, H. Wenisch, M. Fehrer, V. Großmann, M. Behringer, K. Ohkawa, D. Hommel:

Optimierung von Kontakten zu p-Zinkselenid

MBE-Workshop, Hamburg (Germany), September 21–22, 1998.

3. M. Klude, H. Wenisch, M. Fehrer, V. Großmann, M. Behringer, K. Ohkawa, D. Hommel:

Optimization of Contacts to p-ZnSe

Oral presentation at TASC, Prof. Franciosi's group, Trieste (Italy), 1998.

4. M. Klude, H. Wenisch, M. Fehrer, V. Großmann, M. Behringer, K. Ohkawa, D. Hommel:

Optimization of Contacts to p-ZnSe

Oral presentation in the Gemeinsames Seminar des Institutes für Festkörperphysik, Bremen (Germany), 1998.

5. M. Klude, M. Vehse, M. Fehrer, M. Behringer, P. Michler, J. Gutowski, D. Hommel: *Degradation studies in ZnSe-based laser diodes*

International Workshop on Advances in Growth and Characterization of II-VI Semiconductors, Würzburg (Germany), April 14–16, 1999.

6. M. Klude:

Neue Ergebnisse an ZnSe Laserdioden

Oral presentation in the seminar of the working group, Bremen (Germany), 1999.

7. M. Klude, H. Wenisch, M. Fehrer, V. Großmann, D. Hommel:

ZnSe-Based Laser Diodes – Current Status and Future Projects

Oral presentation at the Intensivseminar of the Institut für Festkörperphysik, Universität Bremen, Rietzlern (Austria), September 20–25, 1999.

8. M. Klude, M. Fehrer, V. Großmann, D. Hommel:

Influence of driving conditions on the stability of ZnSe-based cw-laser diodes Poster presentation on the 9th International Conference of II-VI-Compound Semiconductors, Kyoto (Japan), November 1–5, 1999.

9. M. Klude, M. Fehrer, V. Großmann, D. Hommel:

Influence of driving conditions on the stability of ZnSe-based cw-laser diodes
Oral presentation at the Institute for Materials Research, Tohoku University, Prof. Yao's group, Sendai (Japan), 1999.

10. M. Klude, H. Wenisch, M. Fehrer, V. Großmann, D. Hommel:

ZnSe-Based Laser Diodes – Current Status and Future Projects

Oral presentation at Bremen-Rostock-Seminar, Universität Rostock (Germany), 1999.

11. M. Klude, H. Wenisch, M. Fehrer, V. Großmann, D. Hommel:

ZnSe-Based Laser Diodes – Current Status and Future Projects

Oral presentation at the Institut für Festkörperphysik, Technische Universität Berlin, Prof. Bimberg's group, Berlin (Germany), 1999.

12. M. Klude, M. Fehrer, D. Hommel:

High-Power Operation of ZnSe-Based cw-Laser Diodes

Oral presentation on the 3rd International Symposium on Blue Laser and Light Emitting Diodes, Zeuthen/Berlin (Germany), March 6–10, 2000.

13. M. Klude, M. Fehrer, D. Hommel:

High-Power Operation of ZnSe-Based cw-Laser Diodes

Oral presentation at the Institut für Mikroelektronik, Mikromechanik und Mikrooptik, Prof. Wenke's group, Hochschule Bremen, Bremen (Germany), 2000.

14. M. Klude, M. Fehrer, J. Müller, D. Hommel:

Electro-Optical Characterization of ZnSe-Based Laser Diodes

Oral presentation at the Esprit Workshop Practical Blue and UV Laser Diodes (PBULD), Trieste (Italy), May 22–24, 2000.

15. M. Klude, G. Alexe, C. Kruse, T. Passow, H. Heinke, D. Hommel:

New Light Source For Plastic Optical Fibers: 560 nm Emission From ZnSe-Based Laser Diodes

Oral presentation at the 65. Physikertagung der Deutsche Physikalischen Gesellschaft, Hamburg (Germany), March 26–30, 2001.

16. M. Klude, T. Passow, G. Alexe, C. Kruse, H. Heinke, S. Figge, T. Böttcher, D. Hommel:

ZnSe-Based Laser Diodes for the Spectral Region between 55(0) and 560 nm Oral presentation at the Intensivseminar of the Institut für Festkörperphysik, Universität Bremen, Drochtersen (Germany), June 6–8, 2001.

17. M. Klude, G. Alexe, C. Kruse, T. Passow, H. Heinke, D. Hommel:

ZnSe-Based Laser Diodes for the 560 nm Spectral Region

Oral presentation at the 59th Device Research Conference (DRC), University of Notre Dame (USA), June 25–29, 2001.

18. M. Klude, G. Alexe, C. Kruse, T. Passow, H. Heinke, D. Hommel:

500–560 nm Laser Emission from Quaternary CdZnSSe Quantum Wells

Invited Talk on the 10th International Conference of II-VI-Compound Semiconductors, Bremen (Germany), September 9–14, 2001.

19. M. Klude, T. Passow, H. Heinke, D. Hommel:

Electro-Optical Characterization of CdSe Quantum Dot Laser Diodes

Late news poster on the 10th International Conference of II-VI-Compound Semiconductors, Bremen (Germany), September 9–14, 2001.

20. M. Klude:

Degradation studies on ZnSe-laser diodes: Constant current degradation
Oral presentation in the seminar of the working group, Bremen (Germany), 2001.

21. M. Klude, T. Passow, and D. Hommel:

Comparison of ZnSe-based quantum well and quantum dot laser diodes emitting at 560 nm Poster presentation on the Conference on Lasers and Electro-Optics (CLEO), South Beach (USA), May 19–24, 2002.

Award

• Young Author's Award of the Tenth International Conference on II-VI-Compounds, awarded for the the contributed paper: 500–560 nm Laser Emission from Quaternary CdZnSSe Quantum Wells

Bibliography

- [1] Lenkungskreis Optische Technologien für das 21. Jahrhundert, Deutsche Agenda Optische Technologien für das 21. Jahrhundert, VDI-Technologiezentrum, 2000.
- [2] T. Mukai, S. Nagahama, T. Yanamoto, M. Sano, in *Proc. of the 4nd Int. Symp. on Blue Laser and Light Emitting Diodes*, Cordoba, Spain (2002).
- [3] R. M. Park, M. B. Troffer, C. M. Rouleau, J. M. de Puydt, M. A. Haase, Appl. Phys. Lett. 57, 2127 (1990).
- [4] K. Ohkawa, T. Karasawa, T. Mitsuyu, J. Cryst. Growth 111, 797 (1991).
- [5] E. Kato, H. Noguchi, M. Nagai, H. Okuyama, S. Kijima, A. Ishibashi, Electron. Lett. 34, 282 (1998).
- [6] T. Passow, *Untersuchungen zur Bildung selbstorganisierter CdSe/Zn(S)Se-Quantenpunkte*, Ph.D. thesis, Universität Bremen, Institut für Festkörperphysik, 2002.
- [7] W. W. Chow, S. W. Koch, M. S. Sargent III, *Semiconductor-Laser Physics*, Springer-Verlag, Berlin, Heidelberg, 1994.
- [8] H. C. Casey, M. B. Panish, *Heterostructure Lasers—Part A: Fundamental Principles*, Academic Press, New York, San Francisco, London, 1978.
- [9] H. C. Casey, M. B. Panish, *Heterostructure Lasers—Part B: Materials and Operating Characteristics*, Academic Press, New York, San Francisco, London, 1978.
- [10] G. P. Agrawal, N. K. Dutta, *Semiconductor Lasers*, Kluwer Academic Publishers, Bosten/Dordrecht/London, 1993.
- [11] Bremer Institut für Angewandte Strahltechnik (BIAS), http://www.bias.de, 2001.
- [12] M. Ozawa, A. E. A. Ishibashi, Sol. State Comm. 94, 87 (1995).
- [13] H. Yoshida, Y. Gonno, K. Nakano, S. Taniguchi, T. Hino, A. Ishibashi, M. Ikeda, S. L. Chuang, J. Hegarty, Appl. Phys. Lett. 69, 3893 (1996).
- [14] S. M. Sze, Physics of Semiconductor Devices, John Wiley & Sons, 1981.
- [15] P. Michler, M. Pereira Jr., O. Homburg, L. Nerger, J. Gutowski, H. Wenisch, D. Hommel, in *Proc. of the 2nd Int. Symp. on Blue Laser and Light Emitting Diode*, edited by K. Onabe, K. Hiramatsu, K. Itaya, Y. Nakano, Chiba, Japan, 528–531 (1998).
- [16] P. Michler, M. Vehse, J. Gutowski, M. Behringer, D. Hommel, M. F. Pereira Jr., K. Henneberger, Phys. Rev. B 58, 2055 (1998).
- [17] A. Dießel, *Blau-grüne Halbleiterlaser auf der Basis von Zinkselenid*, Ph.D. thesis, Universität Bremen, Institut für Festkörperphysik, 1996.
- [18] M. Vehse, *Mechanismen der stiumlierten Emission in II-VI-Halbleiterlaserstrukturen*, Diploma thesis, Universität Bremen, Institut für Festkörperphysik, 1997.
- [19] O. Homburg, Optische Charakterisierung von ZnSe-basierten Laserstrukturen mit binären Quantentrögen, Ph.D. thesis, Institut für Festkörperphysik, Universität Bremen, 1999.
- [20] L. D. Landau, E. M. Lifshitz, *Electrodynamics of Continuous Media*, Addison-Wesly, Reading, MA (USA), 1960.

- [21] C. F. Klingshirn, Semiconductor Optics, Springer-Verlag, Berlin, Heidelberg, 1997.
- [22] U. Lunz, J. Kuhn, F. Goschenhofer, U. Schüssler, S. Einfeldt, C. R. Becker, G. Landwehr, J. Appl. Phys. 80, 6861 (1996).
- [23] R. N. Hall, G. E. Fenner, J. D. Kingsley, T. J. Soltys, R. O. Carlson, Phys. Rev. Lett. 9, 366 (1962).
- [24] M. I. Nathan, W. P. Dumke, G. Burns, F. H. Dill Jr., G. Lasher, Appl. Phys. Lett. 1, 62 (1962).
- [25] T. M. Quist, R. H. Rediker, R. J. Keyes, W. E. Krag, B. Lax, A. L. McWorter, H. J. Zeiger, Appl. Phys. Lett. 1, 91 (1962).
- [26] N. Holonyak Jr., S. F. Bevacqua, Appl. Phys. Lett. 1, 82 (1962).
- [27] S. M. Sze, *Semiconductor Devices: Pioneering Papers*, World Scientific Publishing Co. Pte. Ltd., Singapore, 1991.
- [28] H. Kroemer, Proc. IEEE 51, 1782 (1963).
- [29] Z. I. Alferov, R. F. Kazarinov, Patent 181737, Authors Certificate 28448 (USSR) (1963 [8]).
- [30] Y. Arakawa, A. Yariv, IEEE J. Quant. Electr. QE-22, 1887 (1986).
- [31] D. Bimberg, M. Grundmann, N. N. Ledentsov, *Quantum Dot Heterostructures*, John Wiley Sons Ltd., Chichester, 1999.
- [32] M. Legge, Laterale Strukturierung von blau-grünen II/VI-Halbleiterlasern und CdTe-Mikroresonatoren, Ph.D. thesis, Universität Würzburg, 2000.
- [33] A. Jakobs, Modellierung und Optimierung von Halbleiterlasern auf der Basis von Zinkselenid, Ph.D. thesis, Universität Würzburg, 1995.
- [34] H. Wenisch, Homoepitaxie und Charakterisierung von Leucht- und Laserdioden auf ZnSe-Einkristallen, Ph.D. thesis, Universität Bremen, Institut für Festkörperphysik, 1999.
- [35] M. Behringer, Molekular-Strahl-Epitaxie von Laserdioden auf der Basis von ZnSe und deren optische und elektrische Charakterisierung, Ph.D. thesis, Universität Bremen, Institut für Festkörperphysik, 1998.
- [36] R. Blachnik, J. Chu, R. R. Galazka, J. Geurts, J. Gutowski, B. Hönerlage, D. Hofmann, J. Kossut, R. Lévy, P. Michler, U. Neukirch, T. Story, D. Strauch, A. Waag, *Landolt-Börnstein: Numerical Data and Functional Relationships in Science and Technology*, vol. III.: Condensed Matter, Semiconductors, Subvolume b: II-VI and I-VII Compounds; Semimagnetic Compounds, Springer-Verlag, 1999.
- [37] M. P. Kulakov, V. D. Kulakovskii, I. B. Savchenko, A. V. Fadeev, Sov. Solid State 18, 526 (1976).
- [38] M. Prokesch, *Selbstkompensation in ZnSe*, Ph.D. thesis, Universität Bremen, Institut für Festkörperphysik, 2000.
- [39] E. Yamaguchi, I. Takayasu, T. Minato, M. Kawashima, J. Appl. Phys. 62, 885 (1987).
- [40] S. Rubini, E. Milocco, L. Sorba, A. Franciosi, J. Cryst. Growth 184/185, 178 (1998).
- [41] N. Shibata, A. Ohki, H. Nakanishi, S. Zembutsu, J. Cryst. Growth 86, 268 (1988).
- [42] M. Tamargo, W. Lin, S. Guo, Y. Guo, Y. Luo, Y. Cheng, J. Cryst. Growth **214/215**, 1058 (2000).
- [43] W. Faschinger, J. Nürnberger, Appl. Phys. Lett. 77, 187 (2000).
- [44] Dowa Semiconductor CO., LTD., Akita-Shi, Japan, *Certificate of Compliance: Lot 2YS-324, EPD: 33–42 cm*², 2001.
- [45] L. Haase, *Hochauflösenede Röntgendiffraktrometrie an II-VI-Epitaxieschichten bei variabler Temperatur*, Diploma thesis, Universität Bremen, Institut für Festkörperphysik, 2000.
- [46] S. Guha, J. M. DePuydt, J. Qui, G. E. Hofler, M. A. Haase, B. J. Wu, H. Cheng, Appl. Phys. Lett. **63**, 3023 (1993).

- [47] G. C. Hua, N. Otsuka, D. C. Grillo, Y. Fan, J. Han, M. D. Ringle, R. L. Gunshor, M. Hovinen, A. V. Nurmikko, Appl. Phys. Lett. **65**, 1331 (1994).
- [48] M. Shiraishi, S. Tomiya, S. Taniguchi, K. Nakano, A. Ishisbashi, M. Ikeda, phys. stat. sol. (a) **152**, 377 (1995).
- [49] J.-M. Bonard, J.-D. Ganière, L. Vanzettis, J. J. Paggel, L. Sorba, A. Franciosi, D. Hervé, E. Molva, J. Appl. Phys. 84, 1263 (1998).
- [50] G. Kiriakidis, K. Moschovis, P. Uusimaa, A. Salokatve, M. Pessa, J. Stoemenos, Thin Sol. Films 360, 195 (2000).
- [51] T. W. Behr, Herstellung und strukturelle Untersuchung von (Mg,Zn)(S,Se)-Epitaxieschichten in Hinsicht auf blau-grün emittierende Laserdioden auf der Basis von ZnSe, Ph.D. thesis, Universität Würzburg, 1997.
- [52] G. D. U'Ren, M. S. Goorsky, G. Meis-Haugen, K. K. Law, T. J. Miller, K. W. Haberern, Appl. Phys. Lett. **69**, 1089 (1996).
- [53] A. Ishibashi, in *Proceedings of SPIE: Physics and Simulation of Optoelectronic Devices VII*, edited by P. Blood, A. Ishibashi, M. Osinski, vol. 3625, San Jose (USA) (1999).
- [54] L. Vegard, Z. Phys. 5, 17 (1921).
- [55] D. Wood, *Optoelectronic Semiconductor Devices*, International Series in Optoelectronics, Prentice Hall, Hertfordshire, United Kingdom, 1994.
- [56] H. Okuyama, Y. Kishita, A. Ishibashi, Phys. Rev. B 57, 2257 (1998).
- [57] I. Ho, G. B. Stringfellow, Appl. Phys. Lett. 69, 2701 (1996).
- [58] T. Saito, Y. Arakawa, Phys. Rev. B 60, 1701 (1999).
- [59] M. A. Haase, J. Qui, J. M. de Puydt, H. Chen, Appl. Phys. Lett. 59, 1273 (1991).
- [60] Y. Fan, Appl. Phys. Lett. 67, 1739 (1995).
- [61] V. Großmann, Mikrocharakterisierung von lichtemittierenden Halbleiterstrukturen mit Hilfe der Röntgenbeugung und -reflexion, Ph.D. thesis, Universität Bremen, Institut für Festkörperphysik, 2000.
- [62] J. M. Gaines, J. Cryst. Growth 137, 187 (1994).
- [63] D. C. Grillo, M. D. Ringle, G. C. Hua, J. Han, R. L. Gunshor, M. Hovinen, A. V. Nurmikko, J. Vac. Sci. Technol. B 13, 720 (1995).
- [64] B. Jobst, $Zn_{1-x}Ca_xC_yCe_{1-y}$ und $Zn_{1-x}Mg_xS_ySe_{1-y}$ -Halbleiterschichten: Wachstum mittels Molekularstrahlepitaxie, Charakterisierung und Anwendung in blau-emittierenden Laserdioden, Ph.D. thesis, Universität Bremen, Institut für Festkörperphysik, 1996.
- [65] N. Nakayama, S. Itoh, T. Ohata, K. Nakano, H. Okuyama, M. Ozawa, A. Ishibashi, M. Ikeda, Y. Mori, Electron. Lett. 29, 1488 (1993).
- [66] J. M. Gaines, R. R. Drenten, K. W. Haberern, T. Marshall, P. Mensz, J. Petruzzelo, Appl. Phys. Lett. 62, 2462 (1993).
- [67] J. M. Gaines, C. A. Ponzoni, Surf. Sci. 310, 307 (1994).
- [68] H. Okuyama, K. Nakano, T. Miyajima, K. Akimoto, Jpn. J. Appl. Phys. 30, L1620 (1991).
- [69] M. T. Litz, K. Watanabe, M. Korn, H. Ress, U. Lunz, W. Ossau, A. Waag, G. Landwehr, T. Walter, B. Neubauer, D. Gerthsen, U. Schüssler, J. Cryst. Growth 159, 54 (1996).
- [70] B. Jobst, D. Hommel, U. Lunz, T. Gerhard, G. Landwehr, Appl. Phys. Lett. 69, 97 (1996).
- [71] S. Itoh, N. Nakayama, T. Ohata, M. Ozawa, H. Okuyama, K. Nakano, M. ikeda, A. Ishibashi, Y. Mori, Jpn. J. Appl. Phys. 33, L639 (1994).
- [72] H. Okuyama, N. Nakayama, S. Itoh, M. Ikeda, A. Ishibashi, Jpn. J. Appl. Phys. **35**, 1410 (1996).

- [73] C. B. O'Donnell, G. Lacey, G. Horsburgh, A. G. Cullis, C. R. Whitehouse, P. J. Parbrook, W. Meredith, I. Galbraith, P. Möck, K. A. Prior, B. C. Cavenett, J. Cryst. Growth 184/185, 95 (1998).
- [74] A. Salokatve, H. Jeon, J. Ding, M. Hovinen, A. V. Nurmikko, D. C. Grillo, L. He, J. Han, Y. Fan, M. Ringle, R. L. Gunshor, G. C. Hua, N. Otsuka, Electron. Lett. 29, 2192 (1993).
- [75] S. Taniguchi, T. Hino, S. Itoh, K. Nakano, N. Nakayama, A. Ishibashi, M. Ikeda, Electron. Lett. 32, 552 (1996).
- [76] K.-K. Law, P. F. Baude, T. J. Miller, M. A. Haase, G. M. Smekalin, K. Haugen, Electron. Lett. 32, 345 (1996).
- [77] M. Kuttler, Diffusionsinduzierte Durchmischung von II-VI Heterostrukturen: Mechanismen und technologische Anwendung, Ph.D. thesis, Technische Universität Berlin, 1998.
- [78] A. Toda, K. Nakano, A. Ishibashi, Appl. Phys. Lett. 73, 1523 (1998).
- [79] M. Behringer, H. Wenisch, M. Fehrer, V. Großmann, A. Isemann, M. Klude, H. Heinke, K. Ohkawa, D. Hommel, Festkörperprobleme/Adv. Solid State Phys. 38, 47 (1999).
- [80] L. Goldstein, F. Glas, J. Y. Marzin, M. N. Charasse, G. Le Roux, Appl. Phys. Lett. 47, 1099 (1985).
- [81] D. Bimberg, N. N. Ledentsov, M. Grundmann, N. Kirchstaedter, O. G. Schmidt, M. H. Mao, V. M. Ustinov, A. Y. Egarov, A. E. Zhukov, P. S. Kopev, Z. I. Alferov, S. S. Ruvimov, U. Gosele, J. Heydenreich, phys. stat. sol. (b) 194, 159 (1996).
- [82] I. L. Krestnikov, V. Ivanov, S, P. S. Kopec, N. N. Ledentsov, M. V. Maximov, A. V. Sakharov, S. V. Sorokin, A. Rosenauer, D. Gerthsen, C. M. Sotomayor Torres, D. Bimberg, Z. I. Alferov, Mat. Sci. Eng. B 51, 26 (1998).
- [83] R. Engelhardt, U. W. Pohl, D. Bimberg, D. Litvinov, A. Rosenauer, D. Gerthsen, J. Appl. Phys. 86, 5578 (1999).
- [84] E. Kurtz, T. Sekiguchi, Z. Zhu, T. Yao, J. X. Shen, Y. Oka, M. Y. Shen, T. Goto, Superlattices and Microstructures 25, 119 (1999).
- [85] T. Passow, K. Leonardi, D. Hommel, phys. stat. sol. (b) 224, 143 (2001).
- [86] H. Luo, J. K. Furdyna, Semicond. Sci. Technol. 10, 1041 (1995).
- [87] D. Eason, J. Ren, Z. Yu, C. Hughes, J. W. Cook Jr., J. F. Schetzina, N. A. El-Masry, G. Cantwell, W. C. Harsh, J. Cryst. Growth 150, 718 (1995).
- [88] D. B. Eason, Z. Yu, W. C. Hughes, W. H. Roland, C. Boney, J. W. Cook Jr., J. F. Schetzina, Appl. Phys. Lett. 66, 115 (1995).
- [89] C. S. Yang, D. Y. Hong, C. Y. Lin, W. C. Chou, C. S. Ro, W. Y. Uen, W. H. Lan, S. L. Tu, J. Appl. Phys. 83, 2555 (1998).
- [90] J. Han, T. S. Stavrinides, M. Kobayashi, R. L. Gunshor, Appl. Phys. Lett. 62, 840 (1993).
- [91] T. Baron, K. Saminadayar, N. Magnea, J. Appl. Phys. 83, 1354 (1998).
- [92] Y. Fan, J. Han, L. He, J. Saraie, R. L. Gunshor, M. Hagerott, H. Jeon, A. V. Nurmikko, G. C. Hua, N. Otsuka, Appl. Phys. Lett. **61**, 3160 (1992).
- [93] F. Hiei, M. Ikeda, M. Ozawa, T. Miyajima, A. Ishibashi, K. Akimoto, Electron. Lett. 29, 878 (1993).
- [94] T. Yao, Y. Makita, S. Maekawa, J. Cryst. Growth 45, 309 (1978).
- [95] M. Klude, *Optimierung von p-Kontakten für II-VI Halbleiterstrukturen*, Diploma thesis, Universität Bremen, Institut für Festkörperphysik, 1998.
- [96] K. Ohkawa, T. Mitsuyu, O. Yamazakai, J. Appl. Phys. 62, 3216 (1987).
- [97] D. Hommel, B. Jobst, T. Behr, G. Bilger, V. Beyersdorfer, E. Kurtz, G. Landwehr, J. Cryst. Growth 138, 331 (1994).

- [98] Y. S. Park, C. H. Chung, Appl. Phys. Lett. 18, 99 (1971).
- [99] Y. S. Park, B. K. Shin, J. Appl. Phys. 45, 1444 (1974).
- [100] M. Yamaguchi, A. Yamamoto, M. Kondo, J. Appl. Phys. 48, 196 (1975).
- [101] K. Akimoto, T. Miyajima, Y. Mori, Jpn. J. Appl. Phys. 28, L528 (1989).
- [102] K. Akimoto, T. Miyajima, Y. Mori, Jpn. J. Appl. Phys. 28, L531 (1989).
- [103] J. M. de Puydt, M. A. Haase, H. Cheng, J. E. Potts, Appl. Phys. Lett. 55, 1103 (1989).
- [104] M. A. Haase, H. Cheng, J. M. de Puydt, J. E. Potts, J. Appl. Phys. 67, 448 (1990).
- [105] K. Ohkawa, T. Karasawa, T. Mitsuyu, Jpn. J. Appl. Phys. 30, L152 (1991).
- [106] A. Toda, T. Margalith, A. Imanishi, K. Yanashima, A. Ishisbashi, Electron. Lett. **31**, 1921 (1995).
- [107] G. Neu, E. Tournié, C. Morhain, M. Teisseire, J.-P. Faurie, Phys. Rev. B 61, 15789 (2000).
- [108] D. Wolverson, J. J. Davies, S. Strauf, P. Michler, J. Gutowski, M. Klude, D. Hommel, K. Ohkawa, Tournié, J.-P. Faurie, phys. stat. sol. (b) 229, 257 (2002).
- [109] D. Seghier, H. P. Gislason, C. Morhain, M. Teisserire, E. Tournié, G. Neu, J.-P. Faurie, phys. stat. sol. (b) 229, 251 (2002).
- [110] H. Jeon, W. Patterson, A. V. Nurmikko, W. Xie, D. C. Grillo, M. Kobayashi, R. L. Gunshor, Appl. Phys. Lett. 59, 3619 (1991).
- [111] H. Jeon, J. Ding, A. V. Nurmikko, W. Xie, D. C. Grillo, M. Kobayashi, R. L. Gunshor, G. C. Hua, N. Otsuka, Appl. Phys. Lett. **60**, 2045 (1992).
- [112] S. Y. Wang, I. Hauksson, S. Simpson, H. Stewart, S. J. A. Adams, J. M. Wallace, Y. Kawakamai, K. A. Prior, B. C. Cavenett, Appl. Phys. Lett. **61**, 506 (1992).
- [113] H. Okuyama, T. Miyajima, Y. Morinaga, F. Hiei, M. Ozawa, K. Akimoto, Electron. Lett. **28**, 1798 (1992).
- [114] S. Hayashi, A. Tsujimura, S. Yoshi, K. Ohkawa, T. Mitsuyu, Jpn. J. Appl. Phys. 31, L1478 (1992).
- [115] Z. Yu, J. Ren, Y. Lansare, B. Sneed, K. A. Bowers, C. Noney, D. B. Eason, R. P. Vaudo, R. J. Gossett, J. W. Cook Jr., J. F. Schetzina, Jpn. J. Appl. Phys. **32**, 663 (1993).
- [116] C. T. Walker, J. M. DePuydt, M. A. Haase, J. Qiu, H. Cheng, Phys. B 185, 27 (1993).
- [117] M. A. Haase, P. F. Baude, M. S. Hagedorn, J. Qui, J. M. DePuydt, H. Cheng, S. Guha, G. E. Höfler, B. J. Wu, Appl. Phys. Lett. **63**, 2315 (1993).
- [118] M. Onomura, M. Ishikawa, Y. Nishikawa, S. Saito, P. J. Parbrook, K. Nitta, J. Rennie, G. Hatakoshi, Electron. Lett. **29**, 2114 (1993).
- [119] N. Nakayama, S. Itoh, H. Okuyama, M. Ozawa, T. Ohata, K. Nakano, M. Ikeda, A. Ishisbashi, Y. Mori, Electron. Lett. **29**, 2194 (1993).
- [120] D. Hommel, E. Kurtz, T. Behr, A. Jakobs, B. Jobst, S. Scholl, K. Schüll, V. Beyersdorfer, G. Landwehr, H. Cerva, J. Cryst. Growth 138, 1076 (1994).
- [121] D. C. Grillo, J. Han, M. Ringle, G. Hua, R. L. Gunshor, P. Kelkar, V. Kozlov, H. Jeon, A. V. Nurmikko, Electron. Lett. 30, 2131 (1994).
- [122] M. Ikeda, A. Ishibashi, Y. Mori, J. Vac. Sci. Technol. A 13, 683 (1995).
- [123] A. Ishibashi, IEEE J. Sel. Topics. Quant. Electr. 1, 741 (1995).
- [124] Z. Yu, C. Boney, W. C. Hughes, W. H. Rowland Jr., J. W. Cook Jr., J. F. Schetzina, G. Cantwell, W. C. Harsch, Electron. Lett. 31, 1341 (1995).
- [125] M. Pessa, K. Rakennus, P. Uusimaa, A. Salokatve, in *Proc. of 22nd Int. Symp. Compound Semiconductors*, Cheju Island, Korea, 1163–1168 (1995).
- [126] T. Kawasumi, N. Nakayama, A. Ishibashi, Y. Mori, Electron. Lett. 31, 1667 (1995).

- [127] G. Bacher, N. Mais, M. Illing, A. Forchel, K. Schüll, J. Nürnberger, G. Landwehr, Electron. Lett. 31, 2184 (1995).
- [128] A. Waag, F. Fischer, H.-J. Lagauer, T. Litz, J. Laubender, U. Lunz, U. Zehnder, W. Ossau, T. Gerhard, M. Möller, G. Landwehr, J. Appl. Phys. **80**, 792 (1996).
- [129] M. Buijs, K. Habereren, T. Marshall, K. K. Law, P. F. Bause, T. J. Miller, M. A. Haase, G. M. Haugen, J. Horikx, Electron. Lett. (1996).
- [130] A. Ohki, T. Ohno, T. Matsuoka, Y. Ichimura, Electron. Lett. 33, 990 (1997).
- [131] M. D. Kim, B. J. Kim, M. Jeon, J. K. Ji, S. D. Lee, E. S. Oh, Kim J. S., H. S. Park, T. I. Kim, J. Cryst. Growth 175, 637 (1997).
- [132] M. Behringer, K. Ohkawa, V. Großmann, H. Heinke, K. Leonardi, M. Fehrer, D. Hommel, M. Kuttler, M. Straßburg, D. Bimberg, J. Cryst. Growth **184/185**, 580 (1998).
- [133] F. Nakanishi, H. Doi, N. Okuda, T. Matusoka, K. Katayama, A. Saegusa, H. Matsubara, T. Yamada, T. Umura, M. Irikura, S. Nishine, Electron. Lett. **34**, 496 (1998).
- [134] H. Wenisch, K. Ohkawa, A. Isemann, M. Fehrer, D. Hommel, Electron. Lett. 34, 891 (1998).
- [135] K. Katayama, H. Yao, F. Nakanishi, H. Doi, A. Saegusa, N. Okuda, T. Yamada, H. Matsubara, M. Irikuda, T. Matsuoka, T. Takebe, S. Nishine, T. Shirakawa, Appl. Phys. Lett. **73**, 102 (1998).
- [136] Y. Sanaka, H. Okuyama, S. Kijima, K. Kato, H. Noguchi, A. Ishibashi, Electron. Lett. 34, 1891 (1998).
- [137] H. Doi, T. Matsukoka, F. Nakanishi, N. Okuda, T. Yamada, K. Katayama, H. Yao, A. Saegusa, H. Matsubara, M. Irikura, K. Kimura, T. Takebe, S. Nishine, T. Shirakawa, in *Proc. of the 2nd Int. Symp. on Blue Laser and Light Emitting Diode*, edited by K. Onabe, K. Hiramatsu, K. Itaya, Y. Nakano, Chiba, Japan, 385–388 (1998).
- [138] S. Ivanov, A. Toropov, S. Sorokin, T. Shubina, A. Lebedev, P. Kop'ev, Z. Alferov, H.-J. Lugauer, G. Reuscher, M. Keim, F. Fischer, A. Waag, G. Landwehr, Appl. Phys. Lett. 73, 2104 (1998).
- [139] H. Jeon, J. Ding, A. V. Nurmikko, H. Luo, N. Samarth, J. K. Furdyna, W. A. Bonner, R. E. Nahory, Appl. Phys. Lett. 57, 2413 (1990).
- [140] S. Guha, J. M. DePuydt, M. A. Haase, J. Qiu, H. Cheng, Appl. Phys. Lett. 63, 3107 (1993).
- [141] S. Itoh, A. Ishibashi, J. Cryst. Growth 150, 701 (1995).
- [142] Y.-K. Song, A. V. Nurmikko, C.-C. Chu, J. Han, T. B. Ng, R. L. Gunshor, Electron. Lett. 32, 1829 (1996).
- [143] S. L. Chuang, M. Ukita, S. Kijama, S. Taniguchi, A. Ishibashi, Appl. Phys. Lett. **69**, 1588 (1996).
- [144] K. Osato, K. Yamamoto, I. Ichimura, F. Maeda, Y. Kasami, M. Yamada, in *Proceedings of SPIE: Optical Data Storage '98*, edited by S. Kubota, T. D. Milster, P. J. Wehrenberg, vol. 3401, SPIE (1998).
- [145] J. Ren, D. B. Eason, Y. Lansari, Z. Yu, K. A. Bowers, C. Boney, B. Sneed, J. W. Cook Jr., J. F. Schetzina, M. W. Koch, G. W. Wicks, J. Vac. Sci. Technol. B 11, 955 (1993).
- [146] L. H. Kuo, L. Salamanca-Riba, B. J. Wu, G. M. Haugen, J. M. DePuydt, G. Hofler, H. Cheng, J. Vac. Sci. Technol. B 13, 1694 (1995).
- [147] C. C. Chu, T. B. Ng, J. Han, G. C. Hua, R. L. Gunshor, E. Ho, E. L. Warlick, L. A. Kolodziejski, A. V. Nurmikko, Appl. Phys. Lett. **69**, 602 (1996).
- [148] S. Guha, H. Munekata, F. K. LeGoues, L. L. Chang, Appl. Phys. Lett. 60, 3220 (1992).
- [149] K. Ohkawa, A. Tsujimura, S. Hayashi, S. Yoshii, T. Mitsuyu, Phys. Bl. 185, 112 (1993).
- [150] K. Kimura, S. Miwa, H. Kajiyama, T. Yasuda, L. H. Kuo, C. G. Jin, K. Tanaka, T. Yao, Appl. Phys. Lett. **71**, 485 (1997).

- [151] R. M. Park, H. A. Mar, N. M. Salansky, J. Appl. Phys. 58, 1047 (1985).
- [152] A. A. El-Emawy, Y. Qui, A. Osinsky, E. Littlefield, H. Temkin, Appl. Phys. Lett. **67**, 1238 (1995).
- [153] Y. Hishida, T. Yoshie, K. Yagi, K. Yodoshi, T. Niina, Appl. Phys. Lett. 67, 270 (1995).
- [154] H. Tsukamoto, M. Nagai, E. Katoh, K. Tamamura, A. Ishibashi, M. Ikeda, Appl. Phys. Lett. **70**, 1453 (1997).
- [155] J. Qiu, J. M. DePuydt, H. Cheng, M. A. Haase, Appl. Phys. Lett. 59, 2992 (1991).
- [156] D. B. Laks, C. G. V. de Walle, Phys. Bl. 185, 118 (1993).
- [157] D. J. Chadi, N. Troullier, Phys. Bl. 185, 128 (1993).
- [158] Y. Nishikawa, M. Ishikawa, P. J. Parbrook, M. Onomura, S. Saito, G. Hatakoshi, J. Cryst. Growth 150, 807 (1995).
- [159] K. Kimura, S. Miwa, C. G. Jin, L. H. Kuo, T. Yasuda, A. Ohtake, K. Tanaka, T. Yao, Appl. Phys. Lett. **71**, 1077 (1997).
- [160] J. Qiu, H. Cheng, J. M. D. Puydt, M. A. Haase, J. Cryst. Growth 127, 279 (1993).
- [161] H. Okuyama, Y. Kishita, T. Miyajima, A. Ishibashi, K. Akimoto, Appl. Phys. Lett. 67, 904 (1994).
- [162] K. Kondo, H. Okuyama, A. Ishibashi, Appl. Phys. Lett. 64, 3434 (1994).
- [163] S. Nakatsuka, J. Gotoh, K. Mochizuki, A. Taike, M. Kawata, M. Momose, Jpn. J. Appl. Phys. **35**, 1431 (1996).
- [164] H. K. Henisch, Semiconductor Contacts An approach to ideas and models, International Series of Monographs on Physics, Oxford University Press, 1984.
- [165] Y. Koide, T. Kawakami, N. Teraguchi, Y. Tomomura, A. Suzuki, M. Murakami, J. Appl. Phys. 82, 2393 (1997).
- [166] T. Ohtsuka, J. Kawamata, Z. Zhu, T. Yao, Appl. Phys. Lett. 65, 486 (1994).
- [167] J. Ren, D. B. Eason, L. E. Churchill, Z. Yu, C. Boney, J. J. W. Cook, J. F. Schetzina, N. A. El-Masry, J. Cryst. Growth 138, 455 (1994).
- [168] S. Einfeldt, M. Behringer, J. Nürnberger, H. Heinke, T. Behr, C. R. Becker, D. Hommel, G. Landwehr, phys. stat. sol. (b) **187**, 439 (1995).
- [169] P. M. Mensz, Appl. Phys. Lett. 64, 2148 (1994).
- [170] T. Yoshida, T. Nagatake, M. Kobayashi, A. Yoshikawa, J. Cryst. Growth 159, 750 (1996).
- [171] M. Ozawa, F. Hiei, A. Ishibashi, K. Akimoto, Electron. Lett. 29, 503 (1993).
- [172] K. Mochizuki, A. Terano, M. Momose, A. Taike, M. Kawata, J. Gotoh, S. Nakatsuka, Electron. Lett. 30, 1984 (1994).
- [173] S. J. Chang, W. R. Chen, Y. K. Su, J. F. Chen, W. H. Lan, C. I. Chiang, W. J. Lin, Y. T. Cherng, C. H. Liu, Electron. Lett. 37, 321 (2001).
- [174] G. L. Yang, H. Luo, L. Lewandowski, J. K. Furdyna, phys. stat. sol. (b) 187, 435 (1995).
- [175] S. Kijima, H. Okuyama, Y. Sanaka, T. Kobayashi, S. Tomiya, A. Ishibashi, Appl. Phys. Lett. 73, 235 (1998).
- [176] M. Fehrer, Untersuchung der elektrischen Eigenschaften breitlückiger Halbleiterschichtstrukturen für optoelektronische Anwendungen, Ph.D. thesis, Universität Bremen, Institut für Festkörperphysik, 1999.
- [177] P. A. Redhead, J. P. Hobsen, E. V. Kornelsen, *The Physical Basis of Ultrahigh Vaccum*, American Institute of Physics, New York, 1993.
- [178] J. Y. Tsao, Materials Fundamentals of Molecular Beam Epitaxy, Academic Press, 1993.
- [179] M. A. Herman, H. Sitter, *Molecular Beam Epitaxy*, vol. 7 from *Springer Series in Materials Science*, Springer, 2nd edition, 1996.

- [180] K. Leonardi, Untersuchungen zur Selbstorganisation in niederdimensionalen II-VI-Halbleiterheterostrukturen, Ph.D. thesis, Universität Bremen, Institut für Festkörperphysik, 2000.
- [181] Applied Epi Inc., http://www.appliedepi.com, 2001.
- [182] Oxford Applied Research Ltd., http://www.oxford.com, 2001.
- [183] P. Bäume, *Untersuchungen der Störstellen-Lumineszenz teilkompensierter Halbleiter*, Ph.D. thesis, Universität Bremen, Institut für Festkörperphysik, 1997.
- [184] S. Stauf, P. Michler, J. Gutowski, M. Klude, D. Hommel, J. Cryst. Growth **214/215**, 497 (2000).
- [185] M. Diaz Waszczynski, Wachstumsoptimierung von ZnSe/ZnCdSe Heterostrukturen mittels einer Selen-Cracker-Zelle, Diploma thesis, Universität Bremen, Institut für Festkörperphysik, 2000.
- [186] SUN Microsystems Inc., http://www.sun.com, 2002.
- [187] P. K. Larsen, P. J. Dobson (Ed.), Reflection High-Energy Electron Diffraction and Reflection Electron Imaging of surfaces, Plenum Press in coorperation with NATO Scientific Affairs Division, 1987.
- [188] Staib Instrumente, Langenbach, Germany, Betriebsanleitung RHEED Elektronenquelle EK-35-R, 1995.
- [189] J. A. Woollam Co., Inc., Lincoln, USA, Guide to Using WVASE 32 Software for VASE and M-44 Ellipsometers, 1995.
- [190] H. G. Tompkins, A Users's Guide to Ellipsometry, Academic Press, Inc., San Diego, USA, 1993.
- [191] R. M. A. Azzam, N. M. Bashara, *Ellipsometry and Polarized Light*, North-Holland, Personal Library, Amsterdam, 1987.
- [192] S. Albensoeder, *Pyrometrie in der MBE*, Student paper (Studienarbeit), Universität Bremen, Institut für Festkörperphysik, 1996.
- [193] Heimann/Heitronics, Wiesbaden, Germany, *Betriebsanleitung Strahlungspyrometer KT19.02*, 1996.
- [194] C. Kruse, G. Alexe, M. Klude, H. Heinke, D. Hommel, phys. stat. sol. (b) (2002).
- [195] Filmetrics, San Diego, USA, Operations Manual for the Filmetrics F30, Thin Film Measurement System, 1999.
- [196] A. Ishibashi, M. Ukita, A. Tomiya, in *Proceedings of the 23rd International Conference on the Physics of Semiconductors*, edited by M. Scheffler, R. Zimmermann, vol. 4, Berlin, page 3155 (1996).
- [197] B. J. Wu, G. M. Haugen, J. M. DePuydt, L. H. Kuo, L. Salamanca-Riba, Appl. Phys. Lett. **68**, 2828 (1996).
- [198] L. H. Kuo, K. Kimura, S. Miwa, T. Yasuda, T. Yao, Appl. Phys. Lett. 69, 1408 (1996).
- [199] H. Heinke, M. Behringer, H. Wenisch, V. Großmann, D. Hommel, J. Cryst. Growth **184/185**, 587 (1998).
- [200] H. Heinke, Characterisierung von epitaktischen Schichten auf der Basis von II-VI-Halbleitern mit Hilfe der hochauflösenden Röntgendiffraktometrie, Ph.D. thesis, Universität Würzburg, 1994.
- [201] J.-S. Kim, J.-H. Song, S.-H. Suh, S.-J. Chung, Sol. State Comm. 101, 57 (1997).
- [202] A. Isemann, *Elektrische und optische Charakterisierung von ZnSe-Laserdioden und LEDs*, Diploma thesis, Institut für Festkörperphysik, Universität Bremen, 1998.

- [203] J. F. Schetzina (North Carolina State University, USA), Integrated heterostructure of Group II-VI semiconductor materials including epitaxial ohmic contact and method of fabricating same, American Patent (05294833), 1994.
- [204] J. Gutowski, N. Presser, G. Kudlek, phys. stat. sol. (a) 120, 11 (1990).
- [205] T. Seedorf, *Untersuchungen zum Wachstum von II-VI Halbleiterheterostrukturen mittels Migration Enhanced Epitaxy*, Diploma thesis, Universität Bremen, Institut für Festkörperphysik, 1999.
- [206] P. M. Young, E. Runge, M. Ziegler, H. Ehrenreich, Phys. Rev. B 49, 7424 (1994).
- [207] P. S. Zory (Ed.), Quantum well lasers, Academic Press, Bosten (USA), 1993.
- [208] M. Klude, *Elektrische Charakterisierung von Halbleiterschichten*, Student paper (Studienarbeit), Universität Bremen, Institut für Festkörperphysik, 1997.
- [209] B. Jobst, *C/V- und Transportmessungen an p- und n-dotierten Zn(S)Se MBE-Schichten*, Diploma thesis, Universität Würzburg, 1993.
- [210] Accent Optical Technologies Inc., http://www.accentopto.com, 2001.
- [211] Bio-Rad Semiconductor Systems Division, PN 4300 PC, Electrochemical C-V Profiler with Photovoltage Spectroscopy, Operating Manual, 1994.
- [212] ILX Lightwave Inc., http://www.ilxlightwave.com, 2001.
- [213] Keithley Instruments, http://www.keithley.com, 2001.
- [214] Jobin Yvon, http://www.jobin-yvon.com, 2001.
- [215] Jobin-Yvon/Spex, Instruments S. A. Group, SpectraMax-Spectroscopic Acquisition and Analysis Software, 1994.
- [216] J. Müller, *Elektro-optische Charakterisierung von ZnSe-Laserdioden*, Student paper (Studienarbeit), Universität Bremen, Institut für Festkörperphysik, 2000.
- [217] H. Okuyama, E. Kato, S. Itoh, N. Nakayama, T. Ohata, A. Ishisbashi, Appl. Phys. Lett. **66**, 656 (1995).
- [218] Z. Yu, J. Ren, Y. Lansari, K. J. Gosset, B. Sneed, K. A. Bowers, J. W. Cook, J. F. Schetzina, in *MRS Symposium Proceedings*, edited by C. W. Tu, D. C. Houghton, R. T. Tung, vol. 281, Bosten (USA) (1993).
- [219] B. W. Hakki, T. L. Paoli, J. Appl. Phys. 44, 4113 (1973).
- [220] N. Nakayama, S. Kijima, S. Itoh, T. Ohata, A. Ishibashi, Y. Mori, Optical Review 2, 167 (1995).
- [221] M. Buijs, R. Tijburg, K. Haberern, J. Gaines, J. Appl. Phys. 79, 578 (1996).
- [222] S. Itoh, in 9th International Conference on II-VI-Compound Semiconductors, Kyoto (Japan) (1999).
- [223] W. Kraus, 1.3 μm laser diode SL-MQW-Structure: Qualification Report 7500 h final report, Siemens, Semiconductor Group/Opto Semiconductors, 1995.
- [224] S. Tomiya, E. Morita, M. Ukita, H. Okuyama, S. Itoh, K. Nakano, A. Ishibashi, Appl. Phys. Lett. **66**, 1208 (1995).
- [225] M. Hovinen, J. Ding, A. V. Nurmikko, G. C. Hua, D. C. Grillo, L. He, J. Han, R. L. Gunshor, Appl. Phys. Lett. 66, 2013 (1995).
- [226] K. Nakano, S. Tomiya, M. Ukita, H. Yoshida, S. Itoh, E. Morita, M. Ikeda, A. Ishibashi, J. El. Mat. 25, 213 (1996).
- [227] G. M. Haugen, S. Guha, H. Cheng, J. M. DePuydt, M. A. Haase, G. E. Högler, J. Qiu, B. J. Wu, Appl. Phys. Lett. **66**, 358 (1995).
- [228] M. Hovinen, J. Ding, A. Salokatve, A. V. Nurmikko, G. C. Hua, D. C. Grillo, L. He, J. Han, M. Ringle, R. L. Gunshor, J. Appl. Phys. 77, 4150 (1995).

- [229] S. Guha, H. Cheng, M. A. Haase, J. M. DePuydt, J. Qiu, B. J. Wu, G. E. Hofler, Appl. Phys. Lett. **66**, 801 (1994).
- [230] S.-L. Chuang, A. Ishibashi, S. Kijima, N. Nakayama, M. Ukita, S. Taniguchi, IEEE J. Quant. Electr. 33, 970 (1997).
- [231] J. D. Weeks, J. C. Tully, L. C. Kimerling, Phys. Rev. Lett. 12, 3286 (1975).
- [232] S. Tomiya, H. Noguchi, Y. Sanaka, T. Hino, S. Taniguchi, A. Ishibashi, Appl. Phys. Lett. 74, 1824 (1999).
- [233] S. Tomiya, H. Okuyama, A. Ishibashi, Appl. Surf. Sci. 159-160, 243 (2000).
- [234] S. Itoh, K. Nakano, A. Ishibashi, J. Cryst. Growth 214/215, 1029 (2000).
- [235] J. Petruzello, K. W. Haberern, S. P. Herko, T. Marshall, J. M. Gaines, S. Guha, G. D. U'Ren, G. M. Haugen, J. Cryst. Growth 159, 573 (1996).
- [236] F. C. Rong, W. A. Barray, J. F. Donegan, G. D. Watkins, Phys. Rev. B 54, 7779 (1996).
- [237] D. Albert, J. Nürnberger, V. Hock, M. Ehinger, W. Faschinger, G. Landwehr, Appl. Phys. Lett. 74, 1957 (1999).
- [238] S. Gundel, W. Faschinger, Phys. Rev. B 65, 35208/1 (2002).
- [239] K. H. Chow, G. D. Watkins, Phys. Rev. Lett. 81, 2084 (1998).
- [240] K. H. Chow, G. D. Watkins, Phys. Rev. B 60, 8626 (1999).
- [241] S. Vignoli, R. Meaudre, M. Meaudre, Phys. Rev. B 50, 7378 (1994).
- [242] C. Jordan, D. T. Fewer, J. F. Donegan, E. M. McCabe, A. Huynh, F. P. Logue, S. Taniguchi, T. Hino, K. Nakano, A. Ishibashi, Appl. Phys. Lett. **72**, 194 (1998).
- [243] M. Tang, K. Shum, L. Zneg, M. C. Tamargo, Appl. Phys. Lett. 73, 1541 (1998).
- [244] M. Adachi, Z. M. Aung, K. Minami, K. Koizumi, M. Watanabe, S. Kawamoto, T. Yamagucchi, H. Kasada, T. Abe, K. Ando, K. Nakano, A. Ishibashi, S. Itoh, J. Cryst. Growth 214/215, 1035 (2000).
- [245] S. Gundel, D. Albert, J. Nürnberger, W. Faschinger, Phys. Rev. B 60, R16271 (2002).
- [246] W. Faschinger, J. Nürnberger, E. Kurtz, R. Schmitt, M. Korn, K. Schüll, M. Ehinger, Semicond. Sci. Technol. 12, 1291 (1997).
- [247] A. L. Chen, W. Walukiewicz, K. Duxstad, E. E. Haller, Appl. Phys. Lett. 68, 1522 (1996).
- [248] M. Kuttler, M. Strassburg, O. Stier, U. W. Pohl, D. Bimberg, E. Kurtz, J. Nürnberger, G. Landwehr, M. Behringer, D. Hommel, Appl. Phys. Lett. **71**, 243 (1997).
- [249] M. Momose, A. Taike, M. Kawata, J. Gotoh, S. Nakatsuka, Appl. Phys. Lett. **69**, 3572 (1996).
- [250] H. Wang, A. A. Hopgood, G. I. Ng, J. Appl. Phys. 81, 3117 (1997).
- [251] M. Kuttler, M. Straßburg, V. Türck, R. Heitz, U. W. Pohl, D. Bimberg, E. Kurtz, G. Landwehr, D. Hommel, Appl. Phys. Lett. 69, 2647 (1996).
- [252] G. Bacher, D. Tönnies, D. Eisert, A. Forchel, M. O. Möller, M. Korn, B. Jobst, D. Hommel, G. Landwehr, J. Söllner, M. Heuken, J. Appl. Phys. **79**, 4368 (1996).
- [253] M. Godlewski, J. P. Bergman, B. Monemar, E. Kurtz, D. Hommel, Appl. Phys. Lett. **69**, 2843 (1996).
- [254] L.-L. Chao, G. S. Cargill III, T. Marshall, E. Snoeks, J. Petruzello, M. Pashley, Appl. Phys. Lett. 72, 1754 (1998).
- [255] K. Endo, K. Kobajyashi, H. Fuji, Y. Ueno, Appl. Phys. Lett. 64, 146 (1994).
- [256] J. C. Hensel, G. Feher, Phys. Rev. 129, 1041 (1963).
- [257] K. Shahzad, D. J. Olego, C. Van de Walle, Phys. Rev. B 38, 1417 (1988).
- [258] B. Rockwell, H. R. Chandrasekhar, M. Chandrasekhar, A. K. Ramdas, M. Kobayashi, R. L. Gunshor, Phys. Rev. B 44, 11307 (1991).

- [259] D. Coquillat, F. Hamdani, J. P. Lascaray, O. Briot, R. L. Aulombard, Phys. Rev. B 47, 10489 (1993).
- [260] J. Wang, X. Wang, Z. Q. Zhu, T. Yao, J. Phys.: Cond. Matter 7, 5835 (1995).
- [261] A. Ivanov, S.Toropov, S. Sorokin, T. Shubina, I. Sedova, P. Kop'ev, Z. Alferov, A. Waag, H.-J. Lugauer, G. Reuscher, M. Keim, G. Landwehr, in *Proc. of the 2nd Int. Symp. on Blue Laser and Light Emitting Diode*, edited by K. Onabe, K. Hiramatsu, K. Itaya, Y. Nakano, Chiba, Japan, 419–424 (1998).
- [262] R. Vogelsang, J. J. Liang, V. Wagner, H. J. Lugauer, J. Geurts, A. Waag, G. Landwehr, Appl. Phys. Lett. 75, 1351 (1999).
- [263] M. Klude, M. Fehrer, V. Großmann, D. Hommel, J. Cryst. Growth 214/215, 1040 (2000).
- [264] M. Klude, M. Fehrer, D. Hommel, phys. stat. sol. (a) 180, 21 (2000).
- [265] T. Kobayashi, Y. Furukawa, IEEE J. Quant. Electr. **QE-15**, 674 (1979).
- [266] A. Isemann, M. Behringer, H. Wenisch, M. Fehrer, K. Ohkawa, D. Hommel, Acta Phys. Pol. A **94**, 355 (1998).
- [267] H. Okuyama, IEICE Trans. Electron. **E83-C**, 536 (2000).
- [268] T. Seedorf, M. Cornelißen, K. Leonardi, D. Hommel, H. Selke, P. L. Ryder, J. Cryst. Growth **214/215**, 602 (2000).
- [269] H. Okuyama, T. Kawasumi, A. Ishibashi, M. Ikeda, J. Cryst. Growth 175/176, 587 (1997).
- [270] H. Okuyama, S. Kijima, Y. Sanaka, A. Ishibashi, J. Cryst. Growth 193, 43 (1998).
- [271] M. Cornelißen, Transmissionselektronenmikroskopische Untersuchungen von epitaktischen Grenzflächen in ZnSe-basierten Halbleiterheterostrukturen, Diploma thesis, Universität Bremen, Institut für Werkstoffphysik und Strukturforschung, 1999.
- [272] H. Luo, N. Samarth, A. Yin, A. Pareek, M. Dobrowolski, J. K. Furdyna, K. Mahalingam, N. Otsuka, F. C. Peiris, J. R. Buschert, J. El. Mat. 22, 467 (1993).
- [273] C. Petter, *Untersuchungen von II-VI Halbleiter-Laserdioden mittels temperaturabhängiger Photolumineszenz*, Student paper (Studienarbeit), Universität Bremen, Institut für Festkörperphysik, 2000.
- [274] K. Leonardi, T. Passow, M. Klude, D. Hommel, J. Cryst. Growth 227/228, 650 (2001).
- [275] J. W. Matthews, A. E. Blakeslee, J. Cryst. Growth 27, 118 (1974).
- [276] D. C. Houghton, M. Davies, M. Dion, Appl. Phys. Lett. 64, 505 (1994).
- [277] Jansen R. W., O. F. Sankey, Phys. Rev. B 39, 3192 (1989).
- [278] C. H. Henry, P. M. Petroff, R. A. Logan, F. R. Merritt, Appl. Phys. Lett. 50, 3721 (1979).
- [279] P. W. Epperlein, P. Buchmann, A. Jakubowicz, Appl. Phys. Lett. 62, 455 (1993).
- [280] L. C. O. Dacal, A. M. Mansanares, W. C. da Silva, J. Appl. Phys. 84, 3491 (1998).
- [281] J. S. Yoo, H. S. Lee, G. T. Park, Y. T. Ko, T. Kim, J. Appl. Phys. 75, 1840 (1994).
- [282] K. H. Park, J. K. Lee, D. H. Jang, H. S. Cho, C. S. Park, K. E. Pyun, Appl. Phys. Lett. 73, 2567 (1998).
- [283] J. Hashimoto, I. Yoshida, M. Murata, T. Katsuyama, IEEE J. Quant. Electr. 33, 66 (1997).
- [284] O. Schulz, M. Straßburg, T. Rissom, S. Rodt, L. Reissmann, U. W. Pohl, D. Bimberg, M. Klude, D. Hommel, S. Itoh, K. Nakano, A. Ishibashi, phys. stat. sol. (b) **229**, 943 (2002).
- [285] C. Petter, Einfluss von Spiegelschichten auf das Betriebsverhalten von Laserdioden, Diploma thesis, Universität Bremen, Institut für Festkörperphysik, 2002.
- [286] K. Itayama, M. Ishikawa, H. Okuda, Y. Watanabe, K. Nitta, H. Shiozawa, Y. Uematsu, Appl. Phys. Lett. 53, 1363 (1988).
- [287] Y. Ueno, Jpn. J. Appl. Phys. 37, L646 (1998).
- [288] K. Shinozaki, Y. Watanabe, R. Furukawa, N. Watanabe, J. Appl. Phys., 2907 (1989).

- [289] C. W. Snyder, J. W. Lee, R. Hull, R. A. Logan, Appl. Phys. Lett. 67, 488 (1995).
- [290] R. E. Mallard, R. Clayton, D. Mayer, L. Hobbs, J. Vac. Sci. Technol. A 16, 825 (1998).
- [291] F. P. Dabkowski, A. K. Chin, P. Gavrilovic, S. Alie, D. M. Beyea, Appl. Phys. Lett. **64**, 13 (1994).
- [292] G. Beister, J. Maege, G. Erbert, G. Tränkle, Sol. State Electron. 42, 1939 (1998).
- [293] M. Bertolotti, G. Liakhou, R. Li Voti, R. P. Wang, C. Sibilia, V. P. Yakovlev, J. Appl. Phys. 74, 7054 (1993).
- [294] OptoPrecision GmbH, http://www.optoprecision.de, 2002.
- [295] M. Nägele, D. Hommel, M. Klude, C. Falldorf, Kranz & Nägele und Institut für Festkörerphysik der Universität Bremen, 2001.
- [296] Boston Laser Inc., http://www.bostonlaserinc.com/packages.php, 2001.
- [297] H. Borchers, H. Hause, K.-H. Hellwege, K. Schäfer, E. Schmidt (Ed.), *Landolt-Börnstein: Zahlenwerte und Funktionen aus Physik, Chemis, Astronomie, Geophysik und Technik*, vol. IV.: Technik, 4. Teil: Wärmetechnik, Springer-Verlag, 1972.
- [298] R. J. Klein Wassink, Weichlöten in der Elektronik, Leuz, Saulgau/Württemberg, 1991.
- [299] M. Fehrer, Herstellung von Spiegelschichten für II-VI-Halbleiterdiodenlaser, Diploma thesis, Universität Würzburg, 1995.
- [300] C. Petter, M. Klude, C. Kruse, S. Figge, D. Hommel, in *Verhandlungen der Deutschen Physikalischen Geslleschaft*, vol. 37 from *VI*, page 161 (2002).
- [301] H. Wenisch, M. Behringer, M. Fehrer, M. Klude, A. Isemann, K. Ohkawa, D. Hommel, Jpn. J. Appl. Phys. 38, 2590 (1999).
- [302] J. Späth, c't **01**, 156 (1999).
- [303] N. Anscombe, Opto Laser Europe 09, 38 (2001).
- [304] H. P. A. van den Boom, T. Onishi, T. Tsukamoto, P. K. van Bennekom, L. J. P. Niessen, G. D. Khoe, A. M. J. Koonen, in *Proc. of the 10 th International Plastic Optical Fibres Conference 2001* (2001).
- [305] L. A. Hornak (Ed.), *Polymers for Ligthwave and Integrated Optics*, Marcel Dekker Inc., New York, 1992.
- [306] Mitsubishi Rayon CO. Ltd.–Optical Fiber Department, http://www.pofeska.com/pofeskae/tece/whatspofe/whatspofe.htm, 2002.
- [307] K. Kobayashi, S. Kawata, A. Gomyo, I. Hino, T. Suzuki, Electron. Lett. 21, 931 (1985).
- [308] M. Ikeda, Y. Mori, H. Sato, K. Kaneko, N. Watanabe, Appl. Phys. Lett. 48, 1027 (1985).
- [309] H. Hamada, K. Tominaga, M. Shono, S. Honda, K. Yodoshi, T. Yamaguchi, Electron. Lett. **28**, 1834 (1992).
- [310] T. Tanaka, H. Yanagisawa, S. Minagawa, Electron. Lett. **30**, 566 (1994).
- [311] D. P. Bour, R. S. Geels, D. W. Treat, T. L. Paoli, F. Ponce, R. L. Thornton, B. S. Krusor, R. D. Bringans, D. F. Welch, IEEE J. Quant. Electr. 30, 593 (1994).
- [312] J. H. Hang, J. S. Song, K. Godo, T. Yao, M. Y. Shen, T. Goto, Appl. Phys. Lett. 78, 566 (2001).
- [313] W. Shinouaki, I. Nomura, H. Shimbo, H. Hattori, T. Sano, S.-B. Che, A. Kikuchi, K. Shimomura, K. Kishino, Jpn. J. Appl. Phys. 38, 2598 (1999).
- [314] M. Klude, D. Hommel, Appl. Phys. Lett. 79, 2523 (2001).
- [315] M. Klude, G. Alexe, C. Kruse, T. Passow, H. Heinke, D. Hommel, phys. stat. sol. (b) 229, 935 (2002).
- [316] T. Passow, K. Leonardi, A. Stockmann, H. Selke, H. Heinke, D. Hommel, J. Phys. D: Appl. Phys. 32, A42 (1999).
- [317] J. Singh, K. K. Baja, J. Appl. Phys. 57, 5433 (1985).

- [318] S. Tomiya, R. Minatoya, H. Tsukamoto, S. Itoh, K. Nakano, E. Morita, A. Ishibashi, J. Appl. Phys. 82, 2938 (1997).
- [319] M. Fujimori, H. Shigematsu, K. Senda, M. Yoshikawa, H. Kubo, Y. Yamada, T. Taguchi, Jpn. J. Appl. Phys. 38, 3550 (1999).
- [320] H. Okuyama, S. Itoh, E. Kato, M. Ozawa, N. Nakayama, K. Nakano, M. Ikeda, A. Ishibashi, Y. Mori, Electron. Lett. **30**, 415 (1994).
- [321] K. Shahzad, M. Buijs, Appl. Phys. Lett. 69, 1423 (1996).
- [322] K. Kondo, M. Ukita, H. Yoshida, Y. Kishita, H. Okuyama, S. Itoh, T. Ohata, K. Nakano, A. Ishibashi, J. Appl. Phys. **76**, 2621 (1994).
- [323] M. Klude, T. Passow, R. Kröger, D. Hommel, Electron. Lett. 37, 1119 (2001).
- [324] M. Klude, T. Passow, G. Alexe, H. Heinke, D. Hommel, in *Proceedings of SPIE: Design, Fabrication and Characterization of Photonic Devices II*, edited by M. Osinski, S. J. Chua, A. Ishibashi, vol. 4594, Singapore, 260–270 (2001).
- [325] M. Klude, T. Passow, H. Heinke, D. Hommel, phys. stat. sol. (b) 229, 1029 (2002).
- [326] M. Grundmann, D. Bimberg, Phys. Bl. 53, 517 (1997).
- [327] M. Asada, Y. Miyamoto, Y. Suematsu, IEEE J. Quant. Electr. QE-22, 1915 (1986).
- [328] M. Arzberger, Wachstum, Eigenschaften und Anwendungen selbstorganisierter InAs-Quantenpunkte, Ph.D. thesis, Walter Schottky Institut, Technische Universität München, 2001.
- [329] H.-C. Ko, D.-C. Park, Y. Kawakami, S. Fujita, S. Fujita, Appl. Phys. Lett. 70, 3278 (1997).
- [330] M. Rabe, M. Lowisch, F. Henneberger, J. Cryst. Growth 184/185, 248 (1998).
- [331] E. Kurtz, J. Shen, M. Schmidt, M. Grün, S. K. Hong, D. Litvinov, D. Gerthsen, T. Oka, T. Yao, C. Klingshirn, Thin Sol. Films 367, 68 (2000).
- [332] K. Leonardi, H. Heinke, K. Ohkawa, D. Hommel, H. Selke, F. Gindele, U. Woggon, Appl. Phys. Lett. 71, 1510 (1997).
- [333] K. Leonardi, D. Hommel, C. Meyne, J.-T. Zettler, W. Richter, J. Cryst. Growth 201/202, 1222 (1999).
- [334] D. Litvinov, A. Rosenauer, D. Gerthsen, H. Preis, S. Bauer, E. Kurtz, J. Appl. Phys. 89, 4150 (2001).
- [335] T. Passow, H. Heinke, J. Falta, K. Leonardi, D. Hommel, Appl. Phys. Lett. 77, 3544 (2000).
- [336] T. Passow, H. Heinke, T. Schmidt, J. Falta, A. Stockmann, H. Selke, P. L. Ryder, K. Leonardi, D. Hommel, Phys. Rev. B **64**, 193311 (2001).
- [337] T. Passow, K. Leonardi, H. Heinke, D. Hommel, J. Seufert, G. Bacher, A. Forchel, phys. stat. sol. (b) 229, 497 (2002).
- [338] A. Stockmann, Transmissionselektronenmikroskopische Untersuchungen von selbstorganisiertem Wachstum in ZnSe-basierten Halbleiterheterostrukturen, Diploma thesis, Universität Bremen, Institut für Werkstoffphysik und Strukturforschung, 1999.
- [339] T. Kümmell, R. Weigand, G. Bacher, A. Forchel, K. Leonardi, D. Hommel, H. Selke, Appl. Phys. Lett. **73**, 3105 (1998).
- [340] T. Passow, M. Klude, K. Leonardi, D. Hommel, in *Proceedings of the 25th International Conference on the Physics of Semiconductors*, edited by M. Miura, T. Ando, Springer-Verlag, Berlin, 1607–1608 (2001).
- [341] A. Rosenauer, S. Kaiser, T. Reisinger, J. Zweck, W. Gebhardt, D. Gerthsen, Optik 102, 63 (1996).
- [342] A. Rosenauer, TEM-Untersuchungen von epitaktischen Grenzflächen in II-VI/III-V Heterostrukturen, Ph.D. thesis, Universität Regensburg, 1996.

- [343] J. Gutowski, K. Sebald, P. Michler, T. Passow, M. Klude, D. Hommel, (2002).
- [344] G. Bacher, H. Schmömig, J. Seufert, M. Rambach, A. Forchel, A. A. Maksimov, V. D. Kulakovskii, T. Passow, D. Hommel, C. R. Becker, L. W. Molenkamp, phys. stat. sol. (b) 229, 415 (2002).
- [345] M. Rambacher, J. Seufert, M. Obert, G. Bacher, A. Forchel, K. Leonardi, T. Passow, D. Hommel, phys. stat. sol. (b) 229, 503 (2002).
- [346] J. Seufert, M. Obert, M. Scheibner, N. A. Gippius, G. Bacher, A. Forchel, T. Passow, K. Leonardi, D. Hommel, Appl. Phys. Lett. **79**, 1033 (2001).
- [347] S. V. Ivanov, A. A. Toropov, S. V. Sorokin, T. V. Shubina, I. V. Sedova, A. A. Sitnikova, P. S. Kop'ev, Z. I. Alferov, H.-J. Lugauer, G. Reuscher, M. Keim, F. Fischer, A. Waag, G. Landwehr, Appl. Phys. Lett. 74, 498 (1999).
- [348] S. V. Ivanov, A. A. Toropov, T. V. Shubina, S. V. Sorokin, A. V. Lebedev, I. V. Sedova, P. S. Kop'ev, G. R. Pozina, J. P. Bergman, B. Monemar, J. Appl. Phys. 83, 3168 (1998).
- [349] A. Hundt, T. Flissikowski, M. Lowisch, M. Rabe, F. Henneberger, phys. stat. sol. (b) 224, 159 (2001).
- [350] U. Bockelmann, G. Bastard, Phys. Rev. B 42, 8947 (1990).
- [351] H. Benisty, C. M. Sotomayor-Torres, C. Weisbuch, Phys. Rev. B 44, 10945 (1991).
- [352] S. Xu, A. A. Mikhailovsky, J. A. Hollingsworth, V. I. Klimov, Phys. Rev. B 6504, 5219 (2002).
- [353] M. Sugawara, K. Mukai, H. Shoji, Appl. Phys. Lett. 71, 2791 (1997).
- [354] Agilent Technologies, http://www.agilent.com, 2002.
- [355] F. D. Nunes, N. B. Patel, J. E. Ripper, IEEE J. Quant. Electr. QE-13, 675 (1977).
- [356] Y. Fan, D. C. Grillo, M. D. Ringle, J. Han, L. He, R. L. Gunshor, A. Salokatve, H. Jeon, M. Hovinen, A. V. Nurmikko, G. C. Hua, N. Otuka, J. Vac. Sci. Technol. B 12, 2480 (1994).
- [357] N. Holonyak Jr., IEEE J. Quant. Electr. 34, 584 (1998).
- [358] O. Schulz, Lateral indexgeführte ZnCdSe-Laser, Diploma thesis, Technische Universität Berlin, 2000.
- [359] M. Kuttler, M. Straßburg, V. Türck, R. Engelhardt, U. W. Pohl, D. Bimberg, M. Behringer, D. Hommel, J. Nürnberger, G. Landwehr, J. Cryst. Growth **184/185**, 566 (1998).
- [360] O. Schluz, M. Straßburg, U. W. Pohl, D. Bimberg, S. Itoh, K. Nakano, A. Ishisbashi, M. Klude, D. Hommel, phys. stat. sol. (a) 180, 213 (2000).
- [361] J. Ziegler et al.: SRIM2000, http://www.SRIM.org, 2001.
- [362] Ionenstrahl-Labor des Hahn-Meitner-Institutes Berlin, http://www.hmi.de/isl/FI/index.html, 2001.
- [363] A. Taike, M. Momose, M. Kawata, J. Gotoh, K. Mochizuki, J. Cryst. Growth 159, 714 (1996).
- [364] J. Nürnberger, W. Faschinger, R. Schmitt, M. Korn, M. Ehinger, G. Landwehr, Appl. Phys. Lett. 70, 1281 (1997).
- [365] T. Honda, S. W. Lim, K. Yanashima, K. Inoue, K. Hara, H. Nuekata, H. Kukimoto, F. Koyama, K. Iga, Jpn. J. Appl. Phys. 53, 3878 (1996).
- [366] M. Straßburg, O. Schulz, U. W. Pohl, D. Bimberg, S. Itoh, K. Nakano, A. Ishibashi, M. Klude, D. Hommel, IEEE J. Sel. Topics. Quant. Electr. 7, 371 (2001).
- [367] U. W. Pohl, G. H. Kudlek, A. Klimakov, A. Hoffmann, J. Cryst. Growth 138, 385 (1994).
- [368] D. Eisert, G. Bacher, M. Legge, A. Forchel, J. Nürnberger, K. Schüll, W. Faschinger, G. Landwehr, Appl. Phys. Lett. 71, 1026 (1997).
- [369] T. Ishihara, G. Brunthaler, W. Walecki, M. Hagerott, A. V. Nurmikko, N. Samarth, h. Luo, J. Furdyna, Appl. Phys. Lett. **60**, 2460 (1992).

- [370] D. Eisert, G. Bacher, N. Mais, J. P. Reithmaier, A. Forchel, B. Jobst, D. Hommel, G. Landwehr, Appl. Phys. Lett. 68, 599 (1996).
- [371] M. Legge, G. Bacher, A. Forchel, M. Klude, M. Fehrer, D. Hommel, Electron. Lett. 35, 718 (1999).
- [372] R. D. Martin, S. Forouhar, S. Keo, R. J. Lang, R. G. Hunsperger, R. C. Tiberio, P. F. Chapman, IEEE Photonics Technol. Lett. 7, 244 (1995).
- [373] M. Kamp, J. Hofmann, A. Forchel, F. Schäfer, J. P. Reithmaier, Appl. Phys. Lett. 74, 483 (1999).
- [374] M. Legge, G. Bacher, A. Forchel, M. Klude, M. Fehrer, D. Hommel, J. Cryst. Growth **214/215**, 1045 (2000).

Acknowledgments!

At the end of a thesis it is a noble and fine academic tradition to thank all people that contributed to the work. Just the same, it is common practice that the ordering of the acknowledgments does not express a degree of relevance of the individual contributions. In the same fashion, as a laser diode can only work if each and every individual layer and processing step functions well, this thesis would not have been possible without the help of you all. Thanks!

- First of all, I would like to thank Prof. Dr. D. Hommel. I started to work in his group as early as in 1996. Today, I can consider myself a veteran of his group. During the whole time, he gave me support, motivation, and encouragement. I appreciate this very much. In addition, he provided me with a very fascinating and interesting research topic. Even though ZnSe-based lasers have been considered a dead-end by many people, he never gave in. As a result, we were able to develop some really nice new results, and now, with the realization of the first GaN laser diode, he can truly consider himself as one of the leaders of the research on semiconductor laser diodes in the short-wavelength part of the visible spectrum.
- Furthermore, I want to thank Prof. Dr. D. Silber, who probably did not know much about ZnSe-based laser diodes before I came to him. Nevertheless, he did not hesitate to referee my thesis. This flexibility is appreciated.
- A semiconductor laser diode can only be as good as the epitaxial process and the system allows it. But maintaining and calibrating a MBE machine is not exactly a Friday-afternoon job. I was very happy to have so many nice and competent colleagues in the MBE lab, and especially in the II-VI crew. Salute to Dr. Helmut Wenisch (who taught me MBE), Dr. Karlheinz Leonardi (always there to rescue samples from the mis-aligned transfer system), Thorsten Passow, Carsten Kruse, Akio Ueta, Kalle Vennen-Damm (chief engineer and Master of the Holy Screw), Thomas Seedorf, and Marcos Diaz.
- Just as well, without characterization, no laser will ever shine. Especially, Dr. Heidrun Heinke's XRD-team namely Dr. Volker Großmann and Gabriela Alexe was always keen on measuring new samples after all, you never know, what the grower put into it. But also, PL played a key role in the characterization. I don't know why, but I think I am the only one, who does not know how to cool down the cryo. Thus, I thank all members of the group who measured for me in general.
- Still, the lasers can not lase, yet. Processing is required! That was the task of Dr. Michael Fehrer, Sonja Hesselmann, and Michael Henken. As everyone can seen in my thesis, they did a fine job.
- During my experimental work, I had some very helpful support from students. Jan Müller performed not only many measurements on the laser diodes, he even took my into the sky. That was cool! Aside of that, he always had a story to tell. Michael Henken though just finishing the first semester did a nice job in developing a very useful new software, and he also measured numerous samples.
- Some very nice results were obtained in co-operation with external partners. Dr. Michael Legge, Dr. Gerd Bacher, and Prof. Dr. A. Forchel, from the Universität

Würzburg, who fabricated the first electrically pumped ZnSe-DFB laser, are one of those.

- Matthias Straßburg, Oliver Schulz, Dr. Udo W. Pohl, and Prof. D. Bimberg, from the Technische Universität Berlin, were able to realize the lowest threshold current density and the highest output power ever obtained from ZnSe-baser laser diodes. In addition, they increased the lifetime of my record structure by almost a factor of 10 just by using a new contact. Respect!
- Pelletizing and top-down mounting was developed together with Claas Falldorf and Dr. Martin Nägele from Kranz & Nägele, Bremen, in a project, supported by the Land Bremen, represented by the Bremer Innovationsagentur, BIA. This successful co-operation and the financial support is acknowledged.
- It was always fun to meet and discuss with the colleagues from the other groups of the institute. This holds especially for my colleagues form the semiconductor optics group, Kathrin Sebald, Dr. Stefan Strauf, and Dr. Martin Vehse, for whom my samples had some interesting physics built-in.
- Even though the technical and experimental equipment of the group is astonishing, sometimes, the resources and assistance of external partners was required. I would like to especially thank the Institut für Mikrosysteme, -aktuatoren und -sensoren (IMSAS) of Prof. Binder and Prof. Benecke and Eva-Maria Meyer for this support.
- Without any doubt, the most fascinating and satisfying moments in the life of a laser grower is when he applies current to a new device for the first time. Even after more than three years in this business, I still feel the tension and sensation when a new device comes out of the processing. I think, my colleagues from the GaN group know, what I am talking about. During my work, it was always helpful and instructive to exchange and discuss experiences and results with them. I thank Dr. Sven Einfeldt, Tim Böttcher, and Stephan Figge, and I especially congratulate them to their success in realizing a GaN laser diode. Well done!
- One of the most interesting but not necessarily nicest jobs in the group is the administration of the computer network. Taking care of it is not always fun, however, I could always rely on my fellow-administrator's help in this task. Thanks, Tim!
- I appreciate the assistance of those, who helped me correcting my thesis: Gabriela Alexe, Stephan Figge, Thorsten Passow, Tim Böttcher, and especially my sister Bettina Klude. She was brave enough to scan through all pages, though she never had a big chance to understand it.
- Cheers to my special friends and colleagues: it was not only fun working with you... Gabriela, Sonja, Jan, Tim, my very dear office-mate Stephan, and especially Carmen. You are cool, You rock!
- Thanks to all those, who I did not mention so far. It was a pleasure to work with you all!
- Finally and specially, to my parents, who supported me and were always interested in my work.

Lebenslauf

Matthias Klude

geboren am 4. Dezember 1972 in Bremen Familienstand: ledig

Schulbildung:

Besuch des Kolleg St. Thomas in Vechta, Niedersachsen			
Abitur, Leistungskurse: Physik und Mathematik			
Hochschulausbildung:			
110chochumuss 11uung.			
Beginn des Studiums an der Universität Bremen, Studiengang			
Physik (Diplom)			
Vordiplom			
1			
Einjähriger USA-Aufenhalt an der University of Maryland als			
Stipendiat des DAAD			
Diplomarbeit bei Prof. Dr. D. Hommel, Institut für Festkörper-			

1979–1982 Besuch der Grundschule in Visbek, Krs. Vechta, Niedersachsen

1997–1998 Diplomarbeit bei Prof. Dr. D. Hommel, Institut für Festkörperphysik, Bereich Halbleiterepitaxie, Universität Bremen, Thema: Optimierung von p-Kontakten für II-VI Halbleiterstrukturen
 22.07.1998 Diplom
 1998–2002 Promotionsstudium am Institut für Festkörerphysik, Bereich

Halbleiterepitaxie, Universität Bremen

Bremen, den 19.3.2002